

Exploring the Chemotherapeutic Potential of Semi-synthetically Derived New Phytochemical Entities and Nano Delivery System

by

Arya J. S.
10CC17J39003

A thesis submitted to the
Academy of Scientific & Innovative Research
for the award of the degree of
DOCTOR OF PHILOSOPHY
in
SCIENCE

Under the supervision of
Dr. Kaustabh Kumar Maiti



CSIR-National Institute for Interdisciplinary Science and Technology
(CSIR-NIIST) Thiruvananthapuram, 695019



Academy of Scientific and Innovative Research
AcSIR Headquarters, CSIR-HRDC campus, Sector 19, Kamla Nehru Nagar,
Ghaziabad, U.P. -201002, India

January 2022

Dedicated to my family....

National Institute for Interdisciplinary Science and Technology
(NIIST)

Council of Scientific and Industrial Research (CSIR)
Industrial estate P.O., Thiruvananthapuram- 695019
Kerala, India




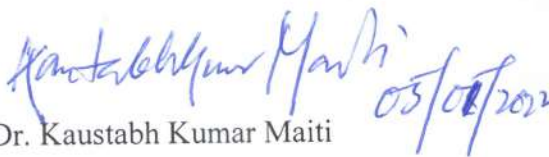
Dr. Kaustabh Kumar Maiti
Principal Scientist
Chemical Sciences and Technology Division

Tel: 0471-2515475
Mob: +91-8547761544
e-mail: kkmaiti@niist.res.in
kkmaiti29@gmail.com

CERTIFICATE

This is to certify that the work incorporated in this Ph.D. thesis entitled, **Exploring the Chemotherapeutic Potential of Semi-synthetically Derived New Phytochemical Entities and Nano Delivery System**", submitted by **Arya J. S.** to the Academy of Scientific and Innovative Research (AcSIR) in fulfilment of the requirements for the award of the **Degree of Doctor of Philosophy in Science**, embodies original research work carried-out by the student. We, further certify that this work has not been submitted to any other University or Institution in part or full for the award of any degree or diploma. Research material(s) obtained from other source(s) and used in this research work has/have been duly acknowledged in the thesis. Image(s), illustration(s), figure(s), table(s) etc., used in the thesis from other source(s), have also been duly cited and acknowledged.


Arya J. S.
5th January 2022


Dr. Kaustabh Kumar Maiti
(Supervisor)
5th January 2022

STATEMENTS OF ACADEMIC INTEGRITY

I **Arya J. S.**, a Ph.D. student of the Academy of Scientific and Innovative Research (AcSIR) with Registration No. 10CC17J39003 hereby undertake that, the thesis entitled “**Exploring the Chemotherapeutic Potential of Semi-synthetically Derived New Phytochemical Entities and Nano Delivery System**” has been prepared by me and that the document reports original work carried out by me and is free of any plagiarism in compliance with the UGC Regulations on “*Promotion of Academic Integrity and Prevention of Plagiarism in Higher Educational Institutions (2018)*” and the CSIR Guidelines for “*Ethics in Research and in Governance (2020)*”.


Arya J. S.

5th January 2022
Thiruvananthapuram

It is hereby certified that the work done by the student, under my/our supervision, is plagiarism-free in accordance with the UGC Regulations on “*Promotion of Academic Integrity and Prevention of Plagiarism in Higher Educational Institutions (2018)*” and the CSIR Guidelines for “*Ethics in Research and in Governance (2020)*”.


Dr. Kaustabh Kumar Maiti

5th January 2022
Thiruvananthapuram

DECLARATION

I, **Arya J. S.** bearing AcSIR Registration No. 10CC17J39003 declare

- (i) that my thesis entitled, “**Exploring the Chemotherapeutic Potential of Semi-synthetically Derived New Phytochemical Entities and Nano Delivery System**” is plagiarism free in accordance with the UGC Regulations on “*Promotion of Academic Integrity and Prevention of Plagiarism in Higher Educational Institutions (2018)*” and the CSIR Guidelines for “*Ethics in Research and in Governance (2020)*”
- (ii) that I would be solely held responsible if any plagiarised content in my thesis is detected, which is violative of the UGC regulations 2018.

5th January 2022
Thiruvananthapuram


Arya J. S.

ACKNOWLEDGEMENTS

It is with great pleasure that I extend my deep sense of gratitude to Dr. Kaustabh Kumar Maiti, my thesis supervisor, for suggesting the research problem, for his valuable guidance, support, motivation and encouragement, leading to the successful completion of this work.

I thank Dr. A. Ajayaghosh, Director, CSIR-National Institute for Interdisciplinary Science and Technology (CSIR-NIIST), Thiruvananthapuram, for providing the necessary facilities to carry out this work.

- ✓ *Dr. V. Karunakaran, Dr. C. H. Suresh and Dr. R. Luxmi Varma, present and former AcSIR co-ordinators.*
- ✓ *Dr. K.V. Radhakrishnan, Dr. L. Ravisankar. and Dr. Priya S., Doctoral Advisory Committee (DAC) members and the whole AcSIR faculty for the successful completion of the course work.*
- ✓ *Dr. P. Sujatha Devi and Dr. R. Luxmi Varma, present and former Head of the Division, Chemical Sciences and Technology Division (CSTD).*
- ✓ *Dr. A. Kumaran, Dr. B. S. Sasidhar, Dr. Sunil Varughese, Dr. Jubi John and Dr. Shridevi. D, Scientists of Organic Chemistry Section, for their help and support extended to me.*
- ✓ *Dr. Mangalam S. Nair for the fruitful discussions and allowing to use the common lab.*
- ✓ *Dr. K. G. Raghu, Dr. K.V. Radhakrishnan, Mr. M. N. Shaw Gurukkal for helping to get the plant materials used in this work.*
- ✓ *Mr. Kiran Mohan & Mr. Robert Philip for TEM analysis, Mrs. Saumini Matthew, Mr. Saran P., Mr. R. Gokul for NMR, Mrs. Viji S., Ms. Athira for mass spectral analyses.*
- ✓ *Dr. T. K. Manojkumar, and Dr. Sherin D. R., IITMK, Thiruvananthapuram for molecular docking studies*
- ✓ *Dr. Manu M. Joseph and Dr. Vishnupriya Murali for their timely suggestions and generous help in completing biological studies.*
- ✓ *Dr. Nisha, Dr. Maniganda, Dr. Jyothi, Dr. Susan, Dr. Vineeth, Dr. Varsha, Dr. Ramya, Dr. Sujai, Dr. Saranya, Mr. Madhu, Mr. Shamjith, Ms. Vidya, Ms. Shamna, Ms. Sreedevi P, Mr. Shihas, Ms. Deepika, Ms. Anjitha Ajith, Ms. Anusree, Ms. Anjitha Nair U. M., and Ms. Sreedevi D for the love, support and companionship.*
- ✓ *Mr. Jerin and Mr. Merin for the general help and support.*

- ✓ *Dr. Parvathy Rathnam, Dr. Dhanya SR, Dr. Adarsh N., Dr. Sajin Francis, Ms. Ranjitha J., Mr. Vishnu K. Omanakuttan for their encouragement and support.*
- ✓ *Dr. S. A. Babu, Dr. Nayyar A. Aslam and all SAB lab mates, IISER Mohali for teaching the techniques of organic synthesis.*
- ✓ *Ms. Kalyani, Ms. Sarin, Ms. Theresa, Mr. Hibathullah and Mr. Hari, internship students for their togetherness and intimacy*
- ✓ *Former and present members of CSTD and friends at CSIR-NIIST, for their help and support.*
- ✓ *All my teachers for their encouragement at different stages of my academic career.*
- ✓ *DST-INSPIRE for the financial assistance*

I would never have completed the dissertation without the support, encouragement and unconditional love from my family. I am deeply and forever indebted to my parents, brother, husband and his family who made it possible for me to reach up to here. I thank the Almighty for all the blessings showered upon me.

TABLE OF CONTENTS

Certificate	i
Statements of Academic Integrity	ii
Declaration	iii
Acknowledgement	iv
Table of Contents	vi
List of Abbreviations	xiii
Preface	xviii

CHAPTER 1

An overview on natural product based phytochemical entities and emerging trends in drug discovery	1-34	
1.1	Introduction	1
1.2	Trends in natural product-based drug research	4
1.3	Phytochemicals in disease management	6
1.3.1	Anti-microbial agents	6
1.3.2	Cardiovascular agents	8
1.3.3	Anti-diabetic agents	8
1.3.4	Anti-obesity agents	9
1.3.5	Anti-malarial agents	9
1.3.6	Immunomodulators	11
1.4	Cancer	11
1.4.1	Importance of chemotherapy in cancer management	13
1.4.2	Importance of natural products in cancer chemotherapeutics	15
1.4.3	Anti-neoplastic agents derived from phytochemicals	15
1.4.3.1	Vinca alkaloids	15
1.4.3.2	Taxanes	16
1.4.3.3	Podophyllotoxin	16
1.4.3.4	Camptothecins	17

1.4.3.5	Other plant derived anti-neoplastic agents in clinical practice	18
1.4.4	Phytochemical entities evaluated in pre-clinical trials	20
1.4.5	Phytochemical entities evaluated in clinical trials	23
1.4.6	Limitations of chemotherapeutic drugs	25
1.4.7	Advancement of drug delivery systems towards better therapeutic outcome	26
1.5	Conclusion	28
1.6	Objectives of the current investigation	29
1.7	References	30
CHAPTER 2A		
Exploring Hydnocarpus wightiana Blume for the Development of New Phyto-chemical Entities Towards Lung cancer and Melanoma		35-64
2A.1	Introduction	35
2A.2	Results and discussion	37
2A.2.1	Chemical synthesis	37
2A.2.2	Primary cytotoxicity screening of Hy- analogues / NPCEs	39
2A.2.3	Evaluation of Hy-derivatives / NPCEs by in-silico studies	41
2A.2.4	Selection strategy based on primary screening and molecular docking studies	48
2A.2.5	Molecular dynamic simulation of selected NPCEs Hy-ISO-G and Hy-ISO-VIII	49
2A.3	Conclusion	50
2A.4	Experimental Section	52
2A.4.1	Chemistry	52
2A.4.1.1	Oxidation of Hydnocarpin to hydnocarpin aldehyde	52
2A.4.1.2	General procedure for the synthesis of hydnocarpin isoxazole derivatives, General procedure A	52
2A.4.1.3	General procedure for the synthesis of hydnocarpin isoxazolone derivatives, General procedure B	56

2A.4.2	Cell culture	59
2A.4.2.2	In vitro cytotoxicity assays	60
2A.4.3	Computational analysis	60
2A.5	References	61
CHAPTER 2B		
Elucidating the mechanism of action of the synthesized Hydnocarpin based NPCEs		65-104
2B.1	Introduction	66
2B.2	Results and discussion	67
2B.2.1	In vitro assessment of Hy-ISO-G and Hy-ISO-VIII for anti-proliferative potential.	67
2B.2.2	Effect on free radicals by Hy-ISO-G and Hy-ISO-VIII.	70
2B.2.3	Apoptotic evaluation of Hy-ISO-G and Hy-ISO-VIII.	72
2B.2.4	Effect of NPCEs on cancer metastasis	75
2B.2.5	Cell cycle regulation by Hy-ISO-G and Hy-ISO-VIII	78
2B.2.6	Evaluation of mitochondrial transmembrane potential by the NPCEs	78
2B.2.7	Evaluation of caspase mediated apoptosis cascade	81
2B.2.8	Molecular level investigation for cellular internalization and cell death mechanism by SERS spectral and mapping analysis	81
2B.2.9	Analysis of NPCEs mediated DNA fragmentation	87
2B.2.10	Estimation of glutathione in cells treated with NPCEs	88
2B.2.11	Evaluation of the involvement of cyt c in the mechanism of action.	88
2B.2.12	Apoptosis antibody array	90
2B.3	Conclusion	93
2B.4	Materials and methods	93
2B.4.1	Cell culture	93

2B.4.2	In vitro cytotoxicity assays	93
2B.4.3	Antioxidant activity	94
2B.4.3.1	DPPH radical scavenging assay	94
2B.4.3.2	FRAP (Ferric reducing antioxidant power) assay	94
2B.4.3.3	Hydroxyl radical scavenging assay	95
2B.4.4	Apoptotic assays	95
2B.4.5	Anti-metastatic assays	96
2B.4.5.1	Invasion and migration assay	96
2B.4.5.2	Wound healing assay	97
2B.4.5.3	Colony formation assay	97
2B.4.6	Caspase assay	97
2B.4.7	Raman spectral imaging	97
2B.4.8	DNA fragmentation analysis	98
2B.4.9	GSH estimation	98
2B.4.10	Cyt c quantitation	98
2B.4.11	Apoptosis antibody array	99
2B.5	References	99

CHAPTER 3

Germacrone Analogues from Curcuma raktakanta Resembling Oxaliplatin 105-133

– Active Molecular Entities against Breast Cancer

3.1	Introduction	106
3.2	Results and Discussion	108
3.2.1	Isolation of germacrone	108
3.2.2	Synthesis of metal-germacrone/pyrogermacrone complexes	109
3.2.3	Cytotoxicity screening of the synthesized metal complexes	110
3.2.4	Structure optimization using DFT calculation	112
3.2.5	Detailed cytotoxic evaluation of the selected metal complexes	112
3.2.6	Effect of Pt-pyger in Pt resistant cancer cells	115
3.2.7	Anticancer properties of Pt-pyger complex	117

3.2.8	Investigation of apoptotic events by tracking the intracellular signature molecular fingerprints by surface enhanced Raman scattering (SERS) modality.	118
3.2.9	Antimetastatic properties of Pt-pyger complex	120
3.2.10	Mechanism of Pt-pyger mediated cell death	122
3.3	Conclusion	122
3.4	Materials and methods	123
3.4.1	Isolation of germacrone	123
3.4.2	Synthesis of pyrogermacrone	123
3.4.3	Synthesis of Pt-ger complex	123
3.4.4	Synthesis of Pt-pyger complex	124
3.4.5	Synthesis of Ir-ger complex	124
3.4.6	Synthesis of Ir-pyger complex	124
3.4.7	Synthesis of Ru-ger complex	125
3.4.8	Synthesis of Ru-pyger complex	125
3.4.9	DFT calculation	126
3.4.10	Cytotoxicity evaluation	126
3.4.11	ICPMS analysis	126
3.4.12	Apoptosis studies	126
3.4.13	Anti-metastatic assays	127
3.4.14	Live cell Raman imaging	127
3.4.15	Apoptosis antibody array	127
3.5	References	128

CHAPTER 4

Biocompatible Polymer Based Targeted Nano-Delivery System for the Combination Chemotherapy of Embelin and RPI-1 against Pancreatic cancer cells

4.1	Introduction	134
4.2	Results and Discussion	136
4.2.1	Plant material collection and extraction	136
4.2.2	Isolation and characterization of embelin	136
4.2.3	Cytotoxicity profiling of Embelin and RPI-1	138

4.2.4	Establishment of the synergic combination of Embelin and RPI-1 using the combination index method	138
4.2.5	Fabrication of chitosan coated PLGA nanoparticle for pH responsive synergic release of embelin and RPI-1	141
4.2.6	Drug loading, drug release kinetics and stability of nano-construct	141
4.2.7	Biocompatibility, cellular internalization, and cytotoxicity evaluation of the nano-construct	142
4.2.8	Apoptotic evaluation of the nano-construct	146
4.2.9	Change in mitochondrial membrane potential	148
4.2.10	Cell cycle regulation	148
4.2.11	Anti-metastatic effects of nano-construct	148
4.2.12	Analysis of the change in metabolomics	151
4.3	Conclusion	153
4.4		
4.4.1	Materials and methods	154
4.4.2	Synthesis of plectin targeting peptide KTLLPTP	155
4.4.3	Synthesis of carrier system	156
4.4.4	Drug loading studies	157
4.4.5	Drug release kinetics	157
4.4.6	In vitro cytotoxicity assays	157
4.4.7	Cellular uptake studies	157
4.4.8	Biocompatibility assays	158
4.4.9	Apoptosis studies	158
4.4.10	Mitochondrial membrane potential assay	158
4.4.11	Anti-metastatic assays	159
4.4.12	Live cell Raman imaging	160
4.4.13	Metabolic profiling	160
4.5	References	160
	Abstract	167
	List of publications	169

List of conference presentations

170

Attachment of the photocopy of publications

List of Abbreviations

A375	Human malignant melanoma cells
A549	Adenocarcinomic human alveolar basal epithelial cells
AFM	Atomic force microscopy
ATCC	American type culture collection
AuNPs	Gold nanoparticles
Bcl-2	B-cell-lymphoma-2-gene
BrdU	5-bromo-2'-deoxyuridine
^{13}C	Carbon
CCD	Charge coupled device
CDCl_3	Deuterated chloroform
CH_2Cl_2	Dichloromethane
CHCl_3	Chloroform
CH_3OH	Methanol
CI	Combination index
CNS	Central nervous system
cm	Centimetre
CO_2	Carbondioxide
CS	Chitosan
Cyt C	Cytochrome C
d	doublet
dd	Doublet of doublet
DCC	N, N'-Dicyclohexylcarbodiimide
DCFDA	dichlorofluoresceindiacetate
DCM	Dichloromethane
DIC	N,N'-Diisopropylcarbodiimide

DIPEA	N,N-Diisopropylethylamine
DLS	Dynamic light scattering
DMEM	Dulbecco's modified Eagle's medium
DMF	Dimethylformamide
DMSO	Dimethyl sulfoxide
DNA	Deoxy ribo-nucleic acid
Dox	Doxorubicin
DPPH	1, 1-diphenyl-2-picrylhydrazil
dt	Doublet of triplet
EDC	1-Ethyl-3-(3-dimethylaminopropyl)carbodiimide
EGFR	Epidermal growth factor receptor
ELISA	Enzyme-linked immunosorbent assay
Emb	Embelin
ER	Estrogen receptor
ESI	Electron spray ionization
FBS	Fetal bovine serum
FDA	Food and drug administration
FITC	Fluorescein isothiocyanate
FRAP	Ferric reducing antioxidant power
g	Gram
GSH	Glutathione
¹ H	Proton
h	hour
HER2	Human epidermal growth factor receptor-2
HGF	Hepatocyte growth factor
H ₂ O	Water

H ₂ O ₂	Hydrogen peroxide
HOBT	Hydroxybenzotriazole
HPLC	High performance liquid chromatography
HRMS	High resolution mass spectroscopy
Hz	Hertz
ICPMS	Inductively coupled plasma mass spectrometry
LDH	Lactate dehydrogenase
LOD	Limit of detection
m	Metre
M	Molar
MCF-7	Human breast cancer cells
MCR	Multi-component reaction
MD	Molecular dynamics
MDA-MB-231	Epithelial, human breast cancer cell line
mg	Milligram
mL	Millilitre
MHz	Mega hertz
min	Minutes
mm	Millimetre
mM	Millimolar
mmol	Millimol
MTT	3-[4,5-dimethylthiazol-2yl]-2, 5 diphenyl tetrazolium
MDR	Multi-drug resistant
NHS	N-hydroxysuccinimide
NIR	Near infrared
nm	Nanometre

NMR	Nuclear magnetic resonance
NPCEs	New phytochemical entities
NPs	Nanoparticles
Nps	Natural products
OCT-2	Organic cation transporter 2
PANC-1	Human pancreatic cancer cell line
PC	Pancreatic cancer
PDA	Photo diode array
P-L	protein-ligand
PLGA	Poly(lactic-co-glycolic acid)
Plectin-1	Plec-1
ppm	Parts per million
PR	Progesterone receptor
RBCs	Red blood cells
ROS	Reactive oxygen species
RMSD	Root mean square deviation
RNA	Ribo nucleic acid
rpm	Revolutions per minute
RT	Room temperature
s	singlet
SASA	Solvent accessible surface area
SERS	Surface enhanced Raman spectroscopy
SKOV3	Ovarian cancer
SPPS	Solid phase peptide synthesis
t	Triplet
T	Temperature

TEM	Transmission electron microscopy
TFA	Trifluoro acetic acid
THF	Tetrahydrofuran
TMRE	Tetramethylrhodamine ethyl ester
TNBC	Triple negative breast cancer
TUNEL	Terminal deoxynucleotidyltransferase (TdT) dUTP nick-end labeling
UV-Vis	Ultraviolet-visible
μM	Micromolar
μm	Micrometre
WI-38	Human lung fibroblast cell line
XIAP	X-linked inhibitor of apoptosis protein

PREFACE

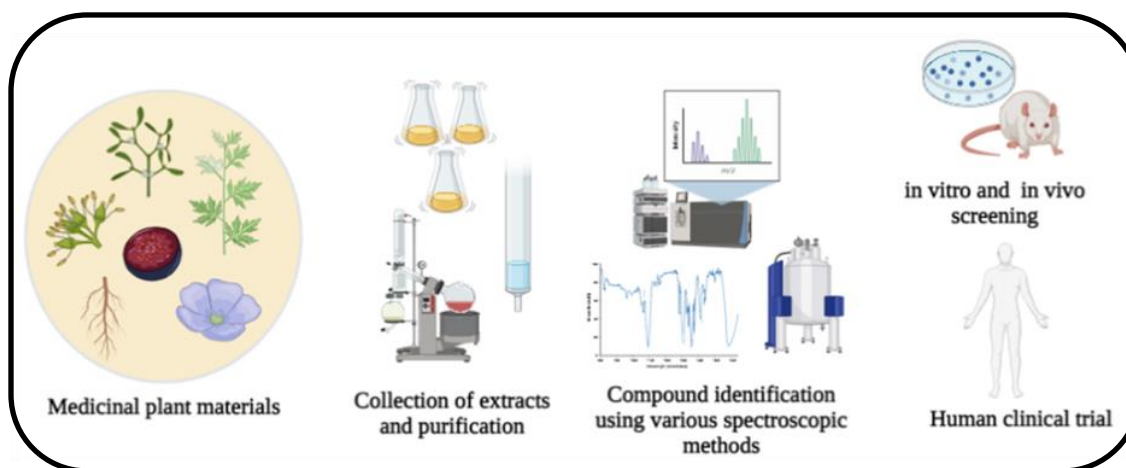
Nature has been a source of drug molecules from ancient times, and many modern medicines have been isolated from various natural sources based on their practice in folklore medicine. Natural products play a title role in meeting the collective demand for novel molecules, much of which are unexplored. Increasing occurrence rate of cancer and extreme complexity caused by chemotherapeutic agents reduces the therapeutic efficacy of a wide range of anti-neoplastic agents that are currently in clinical use. Chapter 1 points up the irreplaceable role natural products have played, and continue to play, in the drug discovery process, particularly in the area of oncology.

In Chapter 2A, synthesis, characterization and screening of hydnocarpin (HY)-isoxazole/isoxazolone derivatives has been demonstrated for the enhanced anticancer effect in human lung cancer and melanoma cells. The semi-synthetic modification on HY by one pot multi-component reaction (MCR) and [3+2] cycloaddition strategy yielded five membered isoxazole and isoxazolone appended HY derivatives. After detailed in vitro cytotoxicity and in silico interaction studies, two derivatives were found to be most potent derivatives against lung and melanoma cancer cells. The detailed mechanistic evaluation of the mode of cell death induced by the selected derivatives is described in chapter 2B. Surface-enhanced Raman spectroscopy (SERS) was employed to real time monitoring of cytochrome C mediated cell death and associated DNA fragmentation.

Chemotherapy of triple negative breast cancer (TNBC) involves the administration of Platinum (Pt) drugs that causes severe side effects including nephrotoxicity and other health risks to the patients. There exists a huge demand for the development of reno-protective strategies for the Pt-drug mediated therapy. In chapter 3, Pt, Ir and Ru metal complexes of germacrone, was synthesized and detailed cytotoxicity evaluation was also carried out. The selected molecule could overcome the Pt resistance along with the selective toxicity towards TNBC cells.

Systemic chemotherapy remains the vital treatment modality for the patient survival affected with pancreatic cancer. In chapter 4, synergic combination of naturally occurring cytotoxic agent embelin and c-Met inhibitor RPI-1 was established for an efficient therapeutic potential against pancreatic carcinoma cell line PANC-1. Biocompatible and biodegradable PLGA nano-carrier targeted delivery system loaded with the optimized drug combination was designed for effective therapeutic utility.

An Overview on Natural Product Based Phytochemical Entities and Emerging Trends in Drug Discovery



Abstract: Nature has been a source of drug molecules for centuries, and quite a large number of modern medicines have been isolated from various natural sources based on their practice in folklore medicine. With the development of new molecular targets-based drug discovery, there is a collective demand for novel molecules for screening. Natural products (Nps) play a title role in meeting this need by continuously investigating the world's biodiversity, much of which remains unexplored. By using combinatorial biosynthetic and semi-synthetic approach, new Np leads can be optimized based on their biological activities to yield potent chemotherapeutic and other bioactive entities. This chapter points up the irreplaceable role that Nps have played, and continue to play, in the drug discovery process, particularly in the area of oncology.

1.1 Introduction

Natural products (Np) have been used to treat a wide range of diseases, and their impact has been referenced copiously. Mother Nature has been a cradle of medicinal products for ages, with many beneficial drugs developed from plant sources. It is evident that nature will continue to be a major source of new fundamental leads, and effective drug development depends on multidisciplinary approaches.¹ Previously, these naturally occurring compounds were used in

the crude form. Advancement in science facilitated the isolation, structural elucidation, and preparation of active metabolites from plants, and numerous naturally occurring bioactive components are now offered in pure form as drugs.²

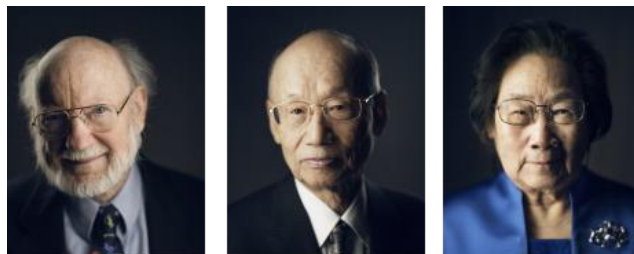


Figure 1: William C. Campbell, Satoshi Omura, and You you Tu, Nobel prize winners in physiology or medicine in 2015.

William C. Campbell, Satoshi Omura, and You you Tu shared the Nobel prize in physiology or medicine in 2015 for the discovery of the avermectins (microbial Np), ivermectin (derivative of avermectin), and artemisinin (plant Np) (Figure 1). These drugs played vital role in reducing the occurrence of onchocerciasis (river blindness), lowering the rate of lymphatic filariasis (elephantiasis), and declining the mortality rates of malarial patients, respectively. These drug molecules revolutionized the management of ruinous parasite diseases and brought the greatest delight to the global Np community.³

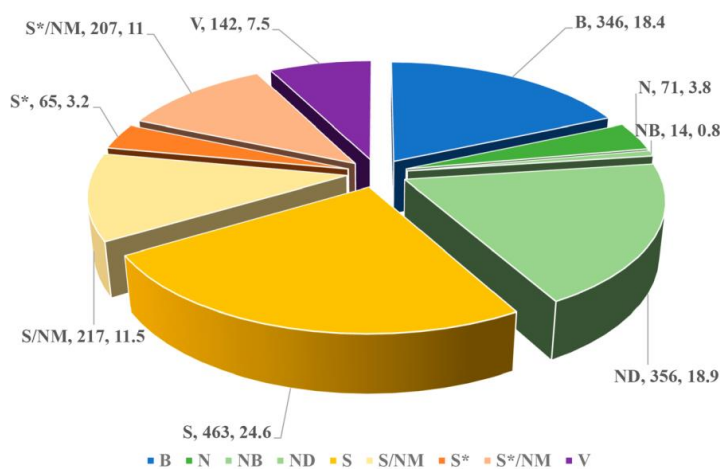


Figure 2: All new approved drugs from 01st JAN 1981 to 30th SEP 2019; n = 1881 ; B: Biological, N: Natural product, NB: Natural product “Botanical”, ND: Derived from a natural product and is usually a semisynthetic modification, S: Totally synthetic drug, S*: Made by total synthesis, V: Vaccine. Adapted with permission, American chemical society, 2020.

Plant-based traditional medicinal systems like traditional Chinese medicine and Ayurveda have been practicing for thousands of years and are extensively documented. These systems represent a reserve of new molecular entities with the anticipation of exhibiting better efficacy in disease management.⁴ According to GIA (Global Industry Analysts), the herbal supplements and remedies market is projected to reach US \$115 billion by 2020. Asian countries have a long tradition of herbal medicine and have a rich diversity of medicinal and herbal plants. The world trade in botanicals is US \$32.702 billion of which Asia accounts for US \$14.505 billion (44.35%). The international market of herbal products is estimated to be US \$62 billion and poised to grow at a rate of 7 percent per annum to US \$5-7 trillion by 2050.⁵

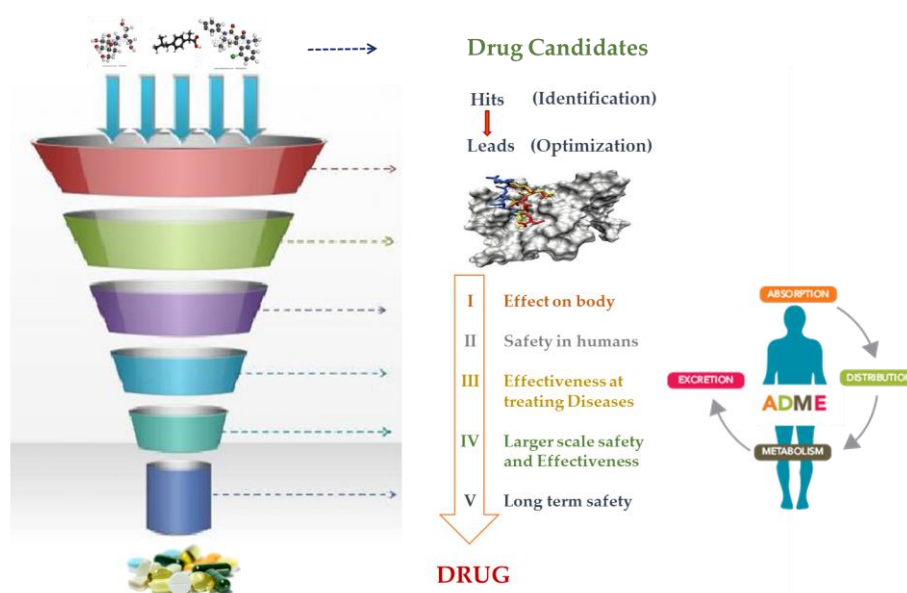


Figure 3: Drug discovery regime.

A review by Newman et.al in 2020, gives a completely updated and expanded version on "Natural products as source of new drugs" in a time frame that have been extended to cover 39 years from January 1, 1981 to September 30, 2019 for all approved antitumor drugs worldwide (Figure 2).⁶ It is evident that Nps are continuing its overwhelming contribution to the expansion of chemotherapeutic armamentarium and much of the nature's "treasure trove of small molecules" still remain to be explored. This multidisciplinary approach to drug discovery involving molecular diversity from Nps sources combined with total and combinatorial synthetic methodologies provides the best solution for the current productivity crisis faced by the research world engaged in pharmacogenetics.^{7,8} Drug development from Nps follows a

systemic approach in today's industry (Figure 3). Hundreds of potential targets with thousands of diverse chemical compounds are tested through high-throughput screening (HTS) techniques so as to identify promising lead molecules.

Rational drug design is another technique of inventing innovative medications that involves computational analysis, design and synthesis of small molecules. Target identification must be followed by target validation to confirm that interfering with the target protein will impact the disease. Once the target is validated, small molecules require examination of several aspects, which includes evaluation of affinity/specificity (binding scores), ADME (absorption, distribution, metabolism, and excretion), toxicity, QSAR (quantitative structure-activity relationship), QSPR (quantitative structure-property relationship). Lead generation and optimization is a tedious and time-consuming process which can take from 12 to 15 years over 800 M US Dollar to bring a drug from concept/isolation to market.⁹

1.2 Trends in natural product-based drug research

Nps refer to products from various natural sources, plants, microbes and animals. It can be a whole organism or a part of an organism, an extract of an organism, an exudate, or pure compound (e.g., alkaloids, coumarins, flavonoids, lignans, steroids and terpenoids) isolated from plants, animals or microorganisms. However, the term Nps refers to secondary metabolites (carotenoids, phytosterines, saponines, phenolic compounds, alkaloids, glycosidates, terpenes etc), small molecules (molecular weight < 1500 amu), produced by an organism, but not strictly necessary for normal growth, development or reproduction and the survival of the organism. Only around 15% of the 250,000 species of terrestrial plants have been chemically and pharmacologically investigated. Even lower is the percentage of insects, marine organisms, fungi, and microbes investigated.¹⁰

Nps can be broadly divided into two classes:

1. **Primary metabolites:** They are compounds essential for a life with an intrinsic function. They are directly involved in normal growth, development, and reproduction, so they are referred to as central metabolites. Examples of primary metabolites include carbohydrates, lipids, proteins, amino acids (L-glutamate, L-lysine), and nucleic acids.
2. **Secondary metabolites:** They are organic compounds produced through the modifications of primary metabolites. They do not play major roles in growth, development, and reproduction

as with primary metabolites and are formed either during the end or near the growth stationary phase. These are produced due to the adaptation to its environment or are produced to assist the survival of the organism by defending predators. They have shown great potential as therapeutic agents without any substantial role in plant life.¹¹ The unique biosynthesis of the secondary metabolites offers the representative chemical structures that hold various pharmacological activities.

Secondary metabolites can be obtained from diverse sources like animal, plants, microbial and marine metabolites. Definitely, one of the most potent Np discoveries that revolutionized the drug discovery scenario was that of penicillin that saved innumerable lives. Alexander Fleming discovered penicillin in 1929 from the fungus *Penicillium notatum*. Chain and Florey won the 1945 Nobel prize in physiology and medicine for developing the separation technique that could yield penicillin in high yields.¹² Most of the early medicines were formulated from traditional medicinal practices with the assistance of chemical, pharmacological and clinical studies. Plants are the primary source of bioactive molecules, and around 25% of the prescribed drugs are plant derived ones. Isolation of morphine, one of the commercially significant drugs, from *Papaver somniferum* (opium poppy) (Figure 4a) by Serturmer in 1803 marked the beginning of Np chemistry. Morphine was derivatized to heroin by boiling in acetic anhydride and was found to be easily transformed to codeine (painkiller).⁸

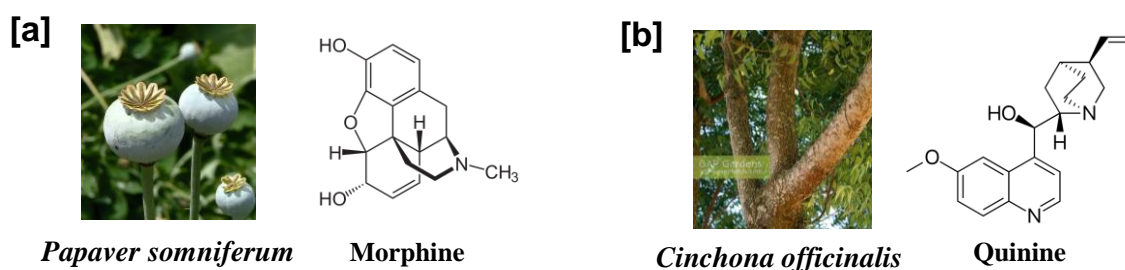


Figure 4: Structure of morphine and quinine.

FDA-approved antimalarial drug quinine was isolated from the bark of *Chinchona* species (Figure 4b). This species' bark had been used for centuries by the indigenous tribes in the amazon area for healing fever, malaria, throat and mouth disease, indigestion, etc. Quinine is an integral part of the synthesis of mefloquine and chloroquine, the commonly used antimalarial drugs. L-histidine-derived alkaloid, Pilocarpine, isolated from *Pilocarpus jaborandi*, was used to treat glaucoma for over 100 years. FDA approved an oral formulation

of this particular compound in 1994 for the treatment of dry mouth (xerostomia).¹³

1.3 Phytochemicals in disease management

Phytochemicals possessing prominent pharmacological activities have traditionally been used to cure various human illnesses like pain, fever, cold, general injuries, etc. These natural agents regulate several crucial pathways that cause cytotoxic, genotoxic, and mitogenic reactions leading to various pathologies. In recent times, many Nps with various bioactivity have been processed and developed as promising pharmacological agents with the assistance of new technological tools like proteomics, genomics, metabolomics, etc. In fact, some Nps with extreme biological relevance have been modified as lead compounds to generate semisynthetic derivatives with enhanced therapeutic efficacy.¹⁴ The flourishing knowledge accumulated over the years encourages us to develop drug molecules with effective anti-inflammatory, antioxidative, anti-infective, antimetabolic, anticarcinogenic properties, etc. Following are some of the examples.

1.3.1 Anti-microbial agents

The fortuitous discovery of penicillin marked the 'golden age of antibiotics.' Following that, many penicillin derivatives were semi-synthetically prepared with the β -lactam core, 6-aminopenicillanic acid (6-APA). Later, many mainstream antibiotics were isolated from other bacterial strains like Cephalosporium, Streptomyces, Actinomycetales, etc. The evolution of resistance made these conventional antibacterial drugs set off less effective. Antimicrobial resistance has turned into a life-threatening issue and affected the socio-economic and medical implications. Among the strategies experimented with overcoming drug resistance was the use of semi-synthetic derivatives of these antibacterial drugs and administering a combination of compounds. Many semi-synthetic derivatives of the parent antibiotic molecules are now used in first-line therapy. For example, doxycycline and minocycline are derived from tetracycline. Similarly, azithromycin is an analog of erythromycin (Figure 5). Many phytochemicals unveiled promising results in mastering the occurrence of antibiotic resistance in bacterial pathogens.¹⁵

Piperine, an alkaloid containing piperidine ring isolated from *Piper longum* and *Piper nigrum* when administered in combination with ciprofloxacin, reduced the MIC value and inhibited the growth of *S. aureus*.¹⁶ Many phenolids terpenoids and alkaloids have been used as anti-viral agents. The common phytosterols like oleanolic acid and ursolic acid found in many

plants are active agents against HIV. More examples of anti-microbial agents derived from phytochemicals are discussed in **table**

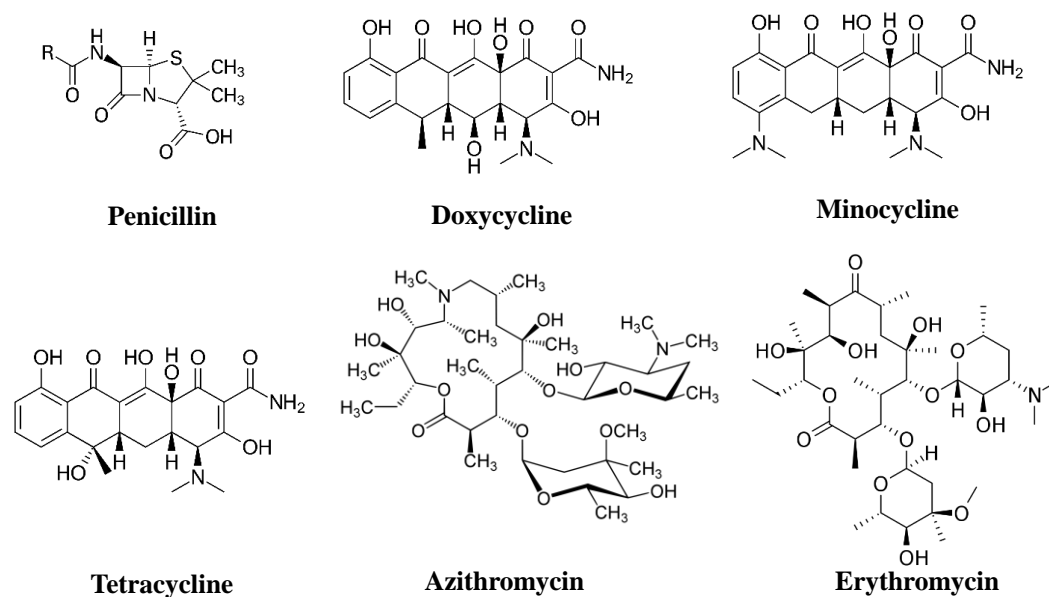


Figure 5: Natural product derived antibacterial agents.

Table 1: Some of plant products with antimicrobial activity¹⁶

Sl no:	Compound	Plant's Scientific name (Common name)	Active against
1	Piperine	<i>Piper nigrum</i> (Black pepper)	Fungi, Lactobacillus, Micrococcus, <i>E. coli</i> , <i>E. faecalis</i>
2	Berberine	<i>Berberis vulgaris</i> (Barberry)	Bacteria, protozoa
3	Eugenol	<i>Syzygium aromaticum</i> (Clove)	General
4	Allicin, ajoene	<i>Allium sativum</i> (Garlic)	General
5	Curcumin	<i>Curcuma longa</i> (Turmeric)	Bacteria, protozoa
6	Allicin	<i>Allium cepa</i> (Onion)	Bacteria, Candida
7	Caffeic acid, Thymol	<i>Thymus vulgaris</i> (Thyme)	Viruses, bacteria, fungi
8	Glabrol	<i>Glycyrrhiza glabra</i> (Licorice)	<i>S. aureus</i> , <i>M. tuberculosis</i>
9	Resveratrol	Multiple sources	<i>Mycobacterium smegmatis</i> , <i>Campylobacter jejuni</i>

1.3.2 Cardiovascular agents

Cardenolides or cardiac glycosides are typically used, therapeutic agents. These are steroidal in nature comprising a lactone group. These molecules act on the membrane-bound Na-K ATPase pump, which results in the reduction of heart rate and increased cardiac output. Two potent cardiac glycoside the vitan A & B were isolated from the plant *Thevetia neriifolia* (Yellow oleander plant). Another compound reserpine isolated from *Rauwolfia serpentine* exhibits promising anti-hypertensive activity.⁸ This compound was first tested in India and the inhibitory activities are explained by blocking mono amine oxidase (MAO). Garlic extracts and some of the *Allium* organosulfur compounds are reported to have hypocholesterolemic effects in animal and human models. The reaction between captopril and allicin yielded a novel antihypertensive agent. Captopril holds promising antihypertensive properties due to its ability to inhibit the angiotensin-converting enzyme.¹⁷ Fulyzaq® (crofelemer; extract from the red latex of *Croton lechleri* Müll.Arg (Dragon's blood tree), Veregen® (sinecatechins; leaf extract of *Camellia sinensis* (green tea) and Grastek® (pollen allergen extract of *Phleum pratense* L (Timothy grass) are some of the FDA approved botanical drugs.¹⁸

1.3.3 Anti-diabetic agents

Diabetes mellitus (DM) is a metabolic disorder caused due to various causes marked by chronic hyperglycemia with instabilities of fat, carbohydrate, and protein metabolism associated with insulin action or/and insulin secretion defects. The major classes of modern medicine used globally for regulating blood glucose levels are sulfonylureas, biguanides (metformin), meglitinides (glinides), thiazolidinediones (glitazones), DPP-4 inhibitors, and alpha-glucosidase inhibitors. Insulin and incretin mimetics are the prescriptions given by injection. Most modern drugs have several adverse effects leading to severe medical problems. Besides allopathic medicine, herbal remedies have been used for a long time. Many phytochemicals have been proved to be active agents in the management of DM.¹⁹

Diosmin, a flavonoid isolated from *Scrophularia nodosa*, exhibited excellent anti-diabetic activity by decreasing glycosylated hemoglobin levels, up-regulates glutathione peroxidase activity, increases insulin levels, and improving oxidative stress. Hesperidin, another flavonoid molecule isolated from *Citrus aurantium*, exhibits anti-diabetic activity by downregulating the generation of free radicals and the release of pro-inflammatory cytokines.²⁰ India is the world's capital of diabetics, and several home remedies are used for the treatment. *Sylvestre gymnema* (gurmar), from which gymnemic acid is isolated which is known for hypoglycaemic activity.

Further, *Momordica charantia*, commonly known as Kerela, is rich in momordicoside, proving to be an excellent anti-diabetic agent. Ethanolic extracts of *Momordica* seeds assure the protection of pancreatic β -cells.¹⁹

1.3.4 Anti-obesity agents

Obesity is a severe health issue characterized by extreme body fat accumulation and occurs due to higher energy intake than energy expenditure. Conventional medicines used to treat obesity have high exploitation potential and usually exhibit side effects. Tea is the second most widely consumed beverage globally in (green, black, and oolong) different forms with different color and phytochemical composition changes. It is the reservoir of numerous phenolic compounds like (-)-epicatechin-3-gallate (ECG), (-)-epigallocatechin-3-gallate (EGCG), proanthocyanidins, etc. The reason for weight loss on consumption with green tea is the high caffeine content, increased triacylglycerol excretion, suppressed leptin levels, suppressed food intake, upregulation of fatty acid synthesis and oxidation, etc.²¹ Another familiar tree, *Mangifera indica* (Mango) is known for its medicinal values in traditional medicine. Alcoholic extracts of stem bark and leaves of *M. indica* exhibited anti-obesity effects in obese rats induced with a high-fat diet. The stem comprises many bioactive molecules like mangiferin, catechin, alanine, protocatechuic acid, shikimic acid, etc. The alcoholic extract is reported to inhibit lipoprotein lipase and pancreatic lipase, reduced serum insulin and glucose levels, increased excretion of fecal fat, and down-regulated genes related to obesity genes the epididymal fat and liver.²² Guggulipid, developed at Central Drug Research Institute (CDRI)-Lucknow, from *Commiphora mukul* resin, exhibits excellent hyperlipidemic property and is widely consumed as an anti-obesity agent.⁸

1.3.5 Anti-malarial agents

Malaria is one of the major global health issues, affecting a large group of people worldwide. Plasmodium parasites which reach the human body through female anopheles mosquitoes bites, get matured, reproduce in the hepatic cells causing malaria. The common symptoms are headache and fever, and in critical cases, it causes death. The ever first anti-malarial drug, quinine, an alkaloid molecule, was isolated from the barks of *Cinchona officinalis* by Caventou and Pelletier in 1820.²³

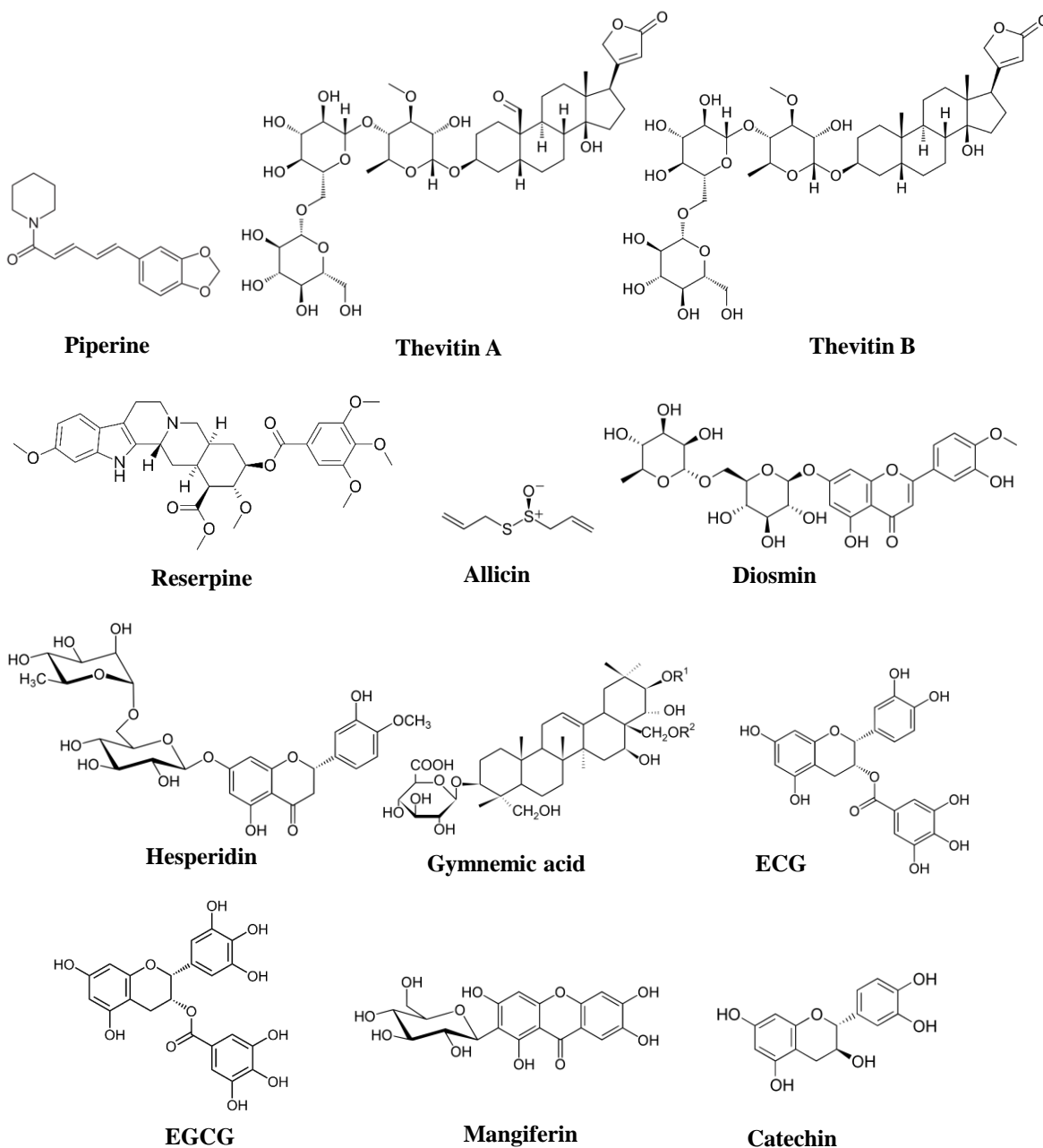


Figure 6: Some of the Plant derived bioactive molecules.

Later, many quinine derivatives like chloroquine, mefloquine, halofantrine, etc. were developed and are still used in the first-line treatment. Strains resistant to these quinine drugs had spread leading to higher mortality rate due to malarial infection. Recently artemisinin-based combinations are found to be most effective in the action of malarial patients.²⁴ In India, neem which have nimbolides, is used in Ayurveda as an antimalarial agent. Alkaloids like anastrocladidine, ancistrotanzanine and ancistrocladinium B isolated from leaf extracts of

Anastrocladus heyneanus exhibited significant anti plasmodial activity and showed promising results against malarial infection.²⁵

1.3.6 Immunomodulators

For maintaining the normal physiological functions and establishing homeostasis, a well-functional immune system is important. This helps to uphold good health by having a sufficient biological defense mechanism towards disease, unwanted biological attack, infection, and tolerance towards autoimmune diseases and allergies. An immune-modulator is a biological or non-biological element that influences or modifies a particular immune function. Quite many traditional or synthetic medicines are accessible in the market, which majorly causes several adverse effects along with its beneficial effect. Numerous phytochemicals have been shown their potential as an immunomodulator. The potential immunomodulatory activities possessed by these moieties can aid the management of some of the long-term diseases like cardiovascular diseases, cancer, etc.^{26,27} The glucoside molecule from *Mangifera indica* exhibited promising immunoregulatory activity by improving the imbalance between cytokines. Berberine has shown excellent immunomodulatory function by regulating TNF- α , IFN- γ , and Nitric oxide (NO). Immunomodulatory action of several polysaccharides isolated from *Lycium barbarum*, *Solanum nigrum*, *Aloe arborescens*, etc has also been evaluated. The immunomodulatory function of these polysaccharides is attributed to their ability to down-regulate cytokines like IL-6, TNF- α and upregulates IL-4, IL-2, and IL-10. Recently polyphenols attained much notice in the food industry due to their biological activity. Presently, a wide range of these molecules displays immunomodulatory activity by varying the development of eicosanoids, nitric oxide, obstructing gene expressions, and proinflammatory cytokines. Molecules like centaurein, orientin, vitexin, naringenin, genistein, etc., are examples of polyphenols showing immuno-stimulatory activity.²⁷

1.4 Cancer

Cancer is a significant public health problem and the second ‘biggest killer’. Cancer is defined as “a malignant tumor of potentially unlimited growth that expands locally by invasion and systemically by metastasis” in the Merriam –Webster dictionary.²⁸ In India, non-communicable diseases (NCDs) were projected to account for 63% of total deaths, and cancer holds the leading causes (9%). Researchers have made remarkable breakthroughs for

understanding the origin and development of cancer in the human body over the past few decades, which made advancements in treatment and diagnosis. The overall mortality rate is showing a declining trend in the last five years, but the average incidence rate is still 20.2%.²⁹ The estimated number of cancer patients in India is more than 1.3 million for the year 2020, and the common five leading sites are breast, lung, mouth, cervix uteri, and tongue. According to a study conducted in 2020, 1 in 29 females (breast cancer), 1 in 68 males (lung cancer), and 1 in 9 Indians will develop cancer during their lifetime (0-74 years of age).³⁰ Based on a recent study based on Indian population, lung cancer stands for the highest occurrence in males. Lung cancer was the leading site in metropolitan cities and the southern region. According to major population-based cancer registries (PBCRs), breast cancer and cervical cancer were the most common cancers in women. Currently, breast and cervical cancer are the leading cancer types amongst women in India, posing a major public health problem which desires important input from various health and other research organizations to tackle.³⁰ Though breast, lung, mouth, cervix, uteri, and tongue are the leading cancer types, there are few varieties which are more deadly due to its very less survival rate. Pancreatic cancer and metastatic melanoma hold the top positions in those. Pancreatic adenocarcinoma is a fatal condition with poor results and an increasing occurrence. Pancreatic cancer is ranked as the 14th most common cancer and the 7th highest cause of cancer mortality in the world. It often diagnosed at an advanced stage that adds to poor five-year survival rates (2%-9%), placing firmly last among all cancer types in terms of predictive outcomes for patients.³¹

Malignant melanoma is the most notorious variant of skin cancer which remains a provoking challenge to multidisciplinary researchers, including chemists, biologists, and clinicians, for better disease management. It is one of the most passive variants of cancer known to therapies in the metastatic stage due to its multi-drug resistance (MDR) and intrinsic resistance to apoptosis triggering pathways. Malignant melanoma is usual among caucasoid trait with roughly ten times higher risk of rising cutaneous melanoma than other traits. In India, malignant melanoma is rare, and its occurrence is less than 0.5%. Most primary cutaneous malignant melanoma cases are treated by surgical excision, but 30% may progress into metastatic lesions later, often in the lung. After ten years of apparent cure, recurrence of malignant melanoma is uncommon, and its incidence is 0.65%-6.7% (Figure 7).³²

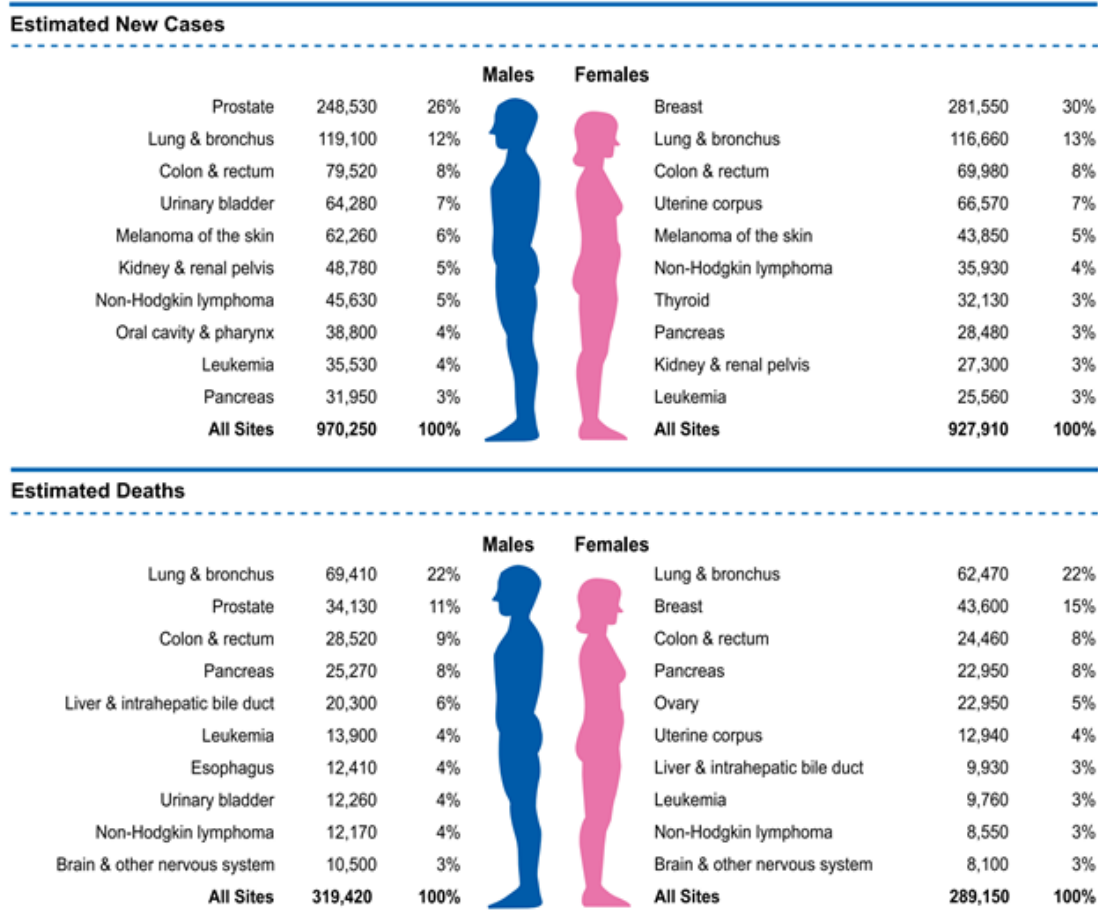


Figure 7: Ten Leading Cancer Types for the Estimated New Cancer Cases and Deaths by Sex in 2021. Adapted with permission, Wiley, 2021.

1.4.1 Importance of chemotherapy in cancer management

Cancer chemotherapy refers to the administration of cytotoxic chemicals, i.e., compounds that can kill cells, with the aim to, in some cases, eliminate the tumor or decrease the tumor growth and, thereby, lowers the tumor-related indications and thus prolong life. The use of synthetic or natural agents to prevent, slow down or reverse the process of carcinogenesis is an important approach for easing this challenging public health burden. For effective cancer management, surgery, radiation therapy, chemotherapy, targeted therapies, and immunotherapy separately or in combination are generally advised. Early diagnosis, surgical removal of tumor followed by effective radiotherapy, chemotherapy, and further treatment modalities are the key aspects in defining the patient's prognosis.

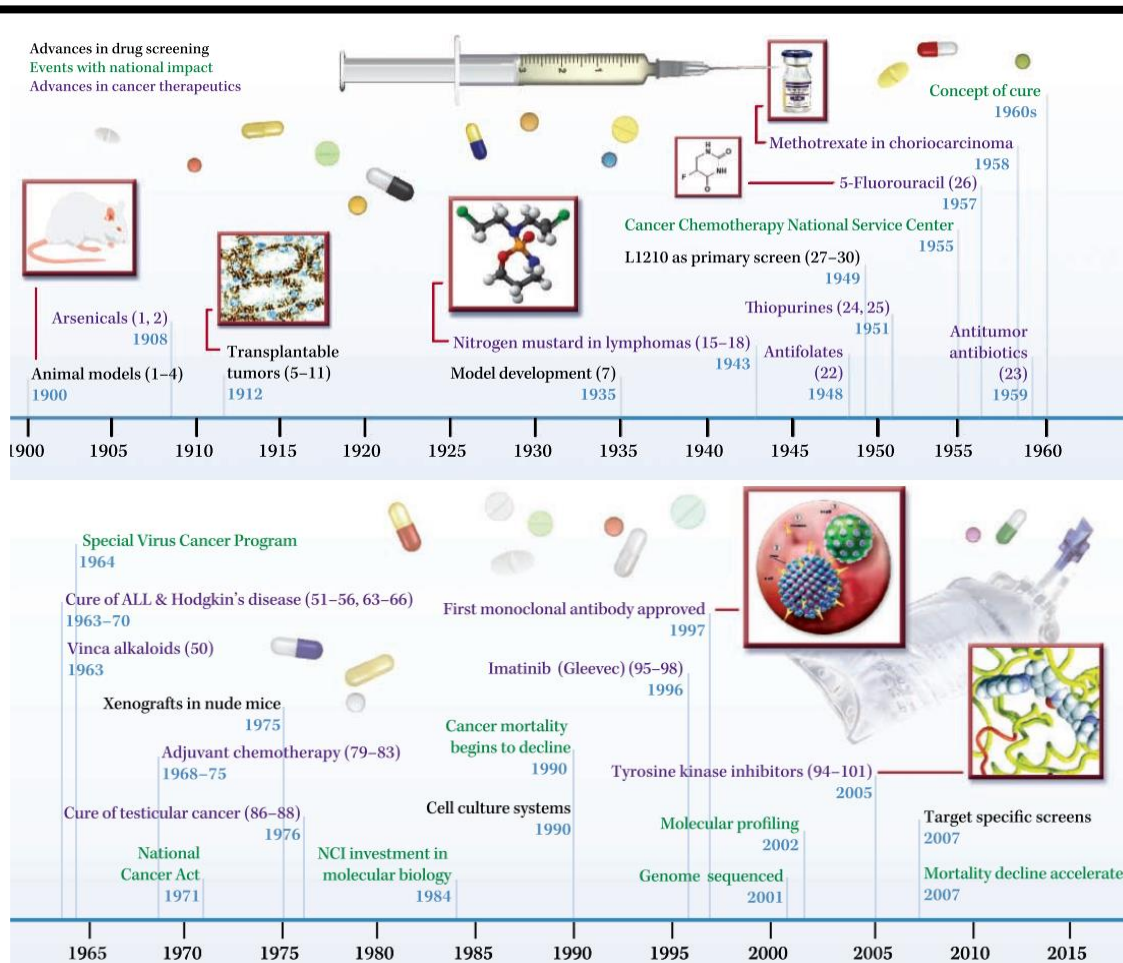


Figure 8: Key advances in the history of cancer chemotherapy, Adapted with permission American Association for Cancer research, 2008.

Undoubtedly, the prevention of human cancer is highly preferable to treatment. However, when dealing with malignant, metastatic types, it is usually necessary to resort to chemotherapy.³³ The different treatment modalities may cause various side effects, and chemotherapy-based procedures seem to have reached a therapeutic plateau. Though cancer chemotherapy was introduced earlier, it was first effectively practiced in the 1950s when nitrogen mustard (war gas) was found to be efficient in hindering tumor progression. By the beginning of the 1970s, cancer chemotherapy flourished to offer, in combination with other treatment modalities, to extend the life span of patients or as a means to cure selected cancer types etc (Figure 8).

Many of the meaningful advances that have been realized for the treatment of cancer are directly correlated with the discovery of natural product derived drugs and drug intermediates.

The current advancement in technology has enabled chemists and biologists to explore the potential use of natural compounds for the efficient treatment or regulation of cancer. In the last 30 years, natural compounds have been the pillar of the source and development of chemotherapeutic drugs. In terms of drugs under clinical trials, as is the case with existing ones, Nps have played a significant role in cancer chemoprevention.^{33,34}

1.4.2 Importance of natural products in cancer chemotherapeutics

Almost 60% of the current anticancer drugs were derived in one way or another from natural sources such as vincristine, irinotecan, etoposide and paclitaxel from plants, actinomycin D and mitomycin C from bacteria as well as marine-derived bleomycin. Nature always remains an abundant source of bio-active and diverse chemotypes, while relatively few of the actual isolated Nps turned into clinically active drugs. Phytochemicals serve as major resources for unique drugs and are also sources for potent antineoplastic agents. Some characteristic examples include taxol analogs, podophyllotoxin analogs and vinca alkaloids. The following sections briefly discuss some of the developments in this area, with discussions limited to new agents derived from phytochemicals currently in some stage of advanced clinical development or agents approved for clinical use.^{33,35}

1.4.3 Anti-neoplastic agents derived from phytochemicals

Traditionally, plant life has been the principal source of Np drug discovery. In the case of the anticancer arena, phytochemicals such as vincristine (VCR) and vinblastine (VBL), paclitaxel (Taxol®), and docetaxel, topotecan, and irinotecan, are among the most effective cancer chemotherapeutics currently available. Nevertheless, many phytochemicals suffer from poor solubility in aqueous media and possess substantial toxic side effects. Thus, extensive research dedicated to reducing the impact of these factors are being conducted, and numerous prodrugs and analogs of these agents have been synthesized, and methods devised for increasing aqueous solubility and targeting specific tumors.³⁶

1.4.3.1 Vinca alkaloids

Vinca alkaloids, VBL, and VCR isolated from the Madagascar periwinkle, *Catharanthus roseus* G. Don (Figure 8a) were the first plant-derived agents to advance into clinical use. While under investigation as a potent oral hypoglycemic agent, the plant extracts reduced WBC counts and triggered bone marrow depression in rats. Further, it was noted that the plant

extract is active against lymphocytic leukemia in mice. Further investigation of the active agents led to the isolation of VBL and VCR, and their discovery paved the way for the observation of an unrelated medicinal use of *C.roseus*. VBL and VCR have been used in clinical oncology for almost 50 years. Vinca alkaloids inhibit cell proliferation by affecting the microtubule dynamics during mitosis causing metaphase arrest leading to apoptosis. Microtubules are accompanied by several other cellular processes like motility, maintenance of cell shape, and transport between organelles. These vinca alkaloids affect both non-malignant and malignant cells in the non-mitotic cell cycle.³⁷ A series of semi-synthetically modified analogs of these two alkaloids have been designed (Table 2).

1.4.3.2 Taxane

Taxanes are another group of promising anti-neoplastic agents that were reported from the bark of the Yew tree. Presently, the two most potent clinical drugs of this class are paclitaxel (Taxol®), formerly isolated from the bark of *Taxus brevifolia* Nutt. and Docetaxel (Taxotere®). Due to the poor water solubility and toxicity towards non-cancerous cells, Docetaxel was synthesized from 10-deacetylbaccatin III (DAB), isolated from the leaves of another species I (Figure 8b) of the same family, *Taxus baccata*. DAB serves as a sustainable source of paclitaxel as it can be semi-synthetically transformed into paclitaxel. Leaves of *T. baccata* were documented in the ayurvedic medicine system and were being used to treat ‘cancer.’ Docetaxel, which is more effective than the parent compound, can be used in patients with paclitaxel resistance as well. The mechanism of action of taxanes was majorly executed by the destabilization of microtubules, causing cell cycle arrest leading to apoptosis. Several semisynthetic derivatives have improved cytotoxicity in resistant tumors, decreased toxicity, and enhanced solubility. For example, a second-generation docetaxel derivative, cabazitaxel, exhibits cytotoxic activity against various docetaxel-resistant tumors with less overall toxicity. Another characteristic of cabazitaxel is its ability to penetrate the blood-brain barrier *in vivo*, which is not achievable with other taxanes.^{33,37}

1.4.3.3 Podophyllotoxin

Podophyllotoxin is a natural product isolated from the roots of *Podophyllum peltatum* and *Podophyllum emodi* (Berberidaceae) (Figure 8c). These plants were used in the Indian subcontinent for the treatment of skin cancer and warts. Though the compound was isolated in

the 1880s, the structure elucidation was done in the 1950s. However, clinical trials of several closely related podophyllotoxin-like lignans failed due to a lack of unacceptable toxicity and efficacy. Two semisynthetic derivatives designed from epipodophyllotoxin (an isomer or of podophyllotoxin) etoposide and teniposide are potent anticancer agents in clinical use for treating bronchial and testicular cancers as well as lymphomas. The mechanism of action of podophyllotoxin is by reversibly binding to tubulin, whereas etoposide and teniposide inhibit topoisomerase II, leading to topoisomerase II-mediated DNA damage. Also, podophyllotoxin exhibits prominent anti-multidrug resistant (MDR) activity against various drug-resistant cancer cells.^{33,37}

1.4.3.4 Camptothecins

Camptothecin (CPT) is a cytotoxic quinolone alkaloid isolated from wood and bark of the tree *Camptotheca acuminata* (Figure 8d). Though the compound's anticancer activity was known in the early 1960s, it took almost 20 years to use it as an anticancer agent until the mechanism of action was revealed. CPT possesses an S-configured lactone form and a carboxylate form which is responsible for the anti-neoplastic activity. CPT precisely traps topoisomerase I, leading to the formation of topoisomerase-DNA complexes.

These complexes eventually cause genomic stress to the ongoing DNA replication fork or transcription machinery contributing to apoptosis. Poor solubility and severe bladder toxicity are the disadvantages of CPT. Extensive research led to the development of two semi-synthetic derivatives, topotecan, and irinotecan, with less toxicity, enhanced solubility, and potent anticancer property than the parent compound. Topotecan and irinotecan are clinically used extensively for first and second-line treatment in various cancer types like lung, ovarian, breast, colon cancers, etc.^{33,35,37}

To avoid the challenges related to unfavorable metabolism, oral bioavailability, drug resistance, and toxicity associated with presently marketed CPTs, many semi-synthetic analogs of CPTs were designed and developed. Cositecan (Karenitecin; BNP1350) and silatecan (AR-67) are lipophilic silicon-containing CPTs modified in the 7-position. Further lipophilic analogs are gimatecan, another 7-substituted CPT derivative, and diflomotecan (BN80915), a 10,11-difluoro-homoCPT. Water-soluble analogs currently in clinical development are the hydrochloride salts of lurtotecan, elemotecan, and namitecan, as well as DRF-1042 being developed by Dr. Reddy's Research Foundation.³³

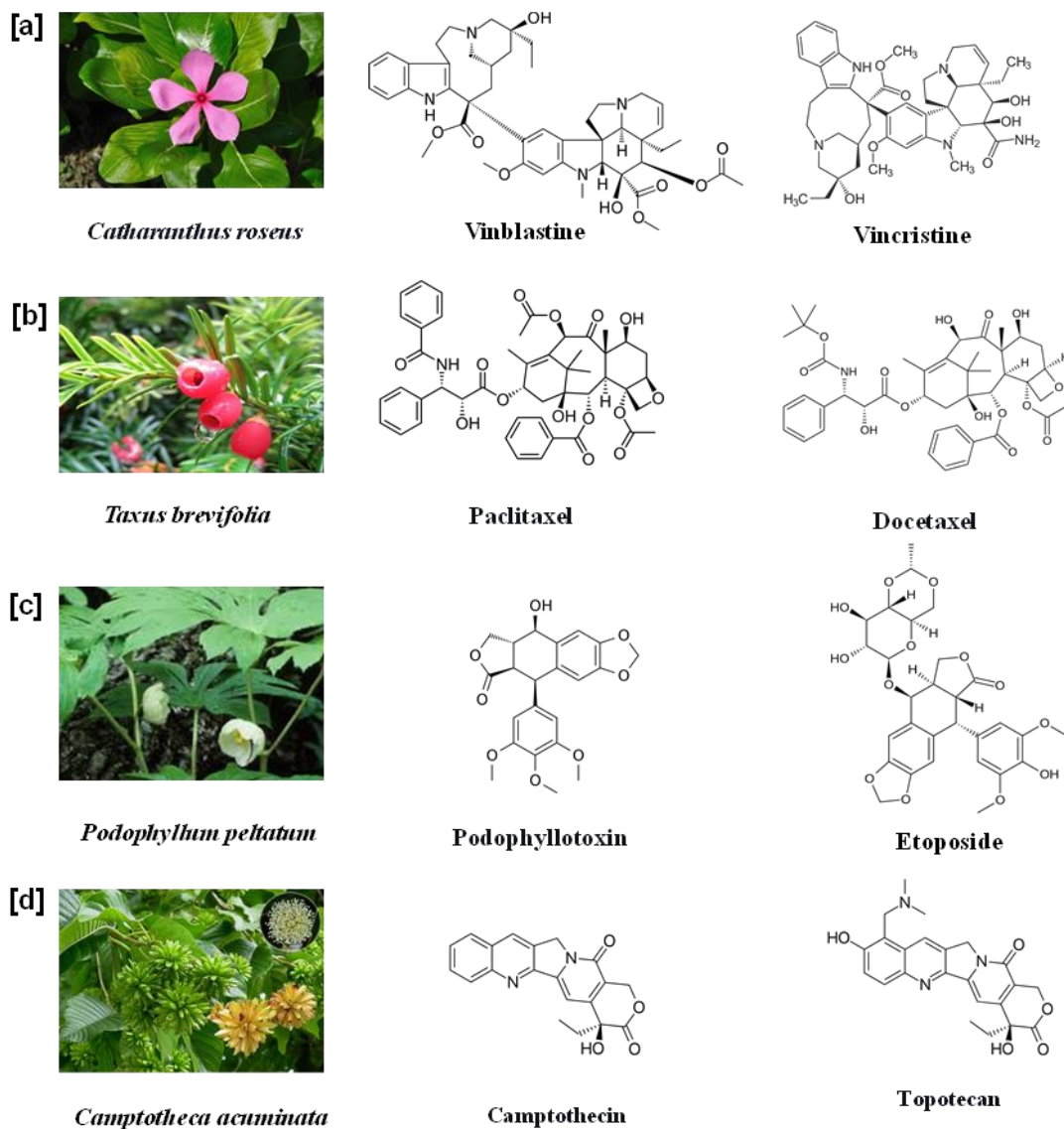


Figure 8: some of the plant derived anti-cancer drugs.

1.4.3.5 Other plant derived anti-neoplastic agents in clinical practice

Combretastatins belongs to the family of cis-stilbenes initially isolated from the root bark of *Combretum caffrum*. These molecules selectively target the endothelial cells in the tumor area and cause vascular disruption. Other than this, they remodel the actin cytoskeleton and disrupt the tubulin cytoskeleton driving a notable change in the 3D shape of immature endothelial cells, leading to nutrient starvation and cell death. Combretastatin A1 and combretastatin A4 are the two naturally isolated compounds. Combretastatin A4 phosphate (CA4P) is a phosphate prodrug of combretastatin A4 that has been designated as an orphan drug by the US FDA and

is approved for the treatment of a range of ovarian and thyroid cancer. Combretastatin A1 diphosphate (CA1P; OXI-4503) is a phosphate prodrug of CA1, and it has shown promising efficacy in the treatment of patients with relapsed and refractory acute myelogenous leukemia (AML) and myelodysplastic syndromes.

Homoharringtonine (HHT) is a naturally occurring alkaloid-ester of cephalotaxine isolated from various trees of the *Cephalotaxus* genus (Cephalotaxaceae) and is approved for the treatment of chronic myeloid leukemia. *Cephalotaxus species* have been used in traditional Chinese medicine for the treatment of various ailments. HHT binds to the A-site cleft in the large ribosomal subunit affecting chain elongation and stops protein synthesis. A semisynthetic derivative of HHT, omacetaxine mepesuccinate, is found to be effective in the treatment of myelodysplastic syndromes and chronic myelomonocytic leukemia (CML). HHT (Synribo) is thought to act as a broad-spectrum protein tyrosine kinase inhibitor and was approved in 2012 by the FDA for the treatment of adult patients with CML or accelerated phase CML.

Ingenol mebutate (IM) is a hydrophobic diterpene ester of ingenol isolated from *Euphorbia peplus* (Euphorbiaceae). IM is approved for the topical treatment of actinic keratosis, a common skin condition that results from exposure to chronic ultraviolet radiation which can lead to squamous cell carcinoma, if not treated. IM presents two mechanisms of action: at high concentrations (~200–300 μM), it induces rapid induction of cell death in the treated area and at low concentrations (~0.1 μM) it activates inflammatory response, capable of eliminating the residual cells.

Table 2: Compounds used for cancer treatment, Adapted with permission from ref ³⁷

Class of phytochemical	Pharmacological action	Type of cancer	Molecular targets
Vinca alkaloids			
Vinblastine	Inhibit microtubule polymerization and assembly, leading to metaphase arrest and cell death.	Non-small-cell lung carcinoma (NSCLC),	Tubulin
Vincristine		breast,	
Vindesine		lung, leukemia,	
Vinflunine		Hodgkin and non-Hodgkin lymphomas,	
Vinorelbine		testicular carcinoma, Kaposi's sarcoma, and second-line transitional cell carcinoma of the urothelium (TCCU)	

Taxanes			
Cabazitaxel	Inhibit microtubule function resulting in cell cycle arrest and aberrant mitosis	Inhibit microtubule function resulting in cell cycle arrest and aberrant mitosis	Tubulin
Docetaxel			
Paclitaxel			
Podophyllotoxin			
Etoposide	Inhibits DNA synthesis by forming a complex with topoisomerase II and DNA.	Osteosarcoma, cervical, colon, prostate, and cancer	NSCLC, nasopharyngeal, breast, and testicular
Teniposide			Topoisomerase II
Camptothecin			
Irinotecan	Stabilizes topoisomerase I-DNA complex thereby preventing religation of single strand breaks resulting in lethal double-stranded breaks in DNA.	Ovarian, cervical, colorectal, and small cell lung cancer (SCLC)	Topoisomerase I
Topotecan			
Other plant-derived anticancer agents			
Homoharringtonine	Binds to large ribosomal subunit, which affects chain elongation and prevents protein synthesis	Chronic myeloid leukemia	Ribosomal protein
Combretastatin A4	Inhibits polymerization of tubulin	Polypoidal choroidal vasculopathy, thyroid cancers	Tubulin

1.4.4 Phytochemical entities evaluated in pre-clinical trials

In the drug development process, meticulous preclinical screening can come about the identification of potential lead compounds for bench to bedside application. This will comprise extensive investigation on preliminary toxicity, efficacy, pharmacokinetic, and safety information which will aid to adopt a molecule further for clinical trials. Some of the phytochemicals and its derivatives which has shown promising results in preclinical analysis are discussed below.

Alliin is an organic allyl sulfur component present in garlic (*Allium sativum*) and was reported to have anti-neoplastic activity in various cancer types. It was majorly studied for its effects on cholangiocarcinoma (CCA). Alliin significantly retarded the growth of human liver bile duct carcinoma in BALB/c nude mice model of CCA. Also, molecular study revealed that alliin (20 μ M) decreased the levels of matrix metalloproteinase (MMP)-2 and -9 to decrease epithelial-mesenchymal transition (EMT) invasion and migration of HuCCT-1 cells. Furthermore, alliin turned down the proliferation by activating the caspase cascade, inducing apoptosis, and reducing the expression of proteins downstream of STAT3, like B-cell lymphoma 2 (Bcl-2), while up-regulating Bcl-2-associated X (Bax) protein.

6-Shogaol is a bioactive component isolated from ginger (*Zingiber officinale*). This compound inhibited the growth of NCI-H1650 lung cancer cells in a nude mice model of NSCLC, which was associated with increased apoptosis and decreased cell proliferation as evidenced by reduced Ki-67-positive cells. 6-shogaol reduced the Akt signaling via direct targeting of Akt1 and Akt2. Intraperitoneal administration of 6-shogaol (100 mg/kg body weight) lowered the tumor volume in a syngeneic FVB/N mice model of prostate cancer. Gingerol is another biologically active molecule presents in the rhizomes of ginger. Gingerol (5 mg/kg) treatment was found to induce caspase-3 activation and inhibited the tumor growth and metastasis in a syngeneic mouse model of spontaneous breast cancer metastasis

Apigenin (APG) is a naturally occurring flavonoid found in vegetables and fruits with prominent anti-neoplastic properties. In an experiment conducted in athymic nude mouse xenograft with human chondrosarcoma Sw1353 cells, APG (5 mg/kg) suppressed tumor growth associated with a decrease in Ki67 expression and induction of apoptosis. At the molecular level, APG regulated the expression of the Bcl-2 family protein and turned on the caspase cascade to induce G2/M phase arrest and apoptosis. In another explorative study, APG (3 mg/kg) targeted the dipeptidyl peptidase IV (DPPIV) enzyme to hinder the growth and metastasis of NSCLC xenografts.

Dicumarol (DC) is an anticoagulant molecule derived from coumarin by the bacterial action in spoiled sweet clover hay (*Melilotus officinalis*). The *in vitro* analysis of the compound suggested that it inhibited the activity of pyruvate dehydrogenase kinase 1 (PDK1), generated an elevated level of ROS, reduced the mitochondrial membrane potential (MMP), promoted

apoptosis, and attenuated cell viability of SKOV3 cells. Remarkably, DC (32 mg/kg) was found to be safe for developing oocytes and ovarian tissues; implicating the importance of DC as a potential anticancer agent when female fertility preservation is a concern.

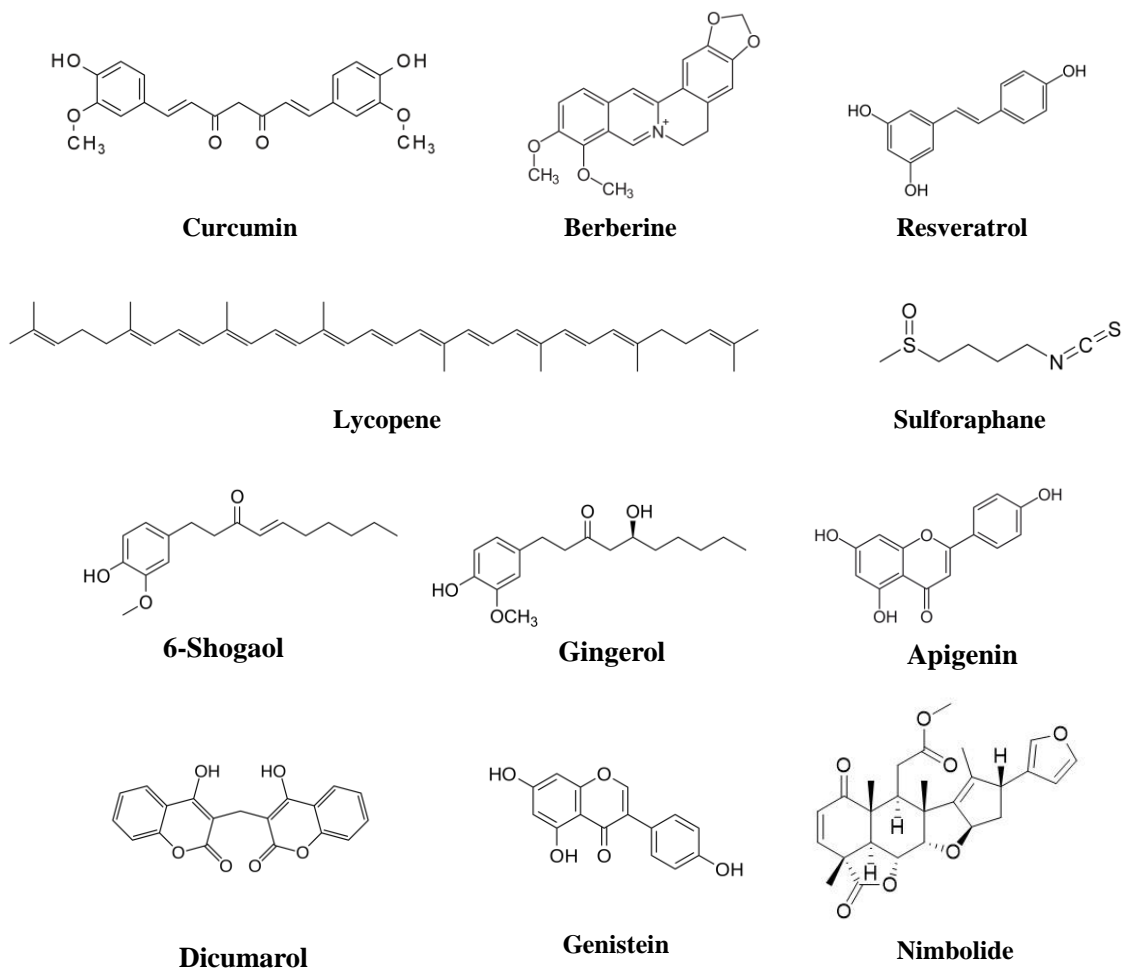


Figure 9: Some of the phytochemicals having anti-neoplastic properties

Genistein is an isoflavone majorly present in soybeans holding estrogen-like properties. The molecule showed promising anti-cancer properties. In a study carried out in azoxymethane (AOM)-induced rat colon cancer model, genistein (140 mg/kg) administration reduced the total aberrant crypts. In another study, athymic BALB/c nu/nu mouse xenograft with human leukemia cell line HL60, intraperitoneal administration of the compound (0.4 mg/kg) for 28 days considerably reduced the tumor weight without having any effect on body weight. The molecule induced G2/M phase arrest at the cellular level, followed by apoptosis of HL60 cells mediated via ROS ER stress.

Nimbolide is a triterpene molecule isolated from the flowers and leaves of the neem tree (*Azadirachta indica*). Nimbolide (5 mg/kg) inhibited the pancreatic cancer cell HPAC growth and metastasis by inducing apoptosis. The molecular mechanistic studies revealed the role of nimbolide in ROS generation, proliferation inhibition (through reduced PI3K/AKT/mTOR and ERK signaling), and metastasis inhibition (through decreased EMT, invasion, migration, and colony-forming abilities) via mitochondrial-mediated apoptotic cell death.

HS-1793 is a semi-synthetic analogue of resveratrol with enhanced photostability. This compound remarkably suppressed the growth of MDA-MB-231 (human breast cancer) cells with decreased expression of Ki-67 and CD31 proteins. Also, HS-1793 administration down-regulated the expression of HIF-1 and vascular endothelial growth factor (VEGF) proteins. Apart from the anti-angiogenesis and growth inhibitory effects, HS-1793 enhanced ionizing radiation-induced apoptosis and inhibited hypoxia-induced cancer stem cell properties in hypoxic mouse breast cancer FM3A cells.

1.4.5 Phytochemical entities evaluated in clinical trials

Clinical trials of drug candidates based on phytochemicals against cancer are still in infancy, though numerous anti-neoplastic agents are presently under development. The clinical trials with phytochemicals majorly focus on the following aspects: 1) decreasing the side effects of standard cancer therapy, 2) enhancing the response towards standard chemo- and radiotherapy, 2 and 3) looking for unwanted interactions with standard therapy. Preclinical studies elucidated the effectiveness of many phytochemicals such as curcumin, berberine, catechins, green tea, including EGCG, resveratrol, quercetin, lycopene, sulforaphane, etc. (Figure 9)

Curcumin, the active ingredient in turmeric (*Curcuma longa*), a yellow polyphenolic pigment, is reported to be an extremely promising chemo-preventive agent against various cancer types. Studies conducted by many research groups warranted the clinical trial of the compound to address the safety, pharmacokinetics, and efficacy issues of the molecule in humans. Phase I clinical trials revealed that even at high doses, curcumin is safe for humans but exhibited poor bioavailability. Despite bioavailability challenges, clinical trials with curcumin in combination with other drugs have shown effectiveness against several cancer types like breast, prostate, pancreatic, etc. for example, in patients with advanced or metastatic pancreatic cancer,

administration of curcumin Meriva® (2,000 mg/day) in complementary to gemcitabine increased the efficacy of gemcitabine without any treatment-related toxicity. More than 15 actively ongoing cancer-related trials using curcumin are registered on clinicaltrials.gov.in.

Berberine is a benzyl-tetra isoquinoline alkaloid majorly found in *Berberis sp.* (Berberidaceae). These plant extracts have long been used in Ayurvedic and traditional Chinese medicine. Though large preclinical efficacy data of berberine is reported in various cancer types, clinical trial data reveals its efficacy in other clinical conditions like type 2 diabetes. Currently, a randomized, double-blind, placebo-controlled phase 2/3 trial is ongoing against the incidence of colorectal adenomas in 1,000 patients to fix the efficacy of berberine hydrochloride (300 mg/twice/day) (NCT03281096).³⁸

Epigallocatechin (EGCG) is a significant catechin molecule isolated from green tea (*Camellia sinensis*). Quite a few studies using *in vitro* and *in vivo* models have recognized the anticancer property of EGCG. Clinical trial data provide evidence regarding the safety of a catechin mixture containing EGCG (200 mg/day) in a group diagnosed with high-grade prostatic intraepithelial neoplasia. Another study has recommended using EGCG in combination with indole-3-carbinol for better therapeutic efficacy in advanced ovarian cancer patients. Currently, a randomized, early phase 1 trial is ongoing to assess the chemopreventive effects of Teavigo™ (purified and refined green tea extract having 94% EGCG) (450 mg/PO/day) in colorectal cancer (CRC) patients with curative resections (NCT03072992).³⁷

Resveratrol (3,5,4'-trihydroxy-trans-stilbene) is a stilbenoid molecule found mainly in the red grape skin (*Polygonum cuspidatum*). In a phase I study on men with elevated PSA (prostate-specific antigen) levels in recurrent prostate cancer, pulverized muscadine grape skin extract containing 4,000 mg resveratrol delayed the development of recurrence by increasing the prostate-specific antigen doubling time (PSADT). In another feasibility study carried out on 39 women having elevated risk for breast cancer, trans-resveratrol (50 mg twice a day for 12 weeks) decreased methylation of Ras association domain family 1 isoform-A gene, amplified levels of resveratrol-glucuronide and trans-resveratrol in the circulation, and reduced cancer-promoting PGE2 expression in the breast. Recently, a clinical trial aimed at the role of resveratrol (2.5 gm/p.o./twice/day) on Notch-1 signaling in low-grade gastrointestinal neuroendocrine tumors was completed (NCT01476592).³⁹

Lycopene, a phytochemical that gives vegetables and fruits a red color, is richly present in red tomatoes (*Solanum lycopersicum*). A lower risk of prostate cancer was found in men consuming a higher level of lycopene. Interestingly, in a metabolomic study carried out in a group of men with elevated PSA levels but no prostate cancer, intake of 15 mg lycopene along with 600 mg EGCG for 6-months reduced the levels of circulating pyruvate. At present, a double-blind, placebo-controlled phase 2 clinical trial is in progress to evaluate the efficacy of lycopene (20 mg/PO/day) to reduce skin toxicity in metastatic colorectal carcinoma patients treated with panitumumab (NCT03167268).

Sulforaphane (SFN), an isothiocyanate found in cruciferous plants like broccoli (*Brassica oleracea*). In a study conducted by Alumkal et al., safety, efficacy, pharmacokinetics, and pharmacodynamics of SFN-rich broccoli sprout extracts (200 mmol/day) administered to patients for 20 weeks with biochemical (PSA) recurrent prostate cancer. They could achieve a significant increase in on-treatment PSADT as compared to pre-treatment PSADT.⁴⁰

1.4.6 Limitations of chemotherapeutic drugs

Chemotherapy is a complicated procedure that involves high risk due to drug toxicity. Generally, the more effective drugs cause more toxicity to the cells irrespective of the cell types. Even for successive chemotherapy, the patient needs to tolerate severe side effects. The significant factors associated are the following:

Dosage form: Most anti-neoplastic agents are extremely hydrophobic thus are not soluble in aqueous medium and under the biological fluids. Sometimes adjuvants may be used for the clinical administration of many such drugs, which may cause serious side effects.

Pharmacokinetics: The dosage of a chemotherapeutic agent is an essential determinant for its success. It is necessary to expose cancer cells to a sufficiently high concentration of the drug for a long enough duration. The administration of appropriate doses at proper intervals is usual to ascertain that the drug concentration is constantly optimized between its effectiveness and tolerability throughout the treatment period.

Toxicity: Anticancer drugs can also affect healthy cells. In general, the toxic drugs in cancer chemotherapy are usually more effective for the cancer cells, which have a more rapid transit through their cell cycle, than normal cells. However, specific cells with rapid turnovers, such

as bone marrow cells and intestinal epithelium cells, may also be seriously affected. Supportive treatment becomes essential for the continuation of chemotherapy.

Drug resistance: Despite the increasing success of chemotherapy, especially in achieving initial responses, it often fails in terms of long-term results because of the development of drug resistance by the cancer cells. This is to be contrasted to radiotherapy and surgery, where the limitation is the access to metastatic lesions. The probability that resistant cells will be present in a tumor increases with the number of cells present. Combinational chemotherapy, i.e., the use of more than one drug, is a usual practice in clinical oncology. However, interactions among various drugs are complicated, with synergistic or antagonistic effects.

1.4.7 Advancement of drug delivery systems towards better therapeutic outcome

Cytotoxic natural products frequently observed a limited solubility in aqueous solvents and considerable toxicity, often resulting in narrow therapeutic indices. This has led to the failure in clinical trials of many natural products. However, recently several of these agents have shown potential as ‘warheads’ which can be attached to monoclonal antibodies specifically targeting epitopes on the tumor of interest.

Frequent challenges encountered by current cancer therapies include nonspecific systemic distribution of antitumor agents, inadequate drug concentrations reaching the tumor, and the limited ability to monitor therapeutic responses. Poor drug delivery to the target site leads to significant complications, such as multidrug resistance.

Ideally, a therapeutic drug would be selectively enriched in the tumor lesions with minimal damage to normal tissues. A rational approach to achieve these goals is to conjugate therapeutic drugs with monoclonal antibodies (mAbs) or other ligands that selectively bind to antigens or receptors that are usually abundantly or uniquely expressed on the tumor cell surface. Several ligand-targeted therapeutic strategies, including immunotoxins, radio-immunotherapeutics, and drug immunoconjugates, are being developed. Although these conjugated agents have demonstrated promising efficacy compared with conventional chemotherapy drugs in preclinical and clinical trials, by applying a vast and diverse array of nanoparticles, whose design derives from the engineering, chemistry, and medicine fields, to molecular imaging and targeted therapy, cancer nanotechnology promises solutions to several of the current obstacles

facing cancer therapies. The methods have been pursued vigorously by administering drug molecules at a controlled rate, targeted fashion, and slow-release profile are other widely focused areas for pharma and medicinal chemistry researchers.

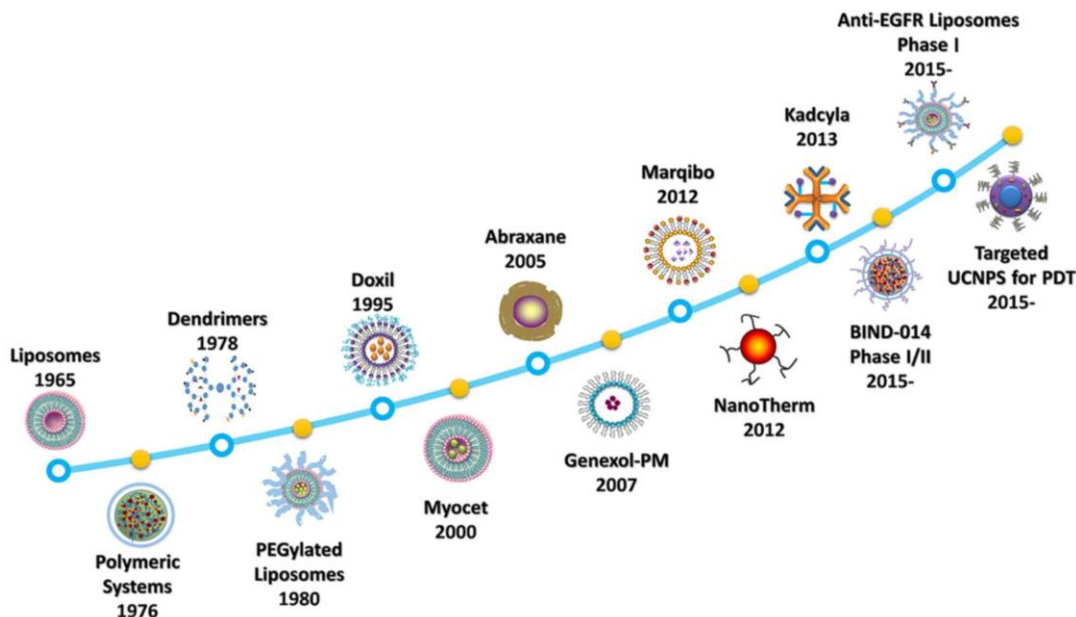


Figure 10: Timeline of the development of nanomedicines, Adapted with permission, Spandidos publications, 2017.

Advancements in nano-carrier development have scrutinized an assortment after several decades of technological enlargement. The delivery vectors and their payloads have also been satisfactorily delivered into the site of action by taking advantage of the pathophysiological conditions, such as the enhanced permeability and retention effect (EPR) and other cellular environmental conditions. Drug delivery vehicles can be readily fabricated from either flexible (organic polymeric and dendritic) or rigid (inorganic) materials, with their sizes being controlled and compositions/structures being fabricated to load different drugs in several configurations. The physicochemical parameters of the delivery systems can also be finely tuned by tailoring their chemical functionalization, surface properties, structures, sizes, shapes, and morphologies. Many such delivery systems have been approved for providing therapeutic output in clinics, with many more currently under clinical trials or preclinical evaluations (Figure 10).

As mentioned above, one of the main challenges in chemotherapy is fixing the right dosage. Nanoparticles based on biodegradable polymers, that have a tunable size to allow intracapillary

or transcapillary passage and appropriate surface coating to escape from macrophage uptake, may provide an ideal solution. Nanoparticles can provide a controlled and targeted way to deliver the encapsulated anticancer drugs and thus result in high efficacy and low side effects. Nanoparticles for cancer chemotherapy have been intensively investigated to evaluate the maximum efficacy with minimum side effect. A number of US FDA-approved biodegradable polymers have been employed to formulate nanoparticles for controlled delivery of various effective anticancer agents to avoid the use of toxic adjuvants, realize the desired pharmacokinetics, and enhance their uptake by cancer cells. Examples of anticancer agents used for nanoparticle delivery include paclitaxel, doxorubicin, etc.

1.5 Conclusion

Increasing occurrence of cancer and extreme intricacy caused by chemotherapeutic agents lessen the therapeutic efficacy of a large array of anti-neoplastic agents that are currently being used. Thus, there is always a constant need to develop alternative or synergistic anticancer drugs with minimal side-effects. Natural products have been acting as a source of potential therapeutic agents and remains as a huge reservoir for bioactive entities. The scope of Np chemistry in designing or development of an anticancer agent is unrestricted and the use of phytochemicals enhances enormous opportunities in this area with the support of multidisciplinary approaches to generate anti-cancer lead molecules. Anticancer agents derived from plants and their derivatives have been proven to be effective for cancer prevention and therapeutics. Many molecules in the preclinical and clinical trials faces barriers like solubility issues, toxicity, drug resistance. In this scenario, rational designing and semi-synthesis of Np i.e., new phytochemical entities (NPCEs) can help in overcoming these issues and can lead to the successful development of a hit or advanced hit or lead molecule. Targeted nano-delivery systems have emerging potential for the effective delivery of drug cargo into the tumor site which will enhance the therapeutic efficacy. Such delivery carriers ensure the specific interaction between a drug and its receptor at the molecular level.

1.6 Objectives of the current investigation

Inspired by the recent progress in Np chemistry specially on phytochemicals and the scope of semi-synthesis of the bioactive phytomolecules, the thesis is planned to explore the possibility of developing new phytochemical entities (NPCEs) for development of anti-cancer hit or advanced hit generation. The role of Ayurveda in Indian drug development is well known, and this knowledge has been utilized to design new phytochemical entities based on semisynthetic modification of potent phytochemicals. Moreover, targeted nano-delivery system with biocompatible polymer both synthetic and natural source has been utilized to facilitate the delivery of NPCEs or in combinations to efficient therapeutic efficacy towards cancer. Plants like *Hydnocarpus wightiana* Blume, *Curcuma raktakanta*, and *Embelia ribes*, explored in the Ayurveda for various ailments, are utilized for the studies.

First objective of this work was to synthesis a library of heterocycle appended hydnocarpin (isolated from *Hydnocarpus wightiana* Blume) derivatives as NPCEs. Around twenty derivatives conjugated with isoxazole and isoxazolone moieties were synthesized and screened for cytotoxicity and assessment the durability through molecular docking. After initial screening, the selected NPCEs were systematically evaluated for the cell death mechanism. Next, objective focused on exploring germacrone, a sesquiterpene molecule isolated from *Curcuma raktakanta*. Germacrone and its derivative, pyrogermacrone was subjected to the formation of different metal complexes in order to develop a promising anticancer agent. These derivatives are expected to reduce the toxicity induced by metal-based drugs towards normal cells. All the derivatives were screened for cytotoxicity evaluation in triple negative breast cancer cells (MDA-MB-231) and normal breast epithelial cells (MCF 10A) *in vitro* in order to evaluate the potent hits.

Recently targeted nano-carrier delivery system is widely practiced in nanomedicine development for effective cancer therapy. Therefore, the next objective of the thesis was to design a nanocarrier that can target cancer by overcoming current drawbacks. A biocompatible polymer-based nanocarrier system has been designed which was decorated with targeting peptide for effective delivery of embelin, a benzoquinone molecule isolated from *Embelia ribes* to evolute the efficacy in pancreatic cancer. In order to enhance the anticancer therapeutic effect of the nanocarrier, we have planned to co-load the system with a c-met inhibitor, RPI-1

as well. The metabolic changes occurring in the cellular environment due to the administration of the nano-drug was also analyzed by Raman spectroscopy and LC-MS. The efficacy of the dual drug loaded nano delivery system was evaluated *in vitro* in human pancreatic adenocarcinoma cells PANC-1 and extended the effective in pancreatic xenograft model of zebra fish.

1.7 References

- (1) Decorte, B. L. Underexplored Opportunities for Natural Products in Drug Discovery. *J. Med. Chem* **2016**, *59*, 9295. <https://doi.org/10.1021/acs.jmedchem.6b00473>.
- (2) Sneader, W. *Drug Discovery: A History*; John Wiley & Sons: Hoboken, NJ, 2015. <https://doi.org/10.1002/0470015535>.
- (3) Campbell, W. C.; Ōmura, S. From Bacteria and Plants to Novel Anti-Parasite Therapies. *Nobel Prize Press Release*. 2015, pp 1–5.
- (4) Mohd Fauzi, F.; Koutsoukas, A.; Lowe, R.; Joshi, K.; Fan, T. P.; Glen, R. C.; Bender, A. Chemogenomics Approaches to Rationalizing the Mode-of-Action of Traditional Chinese and Ayurvedic Medicines. *J. Chem. Inf. Model.* **2013**, *53* (3), 661–673. <https://doi.org/10.1021/ci3005513>.
- (5) BCC Research. *Botanical and Plant-Derived Drugs : Global Markets Use This Report To* .; 2015.
- (6) Newman, D. J.; Cragg, G. M. Natural Products as Sources of New Drugs over the Nearly Four Decades from 01/1981 to 09/2019. *J. Nat. Prod.* **2020**, *83* (3), 770–803. <https://doi.org/10.1021/acs.jnatprod.9b01285>.
- (7) Koehn, F. E.; Carter, G. T. The Evolving Role of Natural Products in Drug Discovery. *Nat. Rev. Drug Discov.* **2005**, *4* (3), 206–220. <https://doi.org/10.1038/nrd1657>.
- (8) Siddiqui, A. A.; Siddiqui, S.; Sahu, K.; Nagar, H. Role of Natural Products in Drug Discovery Process. *Int. J. Drug Dev. Res.* **2014**, *6* (2), 172–204.

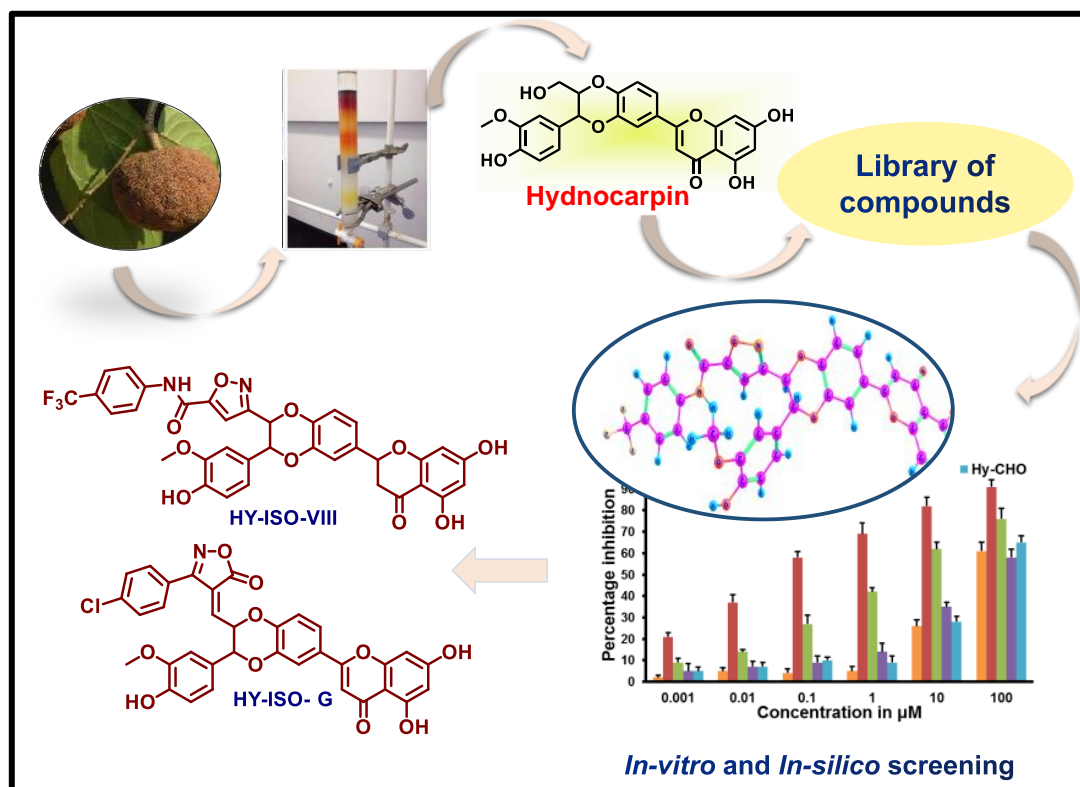
-
- (9) Mandal, S.; Moudgil, M.; Mandal, S. K. Rational Drug Design. *Eur. J. Pharmacol.* **2009**, *625* (1–3), 90–100. <https://doi.org/10.1016/j.ejphar.2009.06.065>.
- (10) LI, J.; Larregieu, C. A.; Benet, L. Z. Classification of Natural Products as Sources of Drugs According to the Biopharmaceutics Drug Disposition Classification System (BDDCS). *Chin. J. Nat. Med.* **2016**, *14* (12), 888–897. [https://doi.org/10.1016/S1875-5364\(17\)30013-4](https://doi.org/10.1016/S1875-5364(17)30013-4).
- (11) Bourgaud, F. Production of Plant Secondary Metabolites: A Historical Perspective. *Plant Sci.* **2001**, *161* (5), 839–851.
- (12) Alder, A. L. *The History of Penicillin Production*; American Institute of Chemical Engineers: New York: New York, 1970. <https://doi.org/10.1002/jps.2600591144>.
- (13) Dias, D. A.; Urban, S.; Roessner, U. A Historical Overview of Natural Products in Drug Discovery. **2012**, *2*, 303–336. <https://doi.org/10.3390/metabo2020303>.
- (14) Kota V. Ramana, Sharad S. Singhal, and A. B. R. Therapeutic Potential of Natural Pharmacological Agents in the Treatment of Human Diseases. *Biomed Res. Int.* **2014**, *573452*. <https://doi.org/10.1155/2014/573452>.
- (15) Mahady, G. B.; Huang, Y.; Doyle, B. J.; Locklear, T. NATURAL PRODUCTS AS ANTIBACTERIAL AGENTS. *Stud. Nat. Prod. Chem.* **2008**, *35*, 423–444. [https://doi.org/10.1016/S1572-5995\(08\)80011-7](https://doi.org/10.1016/S1572-5995(08)80011-7).
- (16) Khameneh, B.; Iranshahy, M.; Soheili, V.; Sedigheh, B.; Bazzaz, F. Review on Plant Antimicrobials : A Mechanistic Viewpoint. *Antimicrob. Resist. Infect. Control* **2019**, *6* (8), 118.
- (17) Rose, P.; Whiteman, M.; Moore, K.; Zhun, Y.; Rose, P.; Whiteman, M. Bioactive S-Alk(En)Yl Cysteine Sulfoxide Metabolites in the Genus Allium: The Chemistry of Potential Therapeutic Agents. *Nat. Prod. Rep.* **2005**, *22*, 351–368.
- (18) Birgit Waltenberger, Andrei Mocan, Karel Šmejkal, Elke H. Heiss, Atanasov, A. G. Natural Products to Counteract the Epidemic of Cardiovascular and Metabolic
-

-
- Disorders. *Molecules* **2016**, *22*, 807. <https://doi.org/10.3390/molecules21060807>.
- (19) Tran, N.; Pham, B.; Le, L. Bioactive Compounds in Anti-Diabetic Plants : *Biology (Basel)*. **2020**, *9* (252), 1–31.
- (20) Aba, P. E.; Asuzu, I. U. Mechanisms of Actions of Some Bioactive Anti-Diabetic Principles from Phytochemicals of Medicinal Plants: A Review. *Indian J. Nat. Prod. Resour.* **2018**, *9* (2), 85–96.
- (21) Vermaak, I.; Viljoen, A. M.; Hamman, J. H. Natural Products in Anti-Obesity Therapy. *Nat. Prod. Rep.* **2011**, *28* (3), 1493–1533. <https://doi.org/10.1039/c1np00035g>.
- (22) Rahul B.BirariKamlesh K.Bhutani. Pancreatic Lipase Inhibitors from Natural Sources: Unexplored Potential. *Drug Discov. Today* **2007**, *12* (19), 879–889.
- (23) Pan, W. H.; Xu, X. Y.; Shi, N.; Tsang, S. W.; Zhang, H. J. Antimalarial Activity of Plant Metabolites. *Int. J. Mol. Sci.* **2018**, *19* (5). <https://doi.org/10.3390/ijms19051382>.
- (24) Tse, E. G.; Korsik, M.; Todd, M. H. The Past, Present and Future of Anti-Malarial Medicines. *Malar. J.* **2019**, *18* (1), 1–21. <https://doi.org/10.1186/s12936-019-2724-z>.
- (25) Bhutani, K. K.; Gohil, V. M. Natural Products Drug Discovery Research in India: Status and Appraisal. *Indian J. Exp. Biol.* **2010**, *48* (3), 199–207.
- (26) Venkatalakshmi, P.; Vadivel, V.; Brindha, P. Role of Phytochemicals as Immunomodulatory Agents: A Review. *Int. J. Green Pharm.* **2016**, *10* (1), 1–18.
- (27) Behl, T.; Kumar, K.; Brisc, C.; Rus, M.; Nistor-Cseppento, D. C.; Bustea, C.; Aron, R. A. C.; Pantis, C.; Zengin, G.; Sehgal, A.; Kaur, R.; Kumar, A.; Arora, S.; Setia, D.; Chandel, D.; Bungau, S. Exploring the Multifocal Role of Phytochemicals as Immunomodulators. *Biomed. Pharmacother.* **2021**, *133* (September 2020), 110959. <https://doi.org/10.1016/j.biopha.2020.110959>.
- (28) Siegel, R. L.; Miller, K. D.; Jemal, A. Cancer Statistics. *CA Cancer J Clin* **2016**, *66*
-

-
- (1), 7–30.
- (29) *Latest World Cancer Statistics Global Cancer Burden Rises to 14 . 1 Million New Cases in 2012 : Marked Increase in Breast Cancers Must Be Addressed*; 2013.
- (30) Mathur, P.; Sathishkumar, K.; Chaturvedi, M.; Das, P.; Sudarshan, K. L.; Santhappan, S.; Nallasamy, V.; John, A.; Narasimhan, S.; Roselind, F. S. Cancer Statistics, 2020: Report From National Cancer Registry Programme, India. *JCO Glob. Oncol.* **2020**, No. 6, 1063–1075. <https://doi.org/10.1200/go.20.00122>.
- (31) Mcguigan, A.; Kelly, P.; Turkington, R. C.; Jones, C.; Coleman, H. G.; McCain, R. S.; Mcguigan, A.; Turkington, R. C.; Cancer, C.; Kelly, P.; Turkington, R. C.; Jones, C. Pancreatic Cancer : A Review of Clinical Diagnosis , Epidemiology , Treatment and Outcomes. *World J. Gastroenterol.* **2018**, *24* (43), 4846–4861. <https://doi.org/10.3748/wjg.v24.i43.4846>.
- (32) Gowrinath, K.; Geetha, V. *Late Recurrence of Malignant Melanoma Presenting with Hemoptysis*; 2010; Vol. 27. <https://doi.org/10.4103/0970-2113.68320>.
- (33) Cragg, G. M.; Pezzuto, J. M. Natural Products as a Vital Source for the Discovery of Cancer Chemotherapeutic and Chemopreventive Agents. *Med. Princ. Pract.* **2016**, *25* (2), 41–59. <https://doi.org/10.1159/000443404>.
- (34) Huang, C. Y.; Ju, D. T.; Chang, C. F.; Muralidhar Reddy, P.; Velmurugan, B. K. A Review on the Effects of Current Chemotherapy Drugs and Natural Agents in Treating Non-Small Cell Lung Cancer. *BioMedicine* **2017**, *7* (4), 12–23. <https://doi.org/10.1051/bmdcn/2017070423>.
- (35) Huang, M.; Lu, J. J.; Ding, J. Natural Products in Cancer Therapy: Past, Present and Future. *Nat. Products Bioprospect.* **2021**, *11* (1), 5–13. <https://doi.org/10.1007/s13659-020-00293-7>.
- (36) Altmann, K. H.; Gertsch, J. Anticancer Drugs from Nature - Natural Products as a Unique Source of New Microtubule-Stabilizing Agents. *Nat. Prod. Rep.* **2007**, *24* (2), 327–357. <https://doi.org/10.1039/b515619j>.
-

-
- (37) Choudhari, A. S.; Mandave, P. C.; Deshpande, M.; Ranjekar, P.; Prakash, O. Phytochemicals in Cancer Treatment: From Preclinical Studies to Clinical Practice. *Front. Pharmacol.* **2020**, *10* (January), 1–17. <https://doi.org/10.3389/fphar.2019.01614>.
- (38) Zhang, Y., Li, X., Zou, D., Liu, W., Yang, J., Zhu, N. Treatment of Type 2 Diabetes and Dyslipidemia with the Natural Plant Alkaloid Berberine. *J. Clin. Endocrinol. Metab* **2008**, *93* (7), 2559–2565. <https://doi.org/10.1210/jc.2007-2404>.
- (39) Zhu, W., Qin, W., Zhang, K., Rottinghaus, G. E., Chen, Y. C., Kliethermes, B. Trans-Resveratrol Alters Mammary Promoter Hypermethylation in Women at Increased Risk for Breast Cancer. *Nutr. Cancer* **2012**, *64* (3), 393–400.
- (40) Alumkal, J. J., Slotke, R., Schwartzman, J., Cherala, G., Munar, M., Graff, J. N. A Phase II Study of Sulforaphane-Rich Broccoli Sprout Extracts in Men with Recurrent Prostate Cancer. *Invest. New Drugs* **2015**, *33* (2), 480–489.

Exploring *Hydnocarpus wightiana* Blume for the Development of New Phyto-chemical Entities Towards Lung cancer and Melanoma



Abstract: *Hydnocarpin* (Hy), isolated and purified from *Hydnocarpus wightiana* Blume promotes moderate cytotoxicity in cancer cells. Herein, we have originated a built-in semi-synthetic modification on Hy by one pot multi-component reaction (MCR) and [3+2] cycloaddition strategy to append five membered isoxazole and isoxazolone as new phytochemical entities (NPCEs). Screening from the library of 20 newly synthesized compounds in terms of cancer-selective cytotoxicity, structure–activity relationships and molecular binding efficiency with the protein domains associated with the apoptotic pathways, we short listed the candidates Hy-ISO-VIII and Hy-ISO-G for further studies.

2A.1 Introduction

If we consider the global mortality scenario, deaths happening due to cancer come second in number. Cancerous cells are finger-marked with unmanageable proliferation and often

possess resistance towards conventional treatment methodologies. One of the significant shortcomings of the current onco-therapeutic regimen is the elusive nature of cancer cells to evade the human body's immune system, accompanied by rapid multiplication and resistance to undergo apoptosis. The most lethal and debilitating attribute of cancer cells is their ability to evolve to a state of malignancy, with critical features like invasion, migration, colony formation, increased angiogenesis, and metastasis.^{1,2} Since tumor metastasis accounts for about 90% of all cancer-related deaths, practical strategies to tackle this condition are a major global concern among oncologists and the research community. Despite an assortment of strategies for the management of cancer, cytotoxic chemotherapeutic drugs are one of the purposeful therapeutic ways in clinical practice. So there is a dire need for the development of more potent and selective anticancer agents.

Natural products can be viewed as a population of privileged structures selected by evolutionary pressures to interact with a wide variety of proteins and other biological targets for specific purposes. Overall, phytochemicals identified from traditional medicinal plants are offering exciting prospects for the development of new drug candidates. Natural sources afford numerous active anticancer molecules which can be tuned to generate promising leads after planned and selective synthetic modifications.³ Co-ordinated semi-synthetic strategies for the modification of bio-active compounds serves as a great platform for generating hit or advanced hits which may further lead to the development of pharmacologically active leads for the effective management of cancer. Structural modification of isolated natural products are intended to increase the potency and selectivity, improve the physico chemical properties such as solubility, distribution, ionizability, enhance the chemical and metabolic stability, improve biochemical and pharmacokinetic properties including absorption, distribution, metabolism and excretion, eliminate or reduce side-effects.⁴

Heterocycles, holds unique physicochemical properties and hence employed for various clinical applications including antitumor, antiviral, antibacterial agents and constitutes to the major structural unit of most marketed drugs. The strategic inclusion of heterocyclic fragments is the rationale behind the drug design and engineering due to their versatility and selective nature of the platform. Out of the many of such designed compounds, which are marketed and are under clinical trials, isoxazole and isoxazolone having oxygen as well as nitrogen as the heteroatom plays a promising role particularly in cancer therapeutics.^{5,6} Keeping this aspect in mind, we attempted the synthesis of different

isoxazole and isoxazolone coupled derivatives of hydnocarpin (Hy), which is a flavonoid isolated from the seeds of *Hydnocarpus wightiana* Blume. The oil extracted from the seed of this plant has been widely explored by traditional healers and folk medical systems for the treatment of leprosy, chronic skin infections, for dressing of wounds and ulcers and ophthalmia.⁷ Previously our group reported the enhanced cancer-selective cytotoxicity and anti-metastatic potential of Hy by conjugation with a highly efficient, non-toxic cell penetrating guanidinium rich poly- (propylene imine) dendron⁸. Because of the impressive anticancer properties of the Hy derivatives we thought of coupling of a bioactive heterocycle like isoxazole and isoxazolone. Hence, we have carried out the synthesis of a library of hydnocarpin-isoxazole/isoxazolone derivatives with an objective to select an ideal candidate for the bed side application. Later in-depth investigations for the lung adenocarcinoma and metastatic melanoma specific cytotoxicity and the underlying molecular, mechanisms were carried out.

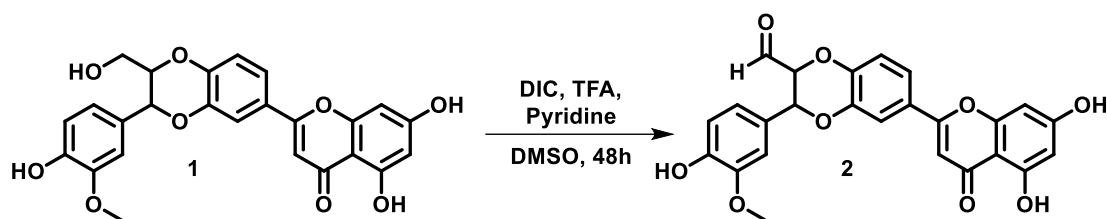
2A.2 Results and discussion

2A.2.1 Chemical synthesis

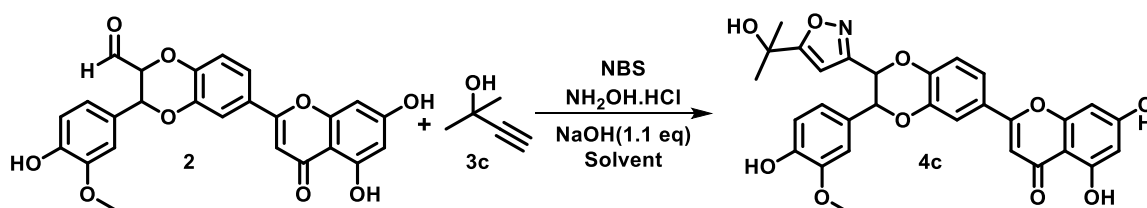
Initially, the isolated pure compound HY (**1**), was chemically modified at C-9' position. The primary hydroxyl group was first oxidized to an aldehyde (**2**), *via* Moffatt oxidation (Scheme 2A.1) for further functionalization towards isoxazole and isoxazolone. To functionalize **1** with isoxazole moiety, one pot [3+2]-dipolar cycloaddition strategy was employed, resulting in a hydnocarpin-isoxazole derivative of **1**. To find out the best reaction conditions for achieving the isoxazole hybrid (Scheme 2A.2), several reactions were performed (Table 2A.1). The best reaction conditions comprised the reaction of **2**, with the alkynyl derivative **3c**, and hydroxylamine hydrochloride in the presence of N-bromosuccinamide (NBS) and NaOH in methanol-ethyl acetate system affording the product isoxazole coupled Hy in 91% yield (entry **7**, Table 2A.1). In a similar manner ten isoxazole derivatives of Hy were synthesized (4a-j). All these derivatives were confirmed by Nuclear Magnetic Resonance (NMR) (¹H and ¹³C) and Mass Spectrometry (MS).

In the second series, Hy was appended with isoxazolone moiety in presence of boric acid catalyzed MCR strategy (Scheme 2A.3). The best reaction condition was achieved where HYCHO **2**, β -keto ester **5a**, and hydroxylamine hydrochloride in the presence of boric acid in aqueous medium in room temperature affording the product isoxazolone coupled Hy in 85% yield (entry **4**, Table 2A.2). Successively, a series of Hy-isoxazole and Hy-

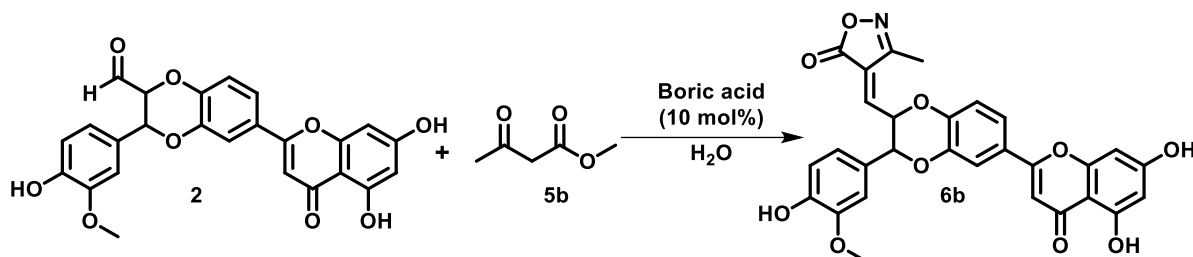
isoxazolone derivatives, were synthesized, 4a-j and 6a-j respectively (Scheme 2A.4). HRMS and NMR (^1H and ^{13}C) confirmed the structure of all the semi-synthetic NPCEs obtained *via* the above methods.



Scheme 2A.1. Oxidation of hydnocarpin to hydnocarpin-aldehyde.



Scheme 2A.2: Synthesis of isoxazole derivatives of HY.



Scheme 2A.3: Synthesis of isoxazolone derivatives of HY.

Isoxazoles and isoxazolones are versatile groups present in many biologically active molecules, with anti-inflammatory, anti-cancer and many other pharmacological properties. Drugs like valdecoxib, leflunomide, oxacyllin, cycloserine acivicin etc having isoxazole core are already in clinical use for many years. Similar kind of heterocyclic derivatives have attracted synthetic chemists which enhances the pharmacokinetic activity.^{9,10} Incorporation of these heterocycle ring changes the molecular structure which promoted the possible interaction with the protein core due to the presence of additional nitrogen and oxygen atoms. In addition, the synthetic easiness as well as excellent yield observed for the derivatives encouraged us to prepare a library of novel HY-ISO derivatives. Hence, the coupling of isoxazole / isoxazolone ring would be a very intelligent approach for developing potent antiproliferative agents from HY.

Table 2A.1: Optimization of reaction conditions for isoxazole derivatives

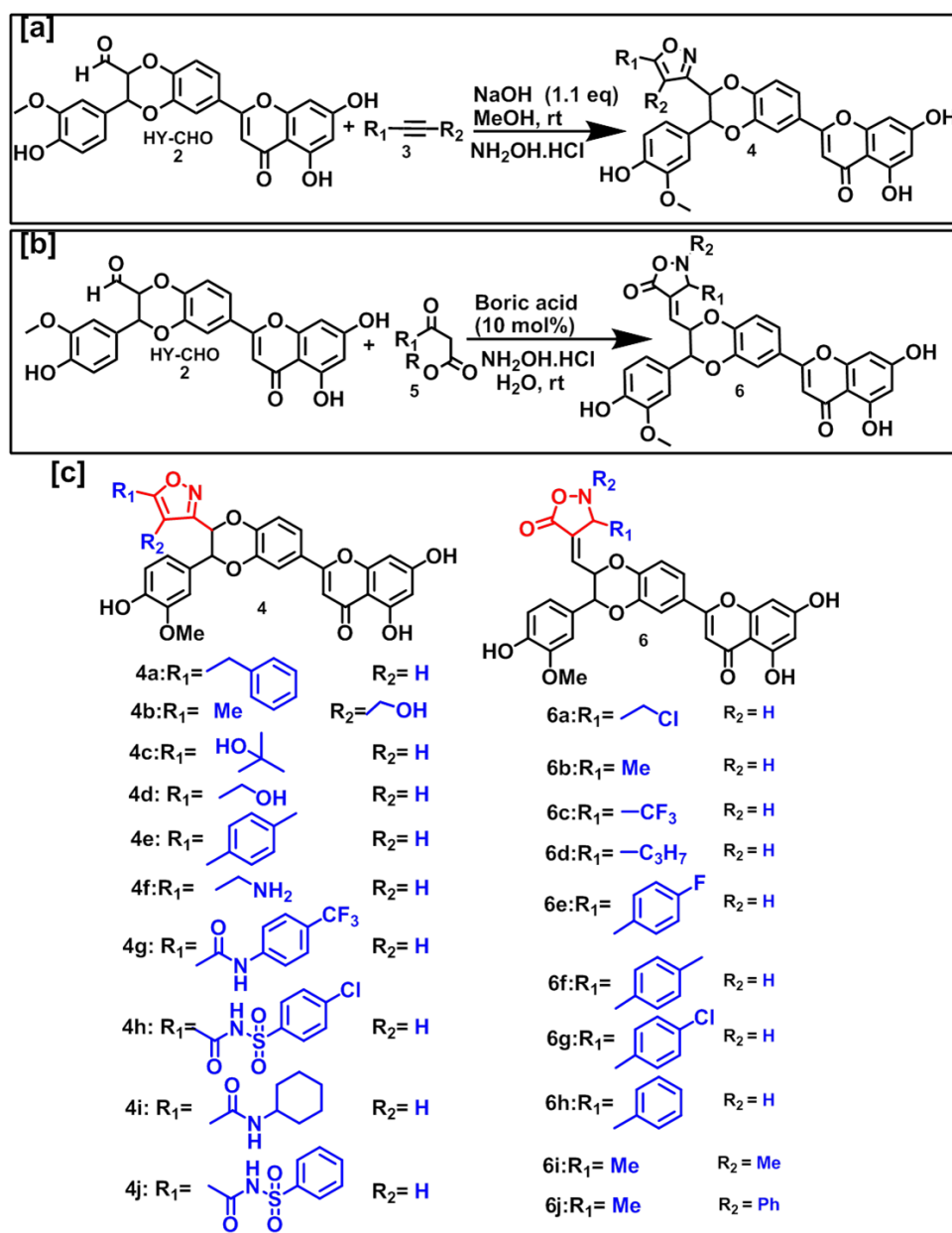
Sl.no:	Solvent	NH ₂ OH	NBS	Alkyne	Time	Yield
1	DMF (1 mL)	2 eq.	2 eq.	2 eq.	24 h	<5%
2	MeOH (2 mL)	2 eq.	2 eq.	2 eq.	24 h	20 %
3	MeCN (2 mL)	2 eq.	2 eq.	2 eq.	24 h	17 %
4	MeCN/DMF (4:1)	2 eq.	2 eq.	2 eq.	24 h	11 %
5	MeOH/DMF (4:1)	2 eq.	2 eq.	2 eq.	24 h	13 %
6	MeOH/DMF (10:1)	4 eq.	4 eq.	4 eq.	12 h	62 %
7	MeOH/ EtOAc (1:4)	4 eq.	4 eq.	4 eq.	24 h	93%
8	MeOH/ EtOAc (1:4)	4 eq.	4 eq.	4 eq.	12 h	66 %
9	MeOH/ EtOAc (1:4)	4 eq.	4 eq.	4 eq.	6 h	53 %
10	MeOH/ EtOAc (1:4)	2 eq.	2 eq.	2 eq.	24 h	73 %
11	MeOH/ EtOAc (1:4)	4 eq.	2 eq.	2 eq.	24 h	72 %
12	MeOH/ EtOAc (1:4)	4 eq.	4 eq.	2 eq.	24 h	78 %
13	MeOH/ EtOAc (1:4)	4 eq.	4 eq.	4 eq.	48 h	54 %

Table 2A.2: Optimization of reaction conditions for isoxazolone derivatives

Sl no:	NH ₂ OH	β -keto ester	time	Yield
1	1 eq	1 eq	6h	67 %
2	1 eq	1 eq	12h	70 %
3	2 eq	1 eq	6h	72 %
4	2 eq	2 eq	12h	82 %
5	1 eq	2 eq	6h	65 %
6	1 eq	2 eq	12h	68 %
7	2 eq	2 eq	6h	78 %

2.2.2 Primary cytotoxicity screening of Hy- analogues / NPCEs

Lung cancer and metastatic melanoma represents two potent forms of cancer which are clinically difficult to vanquish. Primary selection based on the cytotoxicity of Hy-derivatives were evaluated through MTT assay where Hy analogues 4a-j and 6a-j were assessed by comparing with parent Hy and the first intermediate HY-CHO on human metastatic melanoma (A375), human lung adenocarcinoma (A549) and human normal lung fibroblast (WI-38) cell lines after 24 and 48 h of treatment (Figure 2A.1-6).



Scheme 2A.4. (a) 3+2 cycloaddition strategy adopted for the synthesis of isoxazole derivatives; (b) one-pot multicomponent strategy adopted for the synthesis of isoxazolone derivatives; (c) semisynthetic derivatives of HY-isoxazole and HY-isoxazolone hybrids.

It was interesting to observe that all the selected derivatives except for **4d**, **4e**, **6b** and **6j**, were showed significant cell death than parent Hy as reflected in lower IC₅₀s (Table 2A.3). Hy-analogues 4h, 6a and 6c showed indiscriminate cytotoxicity in both cancer and normal lung fibroblast cells, and hence these compounds were eliminated from the primary screening criteria. Based on the observations with the lower IC₅₀s on cancer cells and non-toxicity towards normal fibroblasts, four Hy-derivatives were promoted from

both the series for next level screening studies (Table 2A.4 and 2A.5). This result suggested that the incorporation of isoxazole and /or isoxazolone heterocycles contributed significantly towards the improved cytotoxicity. In fact, isoxazole and isoxazolone rings have been reported as potent heterocycle skeleton in many drug intermediates towards various therapeutic potential including high anti proliferative activity.^{5,11} When these two biologically active heterocyclic moiety were coupled together, the combined effect of Hy-flavonoid induced the enhanced cytotoxicity in cancer cells. The compounds may undergo oxidation to produce cytotoxic hydrogen peroxide that increases the antiproliferative potential of the novel NPCEs.¹²

2.2.3 Evaluation of Hy-derivatives / NPCEs by *in-silico* studies

Next we thought of extending the screening strategy by employing computational tools. We evaluated the molecular docking ability of the previously screened analogues towards the selected protein domains involved in the apoptotic machinery. Hence the selected Hy-isoxazole hybrids **4a**, **4c**, **4f**, **4g** and Hy-isoxazolone hybrids **6e**, **6f**, **6g**, **6i** which exhibited significantly higher cancer selective cytotoxicity was subjected to molecular docking studies. The qikprop screening for pharmacokinetic/ADMET parameters (Table 2A.6a) shows that the compounds **4a**, **4c**, **4f**, **4g**, **6e**, **6f**, **6g** and **6i** are good candidates with few #stars and the molecular weights are below 700. All of them are non-toxic to central nervous system (CNS) with minimum CNS value of -2. The total solvent accessible surface area (SASA) and its hydrophilic components (FISA) are well within the range. All molecules exhibited H-bond donating and accepting capacity, with maximum value of 4 in the case of **4f** and 10 in the case of **4g** and **6f**. The octanol/water partition coefficient (QPlog o/w) and binding to human serum albumin (QPlog Kh_{sa}) values indicate better absorption in the blood stream. The aqueous solubility (QPlog S) values are indicative of better solubility of the drug in water which aids in its bioavailability. To conclude, all the eight selected compounds are good drug candidates with minimum violation from Lipinski's rule of five (Ro5).

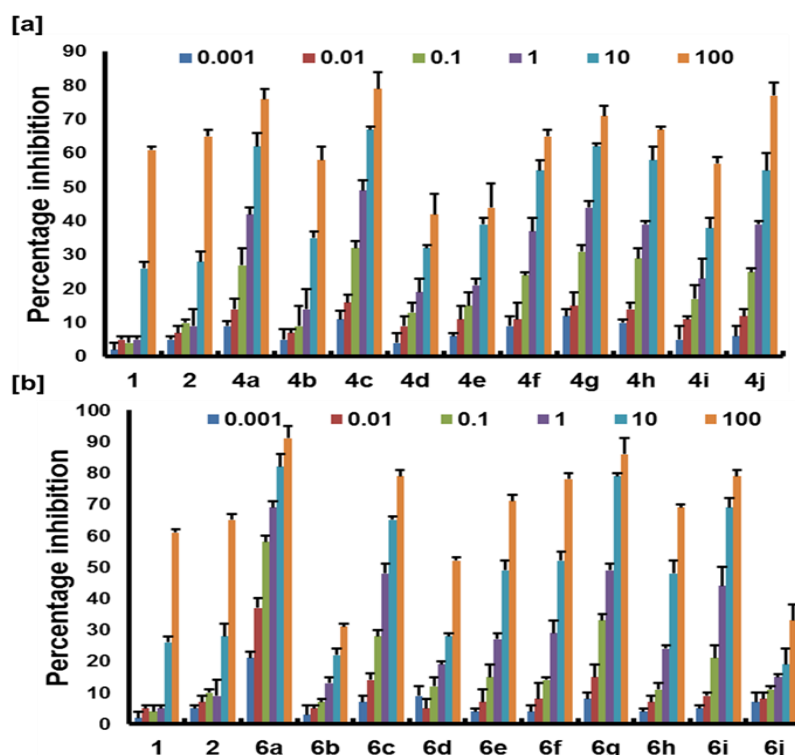


Figure 2A.1: MTT assay on A375 cells on treatment of compounds (0.001 to 100 μM) for 24h. [a] effect of compounds 1 (HY), 2 (Hy-CHO), **4a-4j** and [b] compounds 1, 2, **6a-6j**.

In order to find out the binding affinity of the above said ligands with the selected receptors, we carried out the docking study of prepared ligands against the grid generated for the receptors. The binding affinity was compared in terms of G-score or D-score values of best binding poses. It is clear that the binding affinity of the ligands is maximum with 1OXN and 1OXQ (Figure 2A.7a). The comparison of G-score, D-score and interacted residues in the case of eight selected compounds was tabulated (Table 2A.6b). All the eight ligands show higher affinity towards the receptors through H-bonding and π - π stacking interaction. In the case of both 1OXN and 1OXQ, there is π - π stacking interaction exist between the ligand with Phe81, except in the case of **4a** and **6e**, which act as a vital factor in better binding. Another important interaction observed due to H-accepting capacity of Ala80 from a donor atom of the ligand.

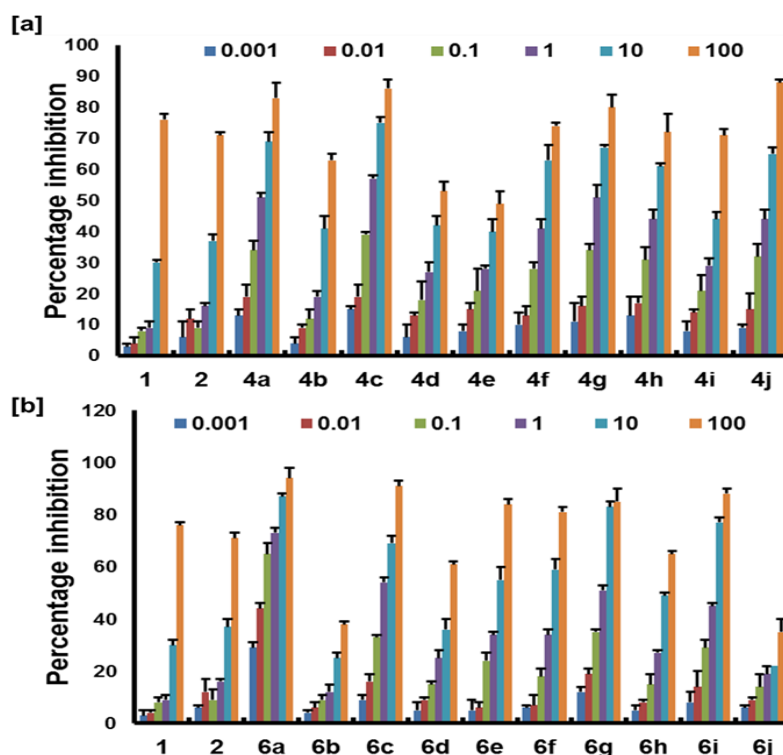


Figure 2A.2: MTT assay on A375 cells on treatment of compounds (0.001 to 100 μM) for 48h. [a] effect of compounds 1 (HY), 2 (Hy-CHO), 4a-4j and [b] compounds 1, 2, 6a-6j .

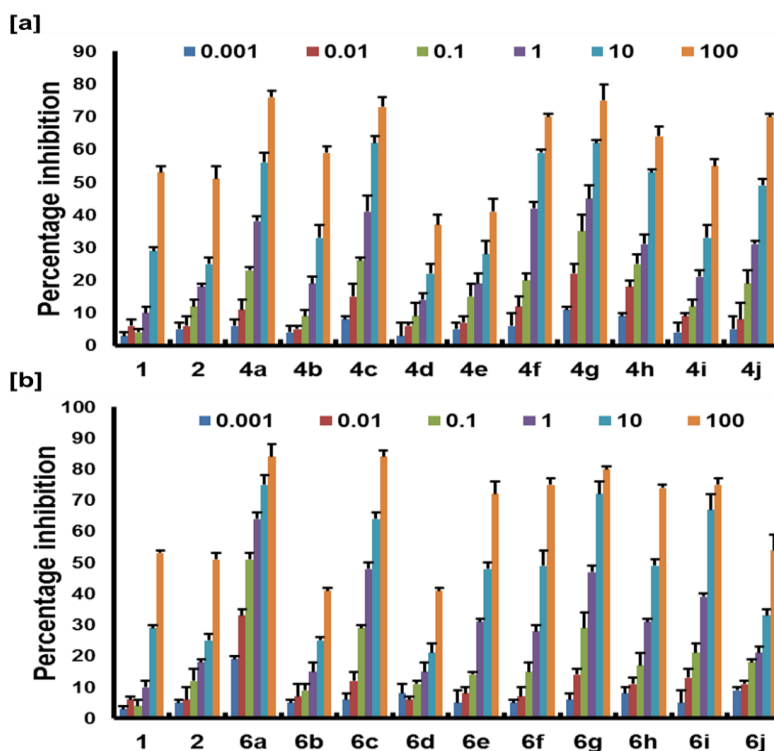


Figure 2A.3: MTT assay on A549 cells on treatment of compounds (μM) for 24h. [a] effect of compounds 1 (HY), (Hy-CHO), 4a-4j and [b] compounds 1, 2, 6a-j.

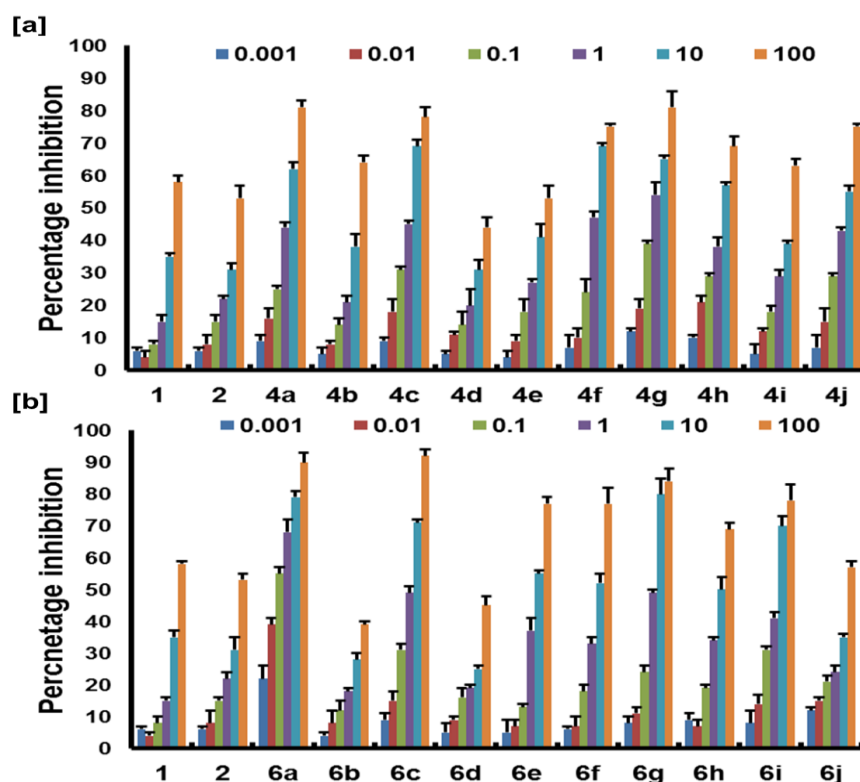


Figure 2A.4: MTT assay on A549 cells on treatment of compounds (μM) for 48h. [a] effect of compounds 1 (HY), 2 (Hy-CHO), 4a-4j and [b] compounds 1, 2, 6a-j.

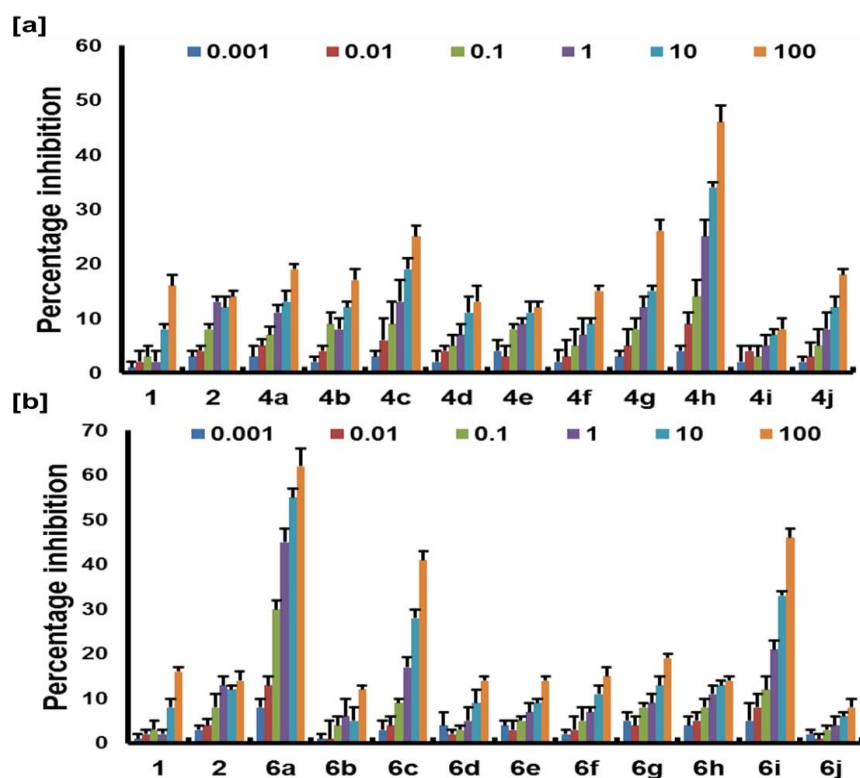


Figure 2A.5: MTT assay on WI-38 cells on treatment of compounds (μM) for 24h. [a] effect of compounds 1 (HY), 2 (Hy-CHO), 4a-4j and [b] compounds 1, 2, 6a-j.

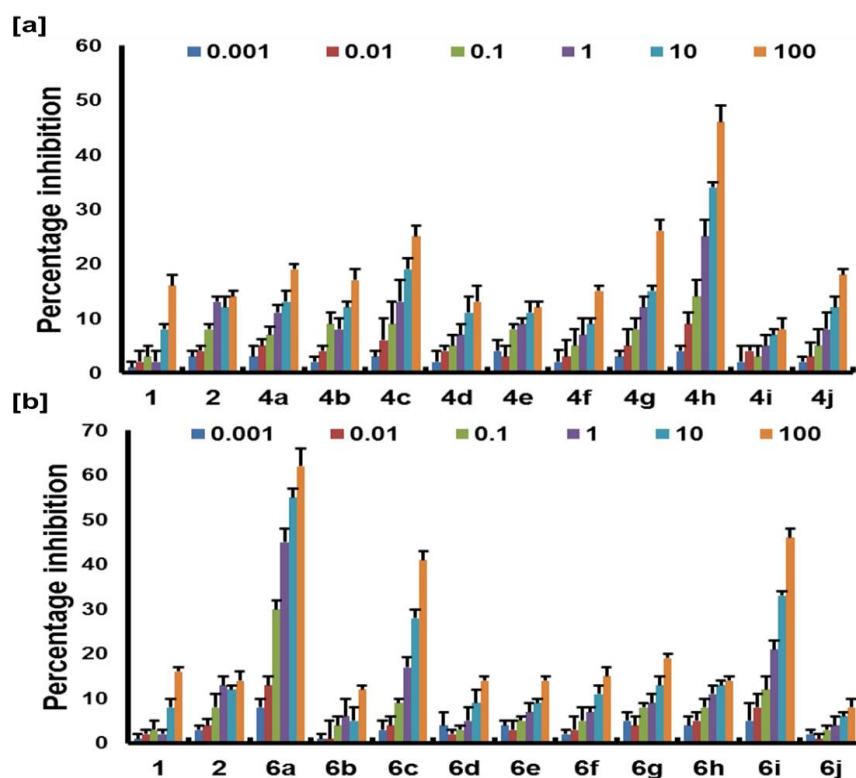


Figure 2A.6: MTT assay on WI-38 cells on treatment of compounds (μM) for 48h. [a] effect of compounds 1 (HY), 2 (Hy-CHO), 4a-4j and [b] compounds 1, 2, 6a-j.

Table 2A.3: IC_{50} values of hydnocarpin-isoxazole/isoxazolone derivatives in A375, A549 and WI-38 cells over a time of 24 and 48 h.

Compound	IC_{50} (μM)					
	A375		A549		WI-38	
	24 h	48 h	24 h	48 h	24 h	48 h
1	71.6±0.9	49.2±1.1	88.6±1.9	68±0.9	Nil	Nil
4a	4.6±1.8	0.9±0.05	7±0.09	3.9±0.18	Nil	Nil
4b	68.7±0.5	46.5±0.7	68±1.8	51±1.5	Nil	Nil
4c	1.43±0.08	0.65±0.07	4.8±0.05	2.9±0.1	Nil	Nil
4d	Nil	74.9±1.7	Nil	Nil	Nil	Nil
4e	Nil	Nil	Nil	77.4±1.8	Nil	Nil
4f	7.5±0.8	4.6±0.4	5.2±0.08	2.2±0.07	Nil	Nil
4g	4±0.5	0.95±0.4	3.6±0.08	0.76±0.04	Nil	Nil
4h	6.2±0.07	4.2±0.06	8.7±0.4	6.6±0.05	Nil	54.6±1.7
4i	66.8±1.8	28.8±0.3	80±2.1	14.5±0.8	Nil	Nil
4j	7.2±0.8	3.5±0.9	51±2.1	6.3±0.6	Nil	Nil

6a	0.04±0.01	0.035±0.01	0.095±0.02	0.07±0.006	5.5±0.04	4.9±0.08
6b	Nil	Nil	Nil	Nil	Nil	Nil
6c	2±0.02	0.83±0.07	2.1±0.1	16.4±0.2	Nil	95±2.1
6d	92.7±2.2	60±1.9	Nil	Nil	Nil	Nil
6e	13.7±0.4	7.9±0.6	1.4±0.08	7.5±0.09	Nil	Nil
6f	9.2±0.1	6.7±0.28	12.7±0.17	9±0.9	Nil	Nil
6g	1.2±0.04	0.94±0.05	2±0.04	1.2±0.05	Nil	Nil
6h	18.5±0.7	15.6±0.9	13.5±0.17	10±0.06	Nil	Nil
6i	3.1±0.04	2.4±0.16	4.5±0.08	3.8±0.14	Nil	68±1.8
6j	Nil	Nil	83±2.4	71.5±2	Nil	Nil
2	63±1.4	43.8±0.8	96±2	87.8±1.8	Nil	Nil

Table 2A.4: Selected candidates of isoxazole group for computational screening with IC₅₀ values and Ranking.

Compound	A375				A549			
	24 h		48 h		24 h		48 h	
	IC ₅₀ (μM)	Ranking	IC ₅₀ (μM)	Ranking	IC ₅₀ (μM)	Ranking	IC ₅₀ (μM)	Ranking
4a	4.6	3	0.9	2	7	4	3.9	4
4c	1.43	1	0.65	1	4.8	2	2.9	3
4f	7.5	4	4.6	4	5.2	3	2.2	2
4g	4	2	0.95	3	3.6	1	0.76	1

*The compound with least IC₅₀ value was given the rank 1 and subsequent ones were given as 2, 3 and 4

Table 2A.5: Selected candidates of isoxazolone group for computational screening with IC₅₀ values and Ranking.

Compound	A375				A549			
	24 h		48 h		24 h		48 h	
	IC ₅₀ (μM)	Ranking	IC ₅₀ (μM)	Ranking	IC ₅₀ (μM)	Ranking	IC ₅₀ (μM)	Ranking
6e	13.7	4	7.9	4	1.4	1	7.5	3
6f	9.2	3	6.7	3	12.7	4	9	4
6g	1.2	1	0.94	1	2	2	1.2	1
6i	3.1	2	2.4	2	4.5	3	3.8	2

*The compound with least IC₅₀ value was given the rank 1 and subsequent ones were given as 2, 3 and 4

Table 2A.6a: Pharmacokinetic parameters of the compounds- 4a, 4c, 4f, 4g, 6e, 6f, 6g and 6i

Compound	#stara	CN S	MW	SASA	FISA	HB D	HB A	QPlogPo/w	QPlog Khsa	QPlog S	Ro5
----------	--------	------	----	------	------	------	------	-----------	------------	---------	-----

4a	4	-2	591.5 7	923.5 0	237.3 6	2	7.5	5.65	1.43	-6.16	2
4c	2	-2	559.5 2	864.5 9	271.6 5	3	8.2 5	4.04	0.94	-5.75	2
4f	1	-2	530.4 9	801.6 7	282.7 3	4	8.5	2.46	0.55	-5.27	2
4g	4	-2	688.5 6	960.5 8	269.1 8	3	10	5.29	1.17	-6.31	3
6e	3	-2	597.4 5	843.6 4	319.2 5	2	9.5	3.44	0.65	-6.43	2
6f	3	-2	619.5 8	893.0 3	314.7 7	2	9.5	4.18	1.07	-5.89	2
6g	3	-2	640.0 0	881.7 4	314.5 6	2	9.5	4.30	1.01	-5.00	2
6i	1	-2	559.5 2	875.2 1	286.4 9	2	10	2.84	0.65	-6.18	2

#stars (few stars-more drug-like): 0 to 5; CNS (Central Nervous System activity): -2 to +2; M.W.(Molecular Weight):130.0 to 725.0; SASA (Total solvent accessible surface area: 300.0 to 1000.0; FISA (Hydrophilic component of total solvent accessible area): 7.0 to 333.0; HBD(hydrogen bond donor): 0.0 to 6.0; HBA (Hydrogen bond acceptor): 2.0 to 20.0; QPlogPo/w(octanol/water partition coefficient): -2.0 to 6.5; QPlogKhsa(binding to human serum albumin): -1.5 to 1.5; QplogS (Aqueous solubility): -6.5 to 0.5; Ro5 (Number of violations of Lipinski's rule of five): maximum is 4

The compound **4g** and **6g** (Figure 2A.7b and c) are the best ones compared to Hy (Figure 2A.7d), in inhibiting 1OXN and 1OXQ as proved by experimental results. The three dimensional crystalline structures of the peptide antagonists (PDB Code: 1OXN and 1OXQ) are given in Figure 2A.7e and f. The interaction diagrams of best scored poses of **4g** and **6g** in 1OXN and 1OXQ are shown in the (Figure 2A.8). **4g** bind with Tyr128 and Arg 123 through H-bond and π - π stacking interaction with Phe81 and Tyr128 while **6g** forms π - π stacking interaction with Phe81 in the binding pocket of 1OXN. In the binding site of 1OXQ, **4g** and forms H-bond with Asp96 and π - π stacking with His118 and Phe81 where as in 6g, there is an additional H-bond with Ala80 which stabilizes the interaction.

Table 2A.6b: G-score, D-score and interacted residues of 1OXN and 1OXQ with **4a**, **4c**, **4f**, **4g**, **6e**, **6f**, **6g** and **6i**

Entry	G-score (kcal/mol)		D-score(kcal/mol)		Interacted Residues	
	1OXN	1OXQ	1OXN	1OXQ	1OXN	1OXQ
4a	-7.9	-7.2	-7.9	-7.2	Gly117(A), His118(B)	Pro79(C), Asp96(B)
4c	-11.3	-10.9	-11.2	-10.9	Ala80(D), Phe81(A), Phe81(B)	Ala80(A), Ala80(C), Phe81(A), Phe81(B)
4f	-10.6	-10.0	-8.3	-9.9	Tyr95(B), Tyr128(C), Ala80(B), Phe81(A), Phe81(B)	Tyr128(B), Ala80(B), Phe81(A), Phe81(B)

4g	-11.8	-8.9	-11.7	-8.9	Tyr128(D), Arg123(B), Phe81(A), Phe81(B), Tyr128(A)	Asp96(B), His118(B), Phe81(B)
6e	-9.3	-11.0	-9.3	-10.9	Ala80(C), Pro79(C), Gly83(D), Gly117(B)	Ala80(D), Phe81(B), Arg123(D)
6f	-11.3	-10.3	-11.3	-10.3	Ala80(C), Arg123(A), Phe81(A), Phe81(B)	Ala80(B), Asp96(B), Ser93(B), Phe81(A), Phe81(B)
6g	-10.2	-11.0	-10.2	-10.9	Phe81(A), Phe81(B)	Asp96(B), Ala80(A), His118(B), Phe81(A), Phe81(B)
6i	-8.3	-9.3	-8.3	-9.3	Gly117(B), Ala80(A), Ala80(B), Phe81(A), Phe81(B), His118(B)	Gly117(B), Ala80(B)

2.2.4 Selection strategy based on primary screening and molecular docking studies

After evaluation of the primary screening based on cancer cell specific IC_{50} s, followed by molecular docking analysis, we come up with a strategy of selecting the most potent candidates for stepping up the next level studies. Initially we shortlisted the most effective compounds in terms of lower IC_{50} s selectively on cancer cells from both the series. Here the candidate with the lowest IC_{50} marked a score value of 1 and the next with a score of 2 and so on. Later, this normalization concept was extended towards docking studies based on G score wherein the candidate with the highest score will be given a value of 1. Finally both these strategies were combined to pick up the most suitable Hy-isoxazole and Hy-isoxazolone analogues in terms of lower IC_{50} and higher docking score (Table 2A.7 and 2A.8). This hierarchical selection approach preferred **4g** (Hy-ISO-VIII) from isoxazole and **6g** (Hy-ISO-G) from isoxazolone series respectively for the detailed molecular mechanistic evaluation.

Table 2A.7: Dock score and rank given for Isoxazole group.

	IOXN		IOXQ		4LVT		1YSW		2O21		1JD4	
compound	Dock score	Rank	Dock score	Rank	Dock score	Rank	Dock score	Rank	Dock score	Rank	Dock score	Rank
4a	7.9	4	7.2	4	5.9	2	3.2	3	4	3	2.9	3
4c	11.3	2	8.9	3	6.6	1	4.8	1	4.2	2	5.2	2
4f	10.6	3	10	2	5.1	3	4.2	2	3.5	4	5.9	1
4g	11.8	1	10.9	1	4	4	4.2	2	4.3	1	5.9	1

*The compound with higher dock score was given the rank 1 and the subsequent ones were given as 2, 3 and 4.

Table 2A.8: Dock score and rank given for Isoxazolone group.

	IOXN		IOXQ		4LVT		1YSW		2O21		1JD4	
comp ound	Dock score	Ra nk	Dock score	Ra nk	Dock score	Ra nk	Dock score	Ra nk	Dock score	Ra nk	Dock score	Ra nk
6e	9.3	3	11	2	4.7	3	3.6	3	3	3	3.6	4
6f	11.3	1	10.3	3	5.1	2	3.8	2	4.6	2	5.8	1
6g	10.2	2	11	2	5.5	1	4.5	1	5.5	1	5.4	2
6i	5.3	4	11.3	1	4.7	3	3.2	4	3	3	4.2	3

*The compound with higher dock score was given the rank 1 and the subsequent ones were given as 2, 3 and 4.

2.2.5 Molecular dynamic simulation of selected NPCEs Hy-ISO-G and Hy-ISO-VIII.

In order to predict the stability and conformational flexibility of the protein-ligand (P-L) complexes, molecular dynamics (MD) studies of best scored compounds were done by Schrodinger-Desmond programme for 10 ns under OPLS-2005 force field.¹³ The root mean square deviation (RMSD) plots shows that the protein and the protein-ligand (P-L) complexes are stable at the end of the trajectory with minimization under 4Å. The P-L interaction histogram (Figure 2A.9) and P-L contacts shows that, in 1OXN-Hy-ISO-VIII complex, Ala80 and Gly83 form H-bond with –NH and –O of amide, which stands for 91% and 60% of the simulation time respectively. The π - π stacking interaction of 1, 4-dioxane with Phe81 last for 3% of the trajectory. The –O of chromone interacts with Tyr128 for 37% of the period, which also stabilizes the complex. In 1OXN-Hy-ISO-G, the terminal phenolic –OHs form strong Hbond with Gly83, Leu89 and Ala80, which stands for 62%, 35% and 47% of the simulation period. The terminal phenolic ring also tied up with Phe81 by π - π stacking interaction for about 45% of the trajectory, which also contributes to the stability of the complex. In 1OXQ-Hy-ISO-VIII, the –OH and –O from benzopyran ring interact with Lys121 by forming H-bond and exist 48% and 37% of the simulation time respectively. The terminal phenolic –OH form strong H-bond with Tyr128 and exist over the entire period of trajectory. There exists a π - π stacking interaction between pyrazole rings with Phe81, which lasts for 36% of the overall period. The amide –NH form H-bond with Ala80, which also favors the binding of 4g inside the binding pocket of 1OXQ. The H-bond formed between the terminal phenolic –OHs with

Gly83 (77%) and Ala80 (9%) and π - π stacking interaction of benzene moiety with Phe81 stabilizes Hy-ISO-G inside 1OXQ.

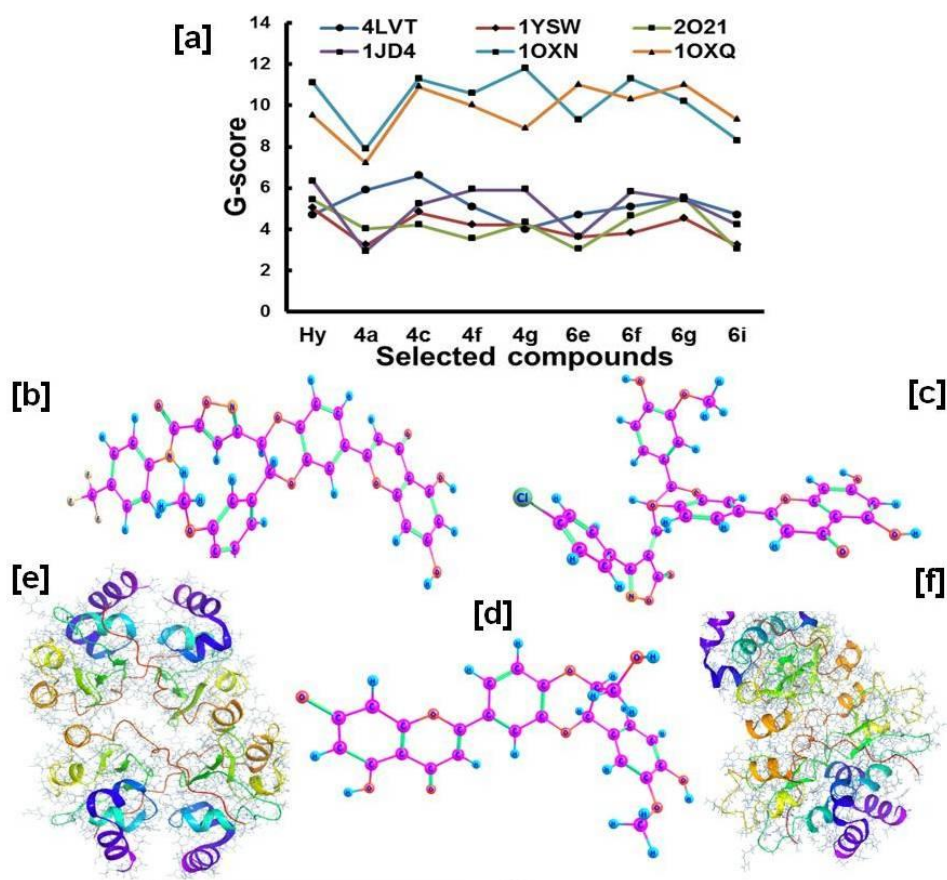


Figure 2A.7: [a] G-score analysis of selected ligands in six different proteins-4LVT, 1YSW, 2021, 1JD4, 1OXN and 1OXQ; optimized structures of [b] HY-ISO-VIII [c] HY-ISO-G [d] Hy; crystal structures of proteins with PDB ID [e] 1OXN [f] 1OXQ.

2A.3 Conclusion

In summary, a semisynthetic approach for evaluating new NPCEs from the library of hydnocarpin-isoxazole and isoxazolone analogues is described in detail. The two potent cytotoxic NPCEs Hy-ISO-G and Hy-ISO-VIII were selected by extensive in vitro assays with complementary in-silico molecular docking analysis. Subsequently, in-depth in-vitro and molecular dynamics exploration were accomplished for substantiating the preferential effectiveness of antiproliferative activity towards lung adenocarcinoma and malignant melanoma cells.

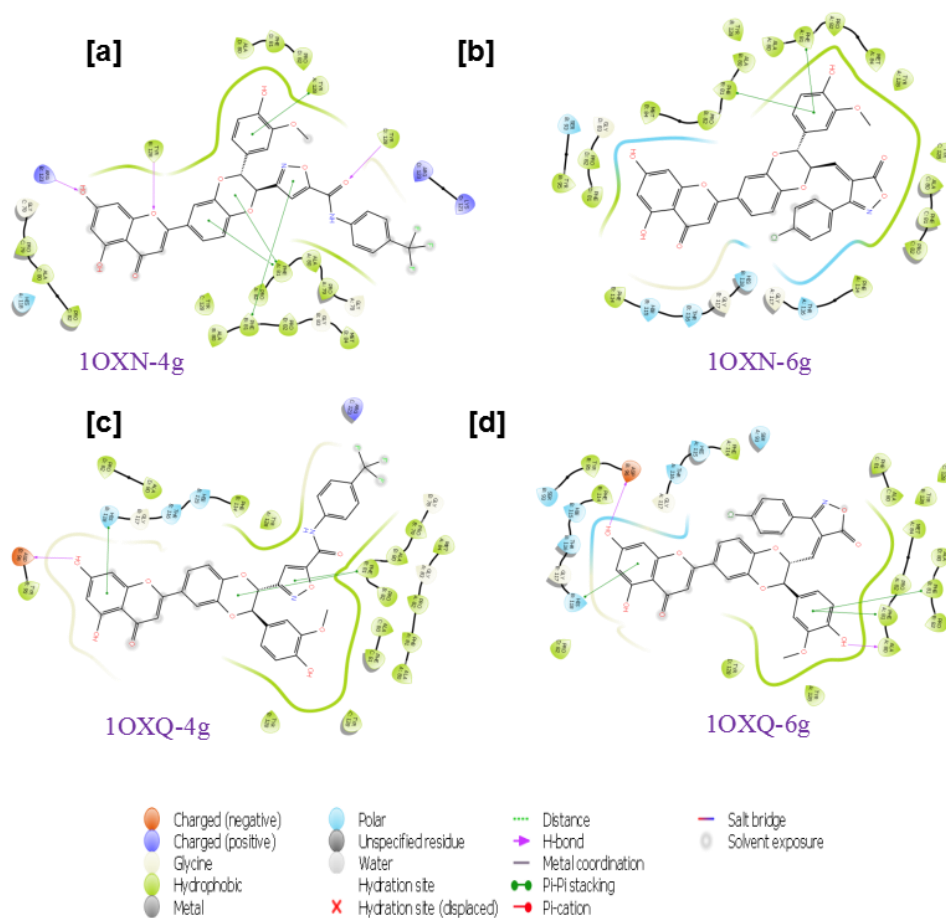


Figure 2A.8: The compounds 4g and 6g in the binding site of 10XN and 10XQ

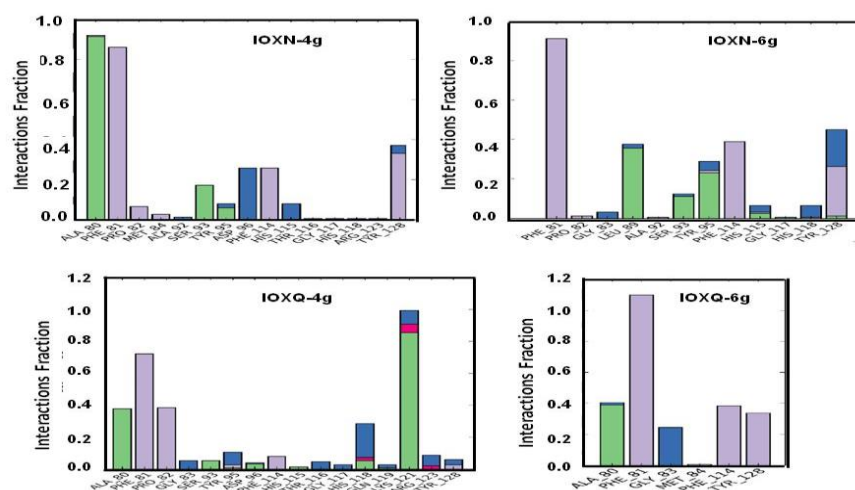


Figure 2A.9: P-L interaction histogram for 4g and 6g in 10XN and 10XQ.

2A.4 Experimental Section

2A.4.1 Chemistry. All commercially available reagents were used without further purification. Anhydrous solvents were dried through routine protocols. All chemicals and solvents were purchased from sigma Aldrich, Merck, and Specrochem, used without further purification. Analytical TLC was performed on a Merck 60 F254 silica gel plate (0.25 mm thickness) and visualization was done with UV light (254 and 365 nm). Column chromatography was performed on Merck 60 silica gel (60–120 or 100–200 mesh). NMR spectra were recorded on Bruker Advance 500 NMR spectrometer, and chemical shifts are expressed in parts per million (ppm). The mass spectra were recorded on Thermo Scientific Exactive ESI-MS spectrophotometer. The purity of all the Hy-ISO derivatives was $\geq 95\%$ as obtained from high-performance liquid chromatography HPLC system (Shimadzu, Kyoto, Japan) with SPD-M20A UV-vis photo diode array (PDA) detector on a 250 mm x 4.6 mm i. d, 5 μ m, YMC-Pack R&D ODS analytical column (9YMC Co., Ltd. Japan).

2A.4.1.1 Oxidation of Hydnocarpin to hydnocarpin aldehyde Compound **1** (30mg, 0.06 mmol) was dissolved in anhydrous DMSO. TFA (4.4 mg, 0.036 mmol) was added to this followed by pyridine (6.06 mg, 0.072 mmol) and allowed to stir for 5 min at room temperature. Then N,N'-Dicyclohexylcarbodiimide (DCC) (26.7 mg, 0.13 mmol) was added to the mixture and allowed to stir at room temperature. After 24 h, 3 mL of water was added to the reaction mixture and the product was precipitated out. The precipitate was filtered and washed thoroughly with hexane and the solid obtained was dried under vacuum in order to afford compound **2** (24.6 mg, 82 %) as yellow powder. ^1H NMR (500 MHz, CD_3OD): δ 12.89 (s, 1H), 9.94 (s, 1H), 7.80 (s, 1H), 7.48-7.43 (m, 2H), 7.02 (s, 1H), 6.94 (d, J = 5Hz, 1H), 6.86 (d, J = 5Hz, 1H), 6.77 (d, J = 5Hz, 1H), 6.56 (s, 1H), 6.46 (s, 1H), 6.15 (s, 1H), 3.75 (s, 3H), 3.43 (d, J = 5Hz, 1H). ^{13}C NMR (125 MHz, CD_3OD) δ 200.3, 176.06, 164.3, 163.0, 161.4, 167.3, 147.6, 146.9, 143.6, 139.9, 126.9, 123.6, 120.5, 119.9, 117.5, 115.3, 114.7, 111.7, 98.4, 94.0, 77.9, 76.33, 60.0, 55.6, 23.2. HRMS (ESI): m/z $[\text{M} + \text{H}]^+$ calcd for $\text{C}_{25}\text{H}_{19}\text{O}_9$: 463.1029; found 463.1027.

2A.4.1.2 General procedure for the synthesis of hydnocarpin isoxazole derivatives, General procedure A: Synthesis of compounds 4a-j. Compound **2** was dissolved in 1:4 mixture of Methanol and ethylacetate to which N-hydroxylamine hydrochloride (0.26 mmol) and NaOH (0.26 mmol) was added and stirred under room temperature for 10 min.

To this mixture, N-bromosuccinimide (0.52 mmol) was added and stirred for another 10 min. Then 2-alkynyl derivative (0.26 mmol) was added and allowed to stir for 12 h. The reaction mixture was subjected to column chromatography and the product was isolated in good to excellent yields.

2-(2-(5-benzylisoxazol-3-yl)-3-(4-hydroxy-3-methoxyphenyl)-2,3

dihydrobenzo[b][1,4]dioxin-6-yl)-5,7-dihydroxy-4H-chromen-4-one (4a): Following the general procedure A, was obtained after purification by column chromatography on silica gel (EtOAc:hexanes = 70:30) as yellow solid; yield: 82%. ¹H NMR (500 MHz, Acetone) δ 13.84 (s, 1H), 7.61 – 7.54 (m, 2H), 7.22 (dd, J = 8.4, 1.2) Hz, 1H), 7.10 – 6.91 (m, 4H), 6.88 (dd, J = 8.1, 1.7 Hz, 2H), 6.78 (dd, J = 5.2, 2.6 Hz, 3H), 5.00 (d, J = 8.1 Hz, 2H), 4.12 (dd, J = 7.3, 3.2 Hz, 3H), 3.80 (d, J = 12.6 Hz, 2H), 3.75 (s, 3H), 3.71 – 3.65 (m, 1H), 3.43 (dd, J = 12.5, 4.1 Hz, 2H). ¹³C NMR(125 MHz, CD₃OD) δ 176.1, 164.3, 163.0, 161.4, 167.3, 147.6, 146.9, 143.6, 139.9, 126.9, 123.6, 120.5, 119.9, 117.5, 115.3, 114.7, 111.7, 98.4, 94.0, 77.9, 76.33, 60.0, 55.6, 23.2. HRMS (ESI): m/z [M + H]⁺ calcd for C₃₅H₂₈NO₉: 606.1764; found 606.1752.

5,7-dihydroxy-2-(3-(4-hydroxy-3-methoxyphenyl)-2-(4-(hydroxymethyl)-5-methylisoxazol-3-yl)-2,3 dihydrobenzo[b][1,4]dioxin-6-yl)-4H-chromen-4-one (4b):

Following the general procedure A, was obtained after purification by column chromatography on silica gel (EtOAc:hexanes = 70:30) as yellow solid; yield: 72%. ¹H NMR (500 MHz, Acetone) δ 13.8 (s, 1H), 7.64 – 7.49 (m, 2H), 7.22 (dd, J = 8.4, 1.3) 1H), 7.81 – 6.89 (m, 2H), 6.78 (dd, J = 5.2, 2.6 Hz, 3H), 5.00 (d, J = 8.1 Hz, 2H), 4.12 (dd, J = 7.3, 3.2 Hz, 3H), 3.80 (d, J = 12.6 Hz, 2H), 3.75 (s, 3H), 3.71 – 3.65 (m, 1H), 3.43 (dd, J = 12.5, 4.1 Hz, 2H). ¹³C NMR(125 MHz, CD₃OD) δ 182.1, 166.4, 163.6, 161.8, 158.9, 150.0, 147.9, 147.5, 144.6, 120.0, 119.5, 115.7, 114.3, 111.0, 104.3, 100.6, 98.6, 94.2, 56.4, 54.5, 15.7. HRMS (ESI): m/z [M + H]⁺ calcd for C₃₀H₂₆NO₁₀: 560.1557; found 560.1548.

5,7-dihydroxy-2-(3-(4-hydroxy-3-methoxyphenyl)-2-(5-(2-hydroxypropan-2-yl)isoxazol-3-yl)-2,3-dihydrobenzo[b][1,4]dioxin-6-yl)-4H-chromen-4-one (4c):

Following the general procedure A, was obtained after purification by column chromatography on silica gel (EtOAc:hexanes = 70:30) as yellow solid; yield: 79%. ¹H NMR (500 MHz, Acetone) δ 13.83 (s, 1H), 7.83 (s, 2H), 7.62 – 7.56 (m, 3H), 7.05 – 6.94 (m, 4H), 6.88 (d, J = 8.0 Hz, 1H), 6.76 (dd, J = 10.2, 2.5 Hz) 2H), 5.00 (d, J = 8.2 Hz, 2H),

4.45 (dd, $J = 9.2, 2.9$ Hz, 3H), 3.75 (d, $J = 9.0$ Hz, 3H), 3.46 – 3.40 (m, 2H), 2.65 (s, 3H), 2.41 (s, 3H). ^{13}C NMR(125 MHz, CD_3OD) δ 182.3, 166.4, 163.6, 161.8, 158.9, 158.8, 150.0, 147.7, 147.6, 147.5, 143.6, 134.2, 121.2, 120.0, 119.7, 115.8, 111.4, 109.8, 104.5, 98.3, 94.0, 92.1, 86.1, 56.1, 31.3, 23.2. HRMS (ESI): m/z $[\text{M} + \text{H}]^+$ calcd for $\text{C}_{32}\text{H}_{30}\text{NO}_{10}$: 588.1870; found 588.1863.

5,7-dihydroxy-2-(3-(4-hydroxy-3-methoxyphenyl)-2-(5-(hydroxymethyl)isoxazol-3-yl)-2,3-dihydrobenzo[b][1,4]dioxin-6-yl)-4H-chromen-4-one (4d): Following the general procedure A, was obtained after purification by column chromatography on silica gel (EtOAc:hexanes = 70:30) as yellow solid; yield: 86%. ^1H NMR (500 MHz, Acetone) δ 13.84 (s, 2H), 7.75 (s, 2H), 7.59 (t, $J = 5.6$ Hz, 2H), 7.08 – 6.93 (m, 4H), 6.88 (dd, $J = 8.0, 1.5$ Hz, 1H), 6.78 (d, $J = 7.9$ Hz, 2H), 5.00 (d, $J = 8.0$ Hz, 1H), 4.15 – 4.07 (m, 2H), 3.76 (s, 3H), 3.50 – 3.37 (m, 3H). ^{13}C NMR(125 MHz, CD_3OD) δ 182.2, 166.3, 163.5, 161.6, 158.7, 158.6, 150.0, 147.7, 147.6, 147.5, 143.4, 133.8, 121.1, 120.0, 119.7, 115.7, 114.5, 111.5, 109.8, 104.4, 101.9, 98.3, 94.0, 92.5, 56.7. HRMS (ESI): m/z $[\text{M} + \text{H}]^+$ calcd for $\text{C}_{29}\text{H}_{26}\text{NO}_{10}$: 548.1557; found 548.1544.

5,7-dihydroxy-2-(3-(4-hydroxy-3-methoxyphenyl)-2-(5-(p-tolyl)isoxazol-3-yl)-2,3-dihydrobenzo[b][1,4]dioxin-6-yl)-4H-chromen-4-one (4e): Following the general procedure A, was obtained after purification by column chromatography on silica gel (EtOAc:hexanes = 70:30) as yellow solid; yield: 82%. ^1H NMR (500 MHz, DMSO) δ 13.84 (s, 1H), 9.25 (s, 1H), 7.71 (d, $J = 2.1$ Hz, 1H), 7.66 (dd, $J = 8.5, 2.1$ Hz, 1H), 7.09 (dd, $J = 14.0, 6.3$ Hz, 2H), 7.01 (t, $J = 11.8$ Hz, 1H), 6.90 – 6.78 (m, 2H), 5.01 (d, $J = 7.9$ Hz, 1H), 4.27 (d, $J = 3.1$ Hz, 1H), 3.77 (s, 3H), 2.50 – 2.49 (m, 6H). ^{13}C NMR(125 MHz, CD_3OD) δ 182.1, 169.5, 166.4, 163.3, 161.8, 158.5, 150.0, 147.7, 147.6, 147.5, 144.2, 135.0, 131.8, 129.7, 129.5, 124.9, 123.7, 120.0, 121.2, 119.7, 115.8, 114.5, 111.4, 109.7, 100.0, 98.3, 94.6, 92.4, 91.8, 56.5, 21.3. HRMS (ESI): m/z $[\text{M} + \text{H}]^+$ calcd for $\text{C}_{35}\text{H}_{28}\text{NO}_9$: 606.1764; found 606.1759.

2-(2-(5-(aminomethyl)isoxazol-3-yl)-3-(4-hydroxy-3-methoxyphenyl)-2,3-dihydrobenzo[b][1,4]dioxin-6-yl)-5,7-dihydroxy-4H-chromen-4-one (4f): Following the general procedure A, was obtained after purification by column chromatography on silica gel (EtOAc:hexane = 70:30) as yellow solid; yield: 73%. ^1H NMR (500 MHz, Acetone) δ 13.79 (s, 1H), 7.56 (d, $J = 11.5$ Hz, 4H), 7.02 (s, 2H), 6.95 (d, $J = 8.4$ Hz, 2H), 6.86 (d, $J = 8.1$ Hz, 2H), 6.79 (s, 1H), 6.76 (d, $J = 15.5$ Hz, 2H), 4.98 (d, $J = 7.6$ Hz, 3H),

4.11 (s, 2H), 3.76 (s, 3H), 3.41 (d, J = 12.4 Hz, 3H). ^{13}C NMR(125 MHz, CD_3OD) δ 182.2, 166.3, 163.5, 161.6, 158.7, 158.6, 150.0, 147.7, 147.6, 147.5, 143.4, 133.8, 121.1, 120.0, 119.7, 115.7, 114.5, 111.5, 109.8, 104.4, 101.9, 98.3, 94.0, 92.5, 56.7. HRMS (ESI): m/z $[\text{M} + \text{H}]^+$ calcd for $\text{C}_{29}\text{H}_{27}\text{N}_2\text{O}_9$: 547.1717; found 547.1716.

3-(6-(5,7-dihydroxy-4-oxo-4H-chromen-2-yl)-3-(4-hydroxy-3-methoxyphenyl)-2,3-dihydrobenzo[b][1,4]dioxin-2-yl)-N-(4-(trifluoromethyl)phenyl)isoxazole-5-

carboxamide (4g): Following the general procedure A, was obtained after purification by column chromatography on silica gel (EtOAc:hexane = 70:30) as yellow solid; yield: 87%. ^1H NMR (500 MHz, Acetone) δ 13.81 (s, 1H), 8.21 (s, 1H), 7.58 (dd, J = 12.8, 6.3 Hz, 2H), 6.98 (dd, J = 24.5, 16.0 Hz, 2H), 6.86 (d, J = 8.0 Hz, 1H), 6.81 – 6.74 (m, 2H), 4.99 (d, J = 8.0 Hz, 1H), 4.11 (d, J = 4.0 Hz, 1H), 3.75 (s, 3H), 3.42 (dd, J = 26.1, 17.5 Hz, 2H). ^{13}C NMR(125 MHz, CD_3OD) δ 182.2, 166.3, 165.2, 163.5, 161.6, 158.7, 158.6, 150.0, 147.7, 147.6, 147.5, 143.4, 141.2, 133.8, 132.5, 125.3, 124.6, 121.1, 120.0, 118.7, 115.7, 114.5, 110.5, 109.7, 104.4, 101.9, 98.3, 94.0, 92.5, 56.7. HRMS (ESI): m/z $[\text{M} + \text{H}]^+$ calcd for $\text{C}_{36}\text{H}_{28}\text{F}_3\text{N}_2\text{O}_{10}$: 705.1696; found 705.1689.

N-((4-chlorophenyl)sulfonyl)-3-(6-(5,7-dihydroxy-4-oxo-4H-chromen-2-yl)-3-(4-hydroxy-3-methoxyphenyl)-2,3-dihydrobenzo[b][1,4]dioxin-2-yl)isoxazole-5-

carboxamide (4h): Following the general procedure A, was obtained after purification by column chromatography on silica gel (EtOAc:hexane = 70:30) as yellow solid; yield: 73%. ^1H NMR (500 MHz, Acetone) δ 13.81 (s, 1H), 8.21 (s, 2H), 7.58 (dd, J = 8.4, 1.3 Hz, 2H), 6.98 (dd, J = 10.2, 2.5 Hz, 4H), 6.86 (d, J = 8.0 Hz, 2H), 6.81 – 6.74 (m, 2H), 4.99 (d, J = 8.0 Hz, 2H), 4.11 (d, J = 4.0 Hz, 1H), 3.75 (s, 3H), 3.42 (dd, J = 26.1, 17.5 Hz, 2H). ^{13}C NMR (125 MHz, CD_3OD) δ 182.2, 169.5, 166.3, 165.2, 163.5, 161.6, 158.7, 158.6, 150.0, 147.7, 147.6, 147.5, 141.2, 137.5, 138.0, 134.2, 124.6, 121.1, 120.0, 118.7, 115.7, 114.5, 110.5, 109.7, 104.4, 101.9, 98.3, 94.0, 92.5, 56.7. HRMS (ESI): m/z $[\text{M} + \text{H}]^+$ calcd for $\text{C}_{35}\text{H}_{28}\text{ClN}_2\text{O}_{12}\text{S}$: 735.1051; found 735.1048.

N-cyclohexyl-3-(6-(5,7-dihydroxy-4-oxo-4H-chromen-2-yl)-3-(4-hydroxy-3-methoxyphenyl)-2,3-dihydrobenzo[b][1,4]dioxin-2-yl)isoxazole-5-carboxamide (4i):

Following the general procedure A, was obtained after purification by column chromatography on silica gel (EtOAc:hexane = 70:30) as yellow solid; yield: 76%. ^1H NMR (500 MHz, DMSO) δ 13.79 (s, 1H), 8.10 (dd, J = 8.3, 1.2 Hz, 2H), 7.39 (s, 2H), 7.29 (s, 4H), 7.19 (s, 2H), 7.02 (d, J = 11.9 Hz, 2H), 6.91 – 6.80 (m, 4H), 6.45 (s, 2H),

4.96 (d, $J = 7.7$ Hz, 3H), 1.47-1.40 (m, 3H), 1.25-1.17 (m, 2H); ^{13}C NMR(125 MHz, CD_3OD) δ 182.2, 166.3, 163.5, 161.6, 158.7, 158.6, 150.0, 147.7, 147.6, 147.5, 143.4, 133.8, 121.1, 120.0, 119.7, 115.7, 114.5, 111.5, 109.8, 104.4, 101.9, 98.3, 94.0, 56.7, 51.5, 34.6, 27.9, 24.4 HRMS (ESI): m/z $[\text{M} + \text{H}]^+$ calcd for $\text{C}_{35}\text{H}_{33}\text{N}_2\text{O}_{10}$: 641.2135; found 641.2127.

3-(6-(5,7-dihydroxy-4-oxo-4H-chromen-2-yl)-3-(4-hydroxy-3-methoxyphenyl)-2,3-dihydrobenzo[b][1,4]dioxin-2-yl)-N-(phenylsulfonyl)isoxazole-5-carboxamide (4j):

Following the general procedure A, was obtained after purification by column chromatography on silica gel (EtOAc:hexane = 70:30) as yellow solid; yield: 80%. ^1H NMR (500 MHz, DMSO) δ 13.79 (s, 1H), 8.10 (dd, $J = 8.3, 1.3$ Hz, 2H), 7.39 (s, 2H), 7.29 (s, 2H), 7.19 (s, 2H), 7.02 (d, $J = 11.9$ Hz, 1H), 6.91 – 6.80 (m, 4H), 6.45 (s, 2H), 4.96 (d, $J = 7.7$ Hz, 2H). ^{13}C NMR(125 MHz, CD_3OD) δ 182.2, 170.2, 163.5, 161.6, 158.7, 158.6, 150.0, 147.7, 147.6, 147.5, 143.4, 133.8, 132.0, 130.8, 127.5, 121.1, 120.0, 119.7, 115.7, 114.5, 111.5, 109.8, 104.4, 101.9, 98.3, 94.0, 56.3. HRMS (ESI): m/z $[\text{M} + \text{H}]^+$ calcd for $\text{C}_{35}\text{H}_{27}\text{N}_2\text{O}_{12}\text{S}$: 699.1285; found 699.1281.

2A.4.1.3 General procedure for the synthesis of hydnocarpin-isoxazolone derivatives, General procedure B: Synthesis of compounds 6a-j A mixture of equimolar quantities of hydroxylamine hydrochloride (0.07 g, 1 mmol) and b-ketoester (0.130 g, 1 mmol) were stirred in 1 mL of water for 5 min. Then, Hy-CHO 10 mol % of boric acid was added and the reaction mixture was stirred at room temperature for 6 h. The solid product formed was isolated by simple filtration and washed with water

(E)-3-(chloromethyl)-4-((6-(5,7-dihydroxy-4-oxo-4H-chromen-2-yl)-3-(4-hydroxy-3-methoxyphenyl)-2,3-dihydrobenzo[b][1,4]dioxin-2-yl)methylene)isoxazolidin-5-one

(6a): Following the general procedure B, was obtained after purification by column chromatography on silica gel (EtOAc:hexane = 70:30) as yellow solid; yield: 73%. ^1H NMR (500 MHz, Acetone) δ 7.51 – 7.44 (m, 4H), 7.03 (d, $J = 1.7$ Hz, 2H), 6.95 (d, $J = 9.1$ Hz, 2H), 6.87 (dd, $J = 8.1, 1.8$ Hz, 2H), 6.77 (d, $J = 8.1$ Hz, 2H), 6.57 (s, 2H), 6.48 (d, $J = 2.0$ Hz, 2H), 6.15 (d, $J = 1.9$ Hz, 2H), 3.75 (s, 6H), 2.71 (s, 5H). ^{13}C NMR (125 MHz, MeOD) δ 182.3, 147.9, 147.5, 144.0, 127.5, 120.6, 119.8, 117.5, 115.2, 114.9, 111.0, 103.7, 93.9, 78.6, 76.9, 60.5, 55.3. HRMS (ESI): m/z $[\text{M} + \text{H}]^+$ calcd for $\text{C}_{29}\text{H}_{21}\text{ClNO}_{10}$: 578.0854; found 578.0848.

(E)-4-((6-(5,7-dihydroxy-4-oxo-4H-chromen-2-yl)-3-(4-hydroxy-3-methoxyphenyl)-2,3-dihydrobenzo[b][1,4]dioxin-2-yl)methylene)-3-methylisoxazolidin-5-one (6b):

Following the general procedure B, was obtained after purification by column chromatography on silica gel (EtOAc:hexane = 70:30) as yellow solid; yield: 81%. ¹H NMR (500 MHz, Acetone) δ 7.51 – 7.44 (m, 4H), 7.03 (d, J = 1.7 Hz, 2H), 6.95 (d, J = 9.1 Hz, 2H), 6.87 (dd, J = 8.1, 1.8 Hz, 2H), 6.77 (d, J = 8.1 Hz, 2H), 6.57 (s, 2H), 6.48 (d, J = 2.0 Hz, 2H), 6.15 (d, J = 1.9 Hz, 2H), 3.75 (s, 6H), 2.71 (s, 5H). ¹³C NMR (125 MHz, MeOD) δ 182.3, 173.8, 162.6, 159.7, 147.9, 147.6, 145.5, 144.0, 143.6, 127.5, 121.3, 120.6, 119.82, 117.5, 115.2, 114.9, 111.0, 103.7, 93.9, 87.4, 78.6, 76.9, 60.5, 55.3, 21.8. HRMS (ESI): m/z [M + H]⁺ calcd for C₂₉H₂₂NO₁₀: 544.1244; found 544.1241.

(E)-4-((6-(5,7-dihydroxy-4-oxo-4H-chromen-2-yl)-3-(4-hydroxy-3-methoxyphenyl)-2,3-dihydrobenzo[b][1,4]dioxin-2-yl)methylene)-3-(trifluoromethyl)isoxazolidin-5-one (6c):

Following the general procedure B, was obtained after purification by column chromatography on silica gel (EtOAc:hexane = 70:30) as yellow solid; yield: 84%. ¹H NMR (500 MHz, MeOD) δ 7.51 (d, J = 2.0 Hz, 1H), 7.44 (dd, J = 8.5, 1.9 Hz, 1H), 6.97 (d, J = 8.7 Hz, 2H), 6.81 (dd, J = 8.0, 2.4 Hz, 2H), 6.57 (s, 1H), 6.38 (s, 1H), 6.13 (s, 1H), 4.92 (d, J = 8.0 Hz, 2H). ¹³C NMR (125 MHz, MeOD) δ 182.3, 173.8, 164.3, 162.6, 159.7, 147.7, 147.6, 145.5, 144.1, 143.6, 127.5, 121.3, 120.6, 119.82, 117.5, 115.2, 114.9, 111.2, 103.7, 93.9, 87.4, 78.6, 76.5, 60.5, 55.3. HRMS (ESI): m/z [M + H]⁺ calcd for C₂₉H₁₉F₃NO₁₀: 598.0961; found 598.0958.

(E)-4-((6-(5,7-dihydroxy-4-oxo-4H-chromen-2-yl)-3-(4-hydroxy-3-methoxyphenyl)-2,3-dihydrobenzo[b][1,4]dioxin-2-yl)methylene)-3-propylisoxazolidin-5-one (6d):

Following the general procedure B, was obtained after purification by column chromatography on silica gel (EtOAc:hexane = 70:30) as yellow solid; yield: 77%. ¹H NMR (500 MHz, MeOD) δ 7.51 (s, 1H), 7.44 (d, J = 7.8 Hz, 1H), 6.96 (s, 2H), 6.79 (dd, J = 14.9, 4.2) Hz, 2H), 6.58 (s, 1H), 6.39 (s, 1H), 6.13 (s, 1H), 3.79 (d, J = 4.8 Hz, 4H), 3.62 (d, J = 12.4 Hz, 1H), 3.40 (d, J = 12.4 Hz, 1H), 3.22 – 3.08 (m, 5H). ¹³C NMR (125 MHz, MeOD) δ 182.3, 181.1, 164.8, 162.6, 159.7, 147.9, 147.6, 145.5, 144.0, 143.6, 127.5, 121.3, 120.6, 119.8, 117.5, 115.2, 104.1, 94.6, 87.5, 78.4, 76.7, 60.4, 56.2, 34.3, 27.5, 22.7. HRMS (ESI): m/z [M + H]⁺ calcd for C₃₁H₂₆NO₁₀: 572.1557; found 572.1554.

(E)-4-((6-(5,7-dihydroxy-4-oxo-4H-chromen-2-yl)-3-(4-hydroxy-3-methoxyphenyl)-2,3-dihydrobenzo[b][1,4]dioxin-2-yl)methylene)-3-(4-fluorophenyl)isoxazolidin-5-one (6e): Following the general procedure B, was obtained after purification by column chromatography on silica gel (EtOAc:hexane = 70:30) as yellow solid; yield: 82%. ¹H NMR (500 MHz, MeOD) δ 7.51 (s, 1H), 7.44 (d, J = 7.8 Hz, 1H), 6.96 (s, 2H), 6.79 (dd, J = 14.9, 4.5 Hz, 2H), 6.58 (s, 1H), 6.39 (s, 1H), 6.13 (s, 1H), 3.79 (d, J = 4.8 Hz, 4H), 3.62 (d, J = 12.4 Hz, 1H), 3.40 (d, J = 12.4 Hz, 1H), 3.22 – 3.08 (m, 5H). ¹³C NMR (125 MHz, DMSO) δ 182.2, 181.1, 166.2, 164.8, 163.4, 161.7, 157.7, 148.1, 147.5, 144.0, 136.1, 127.4, 124.8, 122.7, 122.5, 121.00, 118.0, 115.8, 115.2, 104.1, 94.6, 87.4, 78.4, 76.7, 60.4, 56.2. HRMS (ESI): m/z [M + H]⁺ calcd for C₃₄H₂₃FNO₁₀: 624.1306; found 624.1301.

(E)-4-((6-(5,7-dihydroxy-4-oxo-4H-chromen-2-yl)-3-(4-hydroxy-3-methoxyphenyl)-2,3-dihydrobenzo[b][1,4]dioxin-2-yl)methylene)-3-(p-tolyl)isoxazolidin-5-one (6f): Following the general procedure B, was obtained after purification by column chromatography on silica gel (EtOAc:hexane = 70:30) as yellow solid; yield: 85%. ¹H NMR (500 MHz, CDCl₃) δ 12.69 (s, 1H), 7.94 (s, 1H), 7.49 (s, 1H), 7.36 (d, J = 8.6 Hz, 1H), 7.28 (s, 3H), 6.99 (d, J = 8.5 Hz, 1H), 6.88 (s, 2H), 6.47 (s, 1H), 6.38 (s, 1H), 6.26 (s, 1H). ¹³C NMR (125 MHz, DMSO) δ 182.3, 181.2, 162.6, 159.7, 147.9, 147.6, 145.5, 144.0, 143.6, 142.8, 131.3, 130.6, 130.4, 127.5, 121.3, 120.6, 119.8, 117.5, 115.2, 114.9, 111.0, 103.7, 93.9, 87.4, 78.6, 76.9, 60.5, 55.3, 23.8. HRMS (ESI): m/z [M + H]⁺ calcd for C₃₅H₂₆NO₁₀: 620.1557; found 620.1552.

(E)-3-(4-chlorophenyl)-4-((6-(5,7-dihydroxy-4-oxo-4H-chromen-2-yl)-3-(4-hydroxy-3-methoxyphenyl)-2,3-dihydrobenzo[b][1,4]dioxin-2-yl)methylene)isoxazolidin-5-one (6g): Following the general procedure B, was obtained after purification by column chromatography on silica gel (EtOAc:hexane = 70:30) as yellow solid; yield: 87%. ¹H NMR (500 MHz, CDCl₃) δ 12.69 (s, 1H), 7.92-7.48 (m, 2H), 7.53 – 7.42 (m, 2H), 7.03 (d, J = 1.7 Hz, 1H), 6.82 (dd, J = 14.8, 4.5 Hz, 2H), 6.77 (d, J = 8.1 Hz, 2H), 6.57 (s, 2H), 6.48 (d, J = 2.0 Hz, 2H), 6.15 (d, J = 1.9 Hz, 2H), 5.38-5.27 (m, 2H), 3.81 (s, 3H); ¹³C NMR (125 MHz, DMSO) δ 182.3, 181.1, 162.6, 159.7, 147.9, 147.8, 147.6, 145.5, 144.0, 143.6, 142.8, 131.3, 130.6, 130.4, 127.5, 121.3, 120.6, 119.82, 117.5, 115.2, 114.9, 111.0, 103.7, 93.9, 87.4, 78.6, 76.9, 60.5, 55.3. HRMS (ESI): m/z [M + H]⁺ calcd for C₃₄H₂₃ClNO₁₀: 640.1010; found 640.1013.

(E)-4-((6-(5,7-dihydroxy-4-oxo-4H-chromen-2-yl)-3-(4-hydroxy-3-methoxyphenyl)-2,3-dihydrobenzo[b][1,4]dioxin-2-yl)methylene)-3-phenylisoxazolidin-5-one (6h):

Following the general procedure B, was obtained after purification by column chromatography on silica gel (EtOAc:hexane = 70:30) as yellow solid; yield: 81%. ¹H NMR (500 MHz, MeOD) δ 7.53 (s, 2H), 7.18 (d, J = 8.8 Hz, 2H), 7.01 – 6.92 (m, 5H), 6.80 (dd, J = 14.2, 4.3 Hz, 2H), 6.61 (d, J = 8.8 Hz, 2H), 6.57 (s, 2H), 6.38 (s, 1H), 6.13 (s, 1H), 3.79 (s, 3H). ¹³C NMR (125 MHz, DMSO) δ 182.3, 181.1, 173.8, 162.5, 160.0, 147.9, 147.6, 145.3, 143.8, 143.4, 142.8, 131.3, 130.6, 130.4, 127.5, 121.3, 120.6, 119.8, 117.5, 115.2, 114.6, 111.0, 103.7, 93.9, 87.4, 78.6, 76.9, 60.5, 55.4. HRMS (ESI): m/z [M + H]⁺ calcd for C₃₄H₂₄NO₁₀: 606.1400; found 606.1407.

(E)-4-((6-(5,7-dihydroxy-4-oxo-4H-chromen-2-yl)-3-(4-hydroxy-3-methoxyphenyl)-2,3-dihydrobenzo[b][1,4]dioxin-2-yl)methylene)-2,3-dimethylisoxazolidin-5-one (6i):

Following the general procedure B, was obtained after purification by column chromatography on silica gel (EtOAc:hexane = 70:30) as yellow solid; yield: 79%. ¹H NMR (500 MHz, MeOD) δ 7.50 (s, 2H), 7.43 (d, J = 8.3 Hz, 2H), 6.96 (d, J = 9.2 Hz, 2H), 6.80 (dd, 2H), 6.55 (s, 2H), 6.37 (s, 2H), 6.12 (s, 2H), 3.79 (s, 3H), 3.20 (s, 3H). ¹³C NMR (125 MHz, DMSO) δ 182.3, 181.0, 162.6, 159.7, 147.9, 147.6, 145.5, 144.0, 143.6, 127.5, 121.3, 120.6, 119.8, 117.5, 115.2, 114.9, 111.0, 103.7, 93.9, 87.4, 78.6, 76.9, 60.5, 55.3, 45.7, 21.6. HRMS (ESI): m/z [M + H]⁺ calcd for C₃₀H₂₆NO₁₀: 560.1557; found 560.1552.

(E)-4-((6-(5,7-dihydroxy-4-oxo-4H-chromen-2-yl)-3-(4-hydroxy-3-methoxyphenyl)-2,3-dihydrobenzo[b][1,4]dioxin-2-yl)methylene)-3-methyl-2-phenylisoxazolidin-5-one (6j):

Following the general procedure B, was obtained after purification by column chromatography on silica gel (EtOAc:hexane = 70:30) as yellow solid; yield: 75%. ¹H NMR (500 MHz, MeOD) δ 7.86-7.72 (m, 3 H), 7.61-7.53 (m, 4H), 7.41 (d, J = 8.3 Hz, 2H), 6.96 (d, J = 9.2 Hz, 2H), 6.80 (dd, J = 14.8, 4.3 Hz, 2H), 6.53 (s, 2H), 6.22 (s, 2H), 6.12 (s, 2H), 5.39-5.27 (m, 2H), 3.79 (s, 3H). ¹³C NMR (125 MHz, DMSO) δ 182.3, 181.1, 173.8, 162.7, 160.3, 153.6, 147.9, 147.6, 145.5, 144.0, 143.6, 136.5, 134.8, 127.5, 121.3, 120.6, 119.8+, 117.5, 115.2, 114.7, 111.3, 103.7, 93.9, 87.4, 78.6, 76.9, 60.5, 55.3. HRMS (ESI): m/z [M + H]⁺ calcd for C₃₅H₂₈NO₁₀: 622.1713; found 622.1715.

2A.4.2 Cell culture. The human lung adenocarcinoma cancer cell line A549 and human metastatic melanoma cell line A375 were obtained from American Type Culture

Collection (ATCC, Manassas, VA, USA). Human lung fibroblast cell line WI-38 was kindly gifted from Indian Institute of Chemical Biology (CSIR-IICB), Kolkata, India. Cells were maintained in DMEM with 10% FBS and 5% CO₂ at 37 °C. Cells were cultured in glass bottom, 96-well black plates, T25 flasks, T75 flasks for various experiments 2 days prior to the conduction of experiments.

2A.4.2.2 In vitro cytotoxicity assays. The growth inhibition capacity of parent compounds, intermediates and the derivatives were evaluated in cancer cell and normal cell lines initially using the 3-[4, 5-dimethylthiazol-2-yl]-2,5-diphenyltetrazolium (MTT) assay as previously reported.¹⁴ This assay measures cell viability by assessing the cleavage of tetrazolium salt by mitochondrial dehydrogenase. The absorbance was measured at 570 nm using a microplate spectrophotometer (BioTek Power Wave XS)

2A.4.3 Computational analysis. The crystallized structures of the peptide antagonists of melanoma inhibitor of apoptosis (PDB Code: 1OXN and 1OXQ), crystalline and solution structures of anti-apoptotic protein Bcl-2 (PDB Code: 4LVT, 1YSW and 2O21) and the crystal structure of Death-associated inhibitor of apoptosis 1, DIAP1 (PDB Code: 1JD4) were retrieved from RCSB PDB (Protein Data Bank).¹⁵ 1OXN and 1OXQ exist as pentamer containing 140 amino acids, with a resolution of 2.2 and 2.3 Å respectively. The crystal structure of Bcl-2, 4LVT contains 166 amino acids with a resolution of 2.05 Å while the solution structures 1YSW and 2O21 contains 164 amino acids. 1JD4 comprised of 124 amino acids with a resolution of 2.7 Å. These enzymes were refined, optimized and minimized by Protein Preparation Wizard of Schrodinger suite 2017-2. The grids were generated around the centroid of the workspace ligand except in 1JD4, in which the grid was generated around the centroid of the site assigned by sitemap analysis.¹⁶ The prepared enzymes with three dimensional grid were used for docking against the different conformers of the ligands (4a, 4c, 4f, 4g, 6e, 6f, 6g and 6i) generated by ligprep tool, using glide-ligand docking of Schrodinger suite.^{17,18} The docked poses were then ranked based on Dock score (D-score) and Glide score (G-score) values. The adsorption, distribution, metabolism and excretion/toxicity (ADME/T) were predicted based on the values for pharmacokinetic parameters available from qikprop.

A pharmacophore represents the molecular features that are necessary for molecular recognition of a ligand by the target. In order to predict the structural features/pharmacophore information of multiple ligands (1, 4a,4c,4f,4g,6c,6f,6g and 6i)

that are known to bind to the target, either strongly or weakly, we developed a set of hypotheses. In this approach, the pharmacophore features on each ligand are identified, and a set of common features are sought that satisfy criteria on their positions and directions, to form pharmacophore hypotheses and they can be scored on their geometric alignment. We used Phase module of Schrodinger suite for pharmacophore generation.¹⁹ Here each ligand structure is represented by a set of points in 3D space, and the pharmacophore sites are characterized by type, location and, if applicable, directionality. We used minimum 50% match of actives and find best alignment/common features of 9 ligands by six built-in features of Phase: hydrogen bond acceptor (A), hydrogen bond donor (D), hydrophobic (H), negative ionic (N), positive ionic (P), and aromatic ring (R).

In order to predict the stability and conformational flexibility of the protein-ligand (P-L) complexes, MD studies were done by Schrodinger-Desmond programme. The simulations were carried out for 10 ns under OPLS-2005 force field with 150 approximate number of frames and trajectory of 66.7 ps.¹³ All systems were solvated in orthorhombic boxes with explicit TIP4P water and the system was neutralized by adding counter ions and simulations were performed for the system under isothermal isobaric ensemble (NPT)²⁰ with the temperature of 300K and the pressure of 1.013 bar.²¹ RMSD plots for the backbone atoms for both protein and the ligand bound protein were generated to understand the relative stability of the ligand inside its binding pocket and, the ligand-receptor complexes were visualized. The Protein-Ligand (P-L) interaction histogram shows the interactions which favors the binding.

2A.5 References

- (1) Sun, H.; Su, J.; Meng, Q.; Yin, Q.; Chen, L.; Gu, W.; Zhang, P.; Zhang, Z.; Yu, H.; Wang, S.; Li, Y. Cancer-Cell-Biomimetic Nanoparticles for Targeted Therapy of Homotypic Tumors. *Adv. Mater.* **2016**, *28* (43), 9581–9588. <https://doi.org/10.1002/adma.201602173>.
- (2) Counihan, J. L.; Grossman, E. A.; Nomura, D. K. Cancer Metabolism: Current Understanding and Therapies. *Chem. Rev.* **2018**, *118* (14), 6893–6923. <https://doi.org/10.1021/acs.chemrev.7b00775>.
- (3) Decorte, B. L. Underexplored Opportunities for Natural Products in Drug Discovery. *J. Med. Chem.* **2016**, *59*, 9295.

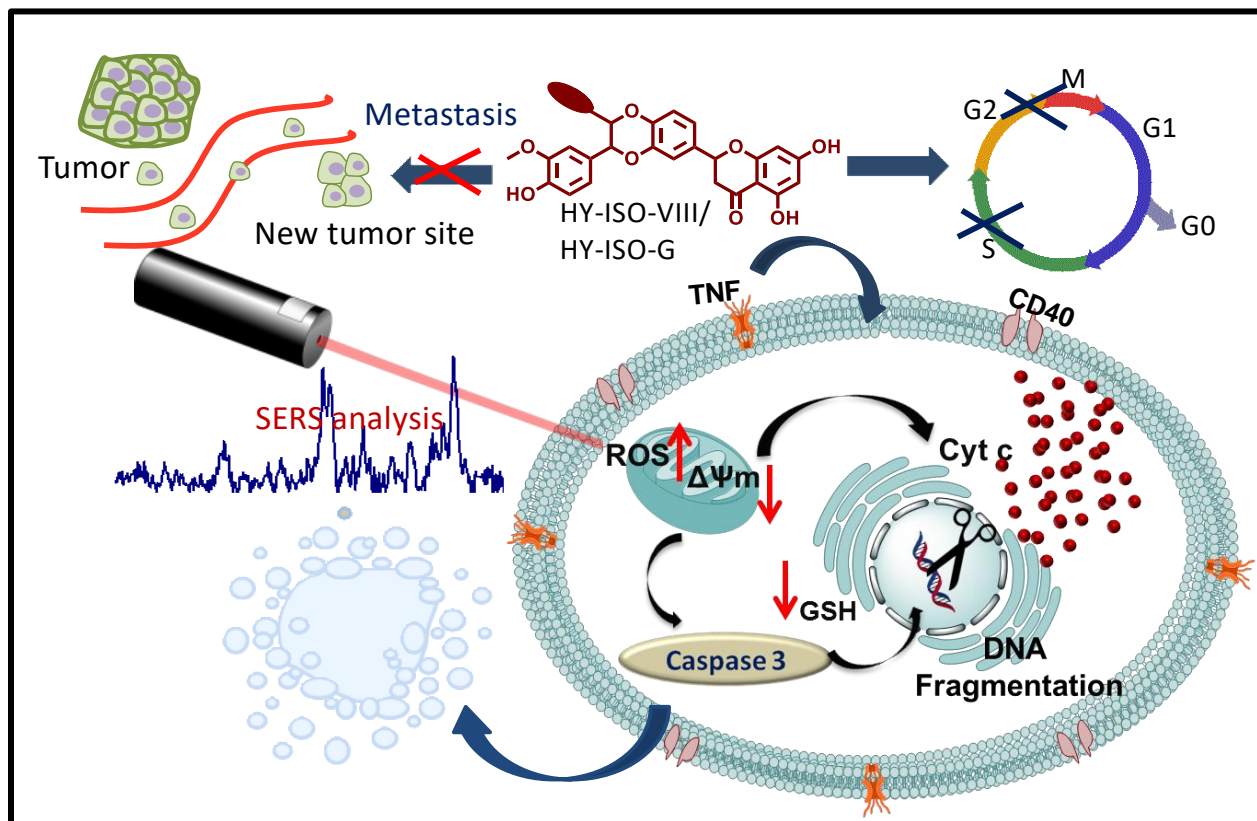
<https://doi.org/10.1021/acs.jmedchem.6b00473>.

- (4) Cragg, G. M.; Newman, D. J.; Snader, K. M. Natural Products in Drug Discovery and Development. *J. Nat. Prod.* **1997**, *60* (1), 52–60. <https://doi.org/10.1021/np9604893>.
- (5) Martins, P.; Jesus, J.; Santos, S.; Raposo, L. R.; Roma-Rodrigues, C.; Baptista, P. V.; Fernandes, A. R. Heterocyclic Anticancer Compounds: Recent Advances and the Paradigm Shift towards the Use of Nanomedicine’s Tool Box. *Molecules* **2015**, *20* (9), 16852–16891. <https://doi.org/10.3390/molecules200916852>.
- (6) Sellers, W. R.; Fisher, D. E. Apoptosis and Cancer Drug Targeting. *J Clin Invest* **1999**, *104* (12), 1655–1661. <https://doi.org/10.1172/JCI9053>.
- (7) Sahoo, M. R.; Dhanabal, S. P.; Jadhav, A. N.; Reddy, V.; Muguli, G.; Babu, U. V.; Rangesh, P. Hydnocarpus: An Ethnopharmacological, Phytochemical and Pharmacological Review. *J. Ethnopharmacol.* **2014**, *154* (1), 17–25. <https://doi.org/10.1016/j.jep.2014.03.029>.
- (8) Mathai, B. M.; Joseph, M. M.; Maniganda, S.; Nair, J. B.; Arya, J. S.; Karunakaran, V.; Radhakrishnan, K. V.; Maiti, K. K. Guanidinium Rich Dendron-Appended Hydnocarpin Exhibits Superior Anti-Neoplastic Effects through Caspase Mediated Apoptosis. *RSC Adv.* **2016**, *6* (58), 52772–52780. <https://doi.org/10.1039/c6ra08724h>.
- (9) Inhibitors, D.; Showing, H.; Kozikowski, A. P.; Tapadar, S.; Luchini, D. N.; Kim, K. H.; Billadeau, D. D. Use of the Nitrile Oxide Cycloaddition (NOC) Reaction for Molecular Probe Generation: A New Class of Enzyme Selective Histone Picomolar Activity at HDAC6. **2008**, 4370–4373.
- (10) Neelarapu, R.; Holzle, D. L.; Velaparthi, S.; Bai, H.; Brunsteiner, M.; Blond, S. Y.; Petukhov, P. A. Design , Synthesis , Docking , and Biological Evaluation of Novel Diazide-Containing Isoxazole- and Pyrazole-Based Histone Deacetylase Probes. **2011**, 4350–4364. <https://doi.org/10.1021/jm2001025>.
- (11) Simoni, D.; Roberti, M.; Invidiata, F. P.; Rondanin, R.; Baruchello, R.; Malagutti, C.; Mazzali, A.; Rossi, M.; Grimaudo, S.; Capone, F.; Dusonchet, L.; Meli, M.; Raimondi, M. V.; Landino, M.; D’Alessandro, N.; Tolomeo, M.; Arindam, D.; Lu,

-
- S.; Benbrook, D. M. Heterocycle-Containing Retinoids. Discovery of a Novel Isoxazole Arotinoid Possessing Potent Apoptotic Activity in Multidrug and Drug-Induced Apoptosis-Resistant Cells. *J. Med. Chem.* **2001**, *44* (14), 2308–2318. <https://doi.org/10.1021/jm0010320>.
- (12) Spencer, J. P. E.; Abd, M. M.; Mohsen, E.; Rice-evans, C. Cellular Uptake and Metabolism of Flavonoids and Their Metabolites: Implications for Their Bioactivity. *Arch. Biochem. Biophys.* **2004**, *423*, 148–161. <https://doi.org/10.1016/j.abb.2003.11.010>.
- (13) Guo, Z.; Mohanty, U.; Noehre, J.; Sawyer, T. K.; Sherman, W.; Krilov, G. Probing the Helical Structural Stability of Stapled P53 Peptides: Molecular Dynamics Simulations and Analysis: Research Article. *Chem. Biol. Drug Des.* **2010**, *75* (4), 348–359. <https://doi.org/10.1111/j.1747-0285.2010.00951.x>.
- (14) Joseph, M. M.; Aravind, S. R.; Varghese, S.; Mini, S.; Sreelekha, T. T. PST-Gold Nanoparticle as an Effective Anticancer Agent with Immunomodulatory Properties. *Colloids Surfaces B Biointerfaces* **2013**, *104*, 32–39. <https://doi.org/10.1016/j.colsurfb.2012.11.046>.
- (15) Franklin, M. C.; Kadkhodayan, S.; Ackerly, H.; Alexandru, D.; Distefano, M. D.; Elliott, L. O.; Flygare, J. A.; Mausisa, G.; Okawa, D. C.; Ong, D.; Vucic, D.; Deshayes, K.; Fairbrother, W. J. Structure and Function Analysis of Peptide Antagonists of Melanoma Inhibitor of Apoptosis (. *ML-IAP*), *Biochem.* **2003**, *42*, 8223–8231.
- (16) Halgren, T. New Method for Fast and Accurate Binding-Site Identification and Analysis. *Chem. Biol. Drug Des.* **2007**, *69* (2), 146–148. <https://doi.org/10.1111/j.1747-0285.2007.00483.x>.
- (17) Friesner, R. A.; Banks, J. L.; Murphy, R. B.; Halgren, T. A.; Klicic, J. J.; Mainz, D. T.; Repasky, M. P.; Knoll, E. H.; Shelley, M.; Perry, J. K.; Shaw, D. E.; Francis, P.; Shenkin, P. S. Glide: A New Approach for Rapid, Accurate Docking and Scoring. 1. Method and Assessment of Docking Accuracy. *J. Med. Chem.* **2004**, *47* (7), 1739–1749. <https://doi.org/10.1021/jm0306430>.
- (18) Steinbrecher, T. B.; Dahlgren, M.; Cappel, D.; Lin, T.; Wang, L.; Krilov, G.; Abel,
-

-
- R.; Friesner, R.; Sherman, W. Accurate Binding Free Energy Predictions in Fragment Optimization. *J. Chem. Inf. Model.* **2015**, *55* (11), 2411–2420. <https://doi.org/10.1021/acs.jcim.5b00538>.
- (19) Knoll, E. H.; Rao, A. S. N.; Shaw, A. D. E.; Friesner, R. A. PHASE : A New Engine for Pharmacophore Perception , 3D QSAR Model Development , and 3D Database Screening : 1 . Methodology and Preliminary Results. *J. Comput. Aided Mol. Des.* **2006**, *20*, 647–671. <https://doi.org/10.1007/s10822-006-9087-6>.
- (20) Azam, M. A.; Jupudi, S. Extra Precision Docking, Free Energy Calculation and Molecular Dynamics Studies on Glutamic Acid Derivatives as MurD Inhibitors. *Comput. Biol. Chem.* **2017**, *69*, 55–63. <https://doi.org/10.1016/j.compbiolchem.2017.05.004>.
- (21) Singh, S. P.; Gupta, D. Discovery of Potential Inhibitor against Human Acetylcholinesterase: A Molecular Docking and Molecular Dynamics Investigation. *Comput. Biol. Chem.* **2017**, *68*, 224–230. <https://doi.org/10.1016/j.compbiolchem.2017.04.002>.

Elucidating the mechanism of action of the synthesized Hydnocarpin based NPCEs



Abstract

The potent cancer cytotoxicity of selected NPCEs against lung adenocarcinoma and malignant melanoma cells was illustrated through the orchestrated execution of apoptosis involving the active participation of caspases in a mitochondria-dependent pathway involving the generation of reactive oxygen species. As a new insight, we used surface-enhanced Raman spectroscopy (SERS) to study the DNA fragmentation and molecular dynamics associated with the synthetic analogs on cancer cells. The unique Raman fingerprints of both the hit molecules enabled us to track the cellular internalization in a time-dependent fashion. Moreover, the exceptional kinetics observed with cytochrome c (Cyt c) were effectively traced with SERS, substantiating the mitochondrial trans-membrane depolarization. Furthermore, both Hy-ISO-VIII and Hy-ISO-G

caused appealing anti-metastatic properties, as revealed by multiple studies. Although further studies are warranted, the present findings emphasize the potential of the semi-synthesized hydnocarpin analogs from a hit molecule to a lead candidate for cancer chemotherapy.

2B.1 Introduction

The well-orchestrated programmed cell death mechanism (apoptosis) is the most preferable mode of cell death and is largely operated by two key pathways: extrinsic pathway that involves the binding of death ligands to death receptors or intrinsic pathway modulated through mitochondria.^{1,2} The former one involves the cascade activation triggering the caspase 8 whereas, the later one involves the release of cytochrome c (cyt c) from the intermembrane space of the mitochondria which in turn activates caspase 9, leading to the activation of downstream caspases giving the death response. Apoptosis is characterized by distinctive morphological alterations like nuclear fragmentation, chromatin condensation, membrane blebbing, and various biochemical and cell surface membrane modifications which permit the apoptotic bodies to be recognized and engulfed by phagocytes³. Failure to respond to the apoptotic machinery often leads to cancer development and resistance to therapy. So drugs that can restore apoptosis in cancer cells may selectively kill tumorous tissue and can act as effective anticancer agents.

Excellent molecular specificity, high sensitivity and the capacity of resolving multifaceted biomolecular compositions made surface-enhanced Raman scattering (SERS) as a versatile platform in cell biology.^{4,5} Label-free SERS measurements will provide rich information for the qualitative and quantitative detection of various analytes in the complex cellular environment. As the Raman spectral bands are narrow, identification of different molecules simultaneously is possible through this approach which will facilitate the real-time monitoring of complex molecular changes associated with therapies. The complex dynamics associated with the translocation of cyt c from mitochondria to cytosol during apoptosis could be effectively traced using the unique Raman cross section of this molecule.⁶ Therefore label-free monitoring of cytochromes in intact mitochondria of living cells could be a meritorious approach in establishing the execution of intrinsic apoptotic pathway. Moreover, SERS can provide a realistic platform for monitoring the changes associated with cell death. Protein denaturation and DNA fragmentation are the major cellular processes during apoptosis which can be reflected in Raman spectral bands of specific functional motif of proteins, DNA and lipids. Since SERS senses

polarisable vibrations with extremely high spacial resolution, it could be employed for monitoring the cellular internalization and release kinetics of Raman active molecules or drugs. This approach could be of greater value especially in the case of drugs which lacks inherent fluorescence property.^{7,8}

Computer-aided drug design approaches supports in virtual screening of natural product derived new chemical entities for rational selection and evaluation of potential drug candidates.⁹ The major emphasis on therapeutic efficiency of NPCEs has been exploited with in-depth biological investigations to decipher its possible molecular mechanism of action. The preferential execution of apoptosis was illustrated with multiple assays. The cell cycle distribution and bimolecular cytoplasmic changes with respect to reactive oxygen species (ROS) mediated glutathione (GSH) depletion were also studied. The invasion, migration and clonogenic assays were intended to measure the anti-metastatic potential of the identified leads. Further as a unique insight, the excellent dynamics with cyt c was traced out intra-cellularly by Raman fingerprint in a label-free manner Suffice it to say that cleverly planned semi-synthetic approaches could produce fruitful outputs which are palpable in the long run for chasing out cancer.

2B.2 Results and discussion

2B.2.1 *In vitro* assessment of Hy-ISO-G and Hy-ISO-VIII for anti-proliferative potential.

The two best selected semi-synthetic analogues Hy-ISO-G and Hy-ISO-VIII were subjected to detailed cytotoxicity evaluation initially by MTT assay against both cancer and normal cells (Figure 2B.1). It was observed that lung cancer cells were arrested with an IC₅₀ value of 3.6 and 0.76 μ M by Hy-ISO-VIII at 24 and 48 h respectively whereas Hy-ISO-G produced the same at 2 and 1.2 μ M. In the case of melanoma cells Hy-ISO-G was found to be more potent with IC₅₀s of 1.2 and 0.94 μ M but Hy-ISO-VIII generated IC₅₀s of 4 and 0.95 μ M with 24 and 48 h incubation. Both the selected analogues were 18-60 fold more potent than the parent Hy in both the cancer cells. Generally, the selected compounds displayed a time and dosage-dependent increase in the cytotoxicity. As a control experiment we noticed no cytotoxic influence in human lung fibroblast cells by the administration of both compounds, even at a higher dosage and incubation time. The cytotoxic effects of the compounds were further confirmed by lactate dehydrogenase (LDH) assay (Figure 2B.2). Plasma membrane damage due to cytotoxic agents

releases LDH into the cell culture media which could be quantified for determining the percentage of cytotoxicity caused by the agent. The cytotoxic pattern was further investigated through 5-bromo-2'-deoxyuridine (BrdU) assay (Figure 2B.3) which showed similar trend in the toxicity profile. The magnitude of the absorbance for the developed color is proportional to the quantity of BrdU incorporated into cells, which is a direct indication of cell proliferation.

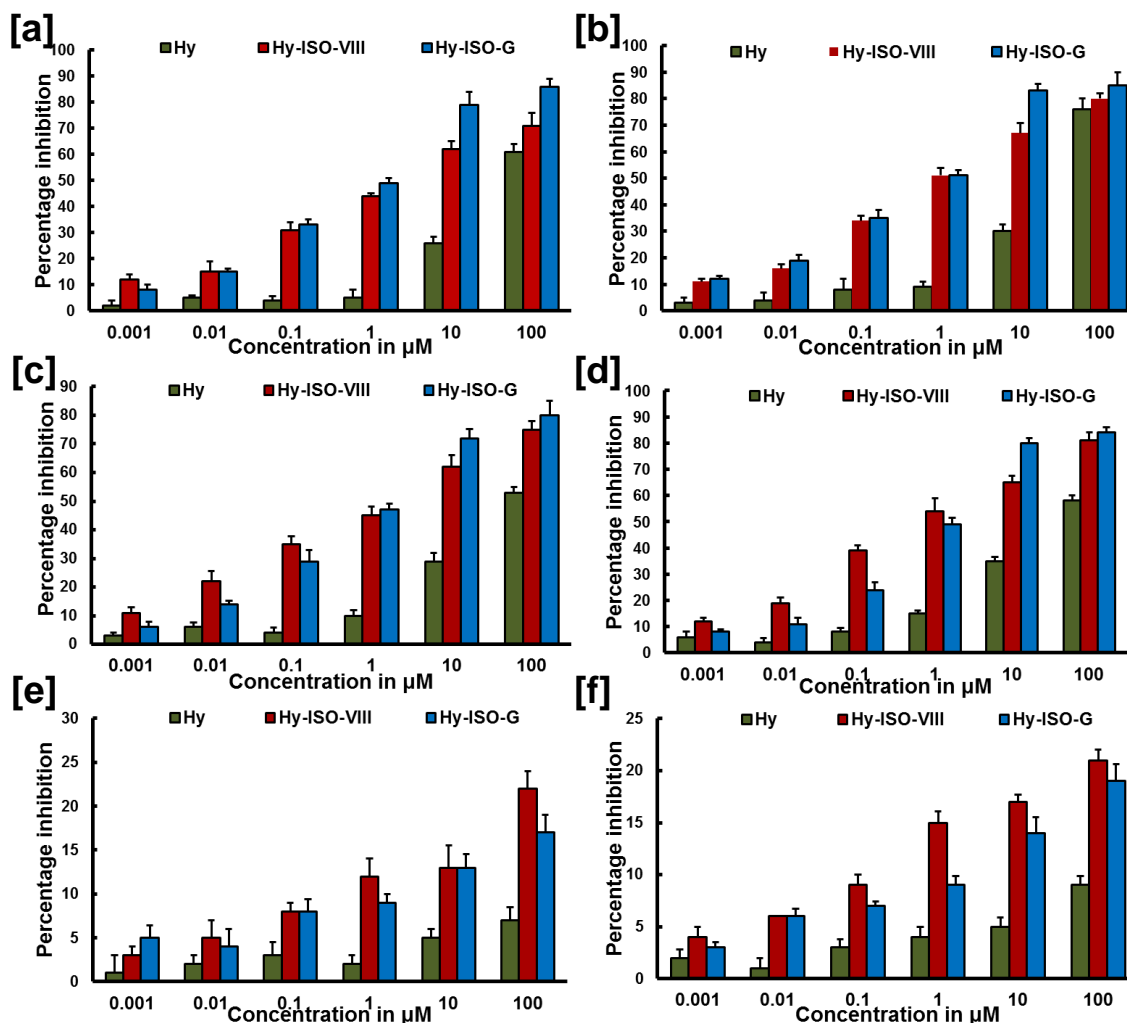


Figure 2B.1: Effect of HY-ISO-VIII and HY-ISO-G on cytotoxicity by MTT assay. [a] on A375 cells (24 h), [b] on A375 cells (48 h), [c] on A549 cells (24 h), [d] on A549 cells (48 h), [e] on WI-38 cells (24 h), [f] on WI-38 cells (48 h).

Taken together, the detailed evaluation for the cytotoxicity confirmed that the isoxazole and isoxazolone appended NPCEs; HY-ISO-VIII and HY-ISO-G promote significant contribution for the selective and enhanced cytotoxicity on A549 and A375 cells. The addition of 5-membered nitrogen and oxygen containing heterocycles on Hy effectively interacted with the

proteins involved in cell proliferation by various hydrophobic interactions to limit the cancer cell proliferation. It is presumed that the metabolites formed out of the Hy core including oxidized, methylated and sulphonated products promotes further cell death. Enzyme mediated breakdown of isoxazole and isoxazolone rings may occur inside the cellular microenvironment.^{10,11} Though Hy was reported as moderate cytotoxic agent, the semi-synthetic derivatives proved to be superior cytotoxic agents with high selectivity as revealed by multiple *in vitro* evaluation in lung and melanoma cancer cells.

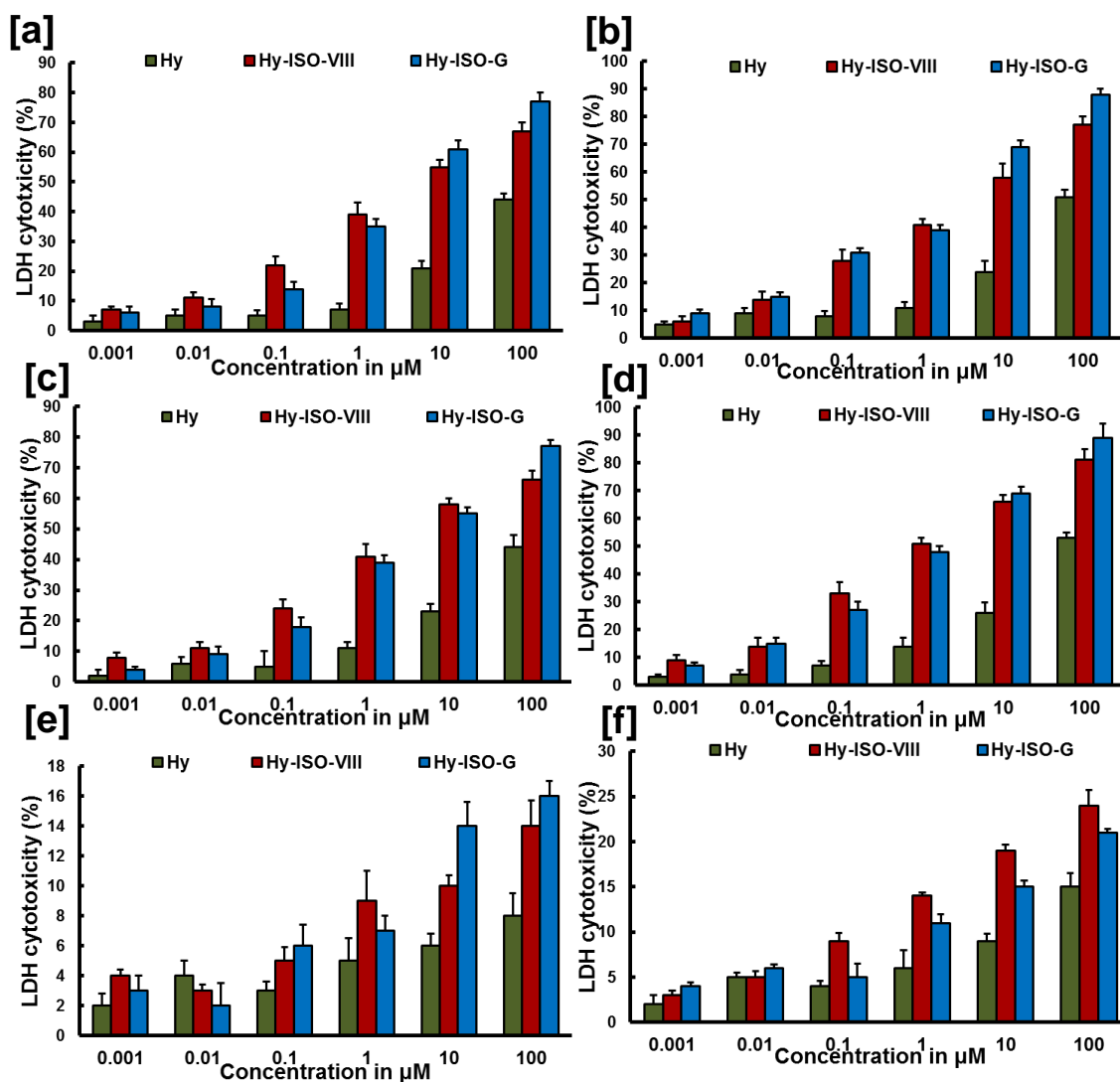


Figure 2B.2: LDH assay of HY-ISO-VIII and HY-ISO-G. [a] on A375 cells (24 h), [b] on A375 cells (48 h), [c] on A549 cells (24 h), [d] on A549 cells (48 h), [e] on WI-38 cells (24 h), [f] on WI-38 cells (48 h).

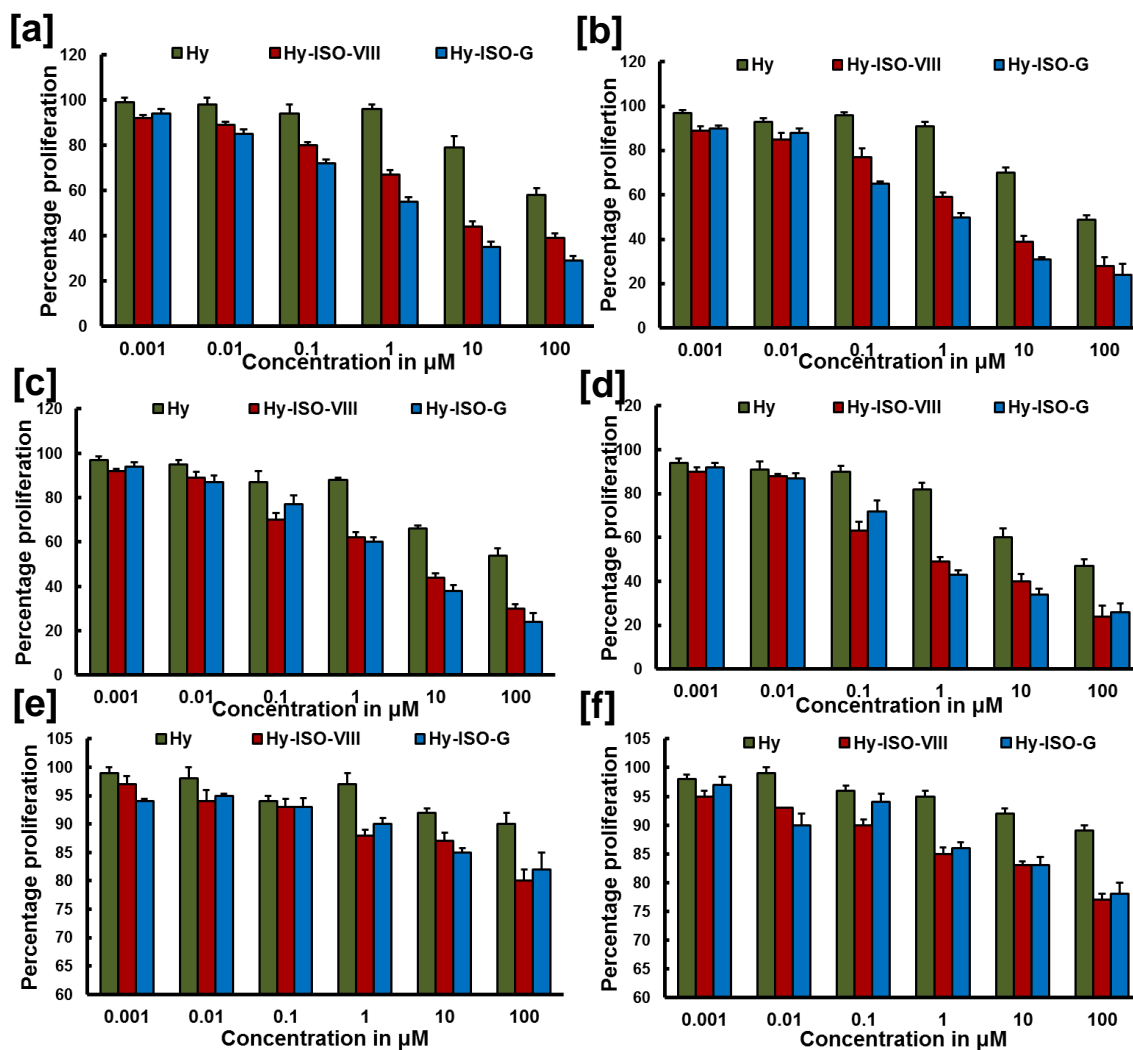


Figure 2B.3: BrdU assay of HY-ISO-VIII and HY-ISO-G. [a] on A375 cells (24 h), [b] on A375 cells (48 h), [c] on A549 cells (24 h), [d] on A549 cells (48 h), [e] on WI-38 cells (24 h), [f] on WI-38 cells (48 h).

2B.2.2 Effect on free radicals by Hy-ISO-G and Hy-ISO-VIII. Earlier studies revealed the impressive radical scavenging activity of the acetone extract from which Hy was isolated.¹² To investigate the efficacy of Hy-ISO-G and Hy-ISO-VIII towards scavenging the free radicals, DPPH radical scavenging assay, FRAP assay and hydroxyl radical scavenging assay were performed (Figure 2B.4). Unfortunately, none of the compounds including Hy showed any good antioxidant activity which rules out the chemo-preventive mode of action against cancer progression.

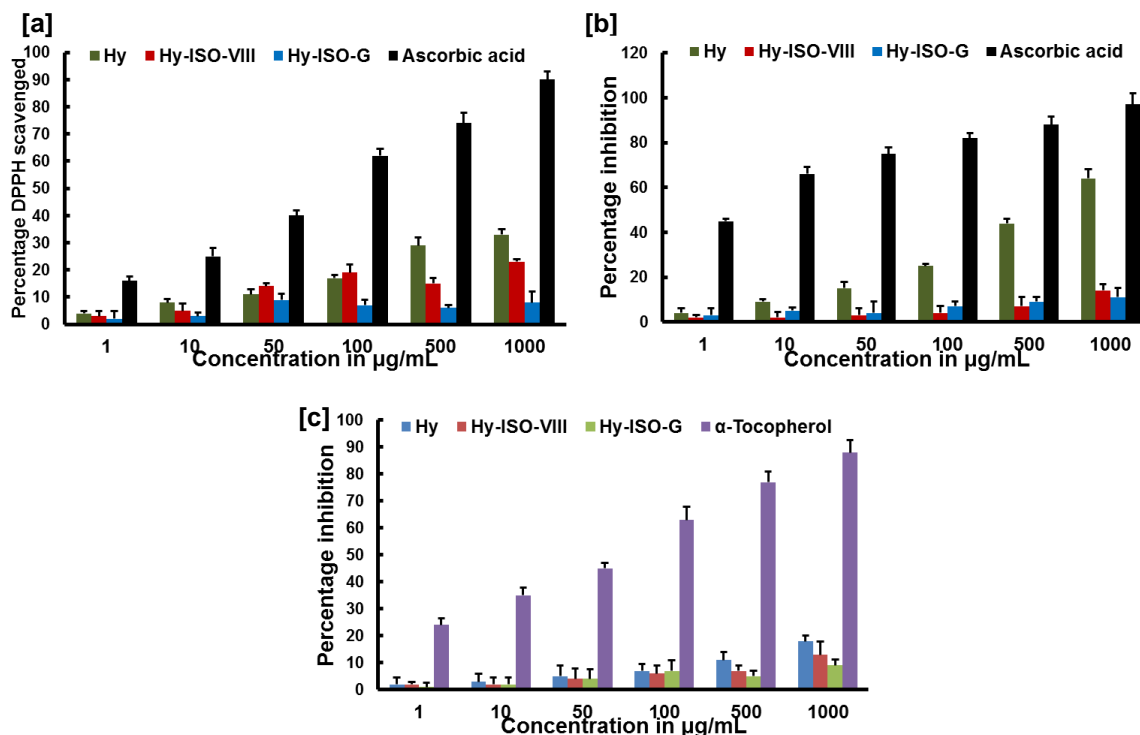


Figure 2B.4: Antioxidant activity of HY-ISO-VIII and HY-ISO-G. [a] DPPH radical scavenging assay using ascorbic acid as standard, [b] FRAP assay using ascorbic acid as standard, [c] Hydroxyl radical scavenging assay using alpha tocopherol as the standard.

The free radical induced oxidative stress causes damage to the cells and this can be overcome by the administration of antioxidants. Natural products like polyphenols are reported to suppress the cellular antioxidant pathways that will sensitize towards chemotherapy.¹³ As none of the selected derivatives displayed antioxidant property, we planned to determine whether they could induce the intracellular generation of reactive oxygen species (ROS). The intracellular ROS generation was analysed in A549 cells using dichlorofluoresceindiacetate (DCFDA) assay using the commonly used chemotherapeutic agent paclitaxel as a positive control. The obtained results highlighted the ROS generation capacity of both the hybrids in a dosage dependent manner wherein Hy-ISO-G was found to be most potent (Figure 2B.5). The fluorescent intensity was enhanced to 0.5-2.5 fold in case of Hy-ISO-VIII with 1 and 100 μM respectively, whereas Hy-ISO-G enhanced the fluorescence intensity more than 3 fold even with lower concentration (1 μM). Most of the natural product derived anticancer agents like doxorubicin, paclitaxel and vinblastin are capable of generating intracellular ROS which further leads to DNA damage and antitumor activity.¹⁴ Also natural products like oridonin and its derivatives that showed excellent

anticancer property executes apoptosis *via* ROS mediated pathway.¹⁵ Similarly, our hybrid molecules which holds the advantages of biosynthesis as well as synthetic modification with the heterocycles might have enhanced the ROS generation capability and hence could act through the involvement of mitochondria in cell death mechanism.

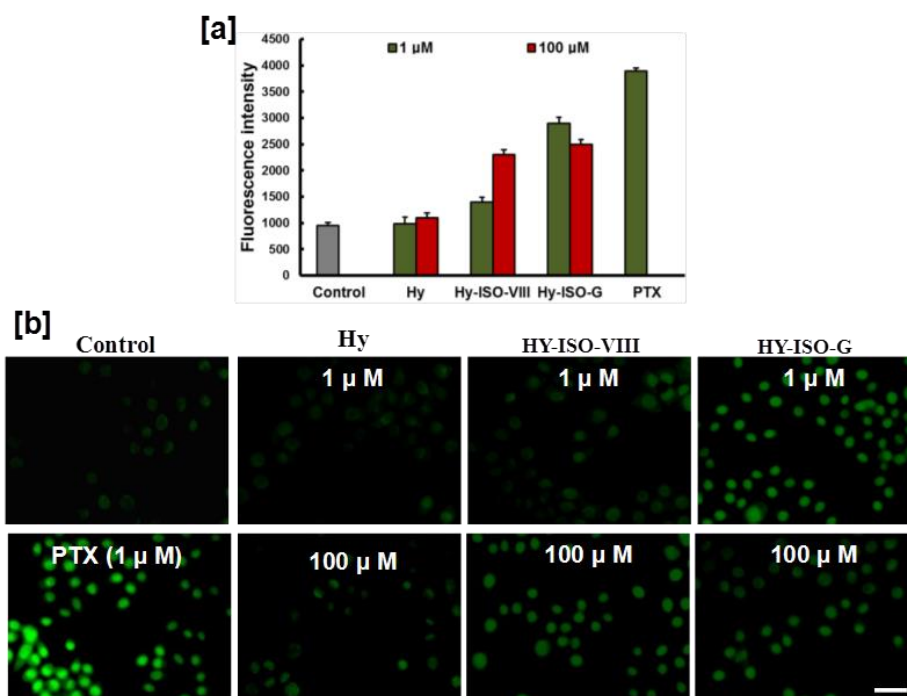


Figure 2B.5: ROS generation quantified by the fluorescence intensity from DCFDA analysis in A549 cells [a] and the representative DCF fluorescence images [b] of A549 cells treated with HY, HY-ISO-VIII, HY-ISO-G and paclitaxel. Scale bar corresponds to 50 μm

2B.2.3 Apoptotic evaluation of Hy-ISO-G and Hy-ISO-VIII. Morphological evaluation of A549 and A375 cells using phase-contrast microscopy after treatment of Hy-ISO-VIII and Hy-ISO-G revealed a significant reduction in the cell number with salient morphological changes associated with apoptosis. Again, we have evaluated the morphological changes through atomic force microscopy (AFM) which clearly demonstrated a change in the shape of cells; from spindle to spherical with associated membrane breakage, blebbing and leakage of intracellular components after 24 h of treatment even with a lower concentration (1 μM) of compounds (Figure 2B.6a&b).

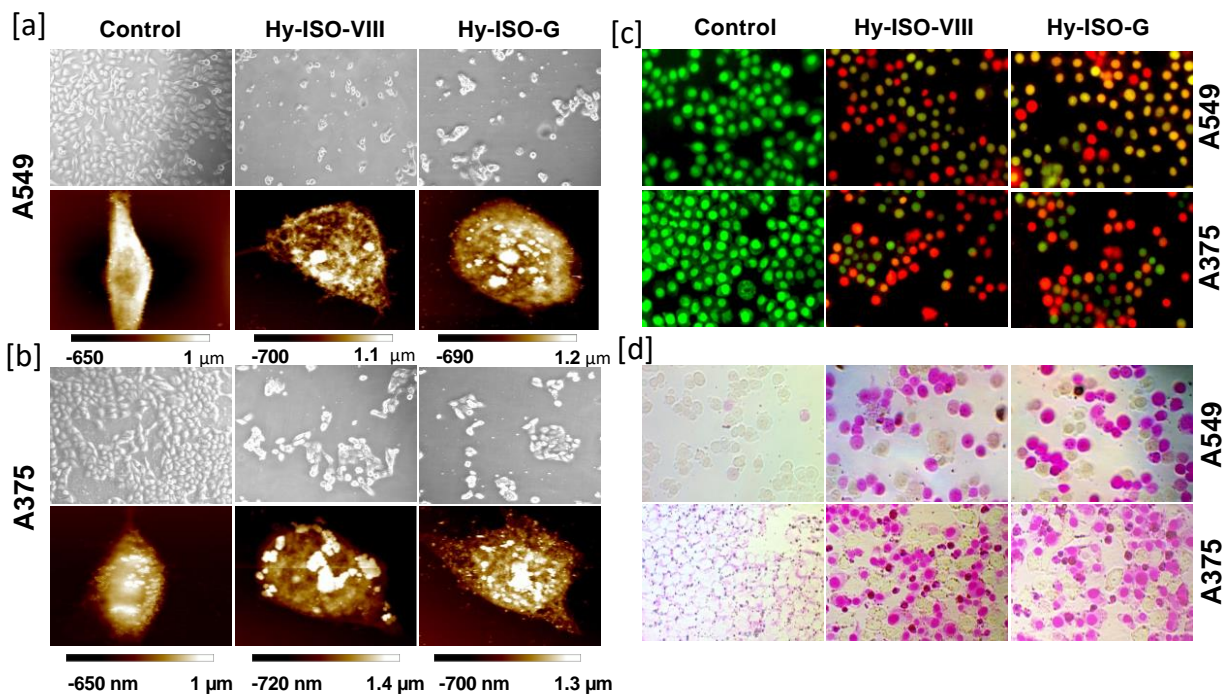


Figure 2B.6: Morphological changes on treatment with HY-ISO -8 and HY-ISO-G Bright field and AFM images of [a] A549 cells [b] A375 cells. Induction of apoptosis by HY-ISO-8 and HY-ISO-G in A549 and A375 cells [c] Live dead assay by AO/EtBr dual staining [d] APOP assay

In order to determine the mechanism of cell death induction by the compounds, various apoptotic assays were further performed. Examination of compound-treated ($1\mu\text{M}$) cells using acridine orange-ethidium bromide staining showed a distinct color change from green to yellow/red with associated apoptotic features (Figure 2B.6c). Early onset of apoptosis induced by the compounds was validated in a non-fluorescent pattern using APOPercentage assay in which both the compound treated A549 and A375 cells up took the dye and were stained intensely purple-red while control cells remained unstained (Figure 2B.6d). Later, the dye accumulation was quantified, which demonstrated a significant ($p < 0.001$) increase in the uptake efficiency upon comparison with the control cells. One of the most distinctive features of apoptosis is the DNA fragmentation and nuclear condensation, which could be clearly spotted by Hoechst 33342 nuclear staining. Both Hy-ISO-VIII and HY-ISO-G indicted appreciable nuclear changes with well-defined fragmentation pattern in both A549 and A375 cells whereas control cells remained healthy (Figure 2B.7a). Also, induction of apoptotic cell death was further confirmed by annexin V staining. The annexin V positivity was significantly ($p < 0.001$) higher in the treated cells. In A549 cells (Figure 2B.7b), the controls were $0.2 \pm 1\%$ annexin-V-positives, while the

compounds treated cells showed 29 ± 1.5 % and 38 ± 2.1 % positivity upon administration with Hy-ISO-VIII and Hy-ISO-G respectively (Figure 2d). A similar trend was observed with A375 cells where control cells were 0.03 ± 0.9 % positive whereas Hy-ISO-VIII treatment causes 28 ± 2 % and Hy-ISO-G generated 39 ± 1.4 % positivity within 24 h. The programmed execution of cell death was further examined with terminal deoxynucleotidyltransferase (TdT) dUTP nick-end labelling (TUNEL) staining assay, where compound treated cells were green in color, indicating TUNEL positivity, while control cells were largely TUNEL negative in nature (Figure 2B.7c).

The programmed cell death executed by the two potent semi-synthetic NPCEs was indisputably established with multiple apoptosis assays wherein the nuclear condensation and DNA fragmentation associated with programmed cell death was visualized by Hoechst staining and TUNEL assay. The distinct visualization of morphological changes with phase contrast microscopy could reveal the changes like reduction in cell number accompanied by predominant apoptotic features. The observation of treated cells under AFM clearly revealed an additional opportunity to locate the damage of cell membrane whereas the untreated cell membrane remains smooth. The difference between top and bottom of the cell morphology defined by the height difference in AFM images was well pronounced up on treatment with our synthetic derivatives which clearly demonstrated the early onset of programmed cell death.¹⁶ The implementation stage of apoptosis begins with the translocation of phosphatidylserine (PS) from the inner to the external surface of plasma membrane. This translocation process accounts for the selective uptake of the APOPercentage dye by the early apoptotic cells, which lasts until the occurrence of blebbing, the classical event of apoptosis. Consequently, the PS translocation was further confirmed with annexin V staining, which could actively distinguish cells from apoptosis and necrosis. Cancer-cell selective cytotoxicity itself could be of great advantage for a lead molecule, which predominantly imparts cell death in a programmed manner. Although most of the heterocyclic anticancer agents imparts apoptotic cell death, few imparts necrotic pathway.¹⁷ Here the heterocycle incorporated HY-ISO derivatives clearly revealed enhanced cancer cell toxicity in a programmed fashion up on comparison with the parent molecule Hy. The notion that isoxazole and isoxazolone derivatives can execute apoptosis in cancer cells could fast promote this semi-synthetic modification approach. Apoptosis is the most appreciable mode of cell death

and several natural products and their derivatives have been shown to induce apoptosis in cancer cell lines.¹⁸

2B.2.4 Effect of NPCEs on cancer metastasis. Since metastasis accounts for the major culprit behind cancer associated mortalities, the anti-metastatic potential of the both the Hy-analogues were investigated. Hence a promising anticancer agent should retard the metastatic potential as well. As a first step towards evaluating the anti-metastatic property, we investigated the effects of both Hy-ISO-VIII and Hy-ISO-G (10 nM) on the invasive and migration ability of cancer cell lines using transwell chamber assay.

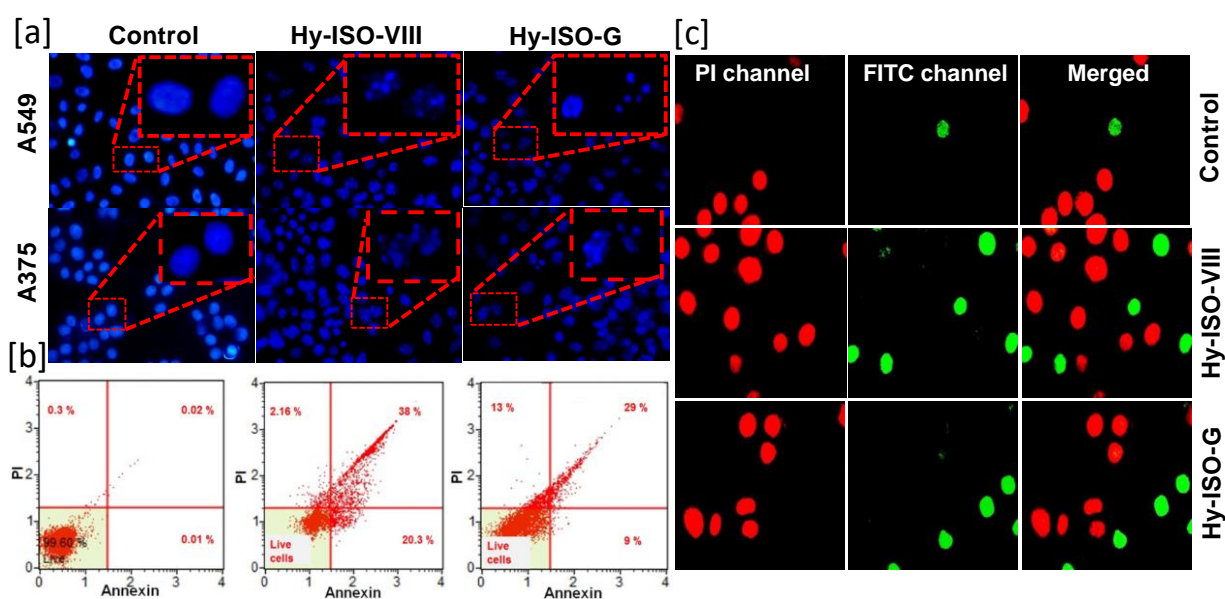


Figure 2B.7: Induction of apoptosis by HY-ISO-8 and HY-ISO-G [a] Hoechst staining [b] annexin V/FITC staining in A549 cells by flow cytometry [c] TUNEL assay in A549 cells

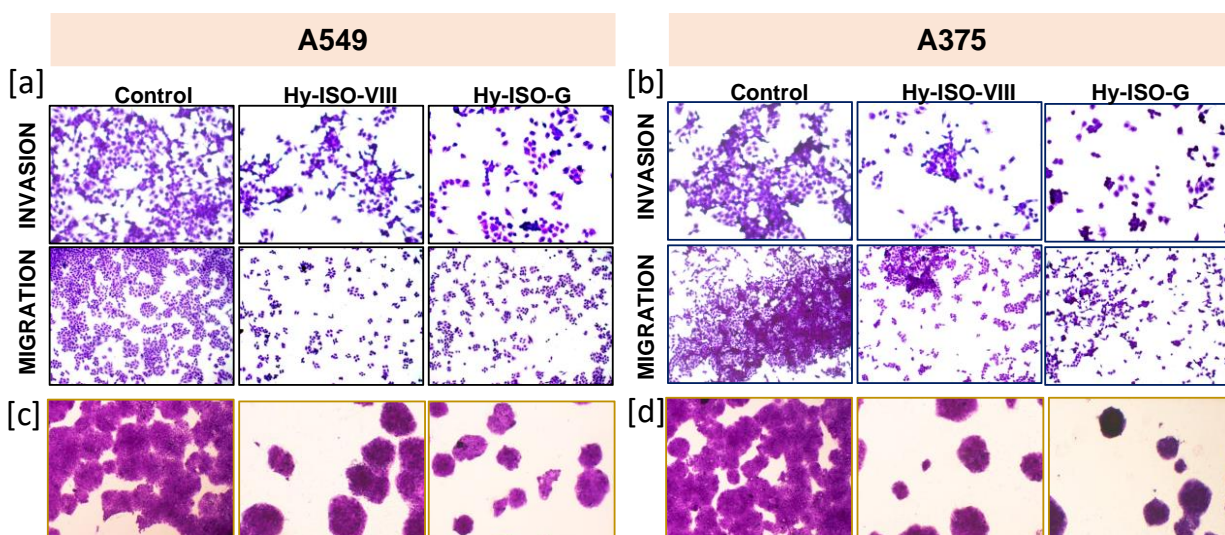


Figure 2B.8: Anti-metastatic potential of HY-ISO-VIII and HY-ISO-G (1nM) [a] Invasion and migration assay in A549 cells [b] Invasion and migration assay in A375 cells. Scale bar corresponds to 150 μm . [c] Colony formation assay in A549 cells [d] Colony formation assay in A375 cells.

While the cancer cells freely moved across the matrigel towards the lower chamber of the transwell plate, the molecules effectively prevented the invasion considerably in both the cells (Figure 2B.8a,b, Figure 2B.9a). It is to be noted that both the derivatives significantly retarded the migration of cancer cells in an impressive manner (Figure 2B.8a,b, Figure 2B.9b). Later we performed wound healing assay which demonstrated that both the molecules prevents the cancer cells from wound closure in a time-dependent manner with significant inhibition in migration rate. The cell free scratch zone of the treated wells are large even after 24 h but the control wells displayed almost closure of the zone even after 12 h, which illuminates the first ray of light towards the inhibition of metastasis (Figure 2B.9c). Finally, the ability of the Hy-ISO-VIII and Hy-ISO-G were checked for the inhibitory effect on colony formation. It was noticed that both the Hy-analogues markedly reduced the clonogenic ability of cancer cells (Figure 2B.8c,d, 9d).

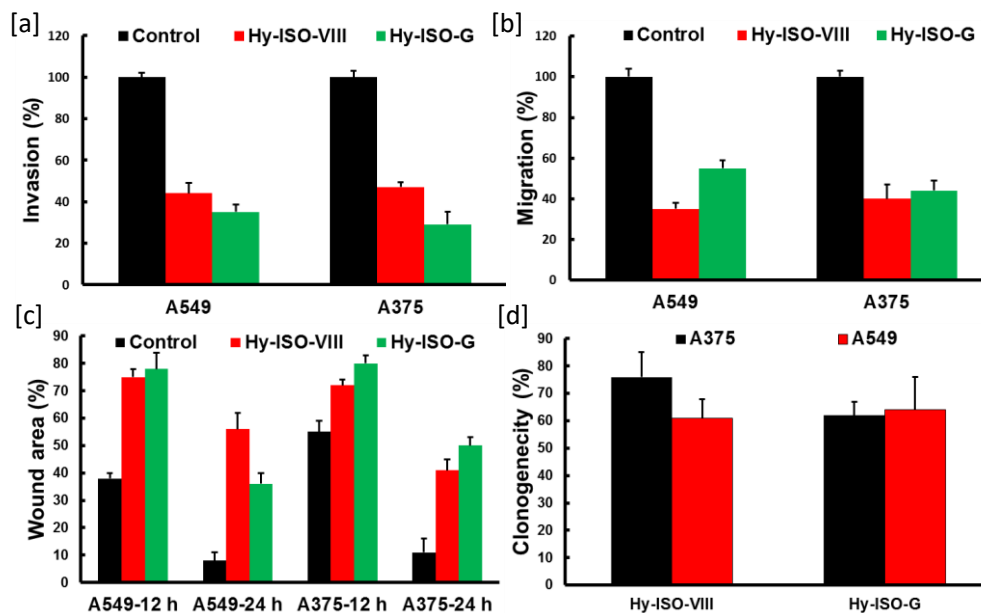


Figure 2B.9: Quantification of [a] invasion, [b] migration, [c] wound healing and [d] colony formation assay.

Clonogenic assay is still being widely used as a standard experimental procedure to understand the sensitivity of cytotoxic agents on the colony formation capability of cancer cells.¹⁵ The initial process of metastasis is the migration of cancer cells towards an approachable niche which includes both invasion and migration. These neoplastic cells become immortal, proliferate rapidly and become aggressive to successfully establish a favourable microenvironment through metastasis. A significant reduction in the colony formation, invasion and migration of aggressive metastatic cancer cells by the compounds indicates their role to retard the metastatic potential. Many polyphenols, flavonoids and most clinically used chemotherapeutic drugs inhibit tumor migration and thus prevent metastasis.^{16,19} Although the parent Hy compound previously displayed little anti-metastatic property, it was indicated that the synthesized novel Hy-derivatives showed enhanced activity due to the incorporation of isoxazole and isoxazolone moieties. Polyphenols like genistein, proanthocyanidins, anthocyanins etc. having flavonoid core exhibit excellent anti-carcinogenic property by retarding cell migration and proliferation. Compounds like oroxylin suppress the expression and activity of MMP-2/9, phosphorylation of PI3K and thus inhibit tumor metastasis. Therefore heterocycles associated with the drug moieties enable to inhibit the MMP-2/9 activity and suppress tumor progression.¹⁶

2B.2.5 Cell cycle regulation by Hy-ISO-G and Hy-ISO-VIII. To investigate the NPCEs mediated suppression of cell proliferation and metastasis, cell cycle analysis was performed with flow cytometric analysis after the DNA was stained with PI. Histograms of the flow cytometry data clearly denote the involvement of cell cycle arrest on the tested cell lines. Hy-ISO-VIII mainly follows G2/M phase cell cycle arrest in both A549 and A375 cells. In the case of Hy-ISO-G, arrest at the G2/M and S phase prevails where a prominent S phase arrest was seen with A549 cells (Figure 2B.10). It has been well practiced that cancer cell proliferation can be blocked upon supplementing cell cycle regulators. For instance, flavonoids like apigenin²⁰ have shown inhibitory activity by blocking cell cycle progression at G2/M checkpoint whereas quercetin²¹ was known for arresting at S phase. The S phase arrest by HY-ISO-G could be due to the interaction with DNA resulting the instantaneous DNA damage. Comberastatin A-4 containing isoxazole core is a promising antimetabolic agent capable to inhibit tubulin polymerization and induces tumor regression via anti-vasculature activity without affecting normal cells.²² Similarly HY-ISO derivatives might also be interacting with various cellular components, which enable them to retard the proliferation potential more effectively. Therefore, the cell cycle arrest brought about by both the NPCEs proved the active involvement of multiple players of apoptosis in their anti-proliferative mechanistic mode of action.

2B.2.6 Evaluation of mitochondrial transmembrane potential by the NPCEs. The elevated production of ROS with both the selected NPCEs indicated the involvement of mitochondria mediated cell death and hence, the mitochondrial membrane potential ($\Delta\Psi_m$) was evaluated on both A549 and A375 cells. Initially, measurement of mitochondrial depolarization was performed with the ratiometric fluorescent dye JC1 which displayed a decrease in red fluorescence and an increase in green fluorescence upon treatment. Simultaneously, the ratio of red to green fluorescent intensity demonstrated the enhanced effect of Hy-ISO-G than Hy-ISO-VIII on both the cells (Figure 2B.11a,b,c). Later, the $\Delta\Psi_m$ variation was further quantified with tetramethylrhodamine, ethyl ester (TMRE) mitochondrial membrane potential assay (Figure 2B.11d). The reduction with $\Delta\Psi_m$ was highly significant with both Hy-ISO-VIII ($p < 0.01$) and Hy-ISO-G ($p < 0.001$) in both the cell lines. TMRE is a cell permeant, positively-charged dye that readily accumulates in active mitochondria due to their relative negative charge. Depolarized or inactive mitochondria have decreased $\Delta\Psi_m$ and fail to sequester TMRE. Mitochondrial function

is fundamental in controlling the life cycle of cells, and plays a major role in cancer therapeutic regimen. Manipulation of the lethal signal transduction pathways is essential to cause the permeabilization of the mitochondrial outer membrane to cause the cytosolic release of proapoptotic proteins and to the impairment of the bioenergetic functions of mitochondria. Most classical anticancer agents including many derivatives with heterocyclic rings employ signaling pathways that lie upstream of mitochondria and converge on these organelles to trigger cell death.²³ A key step in the intrinsic apoptotic pathway is the disruption of the mitochondrial membrane.^{15,24} The involvement of mitochondria in the cell death pathway will aid the execution of cytotoxicity in a more programmed manner. The indication towards the involvement of mitochondria in the cell death pathway will aid the execution of cytotoxicity in a more programmed manner. Mitochondria greatly contribute towards the most prominent source of intracellular ROS. Since the ROS generation capacity of potent Hy-analogues was already established, the additive information about the induction of mitochondrial damage could support the present observation.

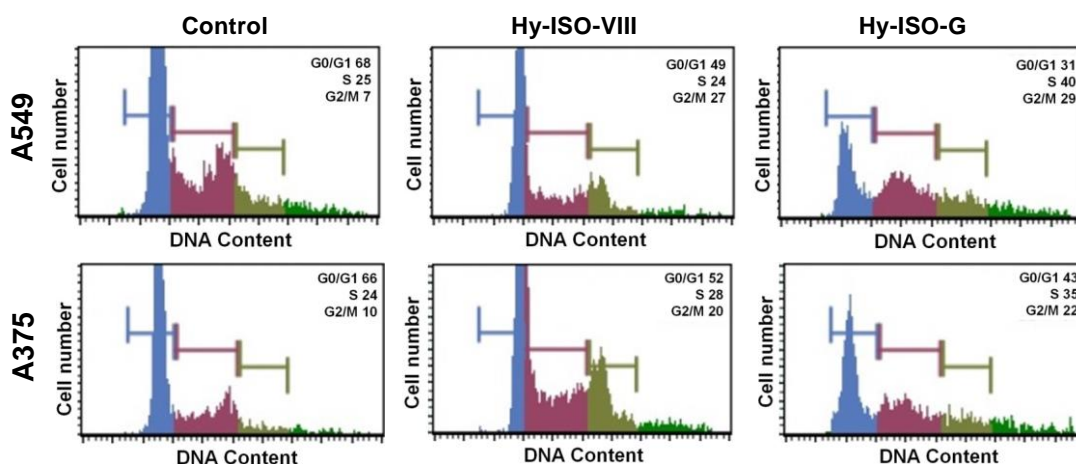


Figure 2B.10: Cell cycle analysis on treatment with HY-ISO-VIII and HY-ISO-G in A549 and A375 cells

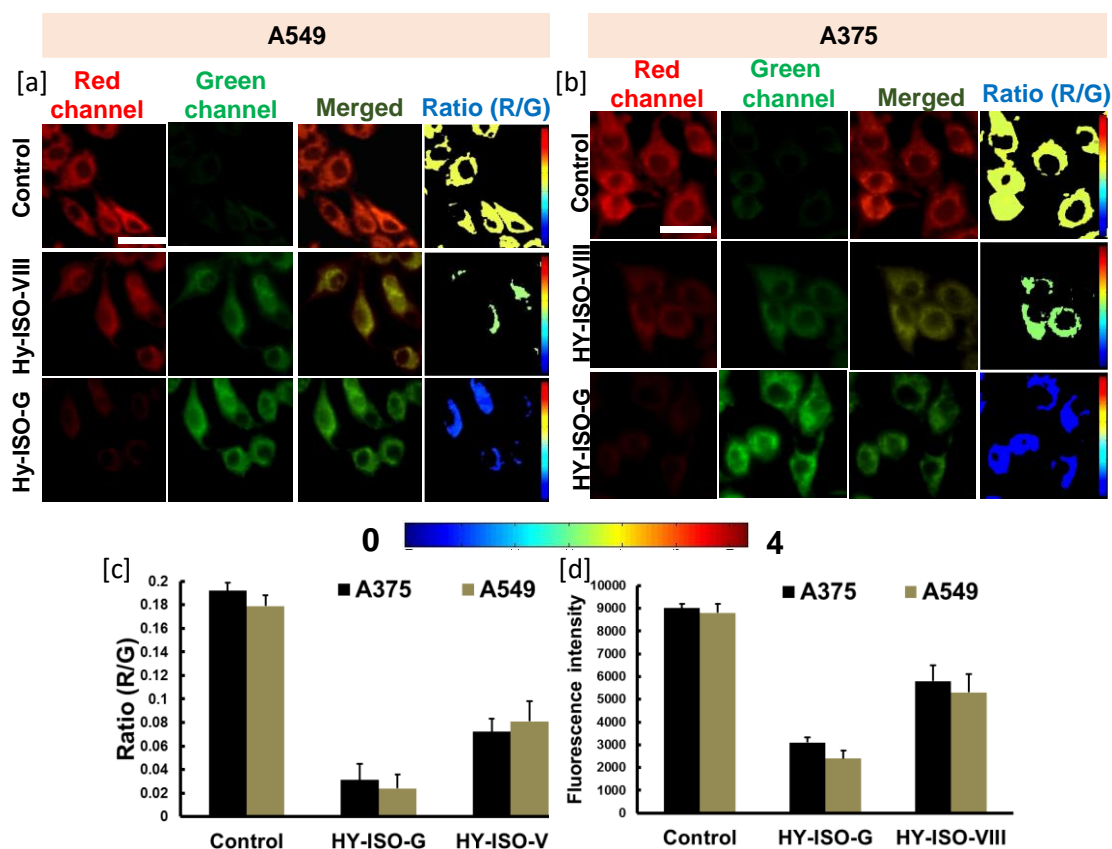


Figure 2B.11: Changes in the mitochondrial membrane potential induced by the administration of HY-ISO-VIII and HY-ISO-G with JC1 assay [a] in A549 cells [b] in A375 cells [c] quantification of JC1 assay. Scale bar corresponds to 50 μm . Mitochondrial membrane potential evaluation with [d] TMRE assay.

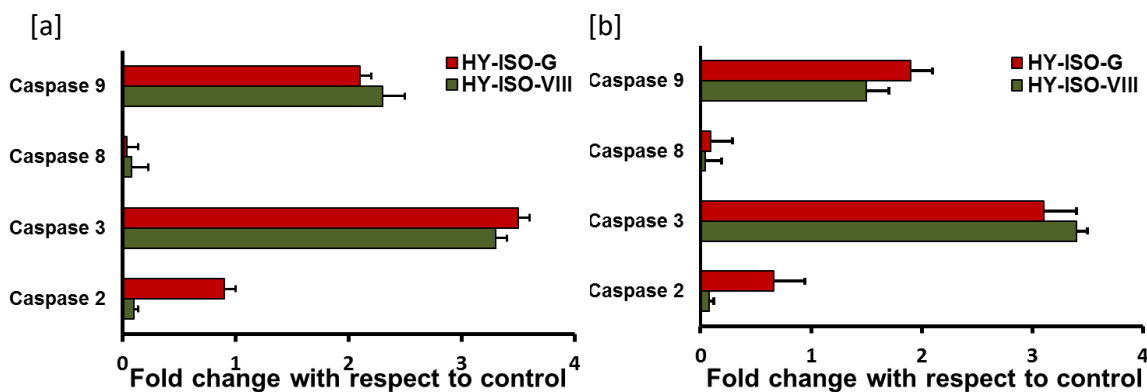


Figure 2B.12: Caspase activity profiling on A549 cells [a] Caspase activity profiling on A375 cells. Results are expressed as mean \pm SD, statistically significant differences at * $p < 0.05$, ** $p < 0.01$, *** $p < 0.001$, and ns, non-significant, when compared with negative control.

2B.2.7 Evaluation of caspase mediated apoptosis cascade. Cysteine-aspartic proteases or caspases are proteolytic enzymes demonstrated to execute a major role in regulating the cell cycle phases and the cell death pathways. Several synthetic and naturally occurring anticancer drugs are established to accomplish apoptosis in a caspase-dependent fashion. As a culmination of apoptosis studies, we planned to investigate the effects of both the initiator and executioner caspases in the mode of cell death induced by Hy-ISO-G and Hy-ISO-VIII. Although there was a significantly ($p < 0.001$) increased expression of caspases 3 and 9 by both the compounds on A375 and A549 cells, the expression of caspase 8 was not varied (Figure 2B.12a & b). Again, Hy-ISO-G caused increased expression on caspase 2 on A549 ($p < 0.01$) and A375 ($p < 0.05$) cells but the mode of action with Hy-ISO-VIII was not through caspase 2. The active involvement of caspase 3 and 9 and the absence of caspase 8 confirmed the intrinsic apoptotic pathway executed by both the Hy analogues. Since the implementation of intrinsic pathway of cell death involves the engagement of mitochondria, the previous observation with the $\Delta\Psi_m$ dysfunction validates the intrinsic mode of programmed cell death. The loss of $\Delta\Psi_m$ releases sequestered pro-apoptotic proteins including cyt c into the cytoplasm which will then influence pro-caspase 9 to activate the caspase pathway for the execution of cell death.¹⁵ Phytochemicals have showed promising chemopreventive and therapeutic efficacy by executing apoptosis via mitochondria mediated caspase activation. Compounds like resveratrol, barberine, apigenin etc have proved to be excellent anticancer agents which performs their cytotoxic effect in the similar fashion.²⁴⁻²⁶ Here, the combined action of Hy flavonoid core and the isoxazole/isoxazolone ring could effectively achieve the anti-proliferative property.

2B.2.8 Molecular level investigation for cellular internalization and cell death mechanism by SERS spectral and mapping analysis. Designed to garner the minuscule biochemical cellular changes after the treatment with the selected NPCEs, Raman spectral investigation through surface enhanced Raman scattering was employed. Raman fingerprint analysis and mapping at a molecular level evolved as novel diagnostic strategy through SERS modality. In the SERS technique the native Raman fingerprints of Hy-ISO-VIII was characterized with the prominent peaks at 1009 and 1082 cm^{-1} corresponds to C-C aromatic chain vibrations, 1374 cm^{-1} and 1547 cm^{-1} corresponds to C=N (hetero ring) and CH_3 stretching of the hybrid molecule (Figure 2B.13a, Table 2B.1). Similarly the prominent Raman peaks at 1250, 1306, 1373 and

1594 cm^{-1} corresponds to C-H vibration, C=O in-plane bending, CH_3 stretching and C=N (hetero ring) respectively in the chemical structure of Hy-ISO-G (Figure 2B.13b, Table 2B.2). Since both the NPCEs displayed unique Raman patterns, we utilized them as Raman signature molecule for inspecting the cellular internalization process. The unique Raman fingerprints of both the compounds were found to be merged with the molecular components of cytoplasmic area as early as 1 h of administration. The signature peaks at 1080 cm^{-1} and 1307 cm^{-1} identified as the marker peak of Hy-ISO-VIII (Figure 2B.14a) and Hy-ISO-G (Figure 2B.14b) respectively which confirmed the effective internalization process. During the time course study, we observed the disappearance of Raman fingerprints of Hy-analogues after 4 h in the cellular environment. Again, the Raman spectra collected from the nuclear area after 4 h showed less intense Raman peaks of DNA up on comparison with the negative control cells which is a definite indication to the probable DNA damage (Figure 2B.14c). Next, the distinctive observation of characteristic Raman peaks of cyt c from the cytoplasm after 3-4 h inspired us to find out the pathway of cell death process. Raman spectra abstracted from the cytoplasmic area upon treatment of Hy-ISO-G / Hy-ISO-VIII displayed the signature peaks of cyt c such as 775, 1106, 1470 and 1510 cm^{-1} which indicated to heme breathing, C-S stretching, C=N stretching and bending mode of C-N(H)-C respectively.

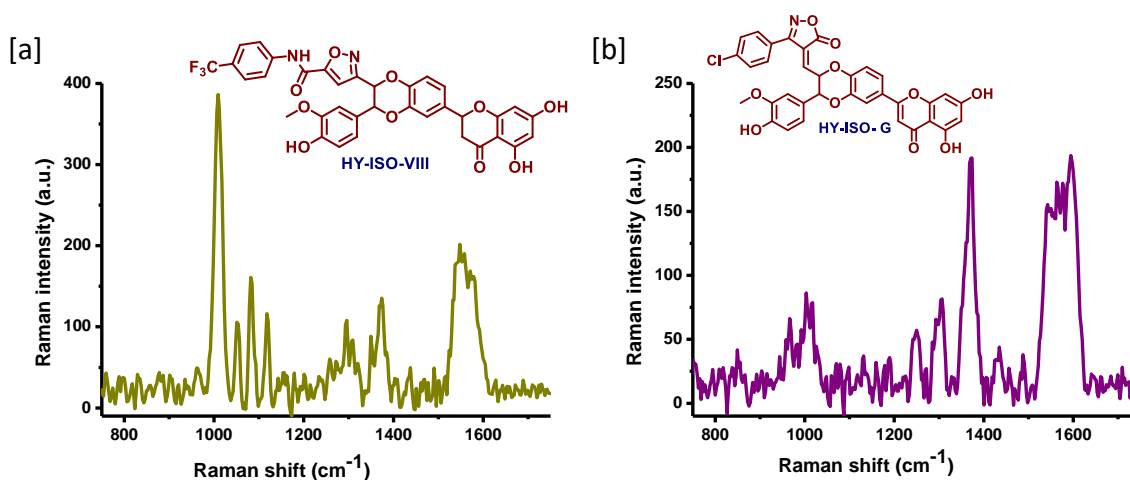


Figure 2B.13: SERS spectrum of HY-ISO-VIII and HY-ISO-G

Table 2B.1: Peak assignment of SERS spectrum of HY-ISO-VIII

Raman Shift (cm^{-1})	Assignment
1009	C-C aromatic chain vibrations
1051	C-C aromatic chain vibrations

1080	C-C aromatic chain vibrations
1118	C-N stretching
1374	$\delta(\text{CH}_3)$

Table 2B.2: Peak assignment of SERS spectrum of HY-ISO-G

Raman Shift (cm^{-1})	Assignment
1003	C-C aromatic chain vibrations
1250	C-H vibration
1307	C=O inplane bending.
1373	$\delta(\text{CH}_3)$
1594	C=N (Hetero ring)

The two distinct marker peaks of cyt c at 775 cm^{-1} and 1510 cm^{-1} were well resolved in compare to the other characteristic bands of proteins/amino acids/phospholipids in the intracellular milieu. A limiting step in the intrinsic apoptotic pathway is the damage of mitochondria and the release of cyt c from mitochondria into the cytosol. Next we thought of investigating the cyt c kinetics in the cells administered with our semi-synthetic derivatives in a label-free manner based on marker Raman peaks which corresponds to heme molecules of cyt c (775 cm^{-1}). The presence of signature Raman peaks of cyt c was observed form 3-4 h and lasts up to 6-8 h with both the molecules in cytoplasmic area of A549 (Figure 2B.15a, b) and A375 cells (Figure 2B.15c, d).

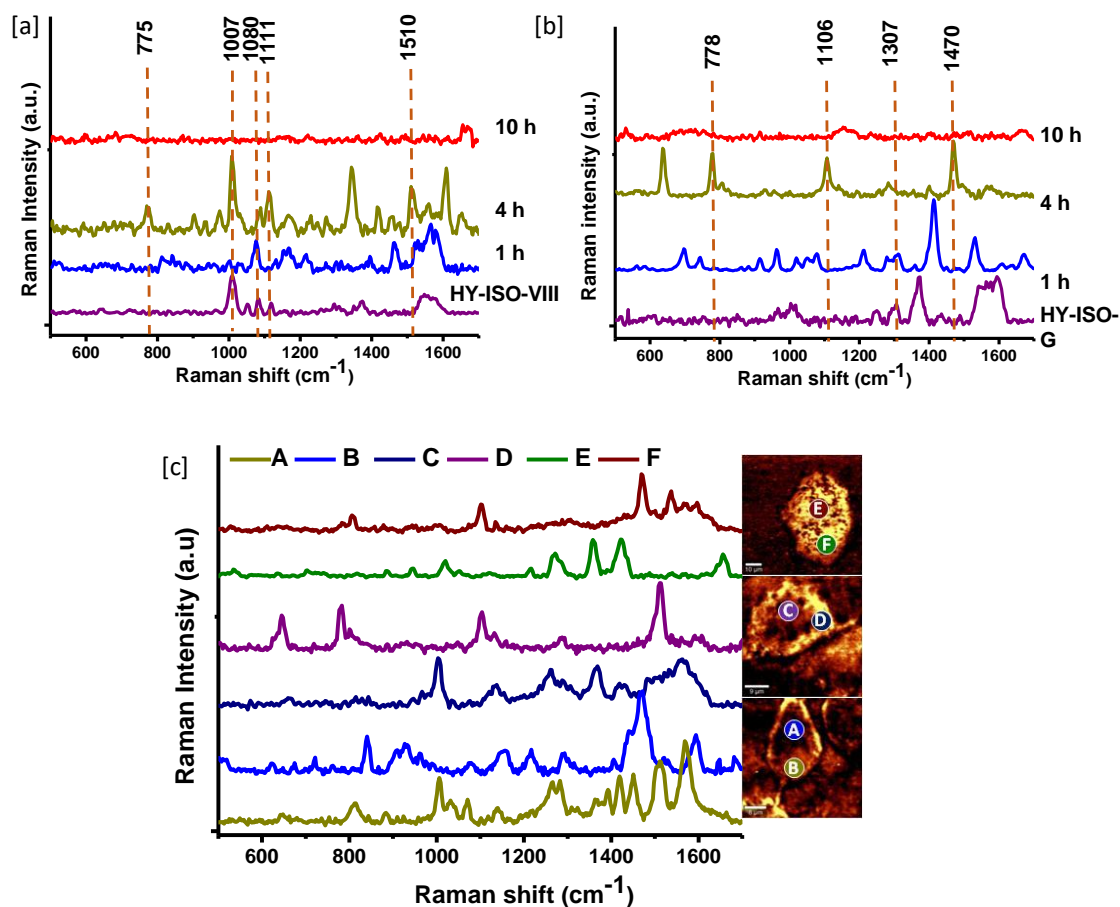


Figure 2B.14: SERS analysis of A549 cells after administration with HY-ISO-VIII [a] and HY-ISO-G [b]. [c] SERS spectra abstracted from nuclear and cytoplasmic region of A549 cells.

The decrease in the DNA peak intensity from the nuclear area after the treatment urged us to study the effects on the nuclear DNA. Raman spectral analysis of the isolated DNA clearly illustrated the NPCEs induced DNA damage with typical signatures with the O-P-O backbone rupture during DNA double strand breakage and laddering process. The isolated DNA of the untreated cells bears all the signature peaks for a healthy DNA with high intensity while both Hy-ISO-VIII and Hy-ISO-G caused effective DNA damage on A549 (Figure 2B.16a) and A375 cells (Figure 2B.16b).

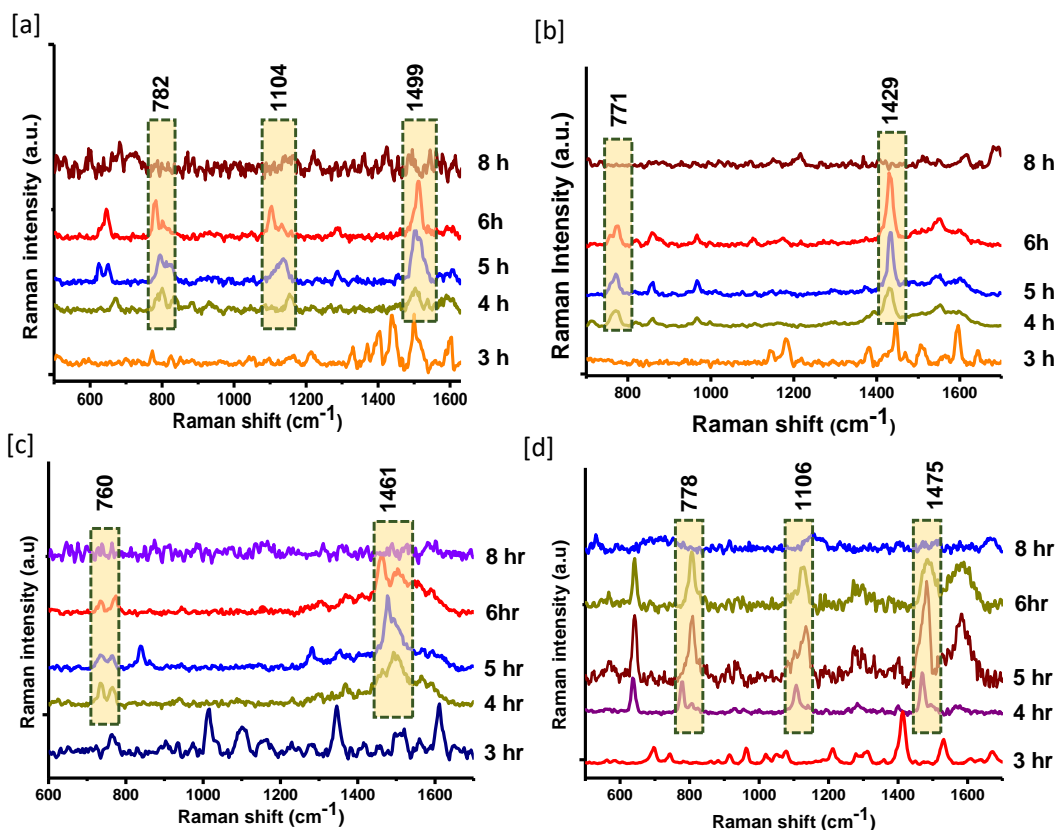


Figure 2B.15: Time dependent analysis of cyt c [a] in A549 on administration with HY-ISO-VIII [b] in A549 on administration with HY-ISO-G [c] in A375 on administration with HY-ISO-VIII [d] in A375 on administration with HY-ISO-G

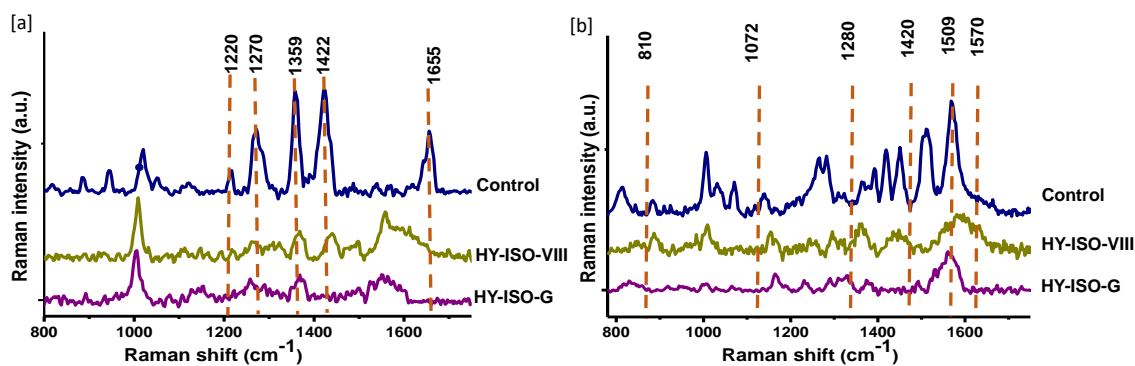


Figure 2B.16: SERS analysis of genomic DNA isolated on administration with HY-ISO-VIII and HY-ISO-G [a] from A549 cells [b] from A375 cells

We have successfully monitored the real-time cellular internalization and apoptotic events exerted by the two promising NPCEs of Hy with SERS modality using the signature Raman

spectral read out. This strategy serves as a dynamic proof-of-concept for the specific and sensitive delivery of hit molecules to the target location. In most of the cases delivery of non-fluorescent molecules was presumed by attaching an auxiliary fluorophore moiety which itself is a very tedious process. But the present demonstration comes out as newly evolved alternative pathway where rapid compound internalization was evident as early as 1 h and the persistence of the compounds up to 4 h indicated the potentiality in the sub-cellular environment. Under certain conditions, the dihydroxylated flavonoids undergo oxidation to produce cytotoxic hydrogen peroxide. Inside the cellular matrix, P450 mediated reductive scission of isoxazole rings are reported.^{10,11} Similarly, the explored NPCEs might also have metabolised inside the cells by 4 h and the absence of any compound signatures from the nuclear area points out towards the lack of nuclear membrane penetration ability or the rapid metabolism in the cytoplasm. We have previously employed SERS for tracking the cellular internalization and metabolism of doxorubicin (Dox).^{8,27} Here the cellular tracking of a non-fluorescent molecule holds special merit. Careful inspection of Raman spectra from the cytoplasmic area exposed the unique fingerprints of cyt c after 4 h compound administration. Cyt c acts as a trigger to the cascade activation of caspases for the orchestrated fashion of cell death. The unique observation with the involvement of cyt c in the mechanistic mode of cell death by both HY-ISO-G and Hy-ISO-VIII further marked an agreement with the studies with $\Delta\Psi_m$ and caspase profiling which confirmed the execution of mitochondria mediated intrinsic pathway of apoptosis. A change in the $\Delta\Psi_m$ may be responsible for the release of the cyt c. The intrinsic apoptotic pathway involves the disruption of $\Delta\Psi_m$ and subsequent release of cyt c which can be observed as the initiation of apoptosis before morphological changes in the apoptotic cell are visible.²⁸ SERS based investigation was previously explored for the study of cyt c in living functional mitochondria²⁹ but its dynamics during apoptosis induced by any natural product or its active semi-synthetic counterpart remains elusive. Since DNA fragmentation stand alone as a gold-standard indicator of intrinsic apoptotic pathway, we performed SERS analysis with the isolated DNA. The spectra isolated from untreated DNA showed prominent peaks at 810, 1072, 1220, 1280 and 1422 cm^{-1} , of which the first three bands are assigned to phosphodiester (Z-marker), symmetric PO_2 stretching, C-N-C stretching (nitrogen bases) and the next two are assigned to the nucleic acids and phosphates and deoxyribose, respectively.^{8,30} Analysis of the DNA after treatment showed a noticeable decrease in the peaks centred at 810, 1072, 1280, and 1422 cm^{-1} .

The reduction in the SERS intensity of these peaks indicates the disruption of DNA compact structure and the degradation of nitrogen bases and phospho diester backbone (Figure 2B.16a, b). We have previously reported the effective real-time monitoring of DNA backbone breakage using differential SERS spectral analysis.^{8,27,31} Therefore, induction of apoptosis and their molecular events by SERS fingerprint analysis prevailed an unique opportunity especially in observation of dynamics of biomolecules because labelling markers may disturb the target molecules.⁵

2B.2.9 Analysis of NPCEs mediated DNA fragmentation. It was evident that apoptotic DNA fragmentation occurred during the execution of apoptosis by both NPCEs. As a proof-of-concept DNA fragmentation was further confirmed by agarose gel electrophoresis. In DNA laddering, the longer DNA is broken down into multiple fragments which can be viewed by agarose gel electrophoresis (Figure 2B.17a). The fragmented DNA up on Hy-ISO-VIII and Hy-ISO-G treatment could effectively establish the nuclear damage induced by the treatment. Since the indications towards DNA laddering was observed only after 4 h of treatment, we thought to investigate the analysis of DNA fragmentation in an early time point of 3 h according to the protocol from chemometec DNA fragmentation assay. The cells were treated with the compounds, cellular fluorescence was quantified and apoptotic cells with fragmented DNA under M1 peak in a DNA content histogram was quantified (Figure 2B.17b). These results show that Hy-ISO-VIII and HY-ISO-G could cause 9.6 % and 14.5% DNA fragmentation as early as 3 h incubation.

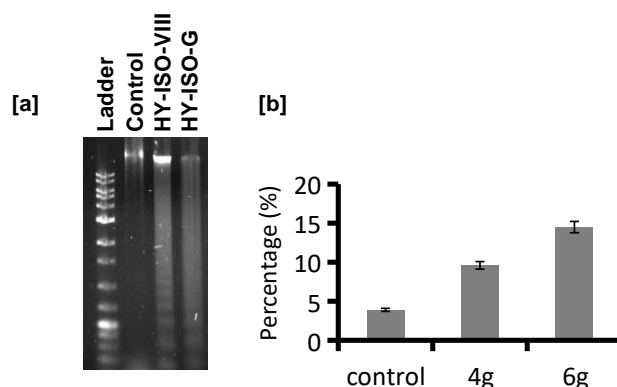


Figure 2B.17: Gel electrophoresis analysis of genomic DNA [a] Quantification of DNA fragmentation analysis with chemometec DNA fragmentation assay

2B.2.10 Estimation of glutathione in cells treated with NPCEs. During apoptosis, normal physiological mechanism of cell collapses. Since glutathione (GSH) is a key modulator of cellular processes, we decided to estimate the GSH level after the treatment with NPCEs. Surprisingly, significant depletion in GSH level was observed in both A375 and A549 cells upon administration with Hy-ISO-G and Hy-ISO-VIII whereas Hy does not account for any meaningful change (Figure 2B.18a). The extent of ROS generation by both the selected derivatives was well proved by DCFDA analysis. Generation of ROS induces the oxidation of cytosolic GSH to GSSG which could be the underlying factor behind the depletion of GSH level. Also some of the flavonoids are reported to form GSH adducts in the cytoplasm which drastically reduced the GSH level.¹⁰ Depletion in GSH level causes imbalance of intracellular redox environment which collapses the normal cellular function and leads to apoptosis. Cancer cells are ominously extra sensitive towards the changes in the levels of GSH and hence may be more vulnerable to oxidative stress, and the extent ROS exposure.³² Our study revealed that NPCEs-induced ROS generation was significantly associated with the consumption of intracellular GSH. Based on the observations with the elevation of cellular ROS and consumption of GSH, we suggest that our NPCEs may consume the cellular antioxidant capacity and upsurge the ROS levels outside a certain threshold, which may promote the induction of apoptosis. The flavonoid core of the molecules can form thiol conjugation with GSH and cause lowering of cellular thiol levels.¹⁰

2B.2.11 Evaluation of the involvement of cyt c in the mechanism of action. The extent of the involvement of intrinsic apoptotic pathway well proved by multiple assays highlights the critical role of cyt c in the mechanism of action related to both the semi-synthetic derivatives. Release of cyt c triggers the mitochondria dependent pathways of apoptosis. Hence we computed the binding affinity of the selected compounds Hy-ISO-VIII and Hy-ISO-G with cyt c. The crystallized structure of cyt c (PDB Code: 1CGO) was obtained from RCSB PDB and it contains 127 amino acids with a resolution of 1.8Å. The prepared receptor was used for docking against the prepared ligands. Both the compounds show less affinity to the binding site of 1CGO with best fitting pose having G-score -5.5 and D-score -3.4 kcal/mol in the case of Hy-ISO-VIII, whereas Hy-ISO-G shows G-score and D-score of -5.2kcal/mol. This indicates the smooth release of cyt c even in the presence of both the NPCEs which points towards the possibility of cyt c mediated apoptosis. However, this theoretical approximation needs to be validated

experimentally in cancer cells. Hence we have carried out the estimation of cyt c release to the cytoplasm during cell death induced by our NCPEs. The percentage of cyt c release in the untreated cells were taken as 100% and corresponding cyt c level in the NCPEs treated cells at different time points were quantified (Figure 2B.18b, c). There was a significant increase in the cyt c release from 4 h to 12 h on treatment with both the compounds on A375 and A549 cells. It appears that the peak cyt c concentration in the cytoplasm lies within 4-8 h after treatment in both the cell lines. The previous observation of a reduced binding affinity of both our NCPEs with cyt c during computational analysis is well proved with the real quantitation of cytosolic cyt c released from the mitochondria. Moreover the unique kinetics associated with cyt c observed in a label-free fashion using SERS was well validated with this cyt c quantitation. The active involvement of cyt c and mechanisms to alter cellular GSH by the NCPEs points out towards its complex mechanistic mode of action in cancer cells. Induction of apoptosis by flavonoids like apigenin is reported to takes place *via* cyt c release and further activation of caspase 9 and 3.²⁶

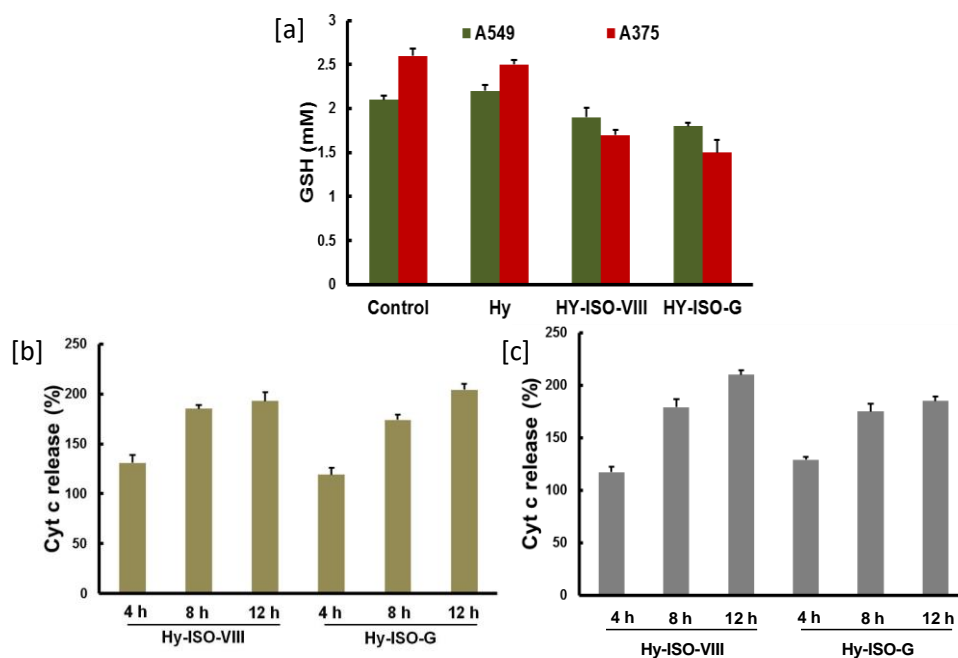


Figure 2B.18: [a]Changes in the GSH level after the administration of HY-ISO-VIII and HY-ISO-G on A549 and A35 cells. [b]Quantification of cyt c in the cytoplasm in A549 cells administered with HY-ISO-VIII and HY-ISO-G. [c]Quantification of cyt c in the cytoplasm in A375 cells administered with HY-ISO-VIII and HY-ISO-G. # Values are normalized with the

respective controls taken as 100 %

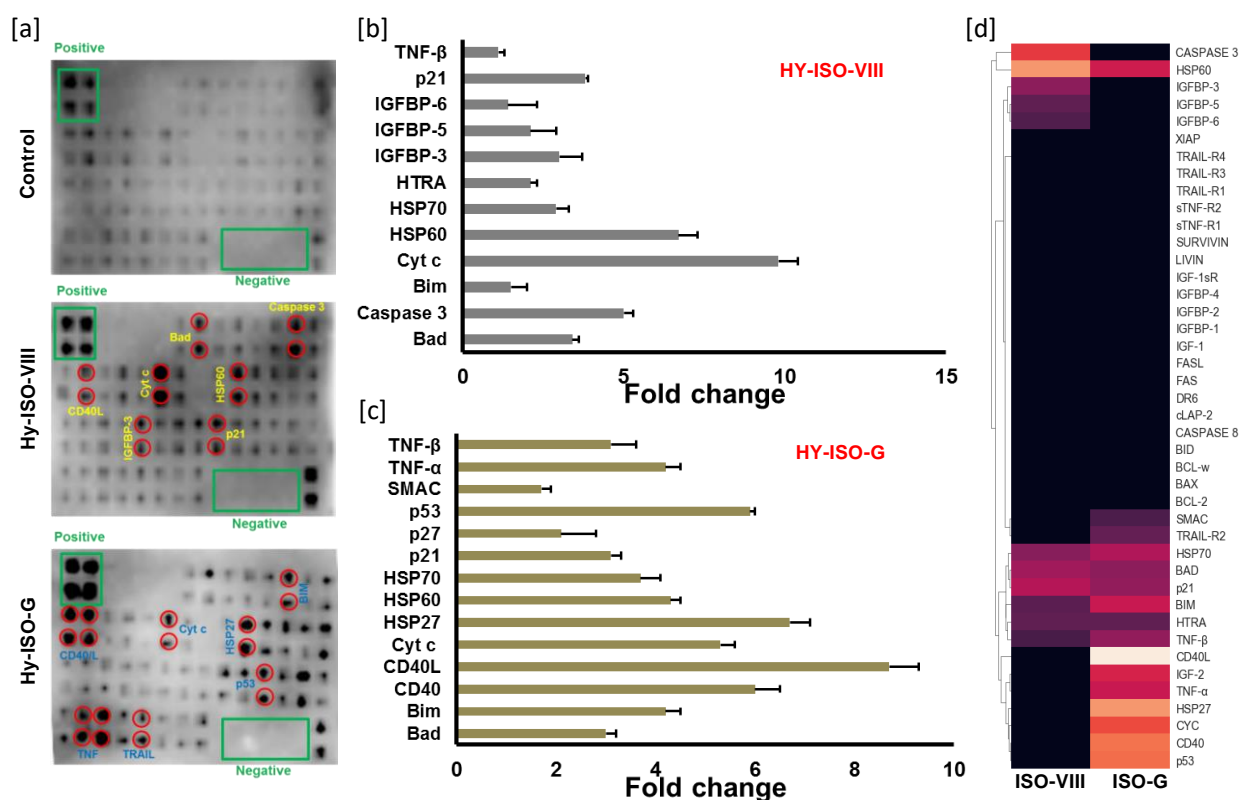


Figure 2B.19: [a] Apoptotic protein chip analysis on A549 cells and [b], [c] Fold changes of proteins calculated after antibody array of apoptotic proteins treated with NPCEs. calculated from the analysis of densitometric data using Image J software after normalization with the positive control of each array and later normalized with vehicle control and treatments [d] corresponding dendrogram based on the hierarchical clustering.

2B.2.12 Apoptosis antibody array. The admirable anti-cancer and anti-metastatic potentials demonstrated by the selected NPCEs made us to investigate the protein level expression variation of major players involved in the cell death pathways. This apoptotic protein chip analysis verified the unique molecular mechanism of action confined to the apoptotic pathways. Although both Hy-ISO-G and Hy-ISO-VIII shared a similar pattern of expression with majority of proteins, some key pattern expression variations also exists which highlighted the uniqueness of each derivative with respect to its structure and mode of action (Figure 2B.19a,b,c). In the case of cells treated with HY-ISO-G, tumor necrosis factor (TNF) is hyper activated by its upstream regulator CD40L/CD40 which is one among the most altered protein ligand. Activation

of TNF results in the generation of ROS *via* P13k pathway which leads to the fluctuation of mitochondrial membrane potential thereby releasing, cyt c and smac which will not only activates all the other downstream caspases but also will lead to a greater depletion of cytosolic GSH, which will further promote apoptosis through a variety of mechanisms. A greater fold increase in the expression of other important proteins such as HSP60, P53, P21, Bim, Bad, and many others will further promote the execution of intrinsic apoptosis pathways which involves the induction of cell cycle arrest and DNA damage (Figure 2B.19.d). TNF was not activated up to a greater extent in the case of cells treated with Hy-ISO-VIII because of the lack of any variation in the protein expression with CD40L/CD40 which marks a major difference between the modes of action of both the NPCEs. Insulin-like growth factor-binding protein 3 (IGFBP3) is differently over expressed with Hy-ISO-VIII which will not only execute cell cycle arrest but also activates Bac and Bax to cause cyt c release. The higher fold change with the cyt c expression observed with Hy-ISO-VIII than HY-ISO-G could be due to the involvement of IGFBP3 in the mechanism of action of the former. A marginal increase in the expression of HTRA, which is an important player involved in the inhibition of apoptosis by Hy-ISO-VIII was not effective enough to prevent the activation of caspase pathway probably due to the hyper activation of all other promoters of apoptosis (SI Figure S38). The similarity in the molecular mechanism of action by both the NPCEs was clearly demonstrated with the dendrogram based on the hierarchical clustering (Figure 2B.20). Similarly, derivatives of oridonin and apigenin also follows intrinsic pathway of apoptosis with the involvement caspases, Bcl2 family proteins, cyt c, smac, p53 and many more which also causes cell cycle arrest. Quercetin and morin are some prominent natural products promoting apoptosis *via* p53 mediated activation of bad protein.^{15,18,26,33} The mitochondria-initiated programmed cell death is the predominant apoptotic pathway operated in mammalian cells and is tightly regulated by Bcl2 family proteins. The greater involvement of these proteins by both our NPCEs observed with this array validated all the previously performed assays to substantiate the active involvement of mitochondria. Our previous attempts with computational analysis demonstrated a feeble interaction of the NPCEs with pro-apoptotic protein domains like 4LVT (Bad) and 1CGO (cyt c) and high docking score with anti-apoptotic protein domain like 1OXN and 1OXQ. This observation is well substantiated with the dot blot analysis.

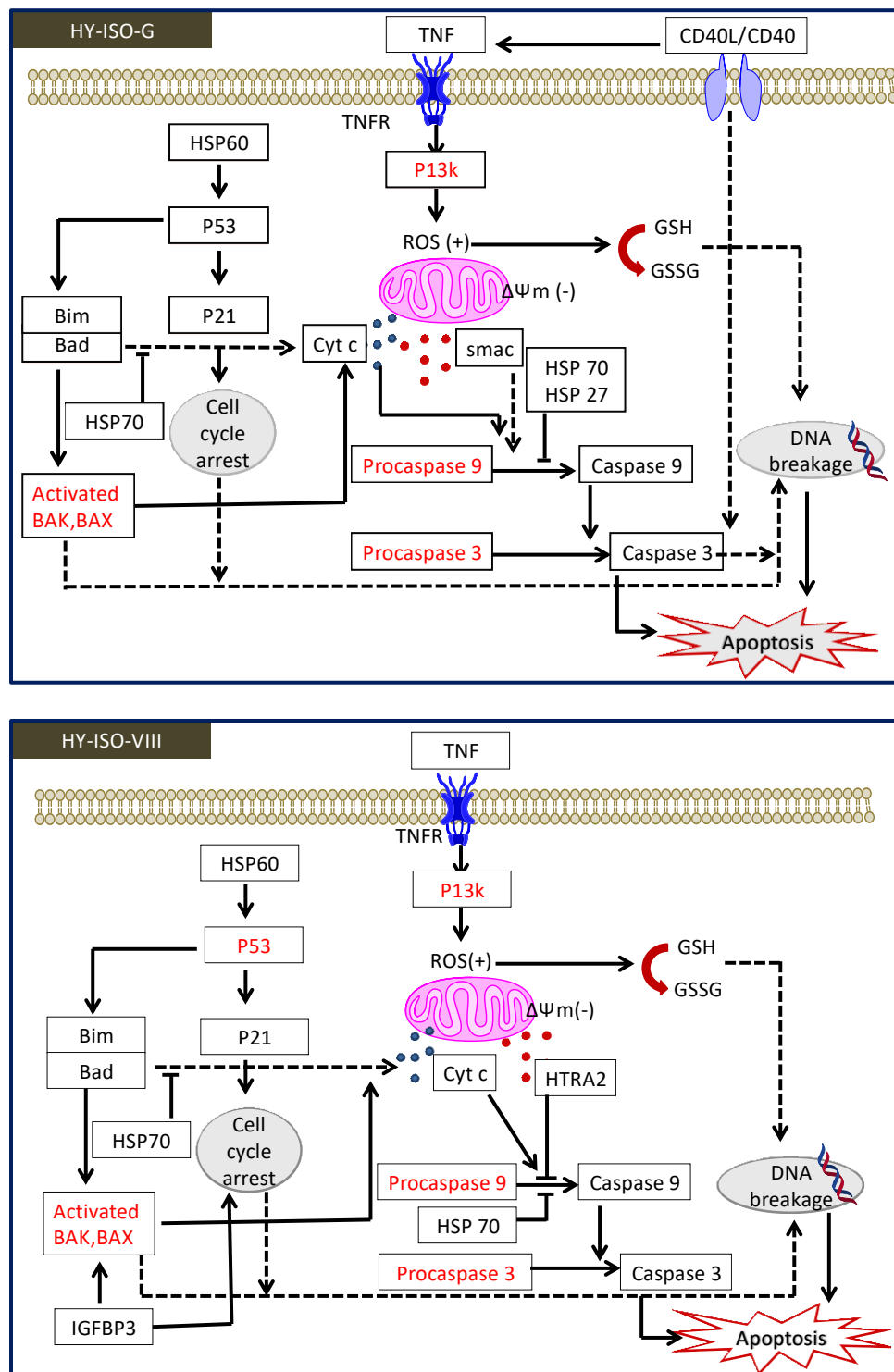


Figure 2B.20: Pathway deciphering the proposed mechanistic mode of action with HY-ISO-G (upper panel) and] HY-ISO-VIII (lower panel) on cancer cells. Red colored entries represent the

possible players, which are not currently evaluated. Filled lines represent direct biological effect while dotted lines denote indirect effect.

2B.3 Conclusion

The selected NPCEs based on *in vitro* and *in silico* screening promote mitochondrial membrane depolarization, which followed intrinsic apoptosis through the release of cyt c. As a new insight, the unique Raman molecular fingerprints of both the Hy-derivatives were established as a chemo-marker for the label-free analysis, especially cellular uptake and intracellular distribution and the subtle dynamics associated with the cyt c release kinetics. Moreover, signature Raman peaks for DNA fragmentation confirmed the molecular-level apoptotic phenomenon exerted by the selected NPCEs in the SERS modality. Notwithstanding, the NPCEs effectively retards the crucial steps of metastatic cascade and colonization of neoplastic cells. Although both the NPCEs follow mitochondrial-mediated apoptosis with the generation of cellular ROS and depletion of GSH, leading to the activation of caspases, there is a slight variation between their mode of action. Consequently, this study provides evidence for the rationale involving intelligent semi-synthetic modification with natural products for the efficacious management of metastatic cancer.

2B.4 Materials and methods

2B.4.1 Cell culture. The human lung adenocarcinoma cancer cell line A549 and human metastatic melanoma cell line A375 were obtained from American Type Culture Collection (ATCC, Manassas, VA, USA). Human lung fibroblast cell line WI-38 was kindly gifted from Indian Institute of Chemical Biology (CSIR-IICB), Kolkata, India. Cells were maintained in DMEM with 10% FBS and 5% CO₂ at 37 °C. Cells were cultured in glass bottom, 96-well black plates, T25 flasks, T75 flasks and 4-well chamber slides for various experiments 2 days prior to the conduction of experiments.

2B.4.2 *In vitro* cytotoxicity assays. The growth inhibition capacity of parent compounds, intermediates and the derivatives were evaluated in cancer cell and normal cell lines initially using the 3-[4, 5-dimethylthiazol-2-yl]-2,5-diphenyltetrazolium (MTT) assay as previously reported.³⁴ This assay measures cell viability by assessing the cleavage of tetrazolium salt by

mitochondrial dehydrogenase. The absorbance was measured at 570 nm using a microplate spectrophotometer (BioTek Power Wave XS). Later the cytotoxicity was confirmed with Lactate dehydrogenase(LDH) assay (Pierce LDH Cytotoxicity Assay Kit-88953, USA) as per kit protocol using respective controls.¹² Finally the absorbance at 490nm and 680nm is measured using a spectrophotometer to determine LDH activity. In order to confirm the cytotoxicity using another working principle, we performed 5'-bromo-2'-deoxyuridine (BrdU) assay kit (colorimetric -11647229001, Roche Diagnostics, IN), as per the instructions given in the kit and explained before³⁵; measurements were made at 450/690 nm.

2B.4.3 Antioxidant activity. Earlier studies revealed that acetone extract of *Hydnocarpus wightiana* Blume possess anti-oxidant activity against selected free radicals. This encouraged us to examine the free radical scavenging property of the selected derivatives against multiple experimentally generated free radicals using assays such as DPPH radical scavenging assay, ferric reducing antioxidant power assay and hydroxyl radical scavenging assay.

2B.4.3.1 DPPH radical scavenging assay

The radical scavenging effects of the acetone extract on a 1, 1-diphenyl-2-picrylhydrazil (DPPH) radical were estimated. Various concentrations of samples and standards (3 mL) were mixed with 1 mL of 0.1mM of DPPH and the mixture were shaken vigorously and allowed to incubate at room temperature ($25 \pm 3^{\circ}\text{C}$) for 30 min. The scavenging activity was quantified spectrophotometrically at 507 nm against 95% ethanol as blank. Ascorbic acid was used as the standard and the percent DPPH scavenging effect was expressed as percent inhibition from the given formulae: % inhibition of DPPH radical = $[A_0 - A_1/A_0] \times 100$ Where A_0 was the absorbance of the control and A_1 was the absorbance of the sample/standard

2B.4.3.2 FRAP (Ferric reducing antioxidant power) assay

This assay measures the total antioxidant capacity of the compound and the procedure was conducted according to Benzie and Strain followed by modification.⁴¹ The working FRAP reagent was prepared by mixing 300 mM acetate buffer (pH 3.6), 10 mM 2, 4, 6-tripyridyl-s-triazine (TPTZ) solution and 20 mM $\text{FeCl}_3 \cdot 6\text{H}_2\text{O}$ in a 10:1:1 ratio prior to use and heated to 37°C in a water bath. Three milli litre (3 mL) of FRAP reagent was added to 100 μL of various concentrations of samples and standards. Absorbance was measured at 593 nm at 0 min and

again after 90 min. Ascorbic acid was used as the standard and changes in the absorbance after 90 min from initial reading were compared and percent inhibition was calculated as described.

2B.4.3.3 Hydroxyl radical scavenging assay

Hydroxyl radical scavenging activity was measured comparing deoxyribose and acetone extract for hydroxyl radical generated by the Fe³⁺-ascorbate-EDTA-H₂O₂ system (Fenton reaction)⁴². The reaction mixture contained (1 mL) 100 μL 2-deoxy-2-ribose (28mM in 20mM phosphate buffer, pH 7.4), 500 μL of different concentrations of samples and controls, 200 μL 1.04 mM FeCl₃, 100 μL 1 mM H₂O₂ and 100 μL ascorbic acid, was incubated at 37 °C for 1 hr. Thiobarbituric acid (1%) and trichloroacetic acid (2.8%) were added and incubated at 100°C for 20 min, after rapid cooling the absorbance was measured at 532 nm. Alpha tocopherol was used as the standard and the percentage inhibition was calculated.

2B.4.4 Apoptotic assays. Evaluation of the mode of cytotoxicity exhibited by the selected derivatives was performed on cancer cells with various apoptotic assays^{3,34,35} after administration of 20 μM of Hy-ISO-VIII and Hy-ISO-G. Morphological evaluation for apoptotic changes were performed under phase contrast microscope (Olympus 1X51, Singapore) under suitable magnification. In order to gain a deeper understanding with the morphological changes in a more appropriate platform, atomic force microscopy (AFM) was employed. Adherent cancer cells were grown overnight on 12 mm circular glass coverslips with 10% DMEM on 24-well culture plates for a period of 24 h. Cells were then incubated with compounds and later the cover slips were washed well with ice cold PBS thrice and fixed with 4% paraformaldehyde and were carefully taken out for imaging. AFM images were recorded under ambient conditions using a NTEGRA (NT-MDT) operating with a tapping mode regime. Micro-fabricated TiN cantilever tips (NSG10) with a resonance frequency of 299 kHz and a spring constant of 8 20-80 Nm⁻¹ was used. AFM section analysis was done offline.

Observation of nucleus for any morphological changes was done with Hoechst staining and the cells were observed under an inverted fluorescent microscope using a DAPI filter (Olympus 1X51). Acridine orange-ethidium bromide dual staining is the most commonly used method to detect apoptosis and is based on the differential uptake of two fluorescent DNA binding dyes by viable and nonviable cells, respectively. Assessment of apoptosis using the acridine orange-

ethidium bromide dual staining procedure was performed as described earlier. The cells were observed under an inverted fluorescent microscope, using a FITC filter (Olympus 1X51, Singapore) to view the apoptotic or non-apoptotic cells. Early onset of programmed cell death was further observed using APOPercentage dye (Biocolor, Belfast, Northern Ireland) as per manufacturer's instructions as previously described. Light microscopic images of APOPercentage dye-labeled cells, which stained pink under a light microscope, were used to quantify the extent of apoptosis. The dye uptake was further quantified using colorimetric method according to the manufacturer's instruction. The cells were lysed and the absorbance was measured at 550 nm using a microplate reader (Biotek, USA). Furthermore, TUNEL assay (Dead EndTM fluorometric TUNEL system G3250, Promega, USA) was used to detect the incorporation of the fluorescein-12-dUTP in the fragmented DNA of apoptotic cells, using the terminal deoxynucleotidyltransferase recombinant (rTdT) enzyme as per the manufacturer's instruction using propidium iodide as counter stain. Furthermore, evaluation of apoptosis by FITC-Annexin V staining (BD Pharmingen no. 556547, BD Biosciences, San Jose, CA) was also performed by flow cytometry, using kit-specified instructions on a Muse[®] Cell Analyzer flow cytometer (Merk-Millipore, Billerica, MA, USA), and the data were analyzed with the Muse[®] software.

2B.4.5 Anti-metastatic assays.

2B.4.5.1 Invasion and migration assay: The invasive and migration potential of cancer cells in presence of compounds was carried out using 24 well plate transwell inserts (353097, Corning Falcon, USA). For the invasion assay, the 24 well transwell chambers (8 μ m pore size polycarbonate filters) were applied with matrigel (354234, Corning Falcon, USA) on the inner side and kept at 37°C in 5% CO₂ incubator. Cancer cells were seeded (1×10^6 cells/mL) in serum free medium onto the trans well chambers with or without compounds (10 nM). DMEM medium with 10% serum was added onto the 24 well plates which served as the chemo-attractant. The plates were kept at 37°C in 5% CO₂ incubator. The transwell inserts were then taken and cells present in the upper chamber were removed using cotton swab and filters were stained using 1% crystal violet. The invaded cells present at the lower side of the inserts were visualized, counted and photographed using an optical microscope. Similarly, the migration assay was carried out using the above protocol except that the transwell inserts were devoid of matrigel coating.

2B.4.5.2 Wound healing assay: The scratch wound healing assay was performed to evaluate the anti-metastatic potential of selected compounds on A375 and A549 cells, as described previously. Briefly, cells were seeded into six-well plates at a density of 1.0×10^5 /well until they reached 80% confluence. A scrape was made through the confluent monolayer with a sterile plastic pipette tip of 1mm diameter. Afterwards, the dishes were washed twice with PBS and incubated at 37 °C in fresh DMEM complemented with 10% fetal bovine serum in the presence or absence of 10 nM of the derivatives. At the bottom side of each dish, three arbitrary places were marked where the width of the wound was measured with an inverted microscope (objective x 10). The culture plates were incubated at 37 °C and in 5% CO₂. Wound closure was expressed as the average \pm SEM of the difference between the measurements at time zero and the 12-24 h time period considered.

2B.4.5.3 Colony formation assay: Cancer cells (1000 cells/mL) were seeded onto a 6 well cell culture plate and subjected to treatments. The medium was removed and the cells were kept in fresh medium for 9 days or till the control cells achieved 50 cells per colony. The medium was removed, fixed in 70% ethanol and stained using 1% crystal violet in ethanol. The plate was air dried and the colonies were counted and photographed. Colonies were counted manually and plotted as a percent clonogenicity. Control colonies were considered as 100 %.

2B.4.6 Caspase assay. The effect of both initiator caspases (caspases 8, 9 and 2) and executioner caspases (caspase 3) was determined by using Apo Alert™ Caspase Profiling kit (Clontech, CA, USA) as per the kit protocol. Cells were treated with compounds for 12 h and finally, samples were transferred to 96-well plates for fluorimetric reading (excitation: 380 nm; emission: 460 nm), and the OD obtained was recorded under a spectrofluorometer (FLx800, BioTek).

2B.4.7 Raman spectral imaging. SERS experiments were performed with the aid of a confocal Raman microscope (WI-Tec, Inc., Germany) with a laser beam directed to the sample through 20× objective with a Peltier cooled CCD detector. For cellular imaging, 20 μ L (1×10^3 m) of gold nanoparticles was added. SERS mapping was recorded by focusing the laser beam on the cell surface selected at a position $z = 0$ μ m using 0.5 as the integration time, 150×150 as points per line, and 50×50 μ m mapping area along the X and Y directions. The Raman and SERS cell

maps were acquired over a motorized scan stage. The chemical images were computed from the 2D collection of Raman/SERS spectra by integrating the intensity of a specific band over a defined wave number range after baseline subtraction. A minimum of three independent measurements were made for each sample. WI-Tec Project plus (v 2.1) software package was used for data analysis. Cellular imaging and spectral analysis of genomic DNA were carried out using previously described procedure.⁸

2B.4.8 DNA fragmentation analysis. A549 cells were grown in 6 well plates and were subjected to treatment with HY-ISO-VIII and HY-ISO-G. Total DNA was isolated using DNA isolation kit from Geneaid (Cat.No. GB300, BR BIOCHEM life sciences) and the experiments were performed as per kit instructions and later the isolated DNA was run on agarose gels. The detailed experimental procedure is described in supporting information (SI section 5.1). Further, DNA fragmentation after 3h treatment with compounds was carried out according to the protocol from chemometec “DNA fragmentation assay” (application note no. 3003. rev. 1.4). NucleoCounter NC-3000 (chemometec) was used for quantification and interpretation.

2B.4.9 GSH estimation. Estimation of the cellular GSH was determined from the cell lysates of A375 and A549 cells. Briefly, cells were plated onto 12-well plates (1×10^5 cells/well) on a 5% CO₂ incubator at 37 °C. When the cells attain almost 70% confluency, they were subjected to different treatments, cells were trypsinized, washed with ice cold phosphate buffered saline (PBS, pH 7.4) thrice, lysed and GSH estimation were performed as per kit protocol (K251-100, BioVision, USA). Further, measurements were made with a fluorometer (FLx800, Bio-Tek, Winooski, VT, USA) at an excitation wavelength of 360 nm and an emission wavelength of 460 nm.

2B.4.10 Cyt c quantitation. Cancer cells were maintained in 10 % DMEM and were treated with Hy-ISO-VIII and Hy-ISO-G (20 μM) for 4 to 12 h. The cytosolic level of cyt c was estimated using an ELISA kit (KH01051, Invitrogen, Camarillo, CA) as per instructions given. The protein content was normalized using BCA assay (Thermo Fischer Scientific, IL, USA). Finally, the absorbance at 450 nm was measured using a microplate spectrophotometer (BioTek Power Wave XS). Concentrations of the controls and test samples were obtained from the

standard curve of cyt c and the data were expressed after the respective controls were normalized to be 100 %.

2B.4.11 Apoptosis antibody array. Semi quantitative analysis of 43 human apoptosis markers were performed using human apoptosis antibody array membrane (ab134001, Abcam, Cambridge, MA) according to the manufacturer's instructions.³⁶ Cancer cells were treated with Hy-ISO-VIII and Hy-ISO-G (20 μ M) for 12 h while maintaining control cells without treatment and the experiments were performed as per kit instructions.. Signals were quantified by a chemiluminescence system (Bio-Rad, CA, USA) immediately after the addition of detection buffers with a exposure time limited within 30 seconds. Densitometry data of the membrane was analyzed using Image J software (version 1.48, NIH, USA).For each array membrane, density of each spot was normalized with respect to its own positive controls and later each treatment was compared with respect to the vehicle control membrane. The fold change was calculated using the intensity value. Proteins that are 2-fold and above, which are differentially expressed with a p value of <0.05 (using Student's t-test), were subjected to unsupervised hierarchical clustering using cluster map function available in seaborn library of an object-oriented programming language, python.

2B.5 References

- (1) Gerl, R.; Vaux, D. L. Apoptosis in the Development and Treatment of Cancer. *Carcinogenesis* **2005**, *26* (2), 263–270. <https://doi.org/10.1093/carcin/bgh283>.
- (2) Lansiaux, a; Facompré, M.; Wattez, N.; Hildebrand, M. P.; Bal, C.; Demarquay, D.; Lavergne, O.; Bigg, D. C.; Bailly, C. Apoptosis Induced by the Homocamptothecin Anticancer Drug BN80915 in HL-60 Cells. *Mol. Pharmacol.* **2001**, *60* (3), 450–461.
- (3) Kamath, P. R.; Sunil, D.; Joseph, M. M.; Abdul Salam, A. A.; T.T., S. Indole-Coumarin-Thiadiazole Hybrids: An Appraisal of Their MCF-7 Cell Growth Inhibition, Apoptotic, Antimetastatic and Computational Bcl-2 Binding Potential. *Eur. J. Med. Chem.* **2017**, *136*, 442–451. <https://doi.org/10.1016/j.ejmech.2017.05.032>.
- (4) Sun, F.; Hung, H. C.; Sinclair, A.; Zhang, P.; Bai, T.; Galvan, D. D.; Jain, P.; Li, B.; Jiang, S.; Yu, Q. Hierarchical Zwitterionic Modification of a SERS Substrate Enables Real-Time

-
- Drug Monitoring in Blood Plasma. *Nat. Commun.* **2016**, *7*, 1–9.
<https://doi.org/10.1038/ncomms13437>.
- (5) Joseph, M. M.; Narayanan, N.; Nair, J. B.; Karunakaran, V.; Ramya, A. N.; Sujai, P. T.; Saranya, G.; Arya, J. S.; Vijayan, V. M.; Maiti, K. K. Exploring the Margins of SERS in Practical Domain: An Emerging Diagnostic Modality for Modern Biomedical Applications. *Biomaterials* **2018**, *181*, 140–181.
<https://doi.org/10.1016/J.BIOMATERIALS.2018.07.045>.
- (6) Okada, M.; Smith, N. I.; Palonpon, A. F.; Endo, H.; Kawata, S.; Sodeoka, M.; Fujita, K. Label-Free Raman Observation of Cytochrome c Dynamics during Apoptosis. *Proc. Natl. Acad. Sci.* **2012**, *109* (1), 28–32. <https://doi.org/10.1073/pnas.1107524108>.
- (7) Kang, B.; Austin, L. A.; El-Sayed, M. A. Observing Real-Time Molecular Event Dynamics of Apoptosis in Living Cancer Cells Using Nuclear-Targeted Plasmonically Enhanced Raman Nanoprobes. *ACS Nano* **2014**, *8* (5), 4883–4892.
<https://doi.org/10.1021/nn500840x>.
- (8) Narayanan, N.; Nair, L. V.; Karunakaran, V.; Joseph, M. M.; Nair, J. B.; Ramya, A. N.; Jayasree, R. S.; Maiti, K. K. Investigation of Apoptotic Events at Molecular Level Induced by SERS Guided Targeted Theranostic Nanoprobe. *Nanoscale* **2016**, *8* (22), 11392–11397. <https://doi.org/10.1039/c6nr03385g>.
- (9) Gassner, N. C.; Tamble, C. M.; Bock, J. E.; Cotton, N.; White, K. N.; Tenney, K.; Onge, R. P. S.; Proctor, M. J.; Giaever, G.; Nislow, C.; Davis, R. W.; Crews, P.; Holman, T. R.; Lokey, R. S. Accelerating the Discovery of Biologically Active Small Molecules Using a High-Throughput Yeast Halo Assay \perp . *J. Nat. Prod.* **2007**, *50*, 383–390.
<https://doi.org/10.1021/np060555t>.
- (10) Spencer, J. P. E.; Abd, M. M.; Mohsen, E.; Rice-evans, C. Cellular Uptake and Metabolism of Flavonoids and Their Metabolites: Implications for Their Bioactivity. *Arch. Biochem. Biophys.* **2004**, *423*, 148–161. <https://doi.org/10.1016/j.abb.2003.11.010>.
- (11) Murray, J. C. ANTI-INFLAMMATORY AGENT LEFLUNOMIDE TO ITS ACTIVE CYANOENOL METABOLITE A771726 : MECHANISTIC SIMILARITIES WITH THE
-

-
- CYTOCHROME P450- CATALYZED DEHYDRATION OF ALDOXIMES. *Drug Metab. Dispos.* **2003**, *31* (10), 1240–1250.
- (12) Mathai, B. M.; Joseph, M. M.; Maniganda, S.; Nair, J. B.; Arya, J. S.; Karunakaran, V.; Radhakrishnan, K. V.; Maiti, K. K. Guanidinium Rich Dendron-Appended Hydnocarpin Exhibits Superior Anti-Neoplastic Effects through Caspase Mediated Apoptosis. *RSC Adv.* **2016**, *6* (58), 52772–52780. <https://doi.org/10.1039/c6ra08724h>.
- (13) Sznarkowska, A.; Kostecka, A.; Meller, K.; Piotr, K. Inhibition of Cancer Antioxidant Defense by Natural Compounds. *Oncotarget* **2017**, *8* (9), 15996–16016.
- (14) Yokoyama, C.; Sueyoshi, Y.; Ema, M.; Mori, Y.; Takaishi, K.; Hisatomi, H. Induction of Oxidative Stress by Anticancer Drugs in the Presence and Absence of Cells. *Oncol. Lett.* **2017**, *14* (5), 6066–6070. <https://doi.org/10.3892/ol.2017.6931>.
- (15) Xu, S.; Yao, H.; Luo, S.; Zhang, Y. K.; Yang, D. H.; Li, D.; Wang, G.; Hu, M.; Qiu, Y.; Wu, X.; Yao, H.; Xie, W.; Chen, Z. S.; Xu, J. A Novel Potent Anticancer Compound Optimized from a Natural Oridonin Scaffold Induces Apoptosis and Cell Cycle Arrest through the Mitochondrial Pathway. *J. Med. Chem.* **2017**, *60* (4), 1449–1468. <https://doi.org/10.1021/acs.jmedchem.6b01652>.
- (16) Alqathama, A.; Prieto, J. M. Natural Products with Therapeutic Potential in Melanoma Metastasis. *Nat. Prod. Rep.* **2015**, *00*, 1–13. <https://doi.org/10.1039/C4NP00130C>.
- (17) Kitchin, K. T.; Brown, J. L.; Lijinsky, W. Biochemical Studies of Six Nitrogen Containing Heterocycles in Rst Tissues. *Biochem. Pharmacol.* **1989**, *38* (16), 2733–2738.
- (18) Priyadarsini, R. V.; Murugan, R. S.; Maitreyi, S.; Ramalingam, K.; Karunakaran, D.; Nagini, S. The Fl Avonoid Quercetin Induces Cell Cycle Arrest and Mitochondria-Mediated Apoptosis in Human Cervical Cancer (HeLa) Cells through P53 Induction and NF- κ B Inhibition. *Eur. J. Pharmacol.* **2010**, *649* (1–3), 84–91. <https://doi.org/10.1016/j.ejphar.2010.09.020>.
- (19) Jiang, Y.; Liu, Z. Natural Products as Anti-Invasive and Anti-Metastatic Agents. *Curr. Med. Chem.* **2011**, *23*, 808–829.
-

-
- (20) Wang, W.; Heideman, L.; Chung, C. S.; Pelling, J. C.; Koehler, K. J.; Birt, D. F. Cell-Cycle Arrest at G2/M and Growth Inhibition by Apigenin in Human Colon Carcinoma Cell Lines. *Mol. Carcinog.* **2000**, 28 (2), 102–110. [https://doi.org/10.1002/1098-2744\(200006\)28:2<102::AID-MC6>3.0.CO;2-2](https://doi.org/10.1002/1098-2744(200006)28:2<102::AID-MC6>3.0.CO;2-2).
- (21) Srivastava, S.; Somasagara, R. R.; Hegde, M. Quercetin , a Natural Flavonoid Interacts with DNA , Arrests Cell Cycle and Causes Tumor Regression by Activating Mitochondrial Pathway of Apoptosis. *Sci. Rep.* **2016**, 6, 1–13. <https://doi.org/10.1038/srep24049>.
- (22) Sysak, A.; Obminska-Mrukowicz, B. Isoxazole Ring as a Useful Scaffold in a Search for New Therapeutic Agents. *Eur. J. Med. Chem.* **2017**, 137, 292–309. <https://doi.org/10.1016/j.ejmech.2017.06.002>.
- (23) Desai, A. G.; Qazi, G. N.; Ganju, R. K.; El-Tamer, M.; Singh, J.; Saxena, A. K.; Bedi, Y. S.; Taneja, S. C.; Bhat, H. K. Medicinal Plants and Cancer Chemoprevention. *Curr. Drug Metab.* **2008**, 9 (7), 581–591. <https://doi.org/10.1037/a0013262>.Open.
- (24) Li, Z.; Gao, Q. Induction of Apoptosis in HT-29 Cells by Quercetin through Mitochondria-Mediated Apoptotic Pathway. *Animal Cells Syst. (Seoul)*. **2013**, 8354 (May), 147–153. <https://doi.org/10.1080/19768354.2013.793210>.
- (25) Gerauer, H.; Wachter, Y.; Zunino, S. J. Resveratrol Induces Extensive Apoptosis by Depolarizing Mitochondrial Membranes and Activating Caspase-9 in Acute Lymphoblastic Leukemia Cells 1. *Cancer Res.* **2001**, 61, 4731–4739.
- (26) Wang, I.; Lin, J. Induction of Apoptosis by Apigenin and Related Flavonoids Through Cytochrome c Release and Activation of Caspase-9 and Caspase-3 in Leukaemia HL-60 Cells. *Eur. J. Cancer* **1999**, 35 (10), 1517–1525.
- (27) Ramya, A. N.; Joseph, M. M.; Maniganda, S.; Karunakaran, V. Emergence of Gold-Mesoporous Silica Hybrid Nanotheranostics : Dox-Encoded , Folate Targeted Chemotherapy with Modulation of SERS Fingerprinting for Apoptosis Toward Tumor Eradication. *small* **2017**, 13, 1700819. <https://doi.org/10.1002/sml.201700819>.
-

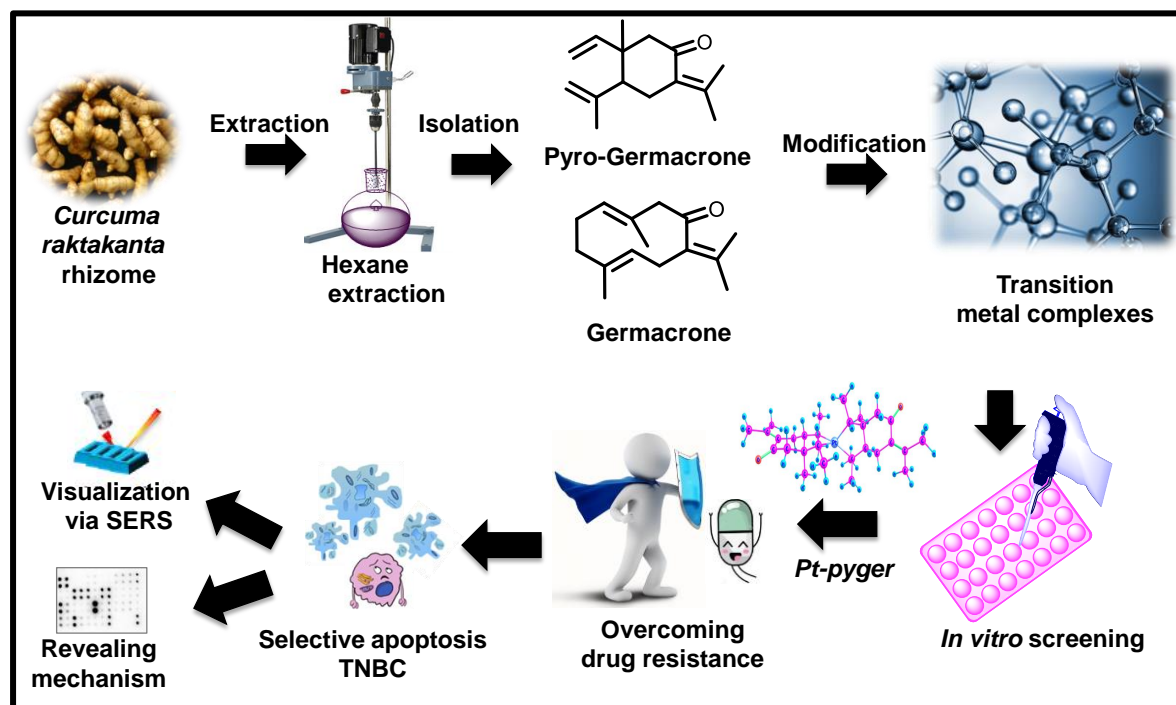
-
- (28) Gottlieb, E.; Armour, S. M.; Harris, M. H.; Thompson, C. B. Mitochondrial Membrane Potential Regulates Matrix Configuration and Cytochrome c Release during Apoptosis. *Cell Death Differ.* **2003**, *10* (6), 709–717. <https://doi.org/10.1038/sj.cdd.4401231>.
- (29) Brazhe, N. A.; Evlyukhin, A. B.; Goodilin, E. A.; Semenova, A. A.; Novikov, S. M.; Bozhevolnyi, S. I.; Chichkov, B. N.; Sarycheva, A. S.; Baizhumanov, A. A.; Nikelshparg, E. I.; Deev, L. I.; Maksimov, E. G.; Maksimov, G. V.; Sosnovtseva, O. Probing Cytochrome c in Living Mitochondria with Surface-Enhanced Raman Spectroscopy. *Sci. Rep.* **2015**, *5*, 1–13. <https://doi.org/10.1038/srep13793>.
- (30) Movasaghi, Z.; Rehman, S.; Rehman, I. U. Raman Spectroscopy of Biological Tissues. *Appl. Spectrosc. Rev.* **2015**, *42* (February), 493–541. <https://doi.org/10.1080/05704920701551530>.
- (31) Joseph, M. M.; Nair, J. B.; Ramya, A. N.; Hari, N.; Pillai, R. K.; Nair, A. J.; Maiti, K. K.; Therakathinal, S. T. Exploration of Biogenic Nano-Chemobiotics Fabricated by Silver Nanoparticle and Galactoxyloglucan with an E Ffi Cient Biodistribution in Solid Tumor Investigated by SERS Fingerprinting. *ACS Appl. Mater. Interfaces* **2017**, *9*, 19578–19590. <https://doi.org/10.1021/acsami.7b03191>.
- (32) Magdalena L. Circu and Tak Yee Aw. Glutathione and Apoptosis. *Free Radic. Res.* **2008**, *64* (12), 2391–2404. <https://doi.org/10.1038/jid.2014.371>.
- (33) Park, C.; Lee, W. S.; Go, S.; Nagappan, A.; Han, M. H. Morin , a Flavonoid from Moraceae , Induces Apoptosis by Induction of BAD Protein in Human Leukemic Cells. *Int. J. Mol. Sci* **2015**, *8733*, 645–659. <https://doi.org/10.3390/ijms16010645>.
- (34) Joseph, M. M.; Aravind, S. R.; Varghese, S.; Mini, S.; Sreelekha, T. T. PST-Gold Nanoparticle as an Effective Anticancer Agent with Immunomodulatory Properties. *Colloids Surfaces B Biointerfaces* **2013**, *104*, 32–39. <https://doi.org/10.1016/j.colsurfb.2012.11.046>.
- (35) Joseph, M. M.; Nair, J. B.; Maiti, K. K.; Therakathinal, S. T. Plasmonically Enhanced Galactoxyloglucan Endowed Gold Nanoparticles Exposed Tumor Targeting Biodistribution Envisaged in a Surface-Enhanced Raman Scattering Platform.
-

Biomacromolecules **2017**, *18* (12), 4041–4053.

<https://doi.org/10.1021/acs.biomac.7b01109>.

- (36) Wu, D.; Wang, Y.; Wang, L.; Chen, C. Y.; Lee, H. A Low MicroRNA-630 Expression Confers Resistance to Tyrosine Kinase Inhibitors in EGFR-Mutated Lung Adenocarcinomas via MiR-630 / YAP1 / ERK Feedback Loop. *Theranostics* **2018**, *8* (5), 1256–1269. <https://doi.org/10.7150/thno.22048>.

Germacrone Analogues from *Curcuma raktakanta* Resembling Oxaliplatin – Active Molecular Entities against Breast Cancer



Abstract: Breast cancer is the most frequently diagnosed type of gynecological cancer where triple negative breast cancer (TNBC) is a subtype with limited treatment options and prognosis. Chemotherapy involves the administration of Platinum (Pt) drugs that causes severe side effects including nephrotoxicity and other health risks to the patients. Hence there is a huge demand for the development of reno-protective strategies for the Pt-drug mediated therapy. Germacrone, a bioactive phytomolecule isolated from the rhizomes of *Curcuma raktakanta* has anticancer, anti-inflammatory and immunomodulatory functions. Herein, Pt, Ir and Ru based metal complexes of germacrone and its derivative pyrogermacrone were achieved semi-synthetically and the potent molecule out of these synthesized derivatives was identified after detailed in vitro cytotoxicity evaluation. The selected molecule Pt-pyger revealed promising selective cytotoxicity towards triple negative breast cancer cells MDA-MB-231 and was found to overcome drug-resistance phenomenon in drug resistant cell line. Interestingly, the marked bio molecular fingerprint changes during cell death process including cellular

DNA damage were precisely analyzed by surface enhanced Raman scattering (SERS) spectral analysis as an emerging diagnostic modality. Finally, the plausible apoptotic pathway was elucidated by high throughput protein screening by antibody array kit.

3.1 Introduction. Breast cancer is the most common malignancy and leading cause of cancer related death in women. Treatment of early-stage breast cancer requires a multimodality approach to eradicate residual cancer and prevent recurrent disease.^{1,2} Targeting the pathways that promote or sustain growth and invasion of carcinoma cells is critical to effective treatment of breast cancer. Triple-negative breast cancer (TNBC), which lacks expression of the estrogen and progesterone receptors (ER and PgR) and the human epidermal receptor 2 (HER2), is a subtype of breast cancer accounting for 12–20% of all breast cancer cases.¹ TNBCs showed some specific pathological characteristics, which are associated with younger age and poor prognosis. Treatment options for TNBCs are limited because of the lack of targeted treatments in large part related to the heterogeneity of emerging molecular signatures. Therefore, the prognosis for TNBC is poorer than that for other types of breast cancers. There has been renewed interest in platinum agents for the treatment of TNBC.³ Although platinum salts have often been combined with targeted agents in clinical trials, single-agent platinum therapy is an accepted treatment for advanced TNBC and is associated with respectable relative risks. A number of studies evaluating conventional platinum agents in patients with metastatic TNBC revealed the enhanced nephrotoxicity.^{4–6}

It is important to note that approximately 50–60% of patients undergoing Pt drug-based cancer chemotherapy acquire acute kidney injury, which caused increased morbidity and mortality rates. The accumulation of Pt drugs in renal tissues results in oxidative stress that leads to inflammatory damage to the tubular epithelium and further spreads to the renal cells, and ultimately decreases the glomerular filtration rate.^{7,8} Therefore, an urgent need to develop more efficient therapeutic agents that confer renoprotection without compromising the anticancer activity. Advancement in developing renoprotective strategies for the Pt-drug mediated therapy is still lacking.

Phytochemicals are being used in traditional medicine for several centuries for treating various ailments. There is considerable evidence from *in vitro* preclinical studies that phytochemicals may retard tumor growth and produce antioxidant and anti-inflammatory effects.^{9,10} Recently there is a renewed interests in the identification of several potential

phytochemicals that are being investigated for their renoprotective actions in preclinical studies.^{11,12} *Curcuma raktakanta* is a widely used traditional herb used in Ayurveda for various ailments. Germacrone, the main component of rhizome, has been shown to possess antitumor, anti-inflammatory and immunomodulatory properties.^{13–15} Germacrone reverses adriamycin resistance by imparting cell apoptosis in multi-drug resistant (MDR) breast cancer cells.^{16,17} The co-administration of germacrone with cisplatin reduced the cellular platinum content compared with cisplatin treatment alone. The germacrone's protective effect on cisplatin-induced cytotoxicity was not observed in cancer cells whereas cisplatin's anti-cancer activity was preserved. Germacrone prevented cisplatin-induced toxicity in renal cells via inhibition of organic cation transporter 2 (OCT2) transport function and reducing cisplatin accumulation.¹⁸

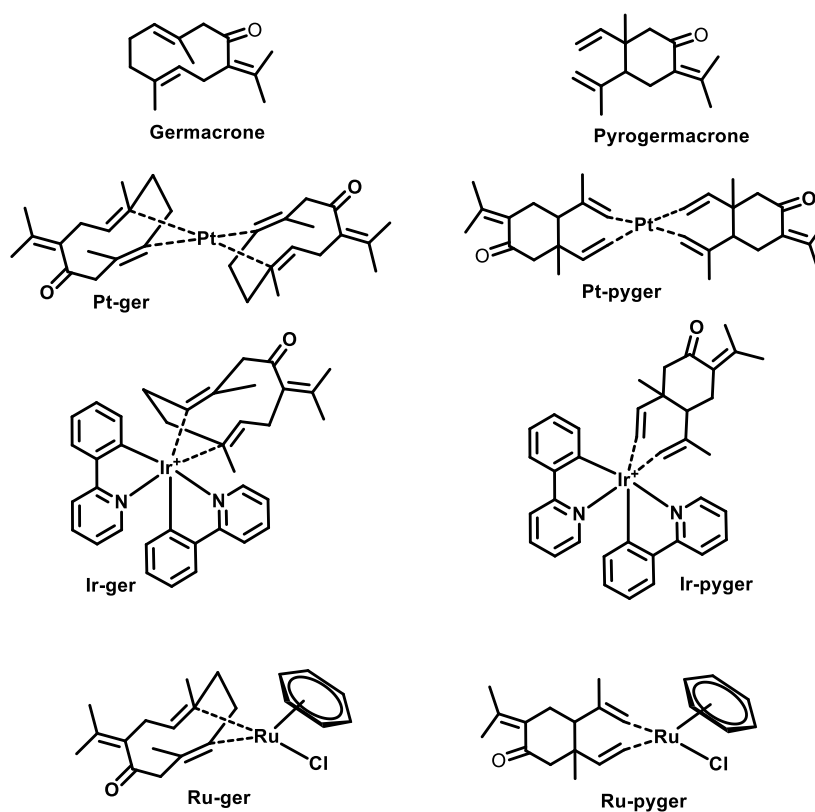


Figure 3.1: Structure of synthesised metal complexes.

Considering all this in mind, a smart design of Pt, Ir, and Ru coordinated germacrone and pyrogermacrone^{19,20} (cope rearranged product of germacrone) metal complexes were synthesized aiming superior anticancer properties in breast cancer cells with reduced toxicity towards normal cells (Figure 3.1). Interestingly the selected molecule showed anticancer effect in Pt-resistant cell line overcoming drug resistance. The potent molecule

from the synthesized metal complexes was identified after extensive cytotoxicity evaluation and further, a detailed apoptotic evaluation was carried out in triple negative breast cancer cells MDA-MB-231.

3.2 Results and Discussion

3.2.1 Isolation of germacrone: *Curcuma raktakanta* rhizomes were collected from JNTBGRI, Thiruvananthapuram, Kerala, medicinal plant garden in February 2014. The rhizomes were thoroughly cleaned and dried in air oven maintained at 40 °C for three days. It was then thoroughly powdered and weighed approximately 500g. The powdered material was first extracted using hexane (1.5 L) three times at room temperature. Then it was extracted using ethyl acetate (1.5 L) three times and finally extracted using acetone (1.5 L) three times at room temperature. The total extracts were concentrated under reduced pressure using Buchii rotary evaporator. This yielded about 30g of the crude hexane extract, 25g of ethyl acetate and 25g of acetone extract. Based on the observation in TLC, the hexane extract was selected for the isolation of compounds.

About 15g of the hexane extract was subjected to column chromatography. For this a glass column of capacity (20g) was cleaned and dried. Cotton pad was placed at the bottom of the column. It was then loaded with 100g of column chromatographic graded silica (mesh size 100-200 µm). The silica was added to the column by making slurry with hexane and was allowed to settle down at appropriate height. The hexane extract (10g) was dissolved in minimum quantity of hexane and mixed until the extract was dissolved. It was then loaded onto the column as liquid application of the sample. The column was kept undisturbed for 30 minutes for the extract to get adsorbed over the silica gel. The applied sample was eluted by a mixture of solvents. At first the elution was started with pure hexane and then the polarity was increased by increasing the volume of ethyl acetate in hexane-ethyl acetate mixture. Finally, the column was eluted using 100% ethyl acetate and there after washed the column with 10% ethyl acetate in methanol mixture.

Different fractions of about 100ml were collected in conical flasks. A total of 304 fractions were collected. Based on the TLC of each fraction and similarities in the TLC they were pooled into thirteen (A-M) fraction pools (Figure 3.2). Each of the fraction pools were concentrated under reduced pressure using Buchii rotary evaporator and vacuum pump. Masses were calculated and the samples were stored in refrigerator.

Further sub columns of different fraction pools were carried out. TLC of fraction pool D (35-60) eluted from the main column at 5% EtOAc-hexane wash showed 4-5 interesting iodine spots with distinguishable R_f values. When subjected to sub column, with 5% EtOAc-hexane single iodine spot was obtained. After concentration, it was subjected to crystallization using hexane-dichloromethane. 300mg fine crystals were obtained and the compound was identified as germacrone using NMR and HRMS data.

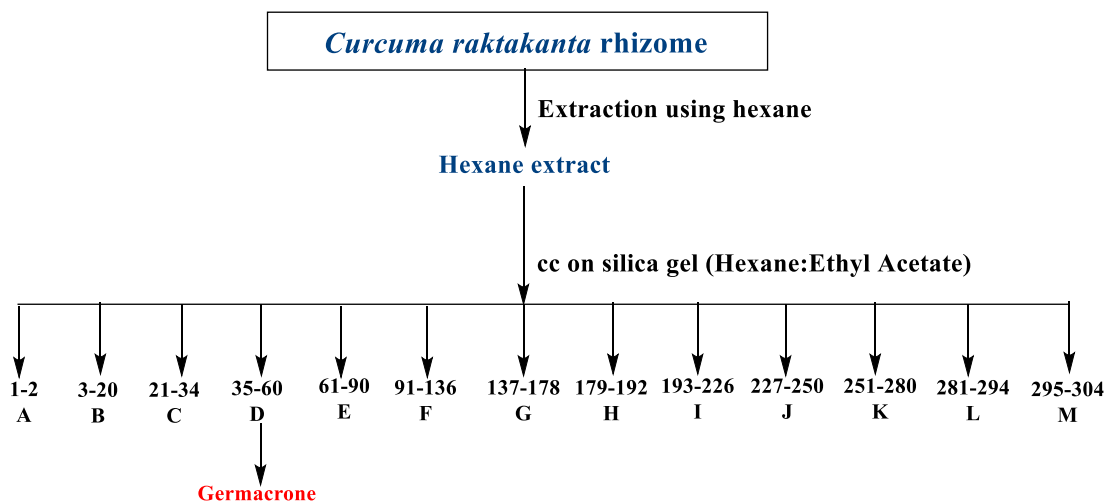


Figure 3.2: A pictorial representation of isolation procedure

3.2.2 Synthesis of metal-germacrone/pyrogermacrone complexes. In the course of synthetic modification, the germacrone was subjected to pyrolysis for undergoing cope rearrangement yielding pyro-germacrone (pyger) or β -elemenone. The reaction was carried out at 80 °C in toluene under nitrogen atmosphere. The cope rearranged product having two terminal diene system is expected to coordinate with the metal centers effectively yielding metal complexes with enhanced anti-cancer properties and reduced toxicity. Then germacrone and the synthesized germacrone analogue pyrogermacrone were complexed with coordinating metals like Pt, Ir and Ru. Potassiumtetrachloroplatinate, in house synthesized IR dimer and Dibenzene-tetrachlorodiruthenium were used for the synthesis of Pt, Ir and Ru metal complexes respectively. The reaction time taken for the complete consumption of germacrone was higher than that for pyrogermacrone complexes. This could be explained due to the ease of formation of metal complexes with terminal dienes than the rigid ones.²¹ Formation of the metal complexes with the natural product derivatives were confirmed by the XPS analysis.²² XPS data of all six derivatives showed characteristic

peak corresponding to the binding energy of O 1s at 529.0 eV (Figure 3.3). Characteristic peak corresponding to Pt 4f_{5/2} (74.3 ± 0.04 eV) was unambiguously observed in the XPS spectra of Pt-ger and Pt-pyger complexes. Similarly, the characteristic peak of Ir 4f_{7/2} (62.4 ± 0.05) and Ru 5d_{5/2} (198.84 ± 0.005) were observed in the XPS spectrum of corresponding metal complexes with germacrone and pyrogermacrone. These results confirmed the coordination of Pt, Ir and Ru with the naturally occurring sesquiterpene derivatives germacrone and pyrogermacrone. In the ¹H-NMR spectrum, the olefinic protons of germacrone resonates between 4.5-5.0 ppm as two doublets. These protons have been shifted up field and resonate between 4.0-4.5 ppm in the germacrone metal complex. This suggests that the coordination is taking place at the olefinic region and not in the α-β unsaturated region. The same pattern was observed for the pyrogermacrone metal complex as well.

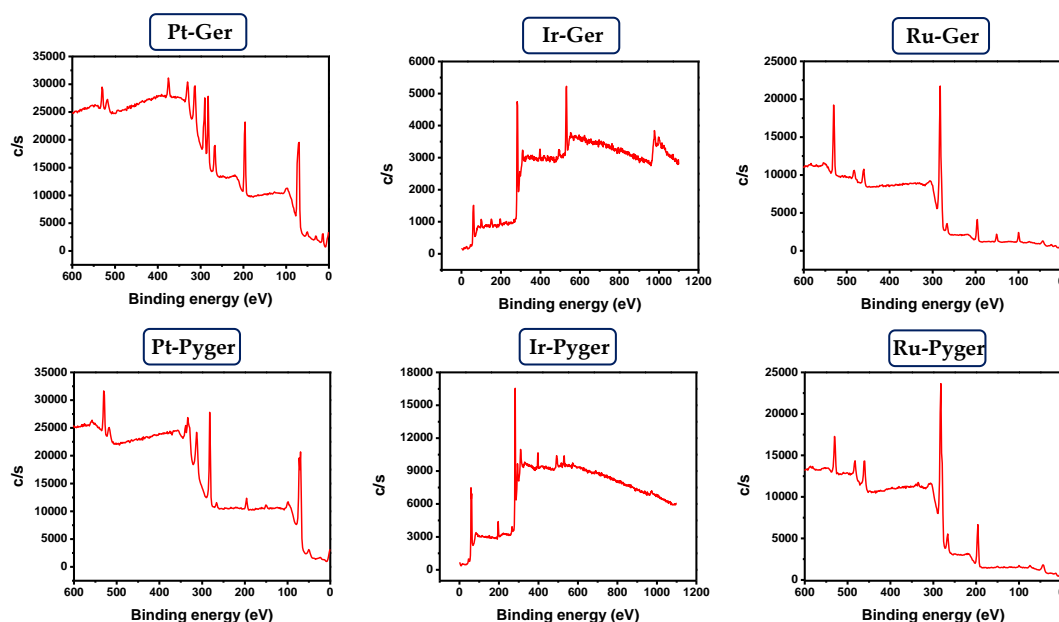


Figure 3.3: XPS analysis of the synthesized metal complexes.

3.2.3 Cytotoxicity screening of the synthesized metal complexes. TNBC worth special attention because of the poor prognosis and no targeted therapy has been approved yet for the clinical use. Primary selection based on the cytotoxicity of Pt, Ir and Ru metal complexes with germacrone and pyrogermacrone was evaluated through 3-[4,5-dimethylthiazol-2-yl]-2,5-diphenyltetrazolium (MTT) assay where the derivatives were assessed on triple negative human breast cancer cell line, MDA-MB-231 (Figure 3.4) and normal fibroblast cell line, WI-38 after 12 and 24h of treatment.

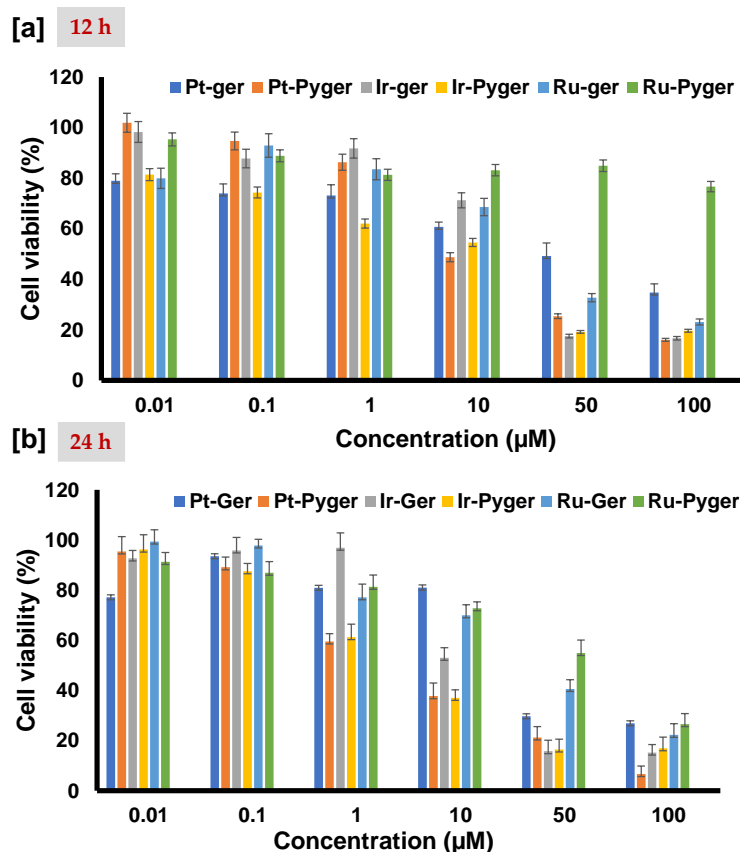


Figure 3.4: Cytotoxic evaluation of metal complexes in MDA-MB-231 cells for [a] 12h, [b] 24h.

Table 3.1: IC₅₀ Values of metal complexes in MDA-MB-231 and WI-38 Cells over 12 and 24h.

Compound	IC ₅₀ (μM)			
	MDA-MB-231		WI-38	
	12h	24h	12h	24h
Pt-ger	32.06 ± 1.1	42.06 ± 1.5	64.12 ± 1.4	36.45 ± 0.9
Pt-pyger	7.08 ± 0.3	2.68 ± 0.1	Nil	Nil
Ir-ger	11.12 ± 0.7	7.9 ± 0.4	24.5 ± 0.8	19.14 ± 0.7
Ir-pyger	9.28 ± 0.2	2.49 ± 0.08	Nil	49.09 ± 1.4
Ru-ger	22.89 ± 0.8	14.31 ± 0.3	47.85 ± 1.3	53.70 ± 1.5
Ru-pyger	Nil	75.48 ± 1.8	Nil	Nil

It was interesting to observe that all the synthesized metal complexes showed significant cell death against MDA-MB-231 cells in 24 h treatment. Metal complexes derived from germacrone showed indiscriminate cytotoxicity in both cancer and normal lung fibroblast cells even after 12h treatment, and hence, these compounds were eliminated from the primary screening criteria (Table 3.1). Pt-pyger, Ir-pyger and Ru-pyger were selected for

the next-level screening studies. These results suggested that the structural modification of the germacrone by cope rearrangement and the incorporation of the metal atoms to the coordination sphere contributed significantly towards selective cytotoxicity in cancer cells.

3.2.4 Structure optimization using DFT calculation. Energy minimized structures were optimized by using B3LYP level of DFT (6-31+G* basis set used for C, H, O, N and ECP for transition metal). Frequency calculations show that the selected Pt-pyger, Ir-pyger and Ru-pyger complexes are stable with “NO” imaginary frequencies (figure 3.5). The minimal energy obtained were -1441.65358921, -1722.24517699 and -1000.55564493 hartree respectively for Pt-pyger, Ir-pyger and Ru-pyger. (A hartree is equal to 2625.5 kJ/mol, 627.5 kcal/mol, 27.211 eV, and 219474.6 cm⁻¹).

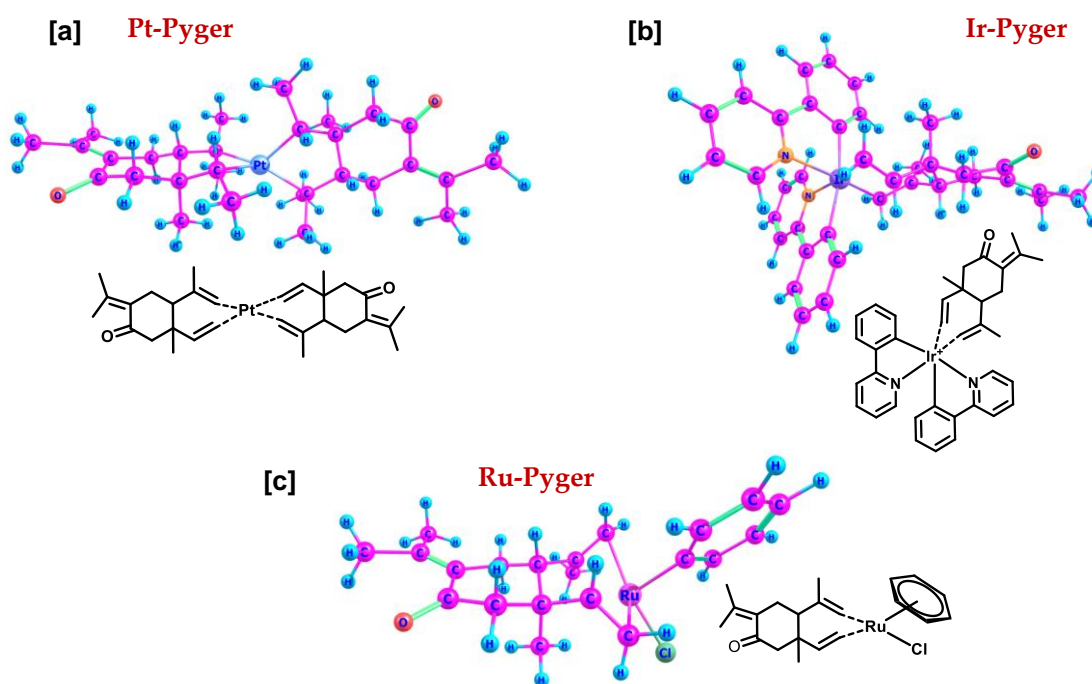


Figure 3.5: Optimized structure of Pt-pyger, Ir-pyger and Ru-pyger by using B3LYP level of DFT.

3.2.5 Detailed cytotoxic evaluation of the selected metal complexes. After screening out the germacrone derived metal complexes of Pt, Ir and Ru and the structure optimization of the other three derivatives, a detailed evaluation of the effect of these compounds in triple negative breast cancer cells and normal breast epithelial cells were carried out. The pyrogermacrone derived metal complexes, Pt-pyger, Ir-pyger, Ru-pyger were scrutinized for the cytotoxic assessment using MTT assay in MDA-MB-231 and

MCF-10-A after 12 and 24h treatment (Figure 3.6a-d). Pt-pyger was found to be selectively toxic towards MDA-MB-231 whereas Ir-pyger caused significant toxicity in both the cell lines. It was observed that MDA-MB-231 cells were arrested with an IC_{50} value of 8.59 and 3.2 μM by Pt-pyger at 12 and 24h and a very lower cytotoxic effect was noticed in MCF-10-A cells. In contrary to this, Ir-pyger complex could generate lower IC_{50} s in both the cell lines. An IC_{50} value of 14.23 and 4.07 μM was observed for the complex in MDA-MB-231 cells at 12 and 24h and in MCF-10-A, the values were 8.52 and 7.04 μM respectively. Ru-pyger complex failed to generate prominent cytotoxicity in both triple negative and normal breast epithelial cells compared to the other two derivatives. From the results, Pt-pyger was selected as the most potent natural product derived metal complex towards selective cytotoxicity in triple negative breast cancer cells causing no harm to the normal breast epithelial cells.

Then the cytotoxicity of the selected derivative, Pt-pyger was compared with the parent molecule germacrone and the third generation Pt drug oxaliplatin (OxPt) (Figure 3.6e-h). Germacrone showed only moderate cytotoxicity in MDA-MB-231 cells with an IC_{50} value of 24.7 μM at 24h treatment. In triple negative breast cancer cells, the cytotoxicity induced by the synthetically modified metallocomplex with pyrogermacrone and Pt was comparable with the clinically used anticancer drug oxaliplatin. It was observed that the MDA-MB-231 cells were arrested with an IC_{50} value of 2.7 and 0.95 μM at 12h and 24h treatment of oxaliplatin respectively. Also, oxaliplatin caused significant cytotoxicity in normal breast epithelial cells with an IC_{50} value of 41.18 and 22.00 μM at 12 and 24h administration. Taken together, the detailed evaluation of the cytotoxicity confirmed that the synthesized metallocomplex derived from the natural product germacrone and Pt metal promoted significant contribution for the selective and enhanced cytotoxicity on MDA-MB-231 cells. The coordination of pyrogermacrone to the Pt metal could be the possible reason for the reduced toxicity in non-tumorigenic breast epithelial cells. The protective effect of the natural products on co-administration with anticancer agents attenuates toxic effect of the drugs and enhanced the antitumor effects. Phytochemical derived agents to combat Pt drug induced toxicity are currently in preclinical studies.^{23,24}

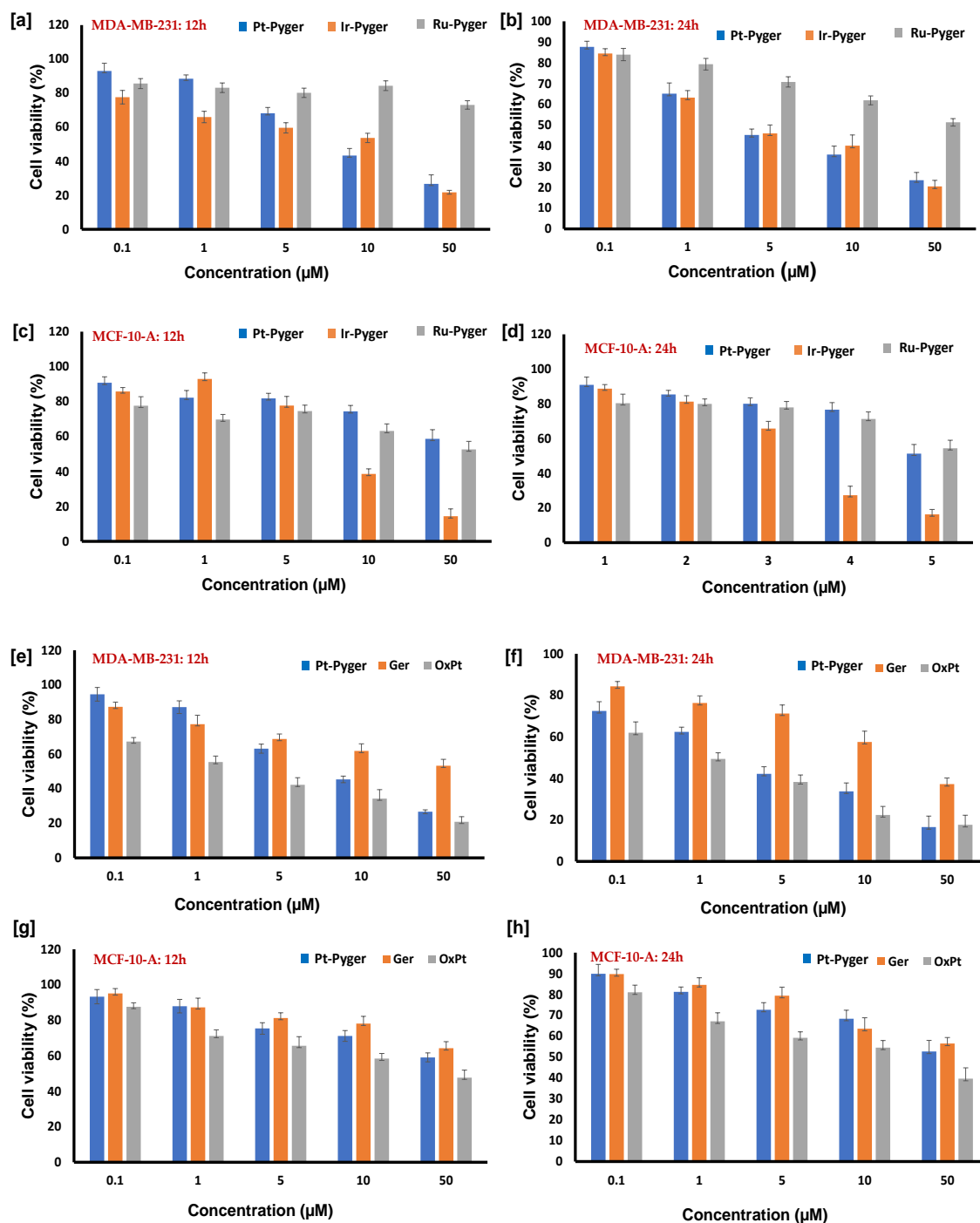


Figure 3.6: Cytotoxic evaluation of compounds Pt-pyger, Ir-pyger and Ru-pyger in MDA-MB-231 cells [a] 12h, [b] 24h. Cytotoxic evaluation of compounds Pt-pyger, Ir-pyger and Ru-pyger in MCF-10-A cells [c] 12h, [d] 24h. Cytotoxic evaluation of compounds Pt-pyger, germacrone (ger) and oxaliplatin (Ox Pt) in MDA-MB-231 cells [e] 12h, [f] 24h. Cytotoxic evaluation of compounds Pt-pyger, germacrone (ger) and oxaliplatin (Ox Pt) in MCF-10-A cells [g] 12h, [h] 24h.

3.2.6 Effect of Pt-pyger in Pt resistant cancer cells. Multidrug resistance (MDR) is an obstacle to the treatment of cancer.^{25,26} Germacrone has been shown to possess antitumor, anti-inflammatory, and immunomodulatory properties and reported to possess a critical role against MDR.¹⁷ To evaluate the effect of Pt-pyger molecule on Pt resistant cancer cells, the cytotoxic effect of the compound in Pt resistant human epithelial ovarian cancer cell line, SKOV-3, was assessed by comparing with parent germacrone and oxaliplatin drug after 12 and 24 h treatment (Figure 3.7a,b). As anticipated, oxaliplatin did not produce any cytotoxicity in SKOV-3 cells till 50 μM at 12 and 24 h administration. In contrast, the synthesized Pt coordinated complex showed dose-dependent cytotoxicity and cell death against parent molecule germacrone and oxaliplatin which is reflected in lower IC_{50} s. Pt-Pyger produced an IC_{50} of 25.1 and 7.2 μM at 12 and 24 h treatment, indicating that the compound favored cell death overcoming the Pt resistance possessed by SKOV-3 cells. The same was confirmed by checking the Pt content in SKOV-3 and MDA-MB-231 cells on treatment with Pt-pyger and oxaliplatin after 12h incubation and Pt concentrations were measured using inductively coupled plasma mass spectrometry (ICPMS) technique (Figure 3.7c).

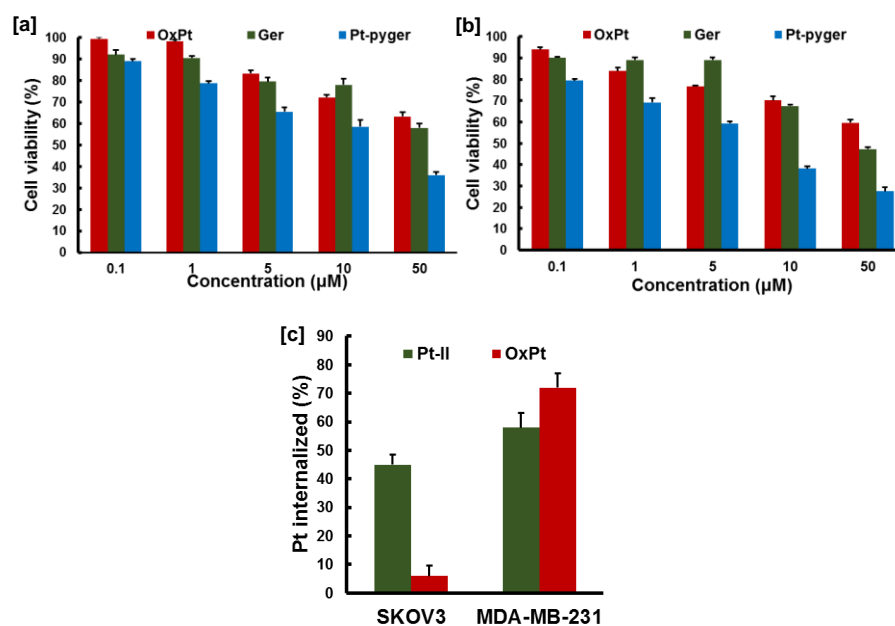


Figure 3.7: Cytotoxic evaluation of compounds Pt-pyger, germacrone (ger) and oxaliplatin (Ox Pt) in SKOV3 cells [a] 12h, [b] 24h. [c] ICPMS analysis of PT content in SKOV3 and MDA-MB-231 cells.

The percentage of Pt content found in MDA-MB-231 on treatment with Pt-pyger and oxaliplatin were 57.51 and 69.47. This correlates with the cytotoxicity produced by in MDA-MB-231 cells. According to the results, Pt-pyger significantly elevates the uptake of the molecule in SKOV-3 cells. The percentage of Pt content found in SKOV-3 cells on administration with the synthesized Pt-pyger complex was 45.41% whereas that for oxaliplatin was only 6.23% which attributes to the cytotoxicity results. The higher retaining of Pt content in the SKOV-3 cells might be responsible for the enhanced cytotoxicity in Pt resistant SKOV-3 cells. Coordination of germacrone derived pyrogermacrone is responsible for the ability of this potential anticancer agent to overcome the drug resistance induction, one of the principal causes of cisplatin-based tumor treatment failure.

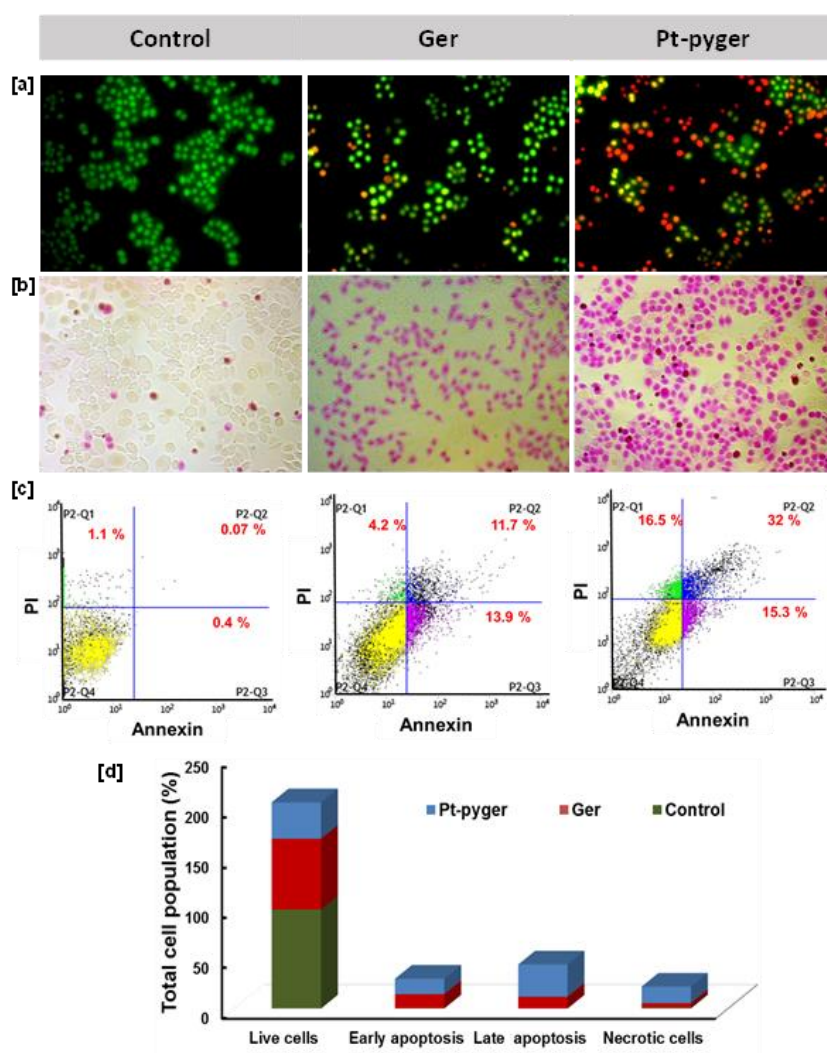


Figure 3.8: Apoptotic evaluation of Pt-pyger in MDA-MB-231 cells [a] Live-dead assay, [b] APOPOP assay, and [c], [d] Annexin V/FITC assay.

3.2.7 Anticancer properties of Pt-pyger complex. Induction of cell death by Pt-pyger was evaluated using conventional apoptotic assays, which provides the cell death mechanism. The acridine orange–ethidium bromide dual staining assay in MDA-MB-231 cells presented a color change from green to orange/red with associated apoptotic features due to the administration (5 μ M) of Pt-pyger. The extent of apoptosis in germacrone treated cells in the same concentration was significantly less than the Pt-pyger treated cells (Figure 3.8a). APOPercentage™ assay is a prevalent colorimetric assessment in which the apoptotic cells will be visualized in pink colour. On analysing the response of the MDA-MB-231 cells after treatment, a significant population of apoptotic cells was observed in Pt-pyger treated cells compared to the control and the germacrone treated ones (Figure 3.8b).

Further, the annexin V staining assay was performed to measure the anticancer effect of the synthesized metal complex Pt-pyger in comparison with the parent molecule germacrone by flow cytometry analysis in MDA-MB-231 cells. The annexin V positivity was significantly ($p < 0.001$) higher in the Pt-pyger treated cells. The control cells were $0.07 \pm 1\%$ annexin V positive, while the selected metal complex treated cells showed $32 \pm 1.2\%$ positivity, whereas the germacrone treated cells showed only 11.7% positivity. The percentage of early and late apoptosis cells was higher in Pt-pyger treated cells than in the germacrone treated ones (Figure 3.8c, d). The execution of programmed cell death was further examined with terminal deoxynucleotidyltransferase dUTP nickend labelling (TUNEL) staining assay. Compound-treated cells turn green in color, indicating TUNEL positivity, while control cells remain TUNEL negative (red) in nature. The extent of TUNEL positivity was higher in Pt-pyger treated cells than the parent germacrone treated cells (Figure 3.9a). Cysteine-aspartic proteases or caspases are a class of important proteolytic enzymes that play an important role in regulating cell cycle phases and cell death pathways. Most of the anticancer drugs are reported to induce apoptosis through caspase mediated pathway. In order to reconfirm the apoptosis mechanism, caspase-3 level before and after laser irradiation was examined. The expression of caspase-3 in Pt-pyger treated cells was 1.7-fold ($p < 0.001$) enhanced compared to the control cells and that for germacrone treated cells, 0.9-fold ($p < 0.01$) enhancement was observed.

The results obtained from multiple apoptotic assays revealed that the synthesized Pt-pyger metallocomplex induces programmed cancer cell death. Cancer cell-selective

cytotoxicity of the Pt-pyger molecule predominantly imparts cell death in a programmed manner due to the incorporation of the metal atom in a coordinated way. Thus, the enhanced apoptotic potential can be explained due to the presence of the Pt atom, which can interact with the biomolecules present in the cellular milieu.

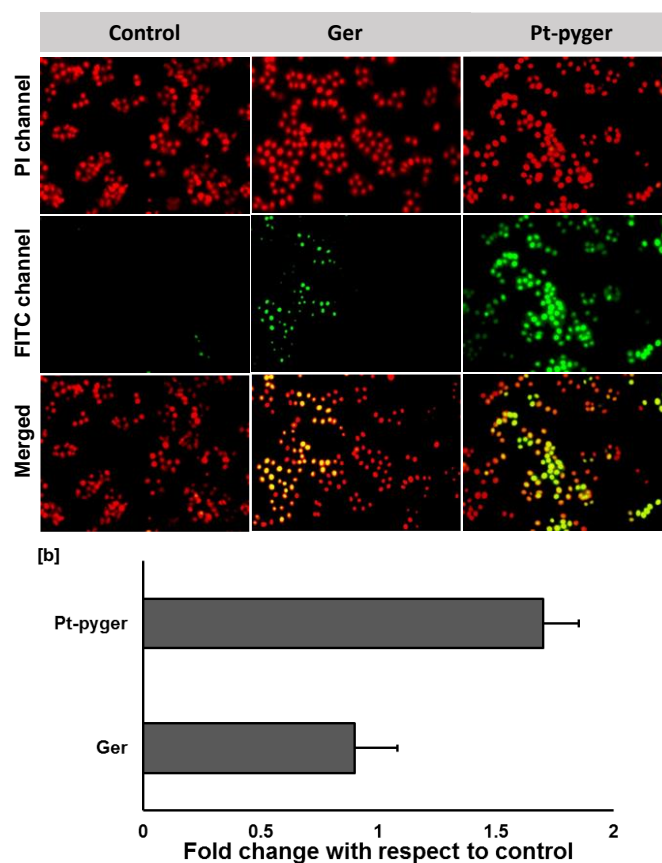


Figure 3.9: [a] TUNEL assay and, [b] caspase assay in MDA-MB-231 cells.

3.2.8 Investigation of apoptotic events by tracking the intracellular signature molecular fingerprints by surface enhanced Raman scattering (SERS) modality.

A detailed analysis on apoptotic cell death mechanism was further validated using SERS platform in a straight forward manner.^{27,28} SERS being one of the most ultrasensitive spectroscopic techniques enable to evaluate the signature spectral pattern of certain biomolecules in a complex macromolecular system. The MDA-MB-231 cells were subjected to SERS analysis before and after 6h treatment with the Pt-Pyger (10 μM) compound (Figure 3.10a). The SERS spectrum of the control cells showed prominent cell peaks emerged from various biomolecules at 762, 1015, 1345 and 1630 cm^{-1} corresponding to aromatic ring breathing, carbohydrates, alkyl wagging and Amide C=O

stretching respectively. A decline in these peaks indicates the disruption of the primary molecular structure of various biomolecules like nucleosides, carbohydrates proteins etc. Two prominent peaks at 670 and 1468 cm^{-1} were observed on SERS spectrum after 6h of Pt-pyger treatment. These peaks were attributed to the porphyrin deformation and C=N stretching which might have prominently evolved from the cytochrome C (cyt C) release and subsequent DNA damage occur at the initial stages of apoptosis. The cytotoxic effect of the synthesised Pt coordinated metal complex derived from germacrone caused maximal damage to the biological macromolecules and the analysis of Raman spectra demonstrated the molecular changes occurring during apoptosis.

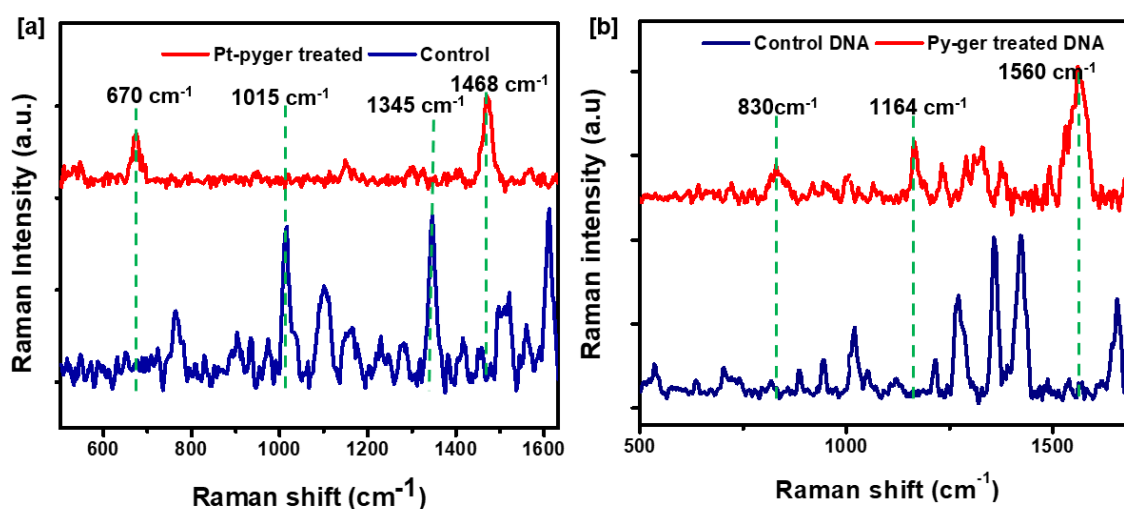


Figure 3.10: SERS analysis of [a] MDA-MB-231 cells before and after Pt-pyger treatment, [b] genomic DNA before and after Pt-pyger treatment.

DNA fragmentation is the hallmark change happening at the time of apoptosis. In molecular level, the phosphate backbone bonds of DNA molecule will be ruptured and the N₇-H vibrations on the nucleic bases will be intensified at the time of DNA fragmentation. SERS analysis can be effectively utilized to monitor these changes happening at the time of apoptosis. So, after 6h Raman spectral analysis of the isolated DNA clearly illustrated the Pt-Pyger induced DNA damage. A comparison of the spectrum from cells before and after Pt-Pyger administration is given in Figure 3.10b. SERS spectra indicated a distinct peak at 830 cm^{-1} and 1164 cm^{-1} which corresponds to the O-P-O backbone breakage and the increase in intensity of N₇-H vibration from nucleic bases at 1560 cm^{-1} substantiates the apoptotic cell death mechanism.²⁹

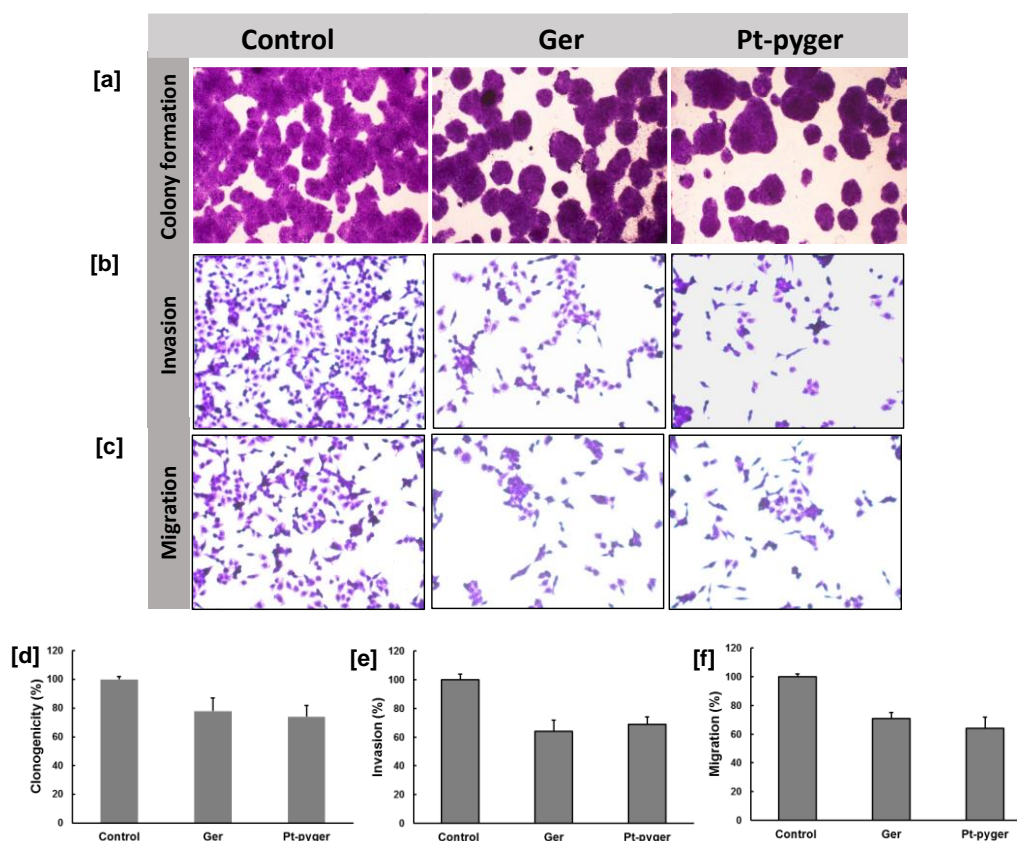


Figure 3.11: Anti-metastatic potential of Pt-pyger. [a], [d] colony formation assay. [b], [e] Invasion assay and [c], [f] migration assay.

We have successfully monitored the real-time apoptotic event in SERS modality by tracking the signature Raman peaks. This serves as a feasibility study for the specific and sensitive delivery of the synthesised germacrone derived metalcomplex to the cellular site leading to programmed cell death. The dynamics during apoptosis induced by any natural product or its active semi-synthetic counterpart was well explored in the previous chapter as well.

3.2.9 Antimetastatic properties of Pt-pyger complex. Metastasis accounts for the major reason behind cancer associated mortalities; the antimetastatic potential of the synthesized Pt-pyger molecule was investigated. As a first step toward evaluating the antimetastatic property, the effects of Pt-pyger (5 $\mu\text{g}/\text{mL}$) was examined on colony formation which was again compared to the parent molecule germacrone (Figure 3.11 a,d) in MDA-MB-231 cells. The results showed that both the molecules reduced the clonogenic ability of cancer cells in a similar rate. There was a reduction of nearly 35% in the clonogenic formation by the administration of Pt-pyger and germacrone. Then the invasion and migration

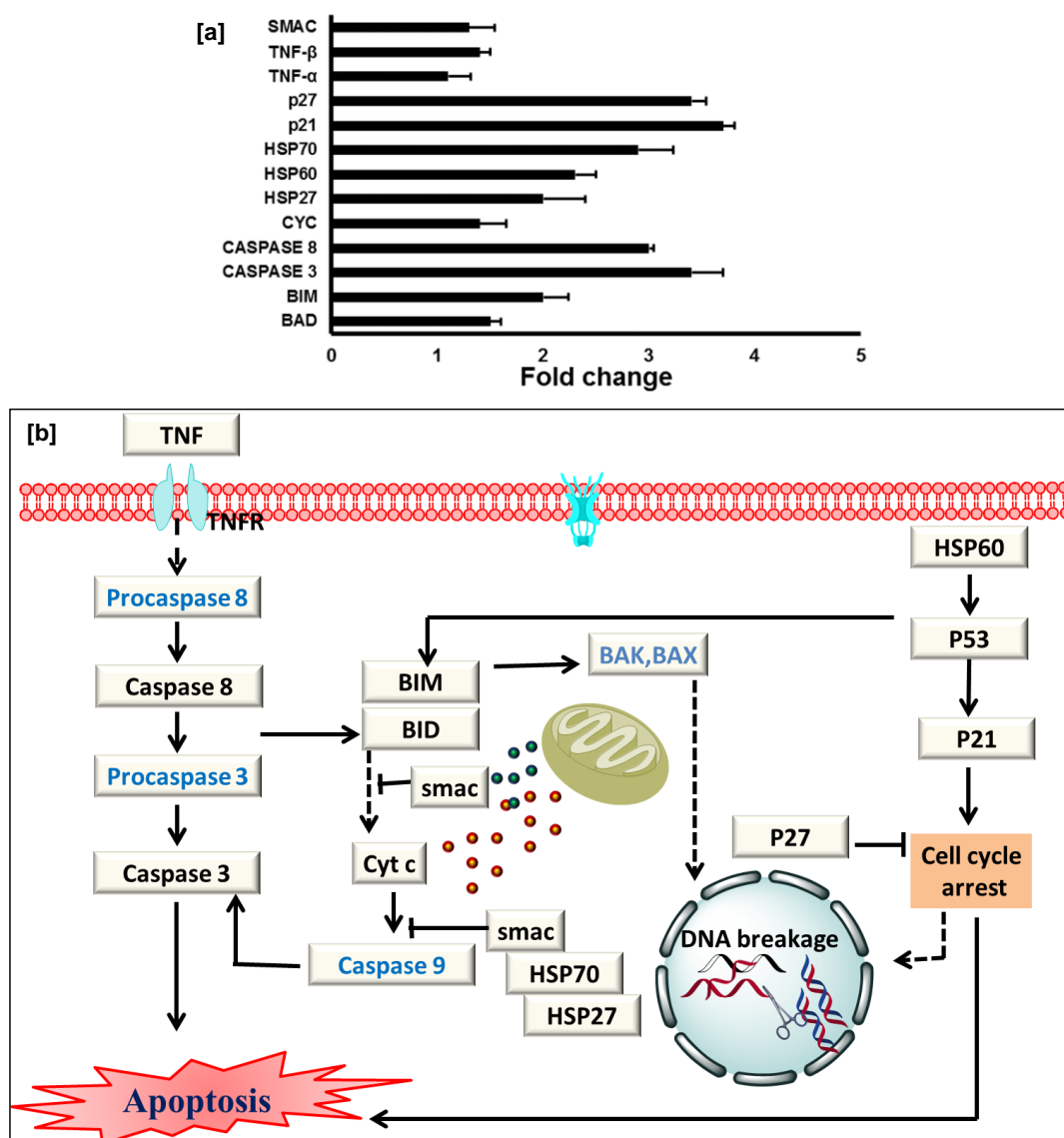


Figure 3.12: [a] Apoptotic protein chip analysis on MDA-MB-231 cells, fold changes of proteins calculated after antibody array of apoptotic proteins treated with Pt-pyger. Calculated from the analysis of densitometric data using Image J software after normalization with the positive control of each array and later normalized with vehicle control and treatments. [b] Pathway deciphering the proposed mechanistic mode of action with Pt-pyger in cancer cells.

capability of the compound treated cells were evaluated using trans well chamber assay. Both the molecules effectively prevented the invasion up to 40% cells (Figure 3.11 b,e). Also, the migration capability of the cancer cells were also retarded in the similar trend (Figure 3.11 c,f). The initial process of metastasis is the migration of cancer cells to an approachable place, which includes both invasion and migration. These cancer cells become immortal, proliferate in a rapid manner, and are aggressive to establish a

favorable microenvironment through metastasis. The parent molecule, germacrone and other sesquiterpene molecules like β -elemene, limonene etc inhibits cancer growth and metastasis via suppressing vascular endothelial growth factor (VEGF)-mediated angiogenesis. It is conclusive that the anti-metastatic property of the synthesized Pt coordinated pyrogermacrone metal complex is mainly attributed by the anti-metastatic potential of germacrone. The enhanced cytotoxicity due to the Pt complexation and the antimetastatic potential make Pt-pyger a potential anticancer agent.

3.2.10 Mechanism of Pt-pyger mediated cell death. The protein-level expression of major components involved in the apoptotic pathways was examined using apoptosis antibody array (Figure 3.12a). Pt-pyger caused elevated expression of major proteins like P27, P21, caspase-8, caspase-3, BIM etc. Mitochondrial proteins like cyt C, smac and other components are being released into the cytoplasm and the higher fold increases of cyt c and caspase 3 expressions facilitated apoptosis. Based on the hierarchical clustering, the molecular mechanism of Pt-pyger action is depicted in the dendrogram (Figure 3.12b)²⁸

3.3 Conclusion

In summary, a semisynthetic approach has been adopted to synthesis metal complexes based on Pt, Ir and Ru on naturally occurring phytomolecule germacrone and its analogue pyrogermacrone. The potent molecule Pt-pyger was selected by extensive *in vitro* cytotoxic assessment of all semi-synthesized metal complexes. Pt-pyger exhibited enhanced cancer-selective cytotoxicity in triple negative breast cancer cells and overcome Pt resistance in ovarian cancer cells. Subsequently, an in-depth *in vitro* analysis of the anticancer properties of the selected Pt-pyger was accomplished. The programmed cell death was monitored under the SERS fingerprint analysis which furnished the biomolecular changes. The Pt-pyger molecule effectively retards the crucial steps of metastatic cascade and colonization of neoplastic cells. The apoptotic antibody array revealed the critical players in the apoptosis process, and the plausible mechanism of programmed cell death was elucidated. The protective effect of the natural product germacrone in the coordination sphere is expected to reduce the overall toxicity exerted by the conventional Pt drugs. Therefore, Pt-pyger has been evolved as a potent anticancer hit based on the detailed *in vitro* assessment which has significant prospect for pre-clinical investigation in the next level.

3.4 Materials and methods

^1H and $^{13}\text{C}\{^1\text{H}\}$ NMR spectra of all products were recorded on 500 MHz and 125 MHz spectrometers respectively (with TMS as an internal standard). Reactions were carried out in anhydrous solvents under a nitrogen atmosphere. Solutions were dried using anhydrous sodium sulfate. Reagents were added to the reaction flask with the help of a syringe. Isolated yields of all the products were reported and yields were not optimized.

3.4.1 Isolation of germacrone: ^1H NMR (500 MHz, CDCl_3) δ 4.98 (d, $J = 15$ Hz, 1H), 4.71 (d, $J = 12.5$ Hz, 1H), 4.12 (dd, $J_1 = 5$ Hz, $J_2 = 15$ Hz, 2H), 3.41 (d, $J = 10$ Hz, 1H), 2.98-2.94 (m, 2H), 2.39-2.33 (m, 1H), 2.18-2.09 (m, 2H), 2.06 (s, 3H), 1.78 (s, 3H), 1.73 (s, 3H), 1.63 (s, 3H). ^{13}C NMR (125 MHz, CDCl_3) δ 207.8, 137.2, 134.9, 132.6, 129.4, 126.6, 125.3, 55.8, 38.0, 29.6, 24.0, 22.3, 19.8, 16.7, 15.5. HRMS (ESI): m/z $[\text{M} + \text{H}]^+$ calcd for $\text{C}_{15}\text{H}_{23}\text{O}$: 219.1749; found 219.1749.

3.4.2 Synthesis of pyrogermacrone: Pyrogermacrone was synthesized by using the standard literature procedures. 20mg of germacrone (0.1 mmol) was taken and dissolved in 2 mL toluene. The mixture was allowed to stir for 12 h at 30 °C. After this period, solvent was evaporated under vacuum. Purification of the resulting crude reaction mixture by column chromatography on silica gel (eluent 5% EtOAc/Hexanes) gave the corresponding product pyrogermacrone. ^1H NMR (500 MHz, CDCl_3) δ 5.80 (dd, $J = 17.4, 10.8$ Hz, 1H), 4.97 (d, $J = 10.7$ Hz, 2H), 4.92 (d, $J = 2.4$ Hz, 1H), 4.77 (s, 1H), 2.64 (dd, $J = 15.6, 4.8$ Hz, 1H), 2.54 (d, $J = 11.7$ Hz, 1H), 2.46 (s, 1H), 2.39 (dd, $J = 11.4, 4.9$ Hz, 1H), 2.29 (d, $J = 15.3$ Hz, 1H), 2.04 (s, 3H), 1.80 (s, 3H), 1.78 (s, 3H), 1.64 (s, 1H), 1.05 (s, 3H). ^{13}C NMR (125 MHz, CDCl_3) δ 202.7, 146.7, 146.4, 144.0, 130.8, 113.0, 111.2, 54.1, 50.6, 41.9, 32.0, 24.7, 23.3, 22.5, 19.1. HRMS (ESI): m/z $[\text{M} + \text{H}]^+$ calcd for $\text{C}_{15}\text{H}_{23}\text{O}$: 219.1749; found 219.1744.

3.4.3 Synthesis of Pt-ger complex: 20mg (0.1 mmol) of germacrone was dissolved in 2mL methanol and to this, Potassium tetrachloroplatinate(II) (41.5 mg, 0.10 mmol) was added. The reaction was allowed to stir for 12h under RT. After the reaction period, solid product was obtained. This was filtered out and washed with hexane to get pure product as brown solid and in 82% yield. ^1H NMR (500 MHz, MeOD) δ 4.01 (d, $J = 15$ Hz, 2H), 3.41 (d, $J = 12.4$ Hz, 2H), 3.12-2.8 (m, 10H), 2.38-2.11 (m, 6H), 2.08 (s, 6H), 1.78-1.60 (m, 17H). ^{13}C NMR (125 MHz, MeOD) δ 203.9, 118.3, 106.9, 90.2, 83.4, 76.1, 71.6,

59.7, 51.6, 42.4, 35.9, 28.9, 25.4, 22.2, 19.2, HRMS (ESI) m/z: [M + H]⁺ calcd for C₃₀H₄₃O₂Pt, 630.2911; found, 630.2914

3.4.4 Synthesis of Pt-pyger complex: 20mg of Pyro-germacrone was dissolved in 2mL methanol and to this, Potassium tetrachloroplatinate(II) (41.5mg, 0.1 mmol) was added. The reaction was allowed to stir for 2h under reflux condition. After the reaction period, solid product was obtained. This was filtered out and washed with hexane to get pure product as brown solid and in 73% yield. ¹H NMR (500 MHz, MeOD) δ 4.19 (t, J = 5.8 Hz, 4H), 3.97 (d, J = 5.9 Hz, 8H), 3.21 (s, 4H), 1.93 (dt, J = 13.0, 6.4 Hz, 6H), 1.68 – 1.57 (m, 4H), 1.36 (dd, J = 14.8, 7.4 Hz, 4H), 1.19 (s, 12H). ¹³C NMR (125 MHz, MeOD) δ 167.9, 130.9, 128.4, 72.3, 71.5, 65.2, 37.7, 31.6, 30.3, 29.3, 29.0, 27.5, 22.3, 18.8, 18.0. HRMS (ESI) m/z: [M + H]⁺ calcd for C₃₀H₄₃O₂Pt, 630.2911; found, 630.2908

3.4.5 Synthesis of Ir-ger complex: The synthesis was started with the preparation of Ir dimer complex, a solution of IrCl₃ · xH₂O (224.36 mg, 0.75 mmol) and 2-phenyl pyridine (350 mg, 1.58 mmol) in 2- methoxy ethanol/H₂O (3:1, v/v%) was refluxed at 90 °C for 24 h, under argon atmosphere. After the reaction the solution was cooled down to room temperature and poured into 50 mL of water. The precipitated yellow solid, was filtered and washed with n-hexane (5 mL x 3) and cold diethyl ether (5mL x 3). The next step was preceded without any further purification. This Ir dimer complex (285 mg, 0.27 mmol) was dissolved in DCM/MeOH (1:1) mixture at 40 °C under argon atmosphere. To this, 1 eq. K₂CO₃ and 60 mg germacrone was added and allowed to stir for 24h. After this period, solvent was evaporated under vacuum. Purification of the resulting crude reaction mixture by column chromatography on silica gel (eluent 10% DCM/MeOH) gave the corresponding product Ir-ger. ¹H NMR (500 MHz, CDCl₃) δ 9.24 (d, J = 5.6 Hz, 1H), 8.86 (d, J = 5.3 Hz, 1H), 7.87 (s, 1H), 7.82 – 7.68 (m, 2H), 7.50 (dd, J = 12.3, 7.9 Hz, 1H), 6.76 (dt, J = 20.4, 7.3 Hz, 2H), 6.59 (dt, J = 31.9, 7.4 Hz, 1H), 6.09 (d, J = 7.7 Hz, 1H), 5.93 (d, J = 7.8 Hz, 1H), 5.58 – 5.27 (m, 5H), 4.93 – 4.81 (m, 1H), 3.69 – 3.54 (m, 2H), 2.33 – 2.24 (m, 6H), 2.20 (s, 3H), 2.08 – 1.92 (m, 6H), 1.52 (s, 2H). ¹³C NMR (125 MHz, CDCl₃) δ 167.7, 149.1, 137.1, 135.8, 133.4, 132.8, 132.6, 129.1, 129.1, 124.3, 124.0, 121.8, 121.0, 118.4, 110.5, 73.7, 40.6, 36.7, 35.2, 34.6, 33.6, 32.0, 31.9, 31.8, 31.7, 27.3, 27.3, 27.2, 25.7, 25.3, 25.1, 24.9, 24.9, 22.6, 14.1, 14.0. HRMS (ESI) m/z: [M + H]⁺ calcd for C₃₇H₃₈IrN₂O, 719.2608; found, 719.2612

3.4.6 Synthesis of Ir-pyger complex: The Ir dimer complex (285 mg, 0.27 mmol) was dissolved in DCM/MeOH (1:1) mixture at 40 °C under argon atmosphere. To this, 1 eq. K_2CO_3 and 60 mg germacrone was added and allowed to stir for 12h. After this period, solvent was evaporated under vacuum. Purification of the resulting crude reaction mixture by column chromatography on silica gel (eluent 10% DCM/MeOH) gave the corresponding product Ir-Pyger. 1H NMR (500 MHz, $CDCl_3$) δ 8.97 (d, $J = 5.0$ Hz, 1H), 7.83 (s, 1H), 7.64 (s, 1H), 7.45 (s, 1H), 7.34 (s, 1H), 6.74 (dt, $J = 69.9, 7.0$ Hz, 2H), 6.01 (d, $J = 7.3$ Hz, 1H), 5.22 (s, 1H), 4.91 (d, $J = 12.0$ Hz, 1H), 4.64 (d, $J = 10.6$ Hz, 1H), 4.23 (t, $J = 5.9$ Hz, 2H), 4.02 (d, $J = 6.3$ Hz, 1H), 3.34 (d, $J = 10.5$ Hz, 1H), 2.83 (dd, $J = 46.9, 12.1$ Hz, 3H), 2.23 (s, 2H), 2.13 – 1.85 (m, 6H), 1.70 (s, 3H), 1.65 (s, 4H), 1.56 (s, 3H), 1.36 (s, 2H). ^{13}C NMR (125 MHz, $CDCl_3$) δ 206.9, 166.7, 166.0, 150.0, 142.9, 142.7, 137.2, 136.2, 134.0, 131.6, 130.2, 129.9, 128.8, 127.8, 124.3, 122.9, 121.5, 118.1, 70.7, 64.5, 54.8, 52.4, 37.0, 30.9, 29.5, 28.6, 28.3, 28.2, 26.7, 23.0, 21.6, 21.3, 18.8, 18.1, 14.5. HRMS (ESI) m/z : $[M + H]^+$ calcd for $C_{37}H_{38}IrN_2O$, 719.2608; found, 719.2602

3.4.7 Synthesis of Ru-ger complex: 20mg (0.1 mmol) of germacrone was dissolved in 2mL methanol and to this, 50 mg (0.1 mmol) $[Ru(\text{benzene})Cl_2]_2$ was added. The reaction was allowed to stir for 24h under RT. After the reaction period, solid product was obtained. This was filtered out and washed with hexane to get pure product as brown solid and in 79% yield. 1H NMR (500 MHz, $CDCl_3$) δ 7.65 (s, 1H), 7.46 (s, 1H), 7.19 (s, 1H), 4.11 (d, $J = 15$ Hz, 2H) 3.52 (d, $J = 12.4$ Hz, 2H) 3.12-2.70 (m, 4H), 2.38-2.11 (m, 6H), 2.06 (s, 6H), 1.75-1.62 (m, 6H). ^{13}C NMR (125 MHz, $CDCl_3$) δ 166.6, 131.3, 130.1, 128.0, 127.9, 71.8, 71.1, 64.5, 35.2, 31.3, 26.7, 28.7, 28.4, 27.5, 26.0, 20.6, 18.7, 18.4, 16.3. HRMS (ESI) m/z : $[M + H]^+$ calcd for $C_{22}H_{31}ClORu$, 448.1107; found, 448.1112

3.4.8 Synthesis of Ru-Pyger complex: 20mg (0.1 mmol) of germacrone was dissolved in 2mL methanol and to this, 50 mg (0.1 mmol) $[Ru(\text{benzene})Cl_2]_2$ was added. The reaction was allowed to stir for 12h under RT. After the reaction period, solid product was obtained. This was filtered out and washed with hexane to get pure product as brown solid and in 73% yield. 1H NMR (500 MHz, $CDCl_3$) δ 7.65 (s, 1H), 7.46 (s, 1H), 7.19 (s, 1H), 4.24 (t, $J = 6.3$ Hz, 3H), 4.02 (d, $J = 6.2$ Hz, 2H), 1.97 (dd, $J = 12.9, 6.4$ Hz, 1H), 1.64 (dd, $J = 14.2, 7.1$ Hz, 4H), 1.53 (s, 6H), 1.37 (dd, $J = 15.1, 7.5$ Hz, 4H), 1.19 (s, 6H). ^{13}C NMR (125 MHz, $CDCl_3$) δ 166.7, 131.3, 129.8, 127.8, 127.6, 71.3, 70.7, 64.5, 37.0,

30.9, 29.5, 28.6, 28.6, 28.3, 26.7, 21.6, 18.7, 18.1, 18.1, 17.6. HRMS (ESI) m/z: [M + H]⁺ calcd for C₂₂H₃₁ClORu, 448.1107; found, 448.1109

3.4.9 DFT calculation: Energy minimized structures were optimized by using B3LYP level of DFT (6-31+G* basis set used for C, H, O, N and ECP for transition metal).

3.4.10 Cytotoxicity evaluation: The growth inhibition capacity of the synthesised metal complexes, germacrone and oxaliplatin were evaluated against MDA-MB-231 cells using well known MTT assay as previously discussed. Cell viability was assessed by the absorbance reading at 570nm due to the cleavage of tetrazolium salt by mitochondrial dehydrogenase.

3.4.11 ICPMS analysis: The compounds (5µM) treated cells were resuspended in 2 mL 1% HNO₃ and vortexed for 20 min before analysis. ICPMS measurements were performed on a Elan-DRC II, Perkin-Elmer Sciex spectrometer. The platinum concentration was calculated according to a known concentration of a K₂PtCl₄ standard solution (10 ng/mL Pt).

3.4.12 Apoptosis studies: Adherent cancer cells were grown overnight with 10% DMEM on 24-well culture plates for a period of 24 h. Acridine orange-ethidium bromide dual staining is the most commonly used method to detect apoptosis and is based on the differential uptake of two fluorescent DNA binding dyes by viable and nonviable cells, respectively. Assessment of apoptosis using the acridine orange-ethidium bromide dual staining procedure was performed as described earlier. The cells were observed under an inverted fluorescent microscope, using a FITC filter (Olympus 1X51, Singapore) to view the apoptotic or non-apoptotic cells. Early onset of programmed cell death was further observed using APOPercentage dye (Biocolor, Belfast, Northern Ireland) as per manufacturer's instructions as previously described. Light microscopic images of APOPercentage dye-labeled cells, which stained pink under a light microscope, were used to quantify the extent of apoptosis. Annexin V/FITC and TUNEL assays were carried out as previously discussed.

3.4.13 Anti-metastatic assays

3.4.13.1 Cologenic assay: Cancer cells (1000 cells/mL) were seeded onto a 6 well cell culture plate and subjected to treatments. The medium was removed and the cells were

kept in fresh medium for 9 days or till the control cells achieved 50 cells per colony. The medium was removed, fixed in 70% ethanol and stained using 1% crystal violet in ethanol. The plate was air dried and the colonies were counted and photographed. Colonies were counted manually and plotted as a percent clonogenicity. Control cells were considered as 100 %.

3.4.13.2 Invasion and migration assay: The invasive and migration potential of cancer cells in presence of compounds was carried out using 24 well plate transwell inserts (353097, Corning Falcon, USA). For the invasion assay, the 24 well transwell chambers (8 μ m pore size polycarbonate filters) were applied with matrigel (354234, Corning Falcon, USA) on the innerside and kept at 37°C in 5% CO₂ incubator. Cancer cells were seeded (1×10^6 cells/mL) in serum free medium onto the transwell chambers with or without compounds (0.5 μ M). DMEM medium with 10% serum was added onto the 24 well plates which served as the chemo-attractant. The plates were kept at 37°C in 5% CO₂ incubator for 24 hour incubation. The transwell inserts were then taken and cells present in the upper chamber were removed using cotton swab and filters were stained using 1% crystal violet. The invaded cells present at the lower side of the inserts were visualized, counted and photographed using an optical microscope. Similarly, the migration assay was carried out using the above protocol except that the transwell inserts were devoid of matrigel coating.

3.4.14 Live cell Raman imaging. Evaluation of the internalization and apoptosis was done with the aid of a confocal Raman microscope (WI-Tec, Inc., Germany) with a laser beam directed to the cell surface through a 20X objective with a Peltier-cooled CCD detector. 5 μ M of Pt-pyger were added to WI-38 and MDA-MB-231 cells followed by incubation at 37 °C for 1 h. 2D SERS mapping was recorded as described before.

3.4.15 Apoptosis antibody array. Semi quantitative analysis of 43 human apoptosis markers were performed using human apoptosis antibody array membrane (ab134001, Abcam, Cambridge, MA) according to the manufacturer's instructions.³⁰ Cancer cells were treated with Pt-pyger (5 μ M) for 12 h while maintaining control cells without treatment and the experiments were performed as per kit instructions.. Signals were quantified by a chemiluminescence system (Bio-Rad, CA, USA) immediately after the addition of detection buffers with an exposure time limited within 30 seconds. Densitometry data of the membrane was analysed using Image J software (version 1.48,

NIH, USA). For each array membrane, density of each spot was normalized with respect to its own positive controls and later each treatment was compared with respect to the vehicle control membrane. The fold change was calculated using the intensity value. Proteins that are 2-fold and above, which are differentially expressed with a p value of <0.05 (using Student's t-test), were subjected to unsupervised hierarchical clustering using cluster map function available in seaborn library of an object-oriented programming language, python.

3.5 References

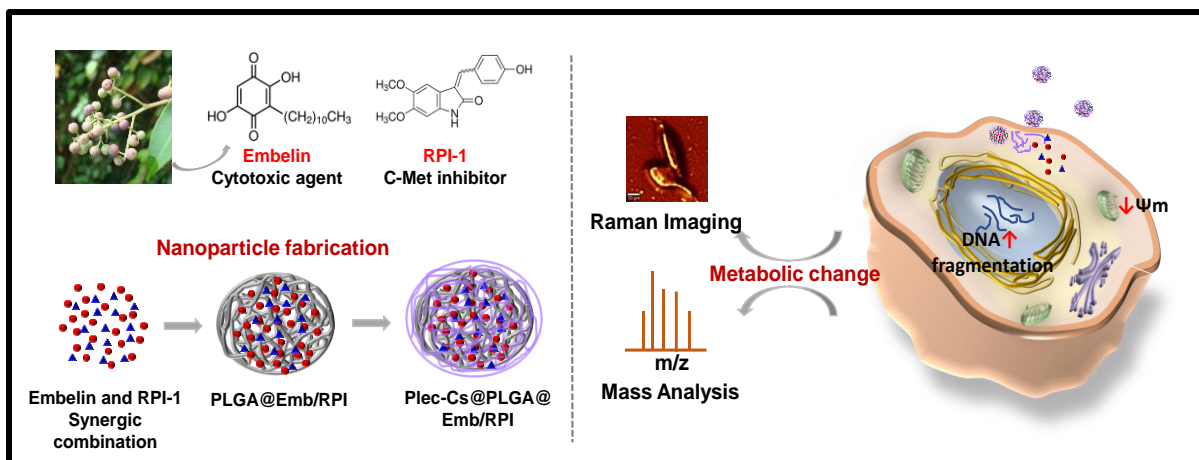
- (1) Schlotter, C. M.; Vogt, U.; Allgayer, H.; Brandt, B. Molecular Targeted Therapies for Breast Cancer Treatment. *Breast Cancer Res.* **2008**, *10* (4). <https://doi.org/10.1186/bcr2112>.
- (2) Jin, J.; Zhang, W.; Ji, W.; Yang, F.; Guan, X. Predictive Biomarkers for Triple Negative Breast Cancer Treated with Platinum-Based Chemotherapy. *Cancer Biol. Ther.* **2017**, *18* (6), 369–378. <https://doi.org/10.1080/15384047.2017.1323582>.
- (3) Guan, X.; Ma, F.; Fan, Y.; Zhu, W.; Hong, R.; Xu, B. Platinum-Based Chemotherapy in Triple-Negative Breast Cancer: A Systematic Review and Meta-Analysis of Randomized-Controlled Trials. *Anticancer. Drugs* **2015**, *26* (8), 894–901. <https://doi.org/10.1097/CAD.000000000000260>.
- (4) Ludwig, T.; Riethmüller, C.; Gekle, M.; Schwerdt, G.; Oberleithner, H. Nephrotoxicity of Platinum Complexes Is Related to Basolateral Organic Cation Transport. *Kidney Int.* **2004**, *66* (1), 196–202. <https://doi.org/10.1111/j.1523-1755.2004.00720.x>.
- (5) Tiong, H. Y.; Huang, P.; Xiong, S.; Li, Y.; Vathsala, A.; Zink, D. Drug-Induced Nephrotoxicity: Clinical Impact and Preclinical in Vitro Models. *Mol. Pharm.* **2014**, *11* (7), 1933–1948. <https://doi.org/10.1021/mp400720w>.
- (6) Yamagishi, Y.; Watari, A.; Hayata, Y.; Li, X.; Kondoh, M.; Yoshioka, Y.; Tsutsumi, Y.; Yagi, K. Acute and Chronic Nephrotoxicity of Platinum Nanoparticles in Mice. *Nanoscale Res. Lett.* **2013**, *8* (1), 1–7. <https://doi.org/10.1186/1556-276X-8-395>.
- (7) Cassidy, J.; Misset, J.-L. Oxaliplatin-Related Side Effects: Characteristics and

-
- Management. *Semin. Oncol.* **2002**, *29* (5 Suppl 15), 11–20.
<https://doi.org/10.1053/sonc.2002.35524>.
- (8) Fantini, M.; Santelmo, C.; Drudi, F.; Ridolfi, C.; Barzotti, E.; Gianni, L.; Arcangeli, V.; Affatato, A.; Ravaoli, A. Triple Negative Breast Cancer Treatment: Use of Platinum and Platinum Analogs. *J. Cancer Ther.* **2012**, *03* (05), 777–781.
<https://doi.org/10.4236/jct.2012.325097>.
- (9) Gordon M. Cragg, David J. Newman, and K. M. S. Natural Products in Drug Discovery and Development. *J. Nat. Prod.* **1997**, *60* (1), 52–60.
<https://doi.org/10.1021/np9604893>.
- (10) Cragg, G. M.; Newman, D. J. Natural Products: A Continuing Source of Novel. *Biochim Biophys Acta* **2013**, *1830* (6), 3670–3695.
<https://doi.org/10.1016/j.bbagen.2013.02.008>.NATURAL.
- (11) Ojha, S.; Venkataraman, B.; Kurdi, A.; Mahgoub, E.; Sadek, B.; Rajesh, M. Plant-Derived Agents for Counteracting Cisplatin-Induced Nephrotoxicity. *Oxid. Med. Cell. Longev.* **2016**, *2016*. <https://doi.org/10.1155/2016/4320374>.
- (12) Kuhad, A.; Pilkhwal, S.; Sharma, S.; Tirkey, N.; Chopra, K. Effect of Curcumin on Inflammation and Oxidative Stress in Cisplatin-Induced Experimental Nephrotoxicity. *J. Agric. Food Chem.* **2007**, *55* (25), 10150–10155.
<https://doi.org/10.1021/jf0723965>.
- (13) Fang, X.; Tan, T. F.; Gao, B. B.; Zhao, Y. L.; Liu, T. T.; Xia, Q. Germacrone Regulates HBXIP-Mediated Cell Cycle, Apoptosis and Promotes the Formation of Autophagosomes to Inhibit the Proliferation of Gastric Cancer Cells. *Front. Oncol.* **2020**, *10* (November), 1–13. <https://doi.org/10.3389/fonc.2020.537322>.
- (14) Yu, Z.; Xu, J.; Shao, M.; Zou, J. Germacrone Induces Apoptosis as Well as Protective Autophagy in Human Prostate Cancer Cells. *Cancer Manag. Res.* **2020**, *12*, 4009–4016. <https://doi.org/10.2147/CMAR.S250522>.
- (15) Lim, M. S.; Choung, S. Y.; Jeong, K. W. Germacrone Inhibits Estrogen Receptor α -Mediated Transcription in MCF-7 Breast Cancer Cells. *Phyther. Res.* **2016**, *30* (12), 2036–2043. <https://doi.org/10.1002/ptr.5711>.
-

-
- (16) Pan, J.; Miao, D.; Chen, L. Germacrone Reverses Adriamycin Resistance in Human Chronic Myelogenous Leukemia K562/ADM Cells by Suppressing MDR1 Gene/P-Glycoprotein Expression. *Chem. Biol. Interact.* **2018**, *288*, 32–37. <https://doi.org/10.1016/j.cbi.2018.04.012>.
- (17) Xie, X. H.; Zhao, H.; Hu, Y. Y.; Gu, X. D. Germacrone Reverses Adriamycin Resistance through Cell Apoptosis in Multidrug-Resistant Breast Cancer Cells. *Exp. Ther. Med.* **2014**, *8* (5), 1611–1615. <https://doi.org/10.3892/etm.2014.1932>.
- (18) Soodvilai, S.; Meetam, P.; Siangjong, L.; Chokchaisiri, R.; Suksamrarn, A.; Soodvilai, S. Germacrone Reduces Cisplatin-Induced Toxicity of Renal Proximal Tubular Cells via Inhibition of Organic Cation Transporter. *Biol. Pharm. Bull.* **2020**, *43* (11), 1693–1698. <https://doi.org/10.1248/bpb.b20-00392>.
- (19) Ken'ichi Takeda, Isao Horibe, and H. M. Cope Rearrangement of Some Germacrane-Type Furan Sesquiterpenes. Part IV Preparation of Some Cyclodeca-Cis,Trans-Diene Derivatives and Their Cope Rearrangements. *J. C. S. Perkin I* **1973**, *201*, 2212–2220.
- (20) Setzer, W. N. Ab Initio Analysis of the Cope Rearrangement of Germacrane Sesquiterpenoids. *J. Mol. Model.* **2008**, *14* (5), 335–342. <https://doi.org/10.1007/s00894-008-0274-3>.
- (21) Shul'pin, A. E. S. and G. B. Activation of C–H Bonds by Metal Complexes Alexander. *Chem. Rev.* **1997**, *97*, 2879–2932. [https://doi.org/10.1016/S1364-8152\(03\)00005-7](https://doi.org/10.1016/S1364-8152(03)00005-7).
- (22) Mukkatt, I.; Nirmala, A.; Madhavan, N. D.; Shankar, S.; Deb, B.; Ajayaghosh, A. Ligand-Controlled Electrochromic Diversification with Multilayer Coated Metallosupramolecular Polymer Assemblies. *ACS Appl. Mater. Interfaces* **2021**, *13* (4), 5245–5255. <https://doi.org/10.1021/acsami.0c20428>.
- (23) Kandemir, F. M.; Yildirim, S.; Caglayan, C.; Kucukler, S.; Eser, G. Protective Effects of Zingerone on Cisplatin-Induced Nephrotoxicity in Female Rats. *Environ. Sci. Pollut. Res.* **2019**, *26* (22), 22562–22574. <https://doi.org/10.1007/s11356-019-05505-3>.
- (24) Lesgards, J. F.; Baldovini, N.; Vidal, N.; Pietri, S. Anticancer Activities of
-

-
- Essential Oils Constituents and Synergy with Conventional Therapies: A Review. *Phyther. Res.* **2014**, *28* (10), 1423–1446. <https://doi.org/10.1002/ptr.5165>.
- (25) Zeng, X.; Wang, Y.; Han, J.; Sun, W.; Butt, H. J.; Liang, X. J.; Wu, S. Fighting against Drug-Resistant Tumors Using a Dual-Responsive Pt(IV)/Ru(II) Bimetallic Polymer. *Adv. Mater.* **2020**, *32* (43), 1–9. <https://doi.org/10.1002/adma.202004766>.
- (26) Kambere Amerigos Daddy, J. C.; Chen, M.; Raza, F.; Xiao, Y.; Su, Z.; Ping, Q. Co-Encapsulation of Mitoxantrone and β -Elemene in Solid Lipid Nanoparticles to Overcome Multidrug Resistance in Leukemia. *Pharmaceutics* **2020**, *12* (2), 1–19. <https://doi.org/10.3390/pharmaceutics12020191>.
- (27) Shin, H. J.; Lee, J. H.; Kim, Y. D.; Shin, I.; Sim, T.; Lim, D. K. Raman-Based in Situ Monitoring of Changes in Molecular Signatures during Mitochondrially Mediated Apoptosis. *ACS Omega* **2019**, *4* (5), 8188–8195. <https://doi.org/10.1021/acsomega.9b00629>.
- (28) Jayadev S. Arya, Manu M. Joseph, Daisy R. Sherin, Jyothi B. Nair, Thanathu K. Manojkumar, and K. K. M. Exploring Mitochondria-Mediated Intrinsic Apoptosis by New Phytochemical Entities: An Explicit Observation of Cytochrome c Dynamics on Lung and Melanoma Cancer Cells. *J. Med. Chem.* **2019**, *62*, 8311–8329. <https://doi.org/10.1021/acs.jmedchem.9b01098>.
- (29) Palasseri T. Sujai, Shanmughan Shamjith, Manu M. Joseph, and K. K. M. Elucidating Gold–MnO₂ Core–Shell Nanoenvelope for Real Time SERS-Guided Photothermal Therapy on Pancreatic Cancer Cells. *ACS Appl. Bio Mater.* **2021**, *4*, 4962–4972.
- (30) Wu, D.; Wang, Y.; Wang, L.; Chen, C. Y.; Lee, H. A Low MicroRNA-630 Expression Confers Resistance to Tyrosine Kinase Inhibitors in EGFR-Mutated Lung Adenocarcinomas via MiR-630 / YAP1 / ERK Feedback Loop. *Theranostics* **2018**, *8* (5), 1256–1269. <https://doi.org/10.7150/thno.22048>.
-

Biocompatible Polymer Based Targeted Nano-Delivery System for the Combination Chemotherapy of Embelin and RPI-1 against Pancreatic cancer cells



Abstract: Pancreatic cancer (PC) develops due to the uncontrolled cell growth in a part of the pancreas which is a notorious variant of human cancer with very low prognosis. Systemic chemotherapy remains the vital treatment modality for the patient survival. Herein, we have ventured a synergic combination of two agents embelin and RPI-1, loaded in a biocompatible PLGA-chitosan nano-delivery system in PC cells. Embelin is a naturally occurring molecule isolated from the seeds of *Embelia ribes*, which is reported for its anticancer effect mediated through NF- κ B pathway. RPI-1 is a c-MET inhibitor where c-MET is a protein encoded by MET gene, a potential PC biomarker. The synergic combination of embelin and RPI obtained from a series of cytotoxicity assessment and further analysis using compusyn software revealed 1: 4.7 ratio between embelin and RPI-1. The optimized drug combination was loaded in a biocompatible and biodegradable PLGA based nanocarrier system coated with a peptide functionalized chitosan for effective therapeutic utility. The conjugation of plectin-1 (surface biomarker overexpressed in PC) targeting peptide-substrate increased specific binding affinity and internalization to the PANC-1 cells. The as fabricated nano-construct displayed enhanced anticancer and antimetastatic properties in PANC-1 cell line. Finally, detailed in vitro

metabolic changes associated with the action of the nano-construct was scrutinized by SERS spectral analysis and LC-MS analysis.

4.1 Introduction

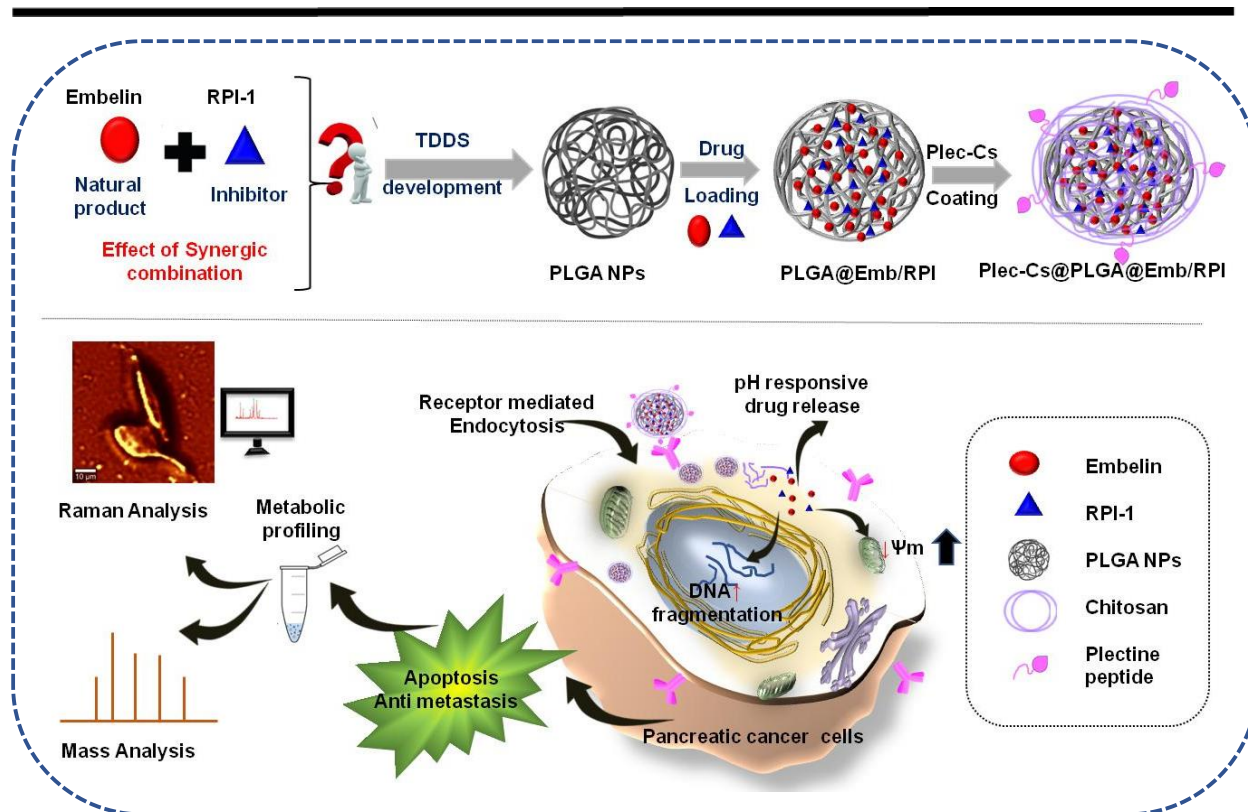
Pancreatic cancer (PC) is projected to be the second leading cause of cancer-related death by 2030 in the United States based on its annual percentage increase in incidence and death rates. PC was metastasized in 52% of patients during diagnosis, among whom the 5-year survival rate is only 3%. In India, pancreas ranks 18th in mortality and it is hypothesized that due to the changing lifestyle, in India, the rates of PC will increase in the near future.¹⁻³ Despite improvement in cancer treatment, metastatic PC remains a major challenge to increase the survival rate. Chemotherapy is still one of the most common and effective treatment strategies, especially for patients with metastatic PC. The failure of clinical treatment in patients with PC is often due to the heterogeneous nature of the disease. Combination chemotherapy of FOLFIRINOX and gemcitabine is more effective than the use of gemcitabine alone.^{4,5} Albumin-bound paclitaxel (nab paclitaxel), which was approved by the FDA in 2013, can also be used in conjunction with gemcitabine to treat PC. However, in most patients with advanced stages of the disease, these treatments prolong survival only for few months, while combination therapy can also lead to significantly increased toxicity.⁶ The development of effective PC treatments is urgently needed to overcome these obstacles. In the last 15 years, there has been a paradigm shift in the treatment of solid tumors from traditional cytotoxic chemotherapies to more targeted therapies. Within the last decade, numerous targeted agents have been examined individually or in combination with cytotoxic agents for the treatment of PC.^{6,7} Poly(lactic-co-glycolic acid) (PLGA) is an FDA approved, most widely used biocompatible polymers for preparing polymeric nanoparticles (NPs) in drug delivery system, which is reported to benefit the NPs–cell interaction and enhance the cellular uptake efficiency.⁸

c-Met, a member of the receptor tyrosine kinase family, has been identified as a proto-oncogene and is expressed in both normal and malignant cells. Met tyrosine kinase represents the high-affinity receptor for hepatocyte growth factor (HGF), which is expressed predominantly in epithelial and endothelial cells. The HGF/Met-mediated signaling is involved in physiologic processes, such as epithelial cell dissociation (scattering), invasion, branching

morphogenesis, and angiogenesis. The mechanisms by which c-Met becomes activated in human cancers include overexpression, activating mutations of pathway components, or HGF-dependent autocrine/paracrine activation.⁹⁻¹¹ Increased levels of c-Met have been linked to human pancreatic carcinoma. c-Met signaling has been reported to stimulate growth and invasion of PC cells. Recent reports have identified c-Met as a novel biomarker for PC therapy.¹² RPI-1 is a small molecular inhibitor of c-Met and retards the spontaneous metastasis spreading. Effective delivery of RPI-1 in combination with a promising cytotoxic agent in their synergic combination would help in enhancing the therapeutic efficacy.^{11,13}

Nature always remains an abundant source of bio-active and diverse chemo types, while relatively few of the actual isolated natural products turned into clinically active drugs.¹⁴⁻¹⁶ Embelin (Emb) is a naturally occurring alkyl substituted hydroxyl benzoquinone compound which is a major constituent of *Embelia ribes* Burm. It exhibits various biological effects including antidiabetic, anti-inflammatory, and hepato-protective activities. Embelin also shows antitumor activity in various types of cancers via inhibiting the activity of X-linked inhibitor of apoptosis protein (XIAP). XIAP is overexpressed in various types of cancer cells, particularly drug-resistant cancer cells and inhibition of XIAP has been employed as a new strategy for the treatment of cancers.¹⁷⁻²⁰ Embelin was chosen as the cytotoxic agent to deliver into the PC site in combination with RPI-1 due to its promising anticancer effects.

In view of the present exigency for the development of an efficient targeted nano-delivery vector towards PC, a dual drug encapsulated polymeric nanoparticle has been constructed in a synergic fashion. For the nanoparticle synthesis, PLGA is chosen as the biocompatible polymer, that degrades by hydrolysis into the monomers lactic acid and glycolic acid, which are easily metabolized by the Krebs cycle.²¹ Functionalization of nano-carriers with a targeting ligand facilitate the recognition of the extracellular complementary receptors which enable selective delivery of therapeutic payload to the intracellular milieu. Plectin-1 is a high molecular weight protein overexpressed in PC cell surface which is involved with an important function in tumor pathogenesis.^{22,23} A plectin-1 targeting small peptide sequence KTLTP was conjugated into the amine terminal of chitosan and coated over the PLGA NPs which is loaded with both embelin and RPI-1 (Scheme 4.1).



Scheme 4.1: Schematic representation of the fabrication of PC-targeting nano delivery system and its mechanistic evaluation

4.2 Results and Discussion

4.2.1 Plant material collection and extraction: Seeds of *Embelia ribes* were collected from Jawaharlal Nehru Tropical Botanical Garden and Research Institute (JNTBGRI), Thiruvananthapuram, medicinal plant garden in February 2017. The seeds were thoroughly cleaned and dried in air oven maintained at room temperature. It was then thoroughly powdered and weighed approximately 250 g. The powdered material was first extracted using hexane two times at room temperature. Then it was extracted using acetone and finally using ethanol (three times) at room temperature. The total extracts were concentrated under reduced pressure using Buchii rotary evaporator. This yielded about 7g of the crude hexane extract, 21g of acetone extract and 27g of ethanol extract.

4.2.2 Isolation and characterization of embelin: The hexane extract was subjected to further isolation using column chromatography. About 4g of the hexane extract was subjected to column chromatography. The hexane extract (4g) was dissolved in minimum quantity of

hexane and mixed until the extract was dissolved. It was then loaded onto the column having column capacity of 5g as liquid application of the sample. The column was kept undisturbed for 30 minutes for the extract to get adsorbed over the silica gel. The applied sample was eluted by a mixture of solvents. At first the elution was started with pure hexane and then the polarity was increased by increasing the volume of ethyl acetate in hexane-ethyl acetate mixture. Finally, the column was eluted using 100% ethyl acetate and there after washed the column with 10% ethyl acetate in methanol mixture. Different fractions of about 100 ml were collected in conical flasks. A total of 54 fractions were collected. Based on the TLC of each fraction and similarities in the TLC they were pooled into nine (A-I) fraction pools. Each of the fraction pools were concentrated under reduced pressure using Buchii rotary evaporator and vacuum pump. Fractions 19-24 eluted at 6% hexane from the main column showed a single spot in TLC after staining with iodine. The compound was isolated and concentrated which yielded around 32mg of orange crystals. The compound was characterized as Embelin using different spectroscopic techniques like IR, $^1\text{H-NMR}$, $^{13}\text{C NMR}$ and HR-MS.

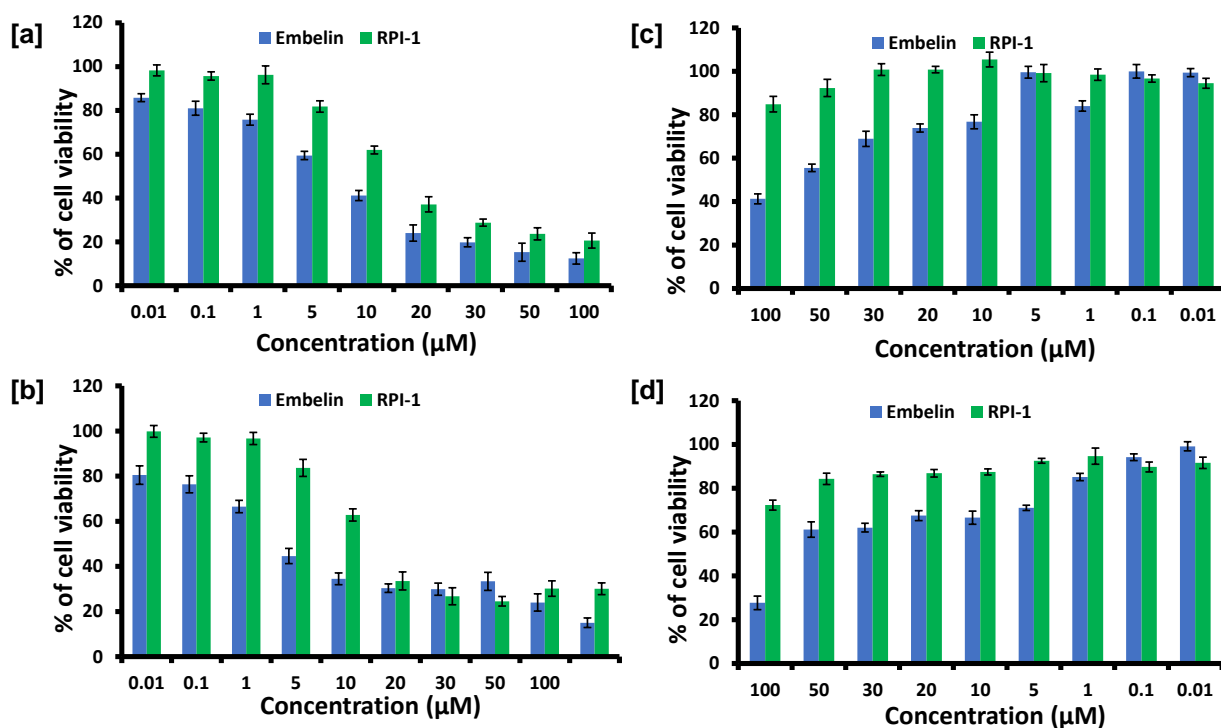


Figure 4.1: Cytotoxic evaluation of Embelin and RPI-1 in PANC-1 cells at [a] 24 h [b] 48 h and in WI-38 cells at [c] 24 h and [d] 48 h.

4.2.3 Cytotoxicity profiling of Embelin and RPI-1. Cytotoxicity evaluation was carried out in human PC cell PANC-1 and normal lung fibroblast cell WI-38. Cytotoxicity of these two compounds were evaluated using 3-[4,5-dimethylthiazol-2-yl]-2,5-diphenyltetrazolium (MTT) assay. In PANC-1 cells, the Emb treatment produced IC_{50} values of 7.7 and 3.8 μ M at 24 and 48h, respectively, whereas RPI-1 showed 17.5 and 17.1 μ M, respectively (Figure 4.1). In WI-38 cells, Emb showed IC_{50} values at much higher concentrations, 87.0 and 83.0 μ M at 24 and 48h, respectively. RPI-1 remained non-toxic to normal fibroblast cells. Emb was observed to be a better cytotoxic agent compared to RPI-1. The less toxic nature of the compounds in WI-38 indicates the possibility as a combination chemotherapy which will be safe to administer for in-vivo experiments as well. The usage of these drugs in combination will spot multiple targets simultaneously.^{24,25}

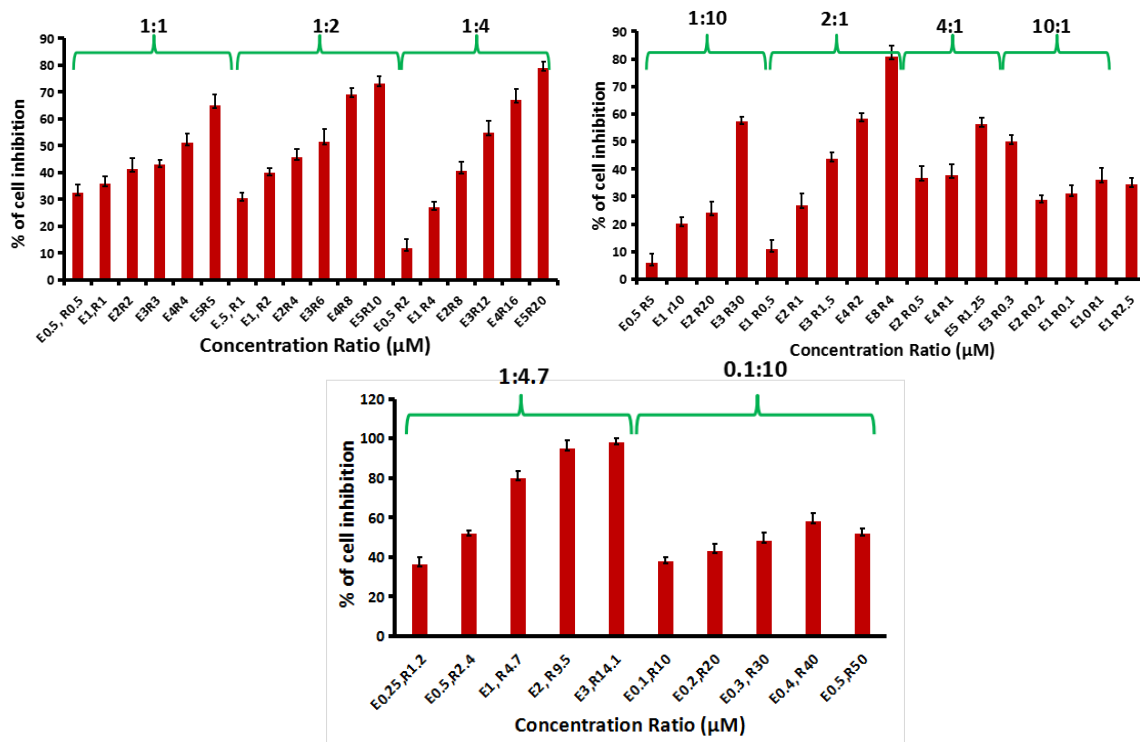


Figure 4.2: Screening various combination of embelin and RPI-1 in different concentrations

4.2.4 Establishment of the synergic combination of Embelin and RPI-1 using the combination index method. The cytotoxicity pattern prompted us to study the synergic combination of Emb and RPI-1, to eradicate PC. An optimal ratio of both the drugs has been used to take full advantage of the therapeutic effects on PC cells with minimal damage on

normal cells. Detailed cytotoxicity analysis was carried out with varying ratios of the compounds on PANC-1 cells. Synergistic effects of Emb and RPI-1 at different fixed combined concentrations and specific ratios were evaluated. We tested the drugs in different concentrations of Emb to RPI-1 ratios like 1:1, 1:2, 1:4, 1:4.7, 1:10, 2:1, 4:1, 10:1, etc., ranging from the combined concentration of 1 μ M to 50 μ M. Concentrations below and above the IC_{50} values were taken for finding the synergic combination (Figure 4.2). The minimum concentration of Emb and RPI used in combination ratios was 0.5 μ M, which is much lower than the respective IC_{50} values. Also, the higher concentration of Emb taken was 10 μ M, and that of RPI-1 was 30 μ M, which is significantly higher than the respective IC_{50} values of the compounds at 48h. The inhibition values obtained from the MTT assay were used for the finding combination-index (CI) using Compusyn software. Strong synergism was revealed from the CI value < 0.5 in higher growth inhibition values of drug combination ratios 1:2, 1:4, and 1:4.7. These ratios were selected and further verified their dose-effect by repeating the cytotoxicity assay using the predicted concentrations in PANC-1 and WI-38 cells (Figure 4.3). The results indicated the synergic effect of the combinations in much lower concentrations. The optimized ratio of 1:4.7 was selected to produce minimum toxic effects on WI-38 cells and enhanced toxicity towards PANC-1 cells. This ratio of 1:4.7 can be correlated to the ratio of the corresponding IC_{50} values produced by the compounds in PANC-1 cells. Administration of Emb alone in PANC-1 cells caused 50% growth inhibition at 3.8 μ M, and RPI-1 could pay the same at 17.1 μ M. Here, from the synergy results, we could formulate a combined lower concentration in the ratio 1:4.7. The dose-reduction index (DRI) value indicates how much fold of dose reduction is allowed for each drug due to synergism compared to the individual dose. DRI helps in reducing the quantity of drugs while maintaining efficacy.^{26,27} We have obtained $DRI > 1$ for both Emb and RPI-1 at higher inhibitory effects, which is beneficial for clinical use. Based on these results, we chose the combination ratio of Emb to RPI as 1:4.7 to fabricate dual targeted polymer based biocompatible nano-construct for attaining promising therapeutic efficacy towards PC.

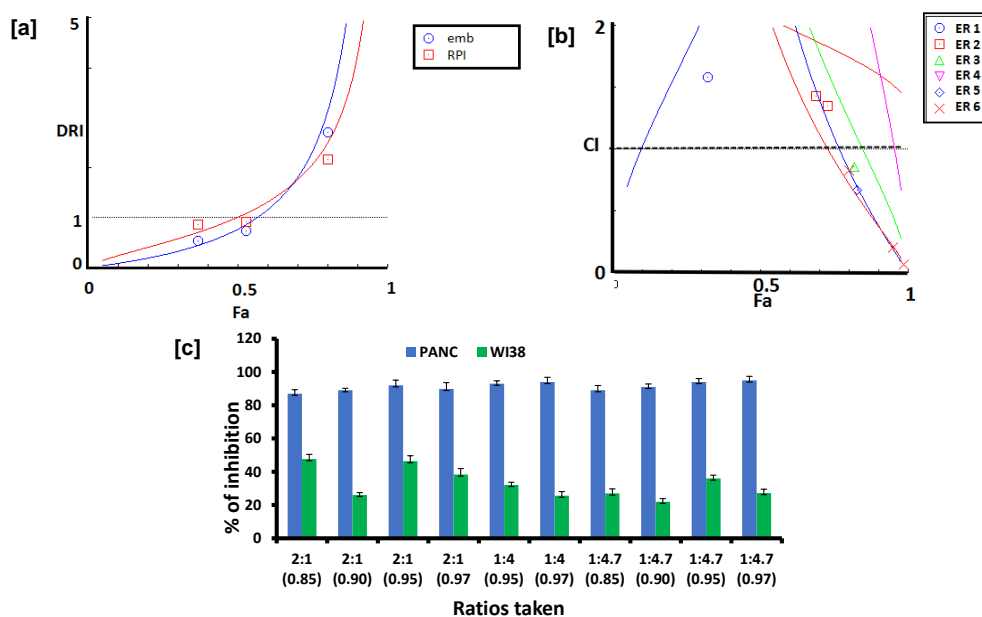


Figure 4.3. [a], [b] Compusyn analysis of various combinations of Embelin and RPI-1. [c] cytotoxic evaluation of the predicted combinations

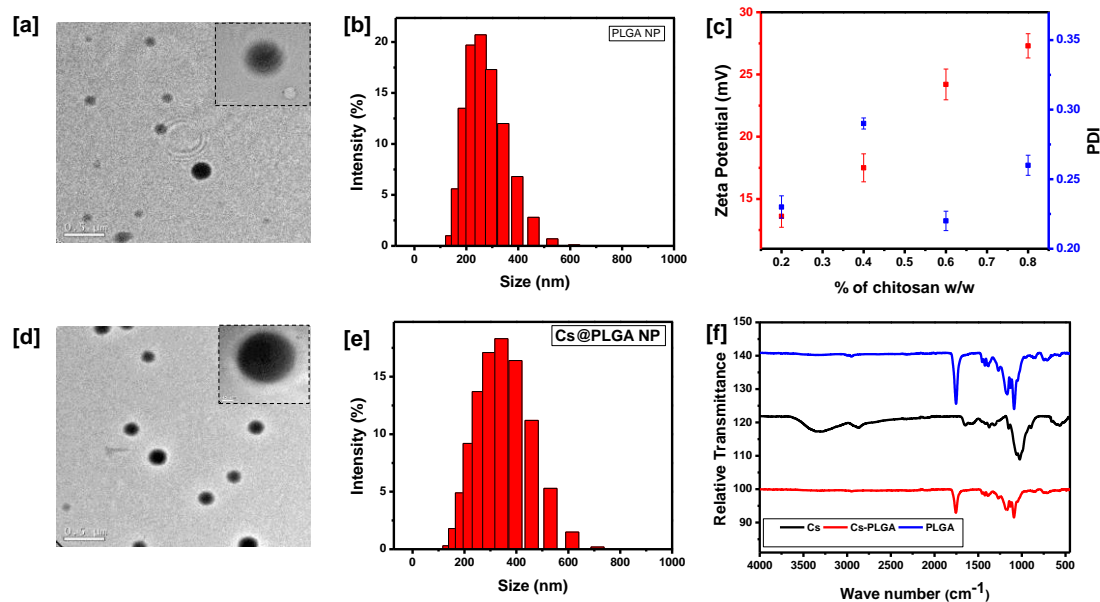


Figure 4.4. Characterization of PLGA NP. [a]TEM image, [b]DLS [c] zeta potential and PDI value of various weight % of chitosan coated PLGA NPs. Characterization of Cs@PLGA NP [d] TEM image [e] DLS [f] IR spectrum

4.2.5 Fabrication of chitosan coated PLGA nanoparticle for pH responsive synergic release of embelin and RPI-1. In order to fabricate the biocompatible nano-carrier delivery system, FDA approved PLGA was chosen and PLGA nanoparticles (PLGA-NPs) were synthesized based on modified o/w solvent evaporation method.²⁸ The naturally derived embelin and the small molecular inhibitor for c-met, (3Z)-3-[(4-hydroxyphenyl)methylidene]-5,6-dimethoxy-1H-indol-2-one, RPI-1 were encapsulated in PLGA NPs. The success of the nano-precipitation was scrutinized by measuring the sizes and the polydispersity indices (PDI) of the NPs by dynamic light scattering (DLS). The sizes were obtained from 200 to 220nm in DLS, and PDIs were between 0.23 and 0.64 for samples tested. The resultant PLGA NPs were coated with functionalized chitosan based on the reported protocol in MES buffer.²⁹ The hydrodynamic diameter and zeta potential of the NPs after coating with pH responsive chitosan biopolymer were evaluated. The negative ζ -potential of PLGA NP was changed to positive, indicating the efficient coating of chitosan over the as synthesized NPs. The weight to volume percentage (w/v%) of CS required to coat the surface of PLGA NPs was optimized by monitoring the zeta potential and PDI of CS@PLGA NPs. The CS@PLGA NPs having zeta potential >20mV and PDI>0.3 was selected based on the optimized CS concentration of 0.8 w/v% for the final nano-construct preparation. The plectin targeting linear peptide sequence (KTLLPTP) was coupled to the terminal amine group of the chitosan moiety using EDC and sulfo-NHS mediated amide coupling strategy.^{23,30} The resulting peptide conjugated chitosan (Plec-CS) was used for the surface coating over the polymeric PLGA NPs for active targeting of plectin biomarker which is overexpressed on PC cells. The surface morphology and size of the nano-carrier PLGA-NPs and Cs@PLGA -NPs were determined by TEM. The TEM images showed both the NPs having diameter of approximately 150 nm and 170nm respectively (Figure 4.4a,d). PLGA NPs has a hydrophobic core containing Embelin and RPI-1 with a corona made up of hydrophilic polymer chitosan. The amine groups of chitosan are available for surface chemistry providing steric stabilization and electrostatic properties against cellular uptake and thus increasing NP circulation time.³¹

4.2.6 Drug loading, drug release kinetics and stability of nano-construct. Encapsulation efficiencies (EE) of 76.3 and 69 % were documented for Embelin and RPI-1, respectively (Figure 4.5a). The difference in EE is due to the variation in the interaction within the PLGA-

NPs. Embelin and RPI-1 are trapped in the PLGA polymeric core due to the hydrophobic interactions. The chitosan coating over the PLGA-NPs prevents the unwanted leakage of the drugs. The pH responsive drug release kinetics was monitored (Figure 4.5b). Interestingly, at pH 5.5, the cumulative release exceeded 70% for both the drugs after 70 h of incubation whereas at pH 7.4, less than 5% of the drugs were released. This clearly deciphers the pH responsiveness of the chitosan polymer that helps in sustained release of the entrapped drugs.²⁵ After loading the NPs with embelin and RPI-1, the stability of the final construct was evaluated in milliQ water, PBS, complete and incomplete cell culture medium at RT and 4 °C for 3 months by measuring the size and PDI value in DLS (Table 4.1). Storage of the nano-construct for upto 3 months in milliQ water, and PBS at RT does not show any change in size and PDI value. In all other conditions, the nanoconstruct remained intact for 2 week and started forming aggregates and larger sized particles. These results indicated that the constructs remain intact during this time period and under the conditions employed.

4.2.7 Biocompatibility, cellular internalization, and cytotoxicity evaluation of the nano-construct. PLGA and chitosan are biocompatible materials for fabricating NPs for biomedical applications. Biocompatibility evaluation of the nano-carrier system through the hemolysis assay displayed the absence of any noticeable toxicity toward red blood cells upon treatment of targeted and non-targeted NPs at lower to higher concentrations (0.01µg/mL to 100 µg/mL) (Figure 4.6a). The experiment was carried out at various pHs ranging from 5.5 to 7.4 and the results were consistent for all the pHs underwent in the study. Similar trend was obtained on treatment of NPs with the isolated peripheral lymphocytes (Figure 4.6b).

Table 4.1: PDI value of the nano-construct in different solvents

Sample	PDI value				
	0 week	2 weeks	4 weeks	8 weeks	12 weeks
milliQ water	0.287±0.013	0.301±0.007	0.321±0.011	0.324±0.012	0.334±0.007
PBS	0.346±0.005	0.381±0.003	0.389±0.001	0.388±0.004	0.368±0.009
DMEM	0.338±0.007	0.339±0.003	0.482±0.004	0.557±0.011	0.261±0.005
10% FBS in DMEM	0.481±0.010	0.387±0.002	0.661±0.012	0.564±0.006	0.425±0.008
milliQ water at 4°C	0.321±0.004	0.443±0.010	0.421±0.005	0.684±0.003	0.824±0.21
PBS at 4°C	0.303±0.002	0.327±0.006	0.3±0.004	0.425±0.009	0.0467±0.017
DMEM at 4°C	0.413±0.010	0.347±0.007	0.526±0.002	0.624±0.013	0.649±0.01

10% FBS in DMEM at 4°C	0.521±0.011	0.557±0.006	0.634±0.004	0.537±0.003	0.672±0.14
------------------------	-------------	-------------	-------------	-------------	------------

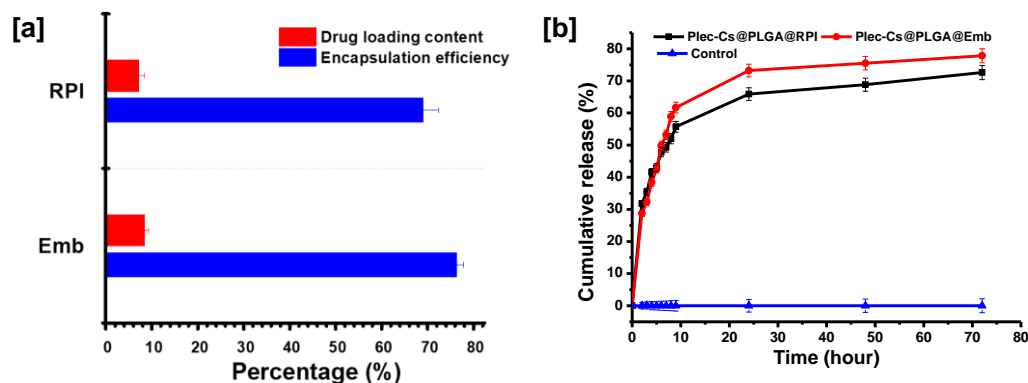


Figure 4.5: Drug loading content and encapsulation efficiency of Cs@PLGA NP

Plectin-1 levels are low in normal cells, but its expression is up regulated in PC. Therefore, the peptide sequence targeting to plectin-1 (Plec) enable the selective uptake of the nano-carrier in PC. Cellular uptake of the nano-construct was examined in PC cells (PANC-1) and normal cells (WI-38), where fluorescein encapsulated Cs@PLGA NPs, with plectin targeting peptide was utilized. (Figure 4.7) The results showed enhanced fluorescein intensity from the targeted nano-carrier compared with non-targeted (without plectin targeting peptide) nanoparticles in PANC-1 cells. In fibroblast cell line WI-38, there was lesser uptake of the targeted nano-construct than in the PANC-1 cells which indicated that the abundance of plectin receptor expression is much higher in PANC-1 cells in compare to WI-38 cells. Binding of Plectin peptide to the Plectin-1 receptors affinity mediates the uptake of NPs. Interestingly, decoration of nanoparticle using positively charged chitosan was reported to have selectivity towards cancer cells compared to normal cells, since cancer cells showed a stronger net-negative surface charge. Therefore, a combined effect of charge-based interaction and Plec based specific targeting might have contributed to the observed cellular accumulation of the nano construct. The cell uptake study highlights that Plectin-1 targeting peptide conjugation selectively increased the uptake of the NPs to human PC cells, but not to normal fibroblast cells. Since PANC-1 cells showed selective uptake of Plec-Cs@PLGA NPs, we further wanted

to determine whether this cell uptake translated to cytotoxicity of delivered drugs embelin and RPI-1.

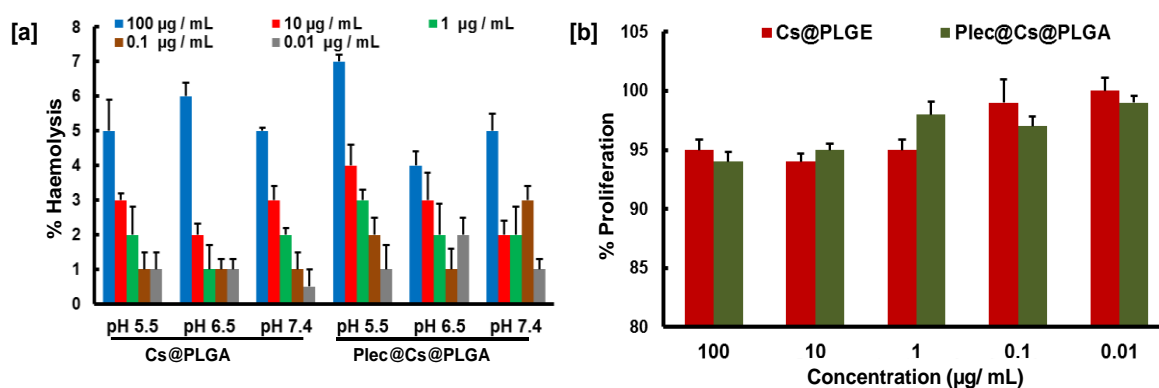


Figure 4.6: Biocompatibility evaluation of targeted nano carrier by [a] hemolysis assay and [b] lymphocyte proliferation assay

As a preliminary step toward appraising the therapeutic potential of fabricated nano-construct containing embelin and RPI-1, cytotoxic evaluation was carried out through MTT assay on PANC-1 cells (Figure 4.8). Cytotoxicity evaluation was carried out using carriers, cargo loaded nano constructs and with the respective molecules. Bare PLGA and Plec-Cs@PLGA NPs were found to be nontoxic even in the higher concentrations. Plec-Cs@PLGA@Emb and Plec-Cs@PLGA@RPI-1 does not show any IC_{50} values up to $100\mu\text{g/mL}$ for 24 h whereas the final construct loaded with both the drugs in the predetermined synergic combination showed a dose dependent cytotoxicity with an IC_{50} of $46.8\mu\text{g/mL}$. This indicates the predominant synergic effect of Emb and RP-1 in the targeted nano-construct as reflected in the cytotoxicity assessment.

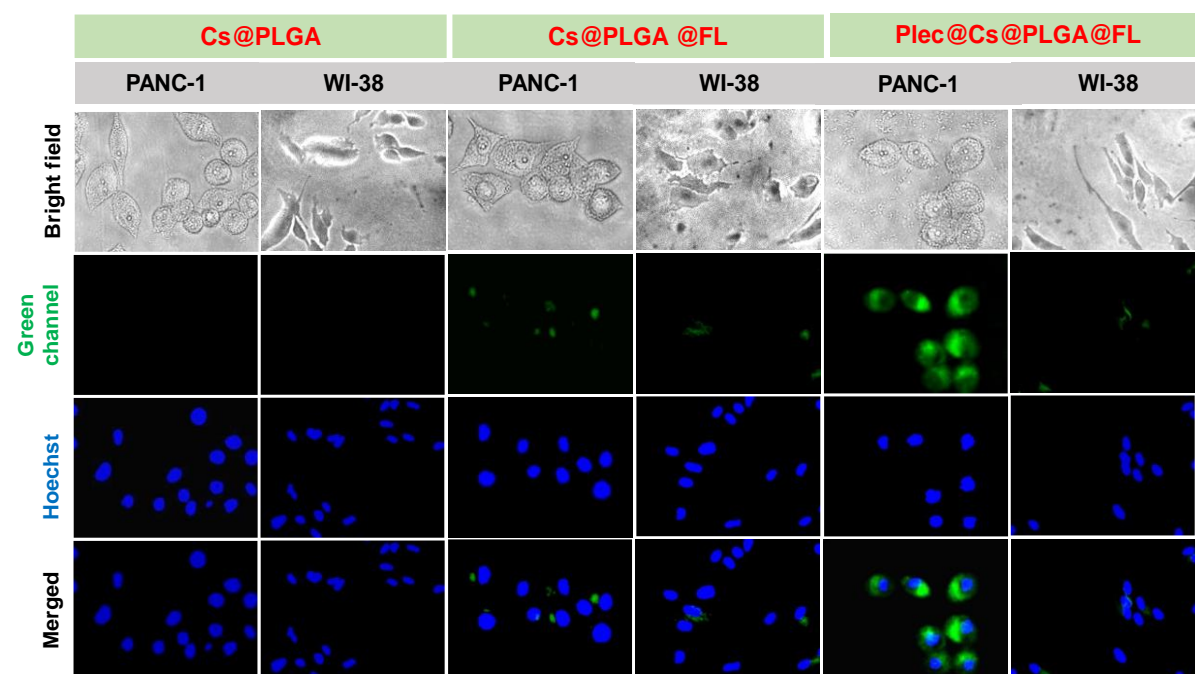


Figure 4.7: Internalization of fluorescein encapsulated targeted and non-targeted NPs in PANC-1 and WI-38 cells.

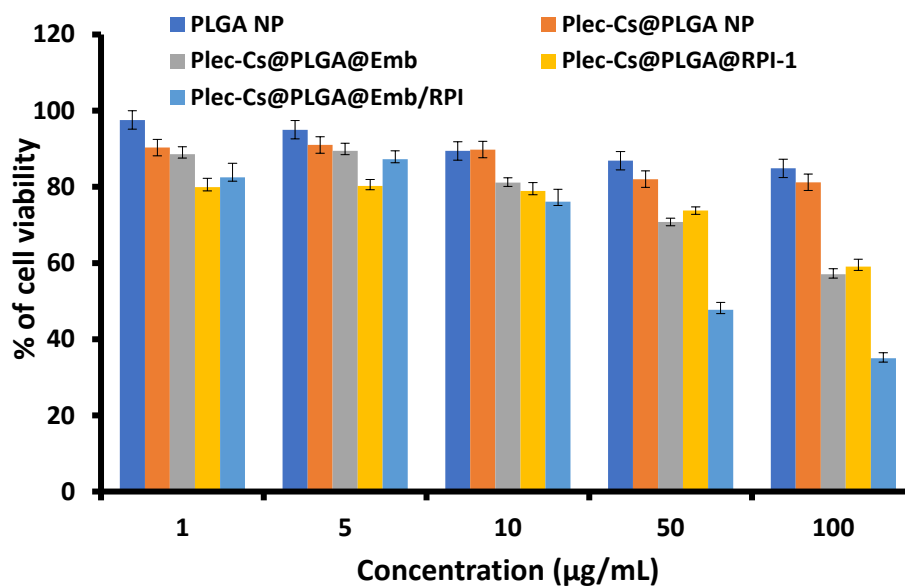


Figure 4.8: Cytotoxic evaluation of PLGA, Plec-Cs@PLGA, Plec-Cs@PLGA@Emb, Plec-Cs@PLGA@RPI-1 and Plec-Cs@PLGA@Emb/RPI-1 NPs in PANC-1 cells.

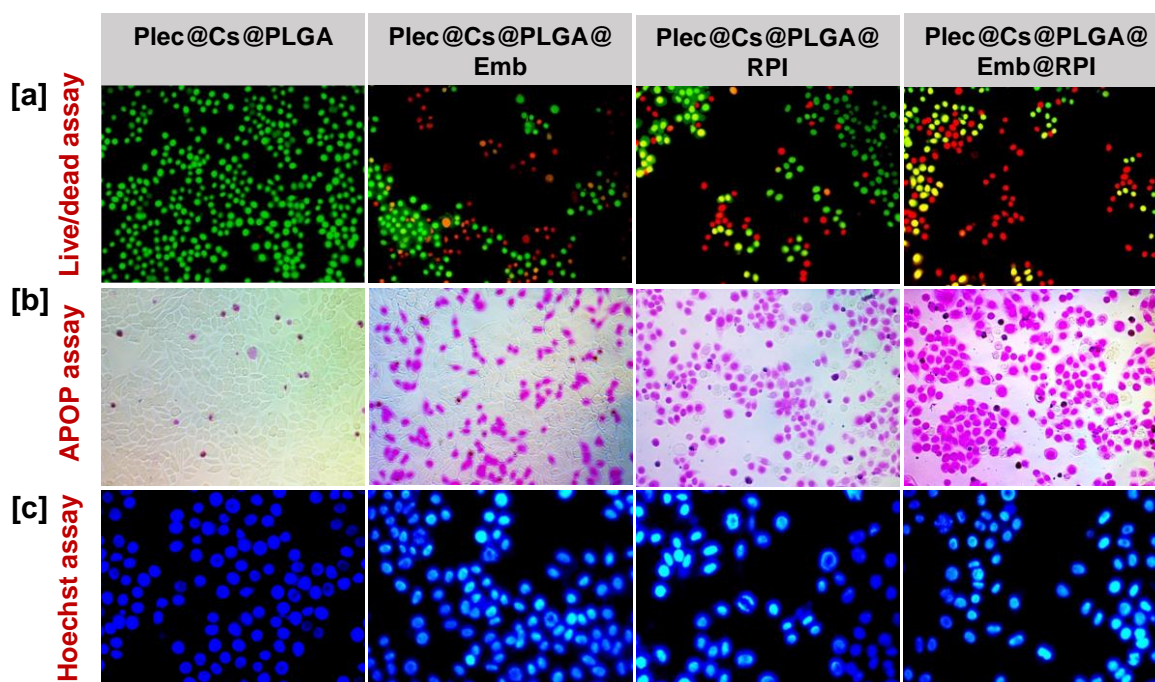


Figure 4.9: Apoptotic evaluation of Plec-Cs@PLGA@Emb/RPI in PANC-1 cells. [a] Live-dead assay, [b]APOP assay and [c] Hoechst staining.

4.2.8 Apoptotic evaluation of the nano-construct. In order to determine the mechanism of cell death exerted by the dual drug loaded nano-construct, various apoptotic assays were carried out. Evaluation of Plec-Cs@PLGA@Emb, Plec-Cs@PLGA@RPI-1 and Plec-Cs@PLGA@Emb/RPI treated (50 $\mu\text{g}/\text{mL}$) PANC-1 cells using acridine orange-ethidium bromide staining showed a distinct change in color from green to yellow/red which is associated with the apoptotic features (Figure 4.9a). The extend of apoptosis was highest in the dual drug loaded plectin targeted nano-construct. The carrier system Plec-Cs@PLGA NPs were taken as the positive control. Early onset of apoptosis was evaluated using APOPercentage assay. A similar pattern of programmed cell death was observed (Figure 4.9b). This result complemented with the acridine orange-ethidium bromide assay. One of the most important features of apoptosis is the nuclear condensation and DNA fragmentation associated with it. This can be clearly spotted by Hoechst 33342 nuclear staining. Indications of DNA fragmentation was observed for Plec-Cs@PLGA@Emb/RPI treated PC cells as compared to Plec-Cs@PLGA@Emb and Plec-Cs@PLGA@RPI-1 treated ones whereas control cells remained unaffected (Figure 4.9c). The execution of programmed cell death was further analysed by terminal deoxynucleotidyltransferase dUTP nickend labeling (TUNEL) staining

assay. TUNEL positivity (green fluorescence) was observed in dual cargo loaded targeted NPs compared to Plec-Cs@PLGA@Emb and Plec-Cs@PLGA@RPI-1 treated ones. Other than this, induction of apoptotic cell death was further examined by annexin V staining. In PANC-1 cells, the controls were $0.07 \pm 1\%$ annexin V positives, while the Plec-Cs@PLGA@Emb/RPI-treated cells showed $22.9 \pm 1.5\%$ positivity (Figure 10a).

Notably, the efficiency of Plec-Cs@PLGA@Emb/RPI is evident from the results compared to either Embelin and RPI-1 loaded variants. Embelin, the benzoquinone molecule is already reported to induce apoptosis in various cancer cells. It targets X-linked inhibitor of apoptosis and inhibits cell growth.^{32,33} Though RPI-1 is a potent c-met inhibitor, its apoptotic consequences are not much discussed in literature. The results obtained revealed the synergic effect of Embelin and RPI-1 would be causing the enhanced apoptotic effect. Similar type of natural product like curcumin, eugenol loaded PLGA based biocompatible systems are also reported to have similar apoptotic effect in cancer cells.^{34,35}

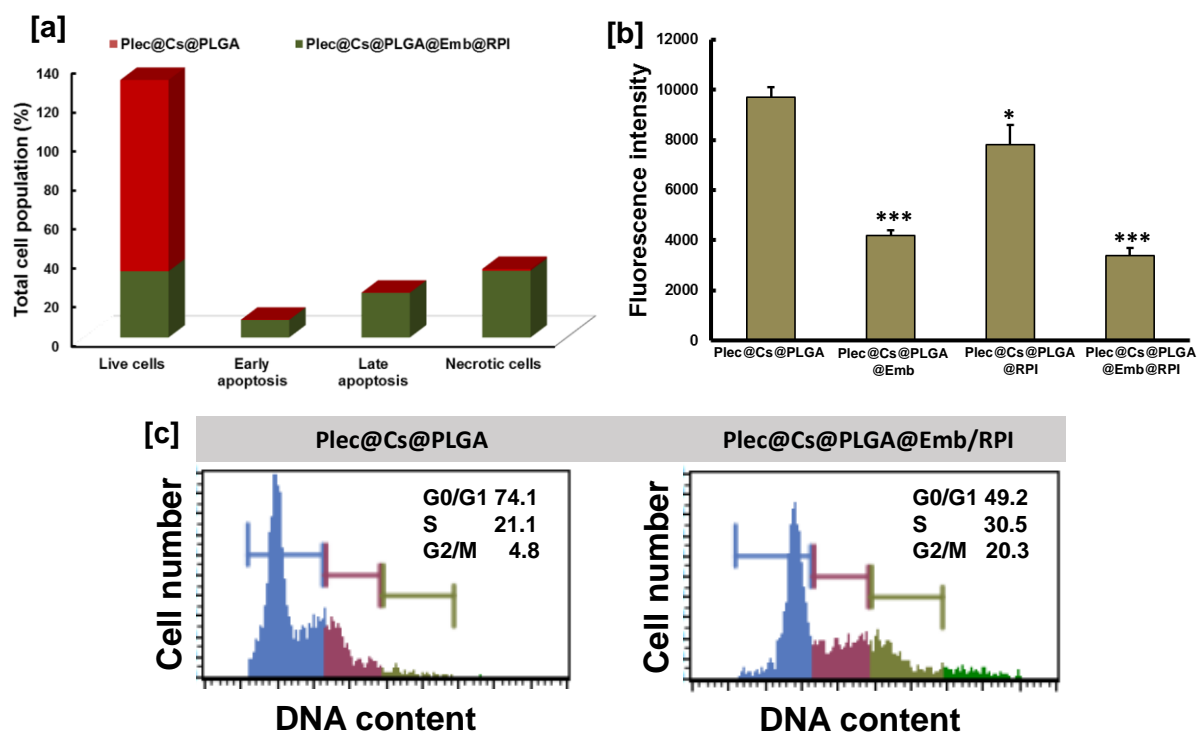


Figure 4.10: [a] Annexin V/FITC assay, [b] TMRE assay and [c] cell cycle analysis in PANC-1 cells

4.2.9 Change in mitochondrial membrane potential. As the next step, mitochondrial membrane potential ($\Delta\Psi_m$) assessment was performed. During apoptosis the release of proapoptotic proteins is distinct due to the disintegration of the electrochemical gradient of mitochondrial outer membrane. Many anticancer agents including natural products and small molecular inhibitors are reported to trigger mitochondrion mediated apoptotic pathway. $\Delta\Psi_m$ variation was quantified with tetramethylrhodamine, ethyl ester (TMRE) mitochondrial membrane potential assay (figure 4.10b). The carrier does not cause any mitochondrial membrane depolarization. Plec-Cs@PLGA@RPI showed significant reduction with $\Delta\Psi_m$ ($p < 0.05$) whereas the action of both Plec-Cs@PLGA@Emb ($p < 0.01$) and Plec-Cs@PLGA@Emb/RPI ($p < 0.001$) was highly significant in PANC-1 cell line. The study suggested that the nanodrug could successfully deliver the drugs to the mitochondria with the mediation of plectin conjugated chitosan coated PLGA NPs, resulting in mitochondrial membrane depolarization and further induce cancer cell apoptosis.^{36,37}

4.2.10 Cell cycle regulation. To evaluate the Plec-Cs@PLGA@Emb/RPI mediated suppression of cell proliferation, cell cycle analysis was performed. Flow cytometric analyses were conducted after the DNA was stained with PI. Histograms denote the involvement of cell cycle arrest on the Plec-Cs@PLGA@Emb/RPI NPs treated cells (figure 4.10c). Plec-Cs@PLGA@Emb/RPI treatment arrests cells at the G2/M and S phase. The effect of the dual drug loaded nano construct on the cell cycle regulation was further confirmed through microscopic observation with the aid of colorimetric cell clock assay, which also substantiated a similar pattern of action. Embelin was reported to induce apoptosis and G0/G1 phase cell cycle arrest in glioma breast, pancreatic and prostate cancer cells.³⁸⁻⁴⁰ Several studies pointed out that RPI-1 induced accumulation of the cells at the G2 cell cycle phase.^{11,13} Therefore, cell cycle arrest brought about by the combinational therapy indicated the synergic effect of the two molecules promoting apoptosis.

4.2.11 Anti-metastatic effects of nano-construct. Metastasis accounts for the high rate of mortality and lower survival rate of PC. We were curious to check the anti-metastatic potential of the targeted NPs. As a first step toward evaluating the antimetastatic property, we carried out the clonogenic assay. It was observed that combinational therapy (5 μ g/mL) significantly reduced ($p < 0.001$) the cologenic ability of PANC-1 cells as compared to the Plec-

Cs@PLGA@Emb and Plec-Cs@PLGA@RPI-1. The carrier system Plec-Cs@PLGA NP was used as negative control (Figure 4.11a,b). Then we tried to explore the effect in invasion and migration capability of the cancer cells. For this we carried out invasion and migration assay using matrigel coated trans-well chamber. The nano-construct could inhibit both invasion and migration in a significant manner (Figure 4.11c-f). Then we performed the classical wound-healing assay for evaluating the migration rate of the PC cells administered with the NPs. It was observed that the dual drug loaded targeted NPs significantly retarded the migration rate of the cells in a time dependent manner. The scratch zone of the wells treated with the Plec-Cs@PLGA@Emb/RPI are significantly larger even after 24 h, but the control wells displayed almost closure of the wound area, which gave the evidence toward the inhibition of metastasis by our nano-construct (Figure 4.12). Plec-Cs@PLGA@RPI-1 was also equally promising in retarding the wound healing which implies that the synergic effect of the RPI-1 in combination with embelin could be the reason for the hopeful results.

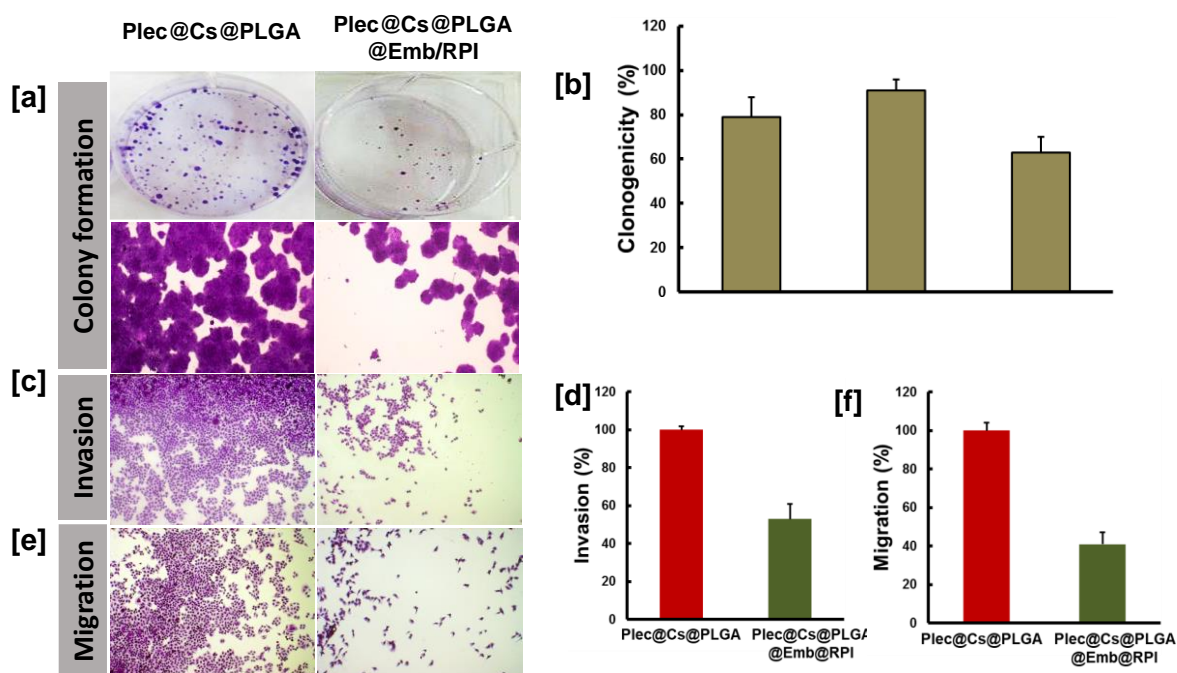


Figure 4.11: Anti metastatic evaluation of Plec-Cs@PLGA@Emb/RPI in PANC-1 cells. [a], [b] colony formation assay. [c], [d] Invasion assay and [e], [f] migration assay.

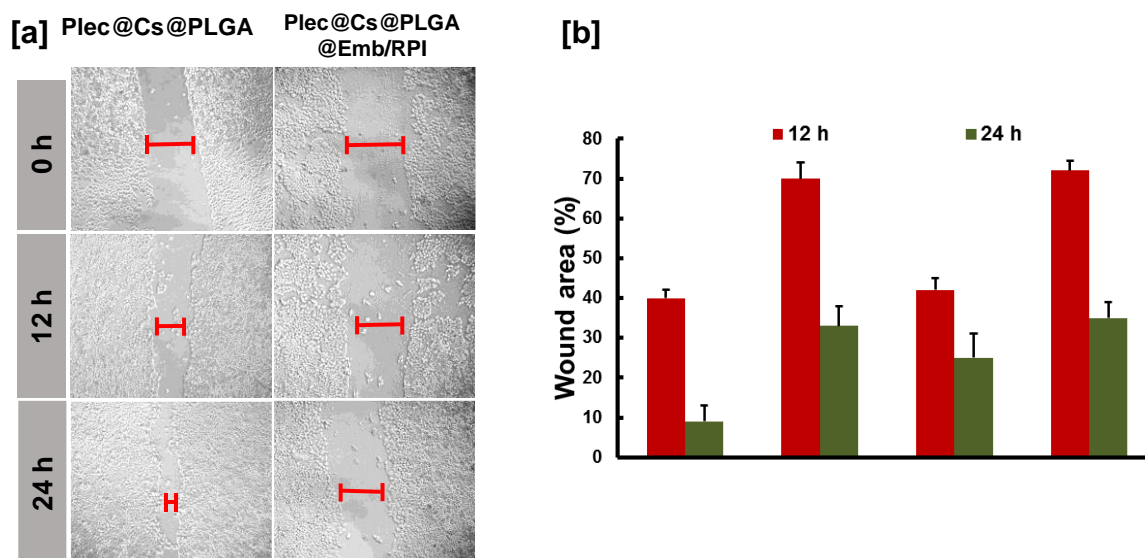


Figure 4.12: [a] Photographic images of the wound healing assay and [b] graph representing the quantitation of percentage wound area in PANC-1 cells

Nearly 50% reduction in invasion and 60% reduction in migration ability was observed in the dual cargo loaded plectin-1 targeted nano-construct up on comparison with to the Plec-Cs@PLGA@Emb and Plec-Cs@PLGA@RPI-1. This enhanced anti-metastatic potential could be due to the synergic effect produced by embelin and RPI-1. The c-Met inhibitory effect of RPI-1 is relevant to its anti-metastatic ability. By targeting the Met signaling pathway down regulation of other signaling pathways like AKT and STAT3 are involved which ultimately reduces the spontaneous metastases in the cancer cells.^{11,13}

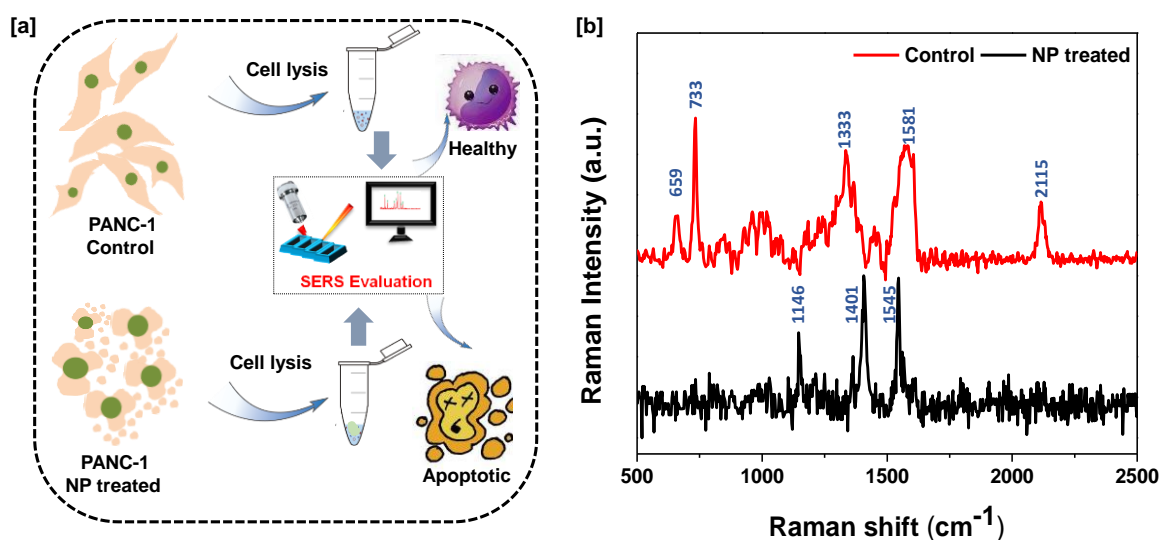


Figure 4.13: [a] Schematic representation of the procedure adopted for the SERS evaluation of the metabolites, [b] SERS spectrum of the metabolites isolated from nano-construct treated and untreated PANC-1 cells

4.2.12 Analysis of the change in metabolomics. The changes in metabolites that triggered the anticancer and antimetastatic effects of the Embelin and RPI-1 loaded, plectin targeted NP were investigated. For that as a preliminary step, we isolated the metabolites from the NP treated and untreated PANC-1 cells and subjected to Raman analysis (Figure 4.13a). The SERS spectra obtained from the samples displayed clear variation in the spectral pattern in comparison with treated and untreated ones (Figure 4.13b). SERS spectra generated from the control sample displayed the signature peaks of 659, 733, 1333, 1581 and 2115 cm^{-1} which indicated the ring breathing mode of DNA, Adenine (purine base) and cytochrome stretching, nucleic acids stretching, C=C stretching and carbohydrate stretching respectively.^{41,42} The three distinct peaks generated from the NP treated sample were 1146, 1401 and 1545 cm^{-1} which corresponds to the carbohydrate peak, N-H in plane vibration and C₆-H deformation mode respectively. This change in spectral pattern clearly indicates that there occurs a prominent change in the signature metabolites due to the action of the delivery of Embelin and RPI-1 towards PANC-1 cells leading to the programmed cell death. Next, we thought of investigating this change in metabolic profile in a semi-quantitative manner using LC-MS. The metabolites were subjected to LC-MS analysis and the detailed metabolite pattern was obtained for the control as well as NP treated samples. The chromatograms obtained from the HILIC and RPLC methods were analyzed and observed a variation in the mass range of metabolites isolated from NP treated and non-treated cells. The major metabolites involved in the carbohydrate metabolism, purine metabolism and pyrimidine metabolism were categorized to various class of mass range from m/z 100-1000. A box plot was generated for control and treated sets and it clearly deciphered the change in mass pattern of the metabolites in the control as well as drug interacted cells (Figure 4.14). The interaction of embelin and RPI-1 with various molecular components changed in metabolic pattern of subcellular environment. We found nearly 25 metabolites contributed to the cell death in various manner. In the case of cells treated with Plec-Cs@PLGA@Emb/RPI-1, there was an up-regulation of adenine which might be affected by the enhanced formation of linoleic acid in the cellular environment. The excess adenine was converted to its oxidized form, fapy-adenine which on further steps significantly

cause a carnage to the purine metabolism.^{43,44} In contrary to this, the level of pyrimidines like deoxy cytidine, DuDP, uridine and thymidine was found to be down-regulated which in turn will lead to the collapse of normal pyrimidine metabolism of the cancer cell. Normal DNA synthesis will be affected in sequence to these changes in the purine and pyrimidine metabolism.⁴⁵ In contrary to the normal cells, neoplastic cells can be forced in the direction of cell death by introducing DNA damage in a catastrophic manner by promoting cell cycle arrest at various stages. The regulation of cell cycle results and the Raman signature peak changes were in par with these metabolic changes occurring in the PANC-1 cells. The disappearance of 653 cm^{-1} peak and the emergence of new peak at 1401 cm^{-1} in the treated sample in comparison to the control one correlates with the changes in purine and pyrimidine metabolism. Another prominent variation occurred in the carbohydrate metabolic pathway. Abundance of molecules like glucose, fructose, N-acetylglucosamine (GlcNAc), Uridine diphosphate N-acetylglucosamine (UDP GlcNAc) has decreased considerably which causes a sequential decline in glucose flux. Compared to the normal cell, glucose metabolism flux is highly accelerated in cancer cells. So the decline in the same will affect the normal functioning of the cancer cell due to low energy supply.^{46,47} The decline of the carbohydrate moieties was evident in the Raman spectrum as well. The disappearance of 2115 cm^{-1} peak in the treated sample compared to the control correlates with the same result. The enhanced concentration of trihexosylceramide along with the decrease in HNE levels are associated with the mitochondrial membrane damage which leads to the cyt C release followed by caspase activation and apoptosis.^{48,49} The changes in the metabolites in the molecular mechanism of action by Plec-Cs@PLGA@Emb/RPI-1 was clearly demonstrated with the dendrogram based on the hierarchical clustering (Figure 4.15). Major changes were observed in purine metabolism, pyrimidine metabolism, glucose metabolism, amino sugar metabolism and lipid metabolism. These alterations in the metabolic pathway due to the interaction of the biomolecules with embelin and RPI leads to the apoptotic event. Thus, the fabricated nano system for the dual delivery of embelin and RPI-1 effectively induces cell death in a more intended manner.

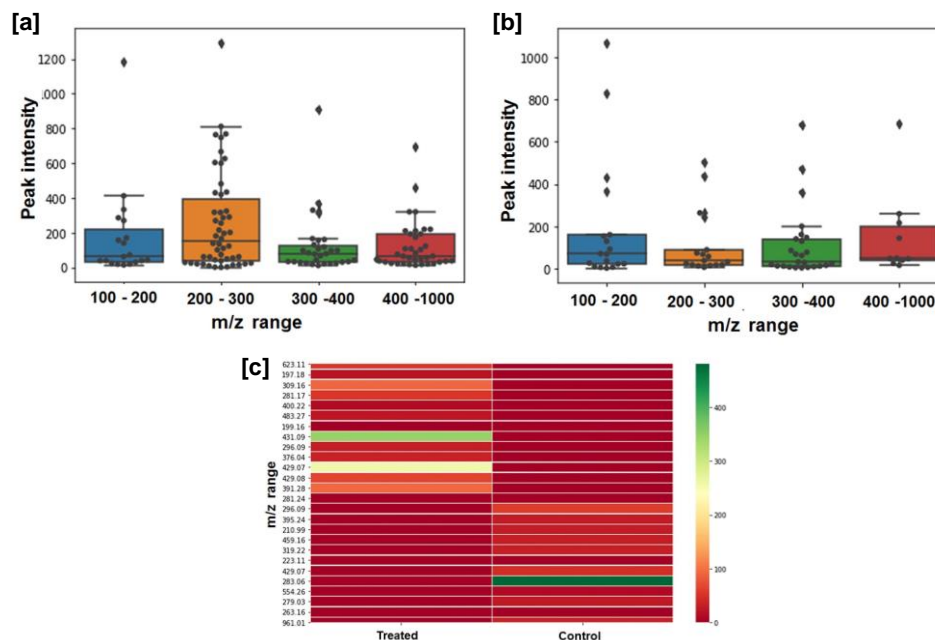


Figure 4.14: Box plot indicating the variation of mass range of the metabolites isolated from [a] control cells, [b] nanoconstruct treated cells and [c] heatmap generated from the variation in mass of metabolites.

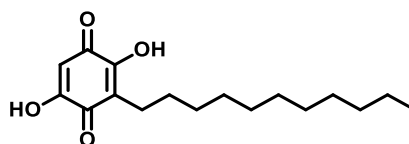
4.3 Conclusion

In summary, the effective synergic combination of naturally occurring cytotoxic agent embelin and c-Met inhibitor RPI-1 was established for an efficient therapeutic potential against pancreatic carcinoma cell line PANC-1. The combination with a pre-optimized ratio was loaded in a biocompatible and biodegradable PLGA nano-carrier delivery system. In the final nano-delivery system, plectin-1 targeting peptide sequence conjugated with another biopolymer chitosan and coated with dual drug loaded PLGA- NPs for selective uptake in the PANC-1 cells. Once internalized by the cells, due the acidic pH in the cancer microenvironment, the chitosan biopolymer swells and releases the entrapped drugs into the cellular milieu. This dual drug release in the synergic ratio causes enhanced anticancer effect which was monitored through various *in vitro* assays. The involvement of mitochondria in cell death mechanism was also evaluated by TMRE assay whereas the signature Raman peaks of the metabolites isolated from the nano-construct treated cells were identified and confirmed the metabolic changes associated with the interaction of the drug moieties and biomolecules

by LC-MS analysis. The designed biocompatible and biodegradable embelin and RPI-1 loaded targeted nano-construct was found to be a potential system for further pre-clinical studies.

4.4 Materials and methods

4.4.1 Characterization of embelin



Molecular formula	: C ₁₇ H ₂₆ O ₄
FT-IR	: 3567, 3307, 2922, 2852, 2099, 1609, 1321, 1121 cm ⁻¹
¹ H NMR (500 MHz, CDCl ₃)	: ¹ H NMR (500 MHz, CDCl ₃) δ 7.68 (s, 2H), 6.01 (s, 1H), 2.52 – 2.37 (m, 2H), 1.59 (s, 7H), 1.49 – 1.45 (m, 1H), 1.25 (s, 10H), 0.88 (t, <i>J</i> = 6.8 Hz, 3H).
¹³ C NMR (125 MHz, CDCl ₃)	: ¹³ C NMR (126 MHz, CDCl ₃) δ 170.17, 169.92, 129.27, 116.94, 102.12, 31.92, 29.65, 29.63, 29.55, 29.45, 29.38, 29.37, 29.34, 27.95, 22.70, 22.53, 14.13.
Mass (HRMS)	m/z 319.0954 [M+Na] ⁺

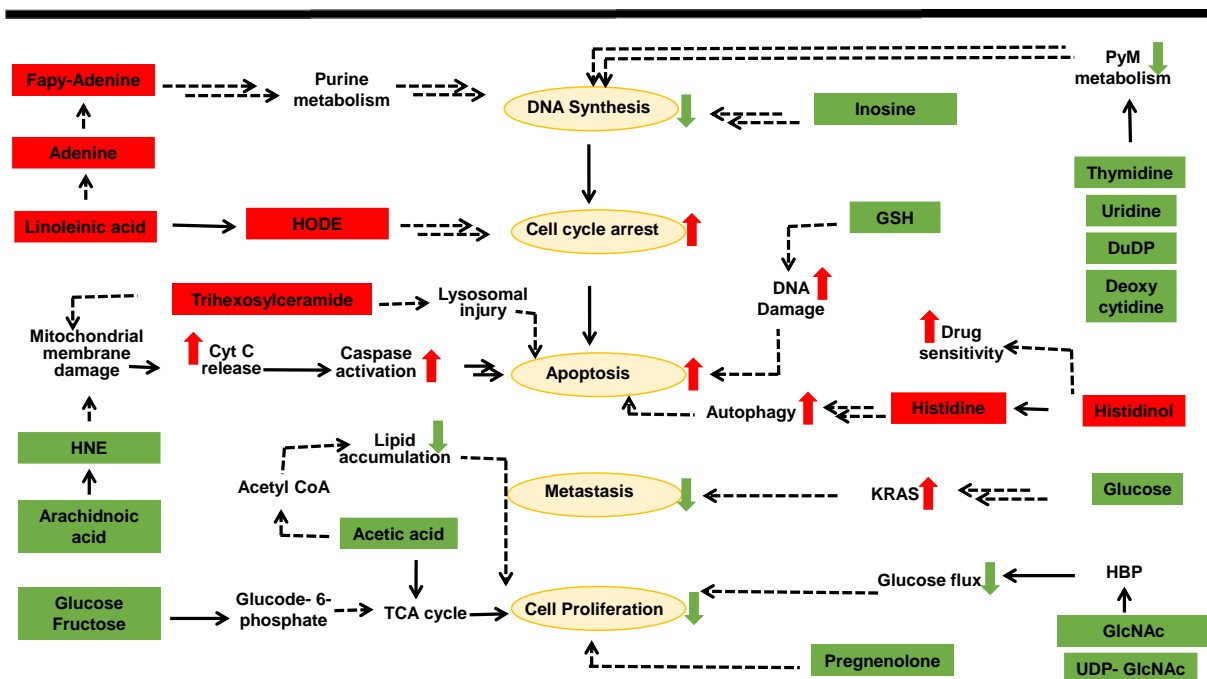


Figure 4.15: Pathway deciphering the proposed metabolic changes due to the interaction of the nano-construct on cancer cells. Entries given in boxes are experimentally validated while the red-colored entries represent the up-regulated metabolites, and green colored entries represent the down-regulated metabolites. Filled lines represent the direct biological effect while dotted lines denote the indirect effect.

4.4.2 Synthesis of plectin targeting peptide KTLTP: The construction of the plectin-targeted peptide, KTLTP, was done via solid-phase peptide synthesis (SPPS) using HMPB-MBHA (200mg, 0.0142mmol) resin as the solid support. Initially, the resin was allowed to swell in anhydrous dichloromethane (DCM) for nearly 30 min; then, the solution was washed with N,N-dimethyl formamide (DMF) (3×3mL). The first amino acid Fmoc-Pro-OH (195mg, 0.426mmol), was activated under N₂ atmosphere with DIC (0.218mL, 0.071mmol) in DCM at 0-5 °C for 1h. DCM was then removed, and the activated proline ester was dissolved in DMF, and DIPEA was further added into the inflated resin bed. The reaction was continued for 16-24 h in the shaker at 300 rpm. After the reaction time, the resin was washed with DMF (3×3mL) to remove the unreacted amino acid, and the Fmoc group in the amine terminal was cleaved by treating with 20% piperidine in DMF. This process was continued similarly with other amino acids in the sequence Fmoc-Thr (tBu)OH (260mg, 0.426mmol), Fmoc-Pro-OH (195mg, 0.426mmol), Fmoc-Leu-OH x2 (195mg, 0.426mmol), Fmoc-Thr (tBu)OH (260mg, 0.426mmol), Fmoc-Lys-(Boc)-OH (260mg, 0.426mmol) were charged to the solid support to

obtain resin-bound peptide. After the completion of the reaction, the unreacted reagents were removed by DMF, followed by Dichloromethane (DCM) (3×5mL) and finally by hexane (1X3mL). The peptides were cleaved from the resin support by treating it with 5% trifluoroacetic acid (TFA) in DCM. The peptide was then concentrated in vacuum using a rotary evaporator and further precipitated in diethyl ether to yield in pure form. ¹H NMR (500 MHz, CD₃OD, TMS): δ 7.69-7.32 (m, 10H), 5.13(bs, 4H), 4.77-3.73 (m, 17H), 3.32-2.84 (m, 14H), 1.51 (s, 18H), 1.15 (s, 12H), 1.08 (s, 12H), 0.83 (s, 9H)ppm. HRMS Calcd for C₈₀H₁₁₃N₈O₁₃[M+1]⁺ is 1393.8427; and found 1393.8409.

Further the Fmoc-C(Tr) KTLTP-COOH peptide was conjugated to Chitosan via EDC-NHS coupling. The peptide (7.09 mg, 7.3x10⁻³mmol) was activated using EDC (1.08mg, 8x10⁻³mmol) and N-hydroxysulfosuccinimide (7.3mg, 7.3x10⁻³mmol) for 10min under N₂ atmosphere. Then Chitosan (4mg, 6.69x 10⁻³mmol) dissolved in 10 mmol MES buffer was poured into the reaction mixture and continued the reaction for 24 h. After this, dialysis was performed for 72h to isolate the peptide conjugated chitosan (Plec-Cs). The residue was removed under rotary evaporator and purified by dialysis using dialysis membrane. ¹H NMR (500 MHz, D₂O, TMS): δ 8.89 (s, 4H), 7.41 (s, 6H), 4.34-3.40 (m, 95H), 3.21 (t, J=5 Hz, 3H), 3.16 (s, 1H), 3.00 (s, 11H).

4.4.3 Synthesis of carrier system: PLGA NPs and chitosan coated PLGA NPs were synthesized using previously reported procedures with slight modifications. 10mg of PLGA was dissolved in 3.6 mL of acetone and 400 μl of methanol. To this, the aqueous phase (1 mL of Milli-Q water, PVA 0.2% w/v) was added drop wise and sonicated for 1min forming the water in oil (w/o) emulsion. This was added drop wise to the aqueous phase (10 mL of Milli-Q water, 2.0% w/v of PVA) and sonicated for another 2 min. The obtained water in oil in water emulsion (w/o/w) was stirred for the complete evaporation of organic solvents. The produced nanoparticles were collected by centrifugation at 9000rpm at RT for 10 min. These NPs were dispersed in 1mL Milli-Q water and 1 mL of 0.2% chitosan (w/v) dissolved in MES buffer was added. This mixture stirred at RT for 6h. Unreacted Chitosan or Plec-chitosan was removed by centrifugation at 9000rpm at RT for 10 min.

4.4.4 Drug loading studies. To load embelin and RPI-1, the loading efficiency of each molecule was studied separately as described before. Then the desired drug content was tuned to load the chosen ratio by considering individual drug release as well. The loading efficiency of embelin and RPI-1 were evaluated separately. 2 mg of embelin was added in to the mixture of organic solvents along with PLGA during nanoparticle formation. After the reaction time, the embelin encapsulated NP was obtained by centrifugation and the pellet was washed with Milli-Q water. The amount of embelin in the supernatant was determined by SERS and the encapsulation efficiency was calculated.

Encapsulation efficiency = (Free embelin- embelin in supernatant)/ Free embelin $\times 100$

Similarly, the loading of RPI-1 was also performed by adding the molecule to the mixture of organic solvents along with PLGA during nanoparticle formation. After the reaction time, the RPI-1 encapsulated NP was obtained by centrifugation and the pellet was washed with Milli-Q water. The amount of embelin in the supernatant was determined by UV-Vis spectrometer and the encapsulation efficiency was calculated in the similar fashion.

4.4.5 Drug release kinetics. The drug loaded NPs were taken in a dialysis membrane and were dipped in a beaker with 100 mL of PBS at pH 5.5 and 7.4. The dialysis membranes were constantly stirred over a magnetic stirrer. At equal interval of time, (1h) 1 mL of the drug release medium was collected and exchanged with 1mL of pH-maintained PBS to maintain the bath condition. The cargo released to the medium was quantified using SERS for embelin and UV-Vis spectroscopy for RPI-1 from the standard curve.

4.4.6 In vitro cytotoxicity assays: The growth inhibition capacity of Embelin, RPI-1, various combinations of embelin and RPI-1, PLGA NP, Plec-CS@PLGA NP, Plec-CS@PLGA@Emb NP, Plec-CS@PLGA@RPI NP and Plec-CS@PLGA@Emb/RPI NP were evaluated against PANC-1 and WI-38 cell lines using well known MTT assay as previously discussed. Cell viability was assessed by the absorbance reading at 570nm due to the cleavage of tetrazolium salt by mitochondrial dehydrogenase.

4.4.7 Cellular uptake studies: Fluorescein encapsulated nanoconstructs, Plec-Cs@PLGA@Fl, Cs@PLGA@Fl were synthesized to study the internalization. Cellular uptake studies were carried out with a fluorescence microscope, and localization was performed after

counter-staining in WI-38 and PANC-1 cells as described before. Cells were treated with Plec-Cs@PLGA@FI, Cs@PLGA@FI for 4 h, washed with PBS, and then counter-stained with dyes. Finally imaging was performed under an inverted fluorescent microscope (Olympus 1 × 51).

4.4.8 Biocompatibility assays:

Haemolysis assay: Human blood samples stabilized with EDTA were used for studying the haemolytic behavior of the nano-constructs on isolated RBCs. The experiment was conducted as earlier reported and the haemolysis percentage was found using the following formula

$$\text{Haemolysis [\%]} = (A_{\text{sample}} - A_{\text{Negative control}}) / (A_{\text{positive control}} - A_{\text{Negative control}}) \times 100$$

Lymphocyte proliferation assay. Lymphocytes were isolated from fresh human blood samples using Ficoll-Paque™ Plus solution (GE Healthcare, Sweden). The lymphocyte proliferation status of the nano-constructs was performed as reported.

4.4.9 Apoptosis studies: Adherent cancer cells were grown overnight on 12 mm circular glass coverslips with 10% DMEM on 24-well culture plates for a period of 24 h. Observation of nucleus for any morphological changes was done with Hoechst staining and the cells were observed under an inverted fluorescent microscope using a DAPI filter (Olympus 1X51). Acridine orange-ethidium bromide dual staining is the most commonly used method to detect apoptosis and is based on the differential uptake of two fluorescent DNA binding dyes by viable and nonviable cells, respectively. Assessment of apoptosis using the acridine orange-ethidium bromide dual staining procedure was performed as described earlier. The cells were observed under an inverted fluorescent microscope, using a FITC filter (Olympus 1X51, Singapore) to view the apoptotic or non-apoptotic cells. Early onset of programmed cell death was further observed using APOPercentage dye (Biocolor, Belfast, Northern Ireland) as per manufacturer's instructions as previously described. Light microscopic images of APOPercentage dye-labeled cells, which stained pink under a light microscope, were used to quantify the extent of apoptosis.

4.4.10 Mitochondrial membrane potential assay. Depolarization of mitochondrial membrane potential was studied using TMRE mitochondrial membrane potential assay.

Cationic lipophilic, dye which can accumulate in the oppositely charged mitochondrial matrix is used to analyse the change in mitochondrial membrane potential as described earlier. Measurements were taken with a fluorimeter (FLx800, Bio-Tek, Winooski, VT, USA) at 490 nm excitation and at 510 nm emission.

4.4.11 Anti-metastatic assays

Cologenic assay: Cancer cells (1000 cells/mL) were seeded onto a 6 well cell culture plate and subjected to treatments. The medium was removed and the cells were kept in fresh medium for 9 days or till the control cells achieved 50 cells per colony. The medium was removed, fixed in 70% ethanol and stained using 1% crystal violet in ethanol. The plate was air dried and the colonies were counted and photographed. Colonies were counted manually and plotted as a percent clonogenicity. Plec@Cs@PLGA treated colonies were considered as 100 %.

Wound healing assay: Cancer cells (1×10^6 cells/mL) were maintained in DMEM medium on 6 well cell culture plates. After the cells attained con-fluency, a wound was created using a sterile 100 μ L micropipette tip. Cells and kept at 37°C in 5% CO₂ incubator. The cells were viewed at 10 X objective and photographed using a phase contrast microscope (Olympus 1 \times 51, Singapore) at various time points (0, 12 and 24 hour) until the monolayer was completely closed. The area of the wound created was quantified using Image J software (version 1.5i).

Invasion and migration assay: The invasive and migration potential of cancer cells in presence of compounds was carried out using 24 well plate transwell inserts (353097, Corning Falcon, USA). For the invasion assay, the 24 well transwell chambers (8 μ m pore size polycarbonate filters) were applied with matrigel (354234, Corning Falcon, USA) on the innerside and kept at 37°C in 5% CO₂ incubator. Cancer cells were seeded (1×10^6 cells/mL) in serum free medium onto the transwell chambers with or without compounds (5 μ g/mL). DMEM medium with 10% serum was added onto the 24 well plates which served as the chemo-attractant. The plates were kept at 37°C in 5% CO₂ incubator for 24 hour incubation. The transwell inserts were then taken and cells present in the upper chamber were removed using cotton swab and filters were stained using 1% crystal violet. The invaded cells present at the lower side of the inserts were visualized, counted and photographed using an optical microscope. Similarly, the

migration assay was carried out using the above protocol except that the transwell inserts were devoid of matrigel coating.

4.4.12 Live cell Raman imaging. Evaluation of the internalization and apoptosis was done with the aid of a confocal Raman microscope (WI-Tec, Inc., Germany) with a laser beam directed to the cell surface through a 20X objective with a Peltier-cooled CCD detector. 20 μ L of nanoconstructs were added to WI-38 and PANC-1 cells followed by incubation at 37 °C for 1 h. 2D SERS mapping was recorded as described before.

4.4.13 Metabolic profiling. The cells were washed using ice-cold PBS and collected with a cell scraper, transferred to a pre-chilled 15-ml conical tube, and kept on ice. A total cell count using a hemocytometer was performed, and approximately 10 million cells were aliquot into tubes and spun down at 4°C. Removed the excess PBS and the cell pellets were re-suspended in 150 μ L molecular biology grade water and lysed by two cycles of freeze-thaw, 30 Sec at 80°C, followed by 90 Sec in a water bath at room temperature, followed by 30 Sec of sonication and measured the protein concentration by Bradford assay to normalize the protein content in all samples. 600 μ l methanol was added to the cell suspension, vortex and incubated on ice for 15 min. To this, 600 μ l of chloroform was added to the tubes, vortex and centrifuged at 13,000 rpm for 10 min at 15°C. The two phases were transferred to a fresh tube, carefully avoiding the interface. Chilled ACN (600 μ l) was added to each tube, vortex, and incubated at -80°C for 2 h. The tubes were centrifuged at 13,000 rpm for 10 min at 4°C; the supernatant was transferred to fresh tubes and dried under vacuum. The metabolic profiling was performed using both positive and negative modes of RPLC and HILIC chromatography. All the raw data obtained from the four assays were analyzed using ProgenesisQI data analysis software (Nonlinear Dynamics, UK) for peak picking, chromatographic alignment, normalization to produce peak intensities, adduct ions deconvolution, and feature identification by searching against the detected and quantified metabolite entries from the human metabolome database (HMDB).

4.5 References

1. Rahib, L.; Smith, B. D.; Aizenberg, R.; Rosenzweig, A. B. . & Fleshman, J. M.; Matrisian, L. M. Projecting cancer incidence and deaths to 2030: the unexpected

-
- burden of thyroid, liver, and pancreas cancers in the United States. *Cancer Res.* **74**, 2913–2921 (2014).
2. Siegel, R. L.; Miller, K. D.; Jemal, A. Cancer statistics, 2018. *CA Cancer J Clin* **68**, 7–30 (2018).
 3. Gaidhani, R. H. & Balasubramaniam, G. An epidemiological review of pancreatic cancer with special reference to India. *Indian J. Med. Sci.* **73**, 1–11 (2021).
 4. Moore, M.J.; Goldstein, D.; Hamm, J.; Figer, A.; Hecht, J.R.; Gallinger, S.; Au, H.J.; Murawa, P.; Walde, D. . & Wolff, R. . Erlotinib plus gemcitabine compared with gemcitabine alone in patients with advanced pancreatic cancer: A phase III trial of the National Cancer Institute of Canada Clinical Trials Group. *J. Clin. Oncol.* **25**, (2007).
 5. Conroy, T.; Desseigne, F.; Ychou, M.; Bouché, O.; Guimbaud, R.; Bécouarn, Y.; Adenis, A.; Raoul, J.-L. . & Gourgou-Bourgade, S.; de la Fouchardière, C. FOLFIRINOX versus gemcitabine for metastatic pancreatic cancer. *N. Engl. J. Med* **364**, 1817–1825 (2011).
 6. Amanam, I. & Chung, V. Targeted therapies for pancreatic cancer. *Cancers (Basel)*. **10**, (2018).
 7. Adamska, A., Domenichini, A. & Falasca, M. Pancreatic ductal adenocarcinoma: Current and evolving therapies. *Int. J. Mol. Sci.* **18**, (2017).
 8. Danhier, F. *et al.* PLGA-based nanoparticles: An overview of biomedical applications. *J. Control. Release* **161**, 505–522 (2012).
 9. Sierra, J. R. & Tsao, M. S. c-MET as a potential therapeutic target and biomarker in cancer. *Ther. Adv. Med. Oncol.* **3**, S21–S35 (2011).
 10. Kim, H. J. *et al.* C-MET as a Potential Therapeutic Target in Ovarian Clear Cell Carcinoma. *Sci. Rep.* **6**, 1–9 (2016).
 11. Cassinelli, G. *et al.* Inhibition of c-Met and prevention of spontaneous metastatic spreading by the 2-indolinone RP-1. *Mol. Cancer Ther.* **5**, 2388–2397 (2006).
-

-
12. Eder, J. P., Vande Woude, G. F., Boerner, S. A. & Lorusso, P. M. Novel therapeutic inhibitors of the c-Met signaling pathway in cancer. *Clin. Cancer Res.* **15**, 2207–2214 (2009).
 13. Caccia, D. *et al.* Dasatinib reduces FAK phosphorylation increasing the effects of RPI-1 inhibition in a RET/PTC1-expressing cell line. *Mol. Cancer* **9**, 1–14 (2010).
 14. Decorte, B. L. Underexplored Opportunities for Natural Products in Drug Discovery. *J. Med. Chem* **59**, 9295 (2016).
 15. Beutler, J. A. Natural Products as a Foundation for Drug Discovery THE USE OF NATURAL PRODUCTS. *Curr. Protoc. Pharmacol.* 1–21 (2009)
doi:10.1002/0471141755.ph0911s46.
 16. Cragg, G. M., Newman, D. J. & Snader, K. M. Natural products in drug discovery and development. *J. Nat. Prod.* **60**, 52–60 (1997).
 17. Kumar, S. & Deshmukh, R. Embelin as a Potential Drug Molecule: A Review. *J. Pharmacogn. Nat. Prod.* **03**, (2017).
 18. Ko, J. H. *et al.* The application of embelin for cancer prevention and therapy. *Molecules* **23**, 1–14 (2018).
 19. Xu, M. *et al.* Embelin derivatives and their anticancer activity through microtubule disassembly. *Planta Med.* **71**, 944–948 (2005).
 20. Wang, A., Zhang, B., Zhang, J. & Wu, W. Embelin-induced brain glioma cell apoptosis and cell cycle arrest via the mitochondrial pathway. *Oncol. Rep.* **29**, 2473–2478 (2013).
 21. Bahrami, B. *et al.* Nanoparticles and targeted drug delivery in cancer therapy. *Immunol. Lett.* **190**, 64–83 (2017).
 22. Kelly, K. A. *et al.* Targeted nanoparticles for imaging incipient pancreatic ductal adenocarcinoma. *PLoS Med.* **5**, 0657–0668 (2008).
 23. Sanna, V. *et al.* Targeted Nanoparticles for the Delivery of Novel Bioactive Molecules
-

-
- to Pancreatic Cancer Cells. *J. Med. Chem.* **59**, 5209–5220 (2016).
24. Nair, J. B. *et al.* Elucidating a Thermoresponsive Multimodal Photo-Chemotherapeutic Nanodelivery Vehicle to Overcome the Barriers of Doxorubicin Therapy. *ACS Appl. Mater. Interfaces* **12**, 43365–43379 (2020).
25. Joseph, M. M. *et al.* Targeted Theranostic Nano Vehicle Endorsed with Self-Destruction and Immunostimulatory Features to Circumvent Drug Resistance and Wipe-Out Tumor Reinitiating Cancer Stem Cells. *Small* **16**, (2020).
26. Zhang, N., Fu, J. N. & Chou, T. C. Synergistic combination of microtubule targeting anticancer fludellone with cytoprotective panaxytriol derived from panax ginseng against MX-1 cells in vitro: Experimental design and data analysis using the combination index method. *Am. J. Cancer Res.* **6**, 97–104 (2016).
27. Fu, J. *et al.* Drug combination in vivo using combination index method: Taxotere and T607 against colon carcinoma HCT-116 xenograft tumor in nude mice. *Synergy* **3**, 15–30 (2016).
28. Su, S. *et al.* ‘Triple-Punch’ Strategy for Triple Negative Breast Cancer Therapy With Minimized Drug Dosage and Improved Antitumor Efficacy. *ACS Nano* **9**, 1367–1378 (2015).
29. Babu, A. *et al.* Chemodrug delivery using integrin-targeted PLGA-Chitosan nanoparticle for lung cancer therapy. *Sci. Rep.* **7**, 1–17 (2017).
30. Wang, F. *et al.* Preparation and characterizations of a novel deoxycholic acid-O-carboxymethylated chitosan-folic acid conjugates and self-aggregates. *Carbohydr. Polym.* **84**, 1192–1200 (2011).
31. Cao, Y., Wang, B., Wang, Y. & Lou, D. Dual drug release from core-shell nanoparticles with distinct release profiles. *J. Pharm. Sci.* **103**, 3205–3216 (2014).
32. Huang, Y. *et al.* PEG-derivatized embelin as a dual functional carrier for the delivery of paclitaxel. *Bioconjug. Chem.* **23**, 1443–1451 (2012).
-

-
33. Nikolovska-Coleska, Z. *et al.* Discovery of Embelin as a Cell-Permeable, Small-Molecular Weight Inhibitor of XIAP through Structure-Based Computational Screening of a Traditional Herbal Medicine Three-Dimensional Structure Database. *J. Med. Chem.* **47**, 2430–2440 (2004).
 34. Xiao, B. *et al.* Co-delivery of camptothecin and curcumin by cationic polymeric nanoparticles for synergistic colon cancer combination chemotherapy. *J. Mater. Chem. B* **3**, 7724–7733 (2015).
 35. Gomes, C., Moreira, R. G. & Castell-Perez, E. Poly (DL-lactide-co-glycolide) (PLGA) Nanoparticles with Entrapped trans-Cinnamaldehyde and Eugenol for Antimicrobial Delivery Applications. *J. Food Sci.* **76**, (2011).
 36. Gottlieb, E., Armour, S. M., Harris, M. H. & Thompson, C. B. Mitochondrial membrane potential regulates matrix configuration and cytochrome c release during apoptosis. *Cell Death Differ.* **10**, 709–717 (2003).
 37. Jayadev S. Arya, Manu M. Joseph, Daisy R. Sherin, Jyothi B. Nair, Thanathu K. Manojkumar, and K. K. M. Exploring Mitochondria-Mediated Intrinsic Apoptosis by New Phytochemical Entities: An Explicit Observation of Cytochrome c Dynamics on Lung and Melanoma Cancer Cells. *J. Med. Chem.* **62**, 8311–8329 (2019).
 38. Park, N., Baek, H. S. & Chun, Y. J. Embelin-induced apoptosis of human prostate cancer cells is mediated through modulation of Akt and β -catenin signaling. *PLoS One* **10**, 1–17 (2015).
 39. Peng, M. *et al.* Embelin inhibits pancreatic cancer progression by directly inducing cancer cell apoptosis and indirectly restricting IL-6 associated inflammatory and immune suppressive cells. *Cancer Lett.* **354**, 407–416 (2014).
 40. Nigam, N. *et al.* Targeting mortalin by embelin causes activation of tumor suppressor p53 and deactivation of metastatic signaling in Human Breast Cancer Cells. *PLoS One* **10**, 1–15 (2015).
 41. Movasaghi, Z., Rehman, S. & Rehman, I. U. Raman Spectroscopy of Biological
-

-
- Tissues. *Appl. Spectrosc. Rev.* **42**, 493–541 (2015).
42. Fenn, M. B. *et al.* Raman spectroscopy for clinical oncology. *Adv. Opt. Technol.* **2011**, (2011).
43. Malins, D. C. *et al.* Age-related radical-induced DNA damage is linked to prostate cancer. *Cancer Res.* **61**, 6025–6028 (2001).
44. Deavall, D. G., Martin, E. A., Horner, J. M. & Roberts, R. Drug-induced oxidative stress and toxicity. *J. Toxicol.* **2012**, (2012).
45. Siddiqui, A. & Ceppi, P. A non-proliferative role of pyrimidine metabolism in cancer. *Mol. Metab.* **35**, 100962 (2020).
46. Nakagawa, T. *et al.* Fructose contributes to the Warburg effect for cancer growth. *Cancer Metab.* **8**, 1–12 (2020).
47. Krause, N. & Wegner, A. Fructose Metabolism in Cancer. *Cells* **9**, (2020).
48. Ji, C., Amarnath, V., Pietenpol, J. A. & Marnett, L. J. 4-Hydroxynonenal induces apoptosis via caspase-3 activation and cytochrome c release. *Chem. Res. Toxicol.* **14**, 1090–1096 (2001).
49. Dalleau, S., Baradat, M., Guéraud, F. & Huc, L. Cell death and diseases related to oxidative stress:4-hydroxynonenal (HNE) in the balance. *Cell Death Differ.* **20**, 1615–1630 (2013).

ABSTRACT

Name of the Student: Arya J. S.	Registration No. :10CC17J39003
Faculty of Study: Chemical sciences	Year of Submission: 2022
CSIR Lab: CSIR-National Institute for Interdisciplinary Science & Technology (CSIR-NIIST), TVM, Kerala	Name of the Supervisor: Dr. Kaustabh Kumar Maiti
Title of the thesis: Exploring the Chemotherapeutic Potential of Semi-synthetically Derived New Phytochemical Entities and Nano Delivery System	

Natural products (Np) play a vital role in the development of modern drug discovery as quiet a large number of modern medicines have been isolated from various natural sources based on their practice in folklore medicine. With the development of new molecular targets-based drug discovery, there is a collective demand for novel molecules for screening. In this scenario our efforts are directed towards the synthetic modification of naturally available bioactive molecules as potential lead molecules towards anti-cancer therapy.

Chapter 1 outlined a brief introduction about the major role of natural products in drug discovery and development with special emphasis on the treatment of cancer. In addition, the chapter also highlighted the major naturally derived drug molecules which are in clinical practice, clinical trial and preclinical trial. In **chapter 2A**, the semi-synthetic modification on Hy by one pot multi-component reaction (MCR) and [3+2] cycloaddition strategy to append five membered isoxazole and isoxazolone moieties was discussed. By executing detailed in vitro and in silico screening we have selected two potent new phytochemical entities (NPCEs) active against lung cancer and melanoma. **Chapter 2B** discussed the detailed mechanistic evaluation of the mode of apoptosis induced by the selected NPCEs. Surface-enhanced Raman spectroscopy (SERS) was employed to study the DNA fragmentation and molecular dynamics associated with the synthetic analogs on cancer cells. Cyt C release kinetics were also monitored with the aid of SERS platform. In **chapter 3**, the synthesis of Pt, Ir and Ru metal complexes of germacrone, a sesquiterpene isolated from the rhizomes of *Curcuma raktakanta* was carried out. Detailed cytotoxicity analysis revealed the potent metal complex from the synthesized derivatives. The selected molecule was able to overcome the drug resistance along with the selective toxicity towards cancer cells. Synergic combination of naturally occurring cytotoxic agent embelin and c-Met inhibitor RPI-1 was established for an efficient therapeutic potential against pancreatic carcinoma cell line PANC-1 was accomplished in **chapter 4**. The combination with a pre-optimized ratio was loaded in a biocompatible and biodegradable PLGA nano-carrier targeted delivery system. The designed biocompatible and biodegradable embelin and RPI-1 loaded targeted nano-construct was found to be a potential system for further pre-clinical studies.

Details of the Publications Emanating from the Thesis Work

Published

1. **Jayadev S. Arya**, Manu M. Joseph, Daisy R. Sherin, Jyothi B. Nair, Thanathu K. Manojkumar and Kaustabh K. Maiti*, Exploring Mitochondria-Mediated Intrinsic Apoptosis by New phytochemical Entities: An Explicit Observation of Cytochrome c Dynamics on Lung and Melanoma Cancer Cells *J. Med. Chem.* **2019**, *62*, 8311–8329

Manuscript under Preparation

1. **Jayadev S. Arya**, Manu M. Joseph, Vishnu Priya Murali, Vidyalakshmi M. S. and Kaustabh K. Maiti*, Development of biocompatible polymer-based core-shell nano delivery system for the synergic release of embelin and RPI-1, 2022, (**Manuscript under preparation**).
2. **Jayadev S. Arya**, Manu M. Joseph, Vishnu Priya Murali, Daisy R. Sherin, Thanathu K. Manojkumar and Kaustabh K. Maiti*, Pyrogermacrone/germacrone substituted oxaliplatin analogues as active molecule against triple negative breast cancer, 2022, (**Manuscript under preparation**)

Papers Published from Other Related Works

1. Manu. M. Joseph, Nisha. Narayanan, Jyothi. B. Nair, Varsha Karunakaran, A. N. Ramya, P. T. Sujai, G. Saranya, **Jayadev. S. Arya**, Vineeth. M. Vijayan, Kaustabh. Kumar Maiti; Exploring the margins of SERS in practical domain: An emerging diagnostic modality for modern biomedical applications *Biomaterials* **2018**, *181*, 140-181.
2. Shruti Mishra, Sumit Singh Verma, Vipin Rai, Nikee Awasthee, **Jayadev S. Arya**, Kaustabh K. Maiti and Subash C. Gupta*, *Curcuma raktakanda* Induces Apoptosis and Suppresses Migration in Cancer Cells: Role of Reactive Oxygen Species, *Biomolecules* **2019**, *9*, 159
3. Jyothi B. Nair, Manu M. Joseph,* **Jayadev S. Arya**, Padincharapad Sreedevi, Palasseri T. Sujai, and Kaustabh Kumar Maiti*, Elucidating a Thermoresponsive Multimodal PhotoChemotherapeutic Nanodelivery Vehicle to Overcome the Barriers of Doxorubicin Therapy, *ACS Appl. Mater. Interfaces* **2020**, *12*, 43365–43379.

4. Adukkadan N Ramya, **Jayadev S Arya**, Murali Madhukrishnan, Shanmughan Shamjith, Murukan S Vidyalakshmi and Kaustabh K. Maiti, Raman Imaging: An Impending approach towards cancer diagnosis, *Chem. Asian J.* **2021**, *16*,409-422.

List of Conference Presentations

1. Biocompatible core-shell polymer-based Nano-carrier system for the synergistic delivery of Embelin and RPI-1 to pancreatic adenocarcinoma Cell, **Arya J. S.**, Vishnupriya Murali, Kaustabh Kumar Maiti, International Conference on Chemistry for Human Development (ICCHD-2020), organized by Professor Asima Chatterjee Foundation with University of Calcutta and Heritage Institute of Technology. (**Poster presentation**)
2. Novel potent anticancer agents derived from hydnocarpin induces mitochondria mediated apoptosis and monitoring cyt c release through Raman fingerprinting, **Arya J. S.**, Kaustabh Kumar Maiti, 8th Annual Meeting of Indian Academy of Biomedical Sciences organized by CSIR-National Institute for Interdisciplinary Science and Technology, Thiruvananthapuram. (**Poster presentation**)
3. Exploration of New Phytochemical Entities from *Hydnocarpus Wightiana* Blume: Evolved as Potent Anticancer Hits inducing Mitochondria mediated Apoptosis through Cyt c Release, **Arya J. S.**, Manu M. Joseph, Kaustabh Kumar Maiti, 31st Kerala Science Congress, Organized by Kerala State Council for Science, Technology and Environment at Fatima Mata National College, Kollam. (**Oral presentation**)
4. Exploring Hydnocarpin wightiana Blume for the Development of New Chemical Entities Towards Cancer Treatment, **Arya J. S.**, Manu M. Joseph, Kaustabh Kumar Maiti, International Conference on Trends in Biochemical and Biomedical Research, Organized by Department of Biochemistry, Institute of Science, Banaras Hindu University, Varanasi. (**Oral presentation**)
5. Semisynthetic modification of hydnocarpin for the Development of New Chemical Entities Towards Anticancer Potential, **Arya J. S.**, Kaustabh Kumar Maiti, 2nd International Conference on Nutraceutical and Chronic Diseases held at Bogmallo Beach Resort, Bogmallo, Goa. (**Poster presentation**)

Exploring Mitochondria-Mediated Intrinsic Apoptosis by New Phytochemical Entities: An Explicit Observation of Cytochrome *c* Dynamics on Lung and Melanoma Cancer CellsJayadev S. Arya,^{†,‡} Manu M. Joseph,^{*,†} Daisy R. Sherin,[§] Jyothi B. Nair,^{†,‡} Thanathu K. Manojkumar,^{*,§} and Kaustabh K. Maiti^{*,†,‡,§}[†]Chemical Sciences and Technology Division and [‡]Academy of Scientific and Innovative Research (AcSIR), CSIR-National Institute for Interdisciplinary Science and Technology (CSIR-NIIST), Thiruvananthapuram 695 019, India[§]Centre for Computational Modeling and Data Engineering, Indian Institute of Information Technology and Management-Kerala (IIITM-K), Thiruvananthapuram 695581, India

Supporting Information

ABSTRACT: Hydnocarpin (Hy) is a flavonoid isolated and purified from the seeds of *Hydnocarpus wightiana* Blume. Herein, we have developed a built-in semi-synthetic modification on Hy by one-pot multi-component reaction and a [3 + 2] cycloaddition strategy to append five membered isoxazole and isoxazolone as new phytochemical entities (NPCEs). Two selected NPCEs viz Hy-ISO-VIII and Hy-ISO-G from the library of 20 newly synthesized derivatives after in vitro screening unveiled promising cytotoxicity and induced caspase-mediated apoptosis against the human lung and melanoma cancer cells which were well supported by virtual screening based on ligand binding affinity and molecular dynamic simulations. As a new insight, we introduced surface-enhanced Raman spectroscopy to identify the chemo-marker molecular fingerprint to confirm the cellular uptake, cytochrome *c* release, and DNA fragmentation in a label-free manner. The present findings throw up a surfeit of seminal reasons behind the semi-synthetic modification of Hy, stepping forward to cancer chemotherapy.



we introduced surface-enhanced Raman spectroscopy to identify the chemo-marker molecular fingerprint to confirm the cellular uptake, cytochrome *c* release, and DNA fragmentation in a label-free manner. The present findings throw up a surfeit of seminal reasons behind the semi-synthetic modification of Hy, stepping forward to cancer chemotherapy.

INTRODUCTION

Phytochemicals can be viewed as a population of privileged structures selected by evolutionary pressure for the treatment of wide range of human diseases. Many of the compounds isolated from natural sources offer moderate to high anticancer properties, and hence, there are persisting opportunities to optimize those molecules to generate promising leads by strategic semi-synthetic modifications.¹ Structural modification of isolated molecules are intended to improve their potency, selectivity, physicochemical properties which again enhance their chemical and metabolic stability for an appealing biochemical and pharmacokinetic properties including absorption, distribution, metabolism, and excretion.² In this context, a potent medicinal plant, *Hydnocarpus wightiana* Blume was widely explored by traditional healers and folk medical systems. The oil extracted from the seeds was used for the treatment of leprosy, chronic skin infections, dressing of wounds, and ulcers. Hydnocarpin (Hy), a flavonoid, is isolated from the acetone extract of the seeds of this plant.³ We have previously reported the enhanced cancer-selective cytotoxicity and anti-metastatic potential of Hy by conjugation with a highly efficient, nontoxic cell-penetrating guanidinium-rich poly(propylene imine) dendron.⁴

In the rational drug design, heterocycles hold promising physicochemical properties in various therapeutic categories including antitumor, antiviral, and antibacterial agents and constitutes to the major structural unit of most marketed drugs. The strategic inclusion of heterocyclic fragments is the rationale behind the drug design, which is again accompanying their versatility and selective nature of the platform. Out of the many synthesized heterocyclic molecules, approved by US FDA or under clinical trials, isoxazole and isoxazolone containing heterocycles play a promising role in cancer therapeutics.⁵ Keeping this aspect in mind, we demonstrated new phytochemical entities (NPCEs) by a semisynthetic inclusion of functionalized isoxazole and isoxazolone pharmacophore into Hy. The moderate anticancer properties of the Hy-flavonoid core obtained in high yield with an easy isolation process encouraged us to adopt the 3 + 2 cycloaddition and one-pot multicomponent reaction (MCR) mode to append isoxazole and isoxazolone heterocycles which is being recognized in various drugs like sulfamethoxazole, valdecocin, and so forth.

Received: July 8, 2019

Published: August 8, 2019

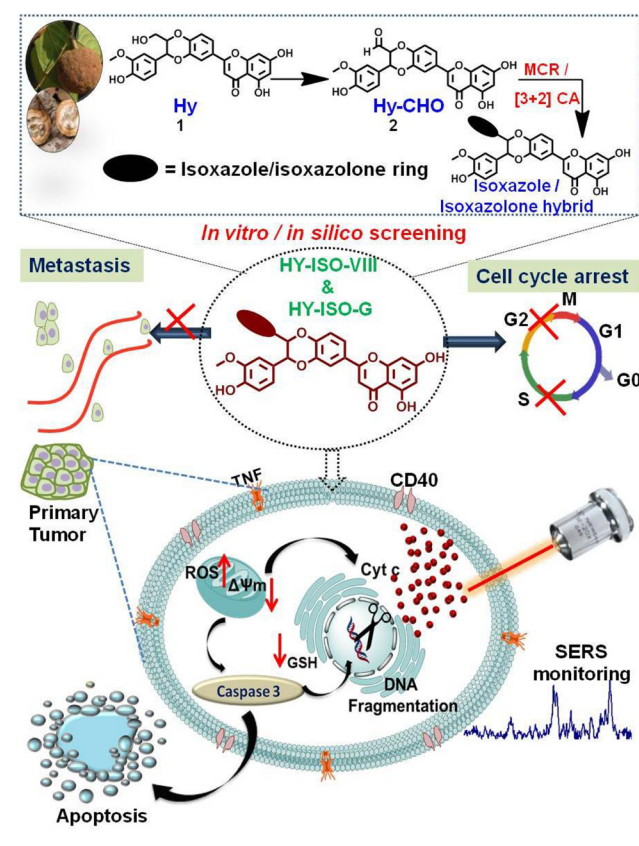
In view of the present exigency for the development of antiproliferative NPCEs, herein, we report the library of 20 novel Hy-isoxazole/isoxazolone (HY-ISO) derivatives with an objective to select an ideal antineoplastic candidate for the bedside application. The major emphasis on therapeutic efficiency of NPCEs has been exploited with in-depth biological investigations to decipher its possible molecular mechanism of action. Two NPCEs viz Hy-ISO-VIII and HyISO-G were selected after primary cytotoxic profiling by *in vitro* as well as *in silico* virtual screening methods. The preferential execution of apoptosis was subjected with the two potent Hy-derivatives by multiple assays. The cell cycle distribution and biomolecular cytoplasmic changes with respect to reactive oxygen species (ROS)-mediated glutathione (GSH) depletion were also studied. Further, the invasion, migration, and clonogenic assays were intended to measure the antimetastatic potential of the identified leads. In addition to this, the complex dynamics associated with the apoptosis were effectively traced using the signature chemo marker Raman peaks. Label-free surface-enhanced Raman spectroscopy (SERS) measurements provided qualitative and semiquantitative identification of various biomolecular analytes in the complex cellular environment.⁶ Moreover, SERS enabled to track minute molecular-level changes associated with the cell death process, including protein denaturation, DNA fragmentation, and changes in the lipid profile. This approach is utilized to monitor the action of drugs, drug metabolites, and imaging agents which lack the inherent fluorescence property.^{7,8} As a novel strategy, intracellular dynamics of cytochrome *c* (cyt *c*) during mitochondria-mediated apoptosis was traced out by the Raman fingerprint in a label-free manner (Scheme 1). It is sufficient to say that very well-planned semi-synthetic approaches could produce fruitful outputs which are palpable in the long run for eradicating cancer.

RESULTS AND DISCUSSION

Semi-synthetic Strategy of Isolated Hydnocarpin.

Initially, Hy (1), was isolated in significant yield (3 g Hy from 20 g of acetone extract) from the acetone extract of the seeds of *Hydnocarpus wightiana* Blume. In the course of synthetic modification, the primary hydroxyl group at the C-9' position of Hy was first transformed to corresponding aldehyde (2) via Moffatt oxidation (Supporting Information Scheme S1). To functionalize Hy with the isoxazole moiety, one-pot [3 + 2] cycloaddition reaction was employed to construct hydnocarpin-isoxazole derivatives. We have optimized the reaction condition (Scheme 2a, Supporting Information Table S1) where hydnocarpin aldehyde 2 (HY-CHO), alkyne derivative 3c, and hydroxylamine hydrochloride in the presence of *N*-bromosuccinimide and NaOH afforded the product isoxazole appended Hy in 91% yield (entry 7, Supporting Information Table S1). In the second series, Hy was appended with the isoxazolone moiety in the presence of the boric acid-catalyzed MCR strategy (Scheme 2b). The best reaction condition (Supporting Information Table S2) was achieved where HYCHO 2, β -keto ester 5a, and hydroxylamine hydrochloride in the presence of boric acid in aqueous medium in room temperature afforded the product isoxazolone-coupled Hy in 85% yield (entry 4, Supporting Information Table S2). Successively, we synthesized a series of Hy-isoxazole and Hy-isoxazolone derivatives, 4a–j and 6a–j, respectively (Scheme 2c). HRMS and NMR (¹H and ¹³C) confirmed all semi-synthetic NPCEs. Isoxazoles and isoxazolones are versatile

Scheme 1. Hy-Issoxazole/Issoxazolone Derivatives Promoting Apoptosis and Inhibiting Metastasis

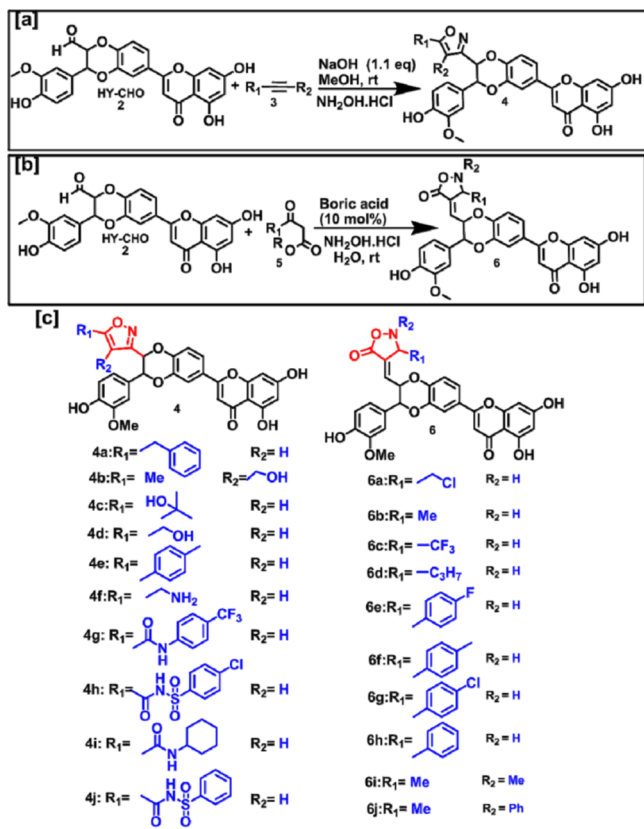


groups present in many biologically active molecules, with anti-inflammatory, anticancer, and many other pharmacological properties.^{9,10} A similar kind of heterocyclic derivatives has attracted synthetic chemists which enhances the pharmacokinetic activity. Incorporation of these heterocycle ring changes the molecular structure which promoted the possible interaction with the protein core because of the presence of the additional nitrogen and oxygen atom. In addition, the synthetic easiness and excellent yield observed for the derivatives encouraged us to prepare a library of novel HY-ISO derivatives. Hence, for developing potent antiproliferative agents from Hy, we envisioned that the coupling of the isoxazole/isoxazolone ring would be an intelligent approach.

Primary Cytotoxicity Screening of Hy-Analogues.

Lung cancer and metastatic melanoma represents two potent forms of cancer which are clinically difficult to vanquish. Primary selection based on the cytotoxicity of Hy-derivatives was evaluated through 3-[4,5-dimethylthiazol-2-yl]-2,5-diphenyltetrazolium (MTT) assay where Hy analogues 4a–j and 6a–j were assessed by comparing with parent Hy and the first intermediate Hy-CHO on human metastatic melanoma (A375), human lung adenocarcinoma (A549), and human normal lung fibroblast (WI-38) cell lines after 24 and 48 h of treatment (Supporting Information Figures S1–S6). It was interesting to observe that all the selected derivatives except 4d, 4e, 6b, and 6j showed significant cell death against parent Hy as reflected in lower IC₅₀s (Table 1). Hy-analogues 4h, 6a, and 6c showed indiscriminate cytotoxicity in both cancer and normal lung fibroblast cells, and hence, these compounds were eliminated from the primary screening criteria. Based on the observations with the lower IC₅₀s on cancer cells and lower

Scheme 2. (a) 3 + 2 Cycloaddition Strategy Adopted for the Synthesis of Isoxazole Derivatives; (b) One-Pot Multicomponent Strategy Adopted for the Synthesis of Isoxazolone Derivatives; (c) Semisynthetic Derivatives of Hy-Isoxazole and Hy-Isoxazolone Hybrids



cytotoxicity toward normal fibroblasts, four Hy-derivatives (Hy-ISOs) were selected from both the series as primary active NCPs for next-level screening studies (Supporting Information Tables S3 and S4). These results suggested that the incorporation of isoxazole and isoxazolone within Hy-analogues contributed significant role toward the improved cytotoxicity. In fact, isoxazole and isoxazolone rings have been reported as the potent heterocycle skeleton in many drug intermediates toward various therapeutic potential including high antiproliferative activity.^{5,11} When these two biologically active heterocyclic moiety were coupled together, the combined effect of Hy-flavonoid induced the enhanced cytotoxicity in cancer cells. The compounds may undergo oxidation to produce cytotoxic hydrogen peroxide that increases the antiproliferative potential of the novel NCPs.¹²

Computational Screening of Hy-Analogues. Next, the screening strategy was extended by employing computational tools where we employed the molecular docking ability of the previously screened analogues toward the selected protein domains involved in the apoptotic machinery. Hence, the selected Hy-isoxazole hybrids 4a, 4c, 4f, 4g, and Hyisoxazolone hybrids 6e, 6f, 6g, 6i, which exhibited significantly higher cytotoxicity, were subjected to molecular docking studies. The QikProp screening for pharmacokinetic/ADMET parameters (Supporting Information Table S5) shows that the compounds 4a, 4c, 4f, 4g, 6e, 6f, 6g, and 6i are good candidates with few #stars and the molecular weights are below 700. All of them are nontoxic to the central nervous system with minimum

CNS value of -2 . The total solvent accessible surface area (SASA) and its hydrophilic components (FISA) are well within the range. All molecules exhibit H-bond donating and accepting capacity, with a maximum value of 4 in the case of 4f, and 10 in the case of 4g and 6f, respectively. The octanol/water partition coefficient (QPlog_{o/w}) and binding to human serum albumin (QPlogK_{hsa}) values indicate better absorption in the blood stream. The aqueous solubility (QPlogS) values are indicative of better solubility of the drug in water, which aids in its bioavailability. To conclude, all the eight selected compounds are good drug candidates with minimum violation from Lipinski's rule of five (Ro5).

In order to find out the binding affinity of the above-mentioned ligands with the selected receptors, we carried out the docking study of prepared ligands against the grid generated for the receptors. The binding affinity was compared in terms of *G*-score or *D*-score values of best binding poses. It is clear that the binding affinity of the ligands is maximum with 1OXN and 1OXQ (Figure 1a). The comparison of *G*-score, *D*-score, and interacted residues in the case of eight selected compounds is tabulated (Supporting Information Table S6). All the eight ligands show higher affinity toward the receptors through H-bonding and π - π stacking interaction. In the case of both 1OXN and 1OXQ, π - π stacking interaction exists between the ligand with Phe81, except in the case of 4a and 6e, which act as a vital factor in better binding. Another important interaction observed because of H-accepting capacity of Ala80 from a donor atom of the ligand. The compound 4g and 6g (Figure 1b,c) are the best ones compared to Hy (Figure 1d), in inhibiting 1OXN and 1OXQ as proved by experimental results. The three-dimensional crystalline structures of the peptide antagonists (PDB code: 1OXN and 1OXQ) are given in Figure 1e,f. The interaction diagrams of best-scored poses of 4g and 6g in 1OXN and 1OXQ are shown in the Supporting Information Figure S7. 4g binds with Tyr128 and Arg123 through H-bond and π - π stacking interaction with Phe81 and Tyr128 while 6g forms π - π stacking interaction with Phe81 in the binding pocket of 1OXN. In the binding site of 1OXQ, 4g forms H-bond with Asp96 and π - π stacking with His118 and Phe81, whereas in 6g, there is an additional H-bond with Ala80 which stabilizes the interaction.

Pharmacophore Modelling. The pharmacophore (Supporting Information Figure S8a) identified from nine ligands are screened based on different scores to identify the best one (ADHRRR), which has a survival score: 6.283, site score: 0.842, vector score: 0.945, volume score: 0.701, and phase hypo score of 1.377. The best model obtained have one acceptor, one donor, one hydrophobic region, one negative ionic, and three aromatic regions, in which R(17), R(19), and A(10) are in one plane while the others are aligned in a perpendicular plane. One of the most active compounds HY-ISO-G was mapped in the best model and depicted in the Supporting Information Figure S8b. This pharmacophore model effectively predicts the important features of antimetastatic compounds, which would help in the generation of novel leads in this category.

Selection Strategy Based on Primary Screening Studies. After evaluation of the primary screening based on cancer cell-specific IC₅₀s, followed by molecular docking analysis, we come up with a strategy of selecting the most potent candidates for the next-level studies. Initially, the most effective compounds are shortlisted in terms of IC₅₀s selectively on cancer cells from both the series. Here, the

Table 1. IC₅₀ Values of Hydnocarpin-Isoxazole/Isoxazolone Derivatives in A375, A549, and WI-38 Cells over a Time of 24 and 48 h^a

no:	IC ₅₀ (μM)					
	A375		A549		WI38	
	24 h	48 h	24 h	48 h	24 h	48 h
1	71.6 ± 0.9	49.2 ± 1.1	88.6 ± 1.9	68 ± 0.9	nil	nil
2	63 ± 1.4	43.8 ± 0.8	96 ± 2	87.8 ± 1.8	nil	nil
4a	4.6 ± 1.8	0.9 ± 0.05	7 ± 0.09	3.9 ± 0.18	nil	nil
4b	68.7 ± 0.5	46.5 ± 0.7	68 ± 1.8	51 ± 1.5	nil	nil
4c	1.43 ± 0.08	0.65 ± 0.07	4.8 ± 0.05	2.9 ± 0.1	nil	nil
4d	nil	74.9 ± 1.7	nil	nil	nil	nil
4e	nil	nil	nil	77.4	nil	nil
4f	7.5 ± 0.8	4.6 ± 0.4	5.2 ± 0.08	2.2 ± 0.07	nil	nil
4g	4 ± 0.5	0.95 ± 0.06	3.6 ± 0.08	0.76 ± 0.04	nil	nil
4h	6.2 ± 0.07	4.2 ± 0.3	8.7 ± 0.4	6.6 ± 0.05	nil	54.6 ± 1.7
4i	66.8 ± 1.8	28.8 ± 0.9	80 ± 2.1	14.5 ± 0.8	nil	nil
4j	7.2 ± 0.8	3.5 ± 0.08	51 ± 2.1	6.3 ± 0.6	nil	nil
6a	0.04 ± 0.01	0.035 ± 0.01	0.095 ± 0.02	0.07 ± 0.006	5.5 ± 0.04	4.9 ± 0.08
6b	nil	nil	nil	nil	nil	nil
6c	2 ± 0.04	0.83 ± 0.07	2.1 ± 0.1	16.4 ± 0.2	nil	95
6d	92.7 ± 2.2	60 ± 1.9	nil	nil	nil	nil
6e	13.7 ± 0.4	7.9 ± 0.6	1.4 ± 0.08	7.5 ± 0.09	nil	nil
6f	9.2 ± 0.1	6.7 ± 0.28	12.7 ± 0.17	9 ± 0.9	nil	nil
6g	1.2 ± 0.08	0.94 ± 0.05	2 ± 0.04	1.2 ± 0.05	nil	nil
6h	18.5 ± 0.7	15.6 ± 0.9	13.5 ± 0.17	10 ± 0.06	nil	nil
6i	3.1 ± 0.04	2.4 ± 0.16	4.5 ± 0.08	3.8 ± 0.14	nil	68 ± 1.8
6j	nil	nil	83 ± 2.4	71.5 ± 2	nil	nil

^aResults are expressed as the mean ± SD.

candidate with the lowest IC₅₀ marked a score value of 1 and the next with a score of 2 and so on. Later, this normalization concept was extended toward docking studies based on the *G* score wherein the candidate with the highest score will be given a value of one. Finally, both these strategies were combined to pick up the most suitable Hy-isoxazole and Hy-isoxazolone analogues in terms of lower IC₅₀ and higher docking score (Supporting Information Tables S7 and S8). This hierarchical selection approach preferred 4g (Hy-ISO-VIII) from isoxazole and 6g (Hy-ISO-G) from isoxazolone series (Supporting Information Tables S9 and S10), respectively, as a best candidate for the detailed in vitro evaluation.

Molecular Dynamic Simulation of Selected NPCEs Hy-ISO-G and Hy-ISO-VIII. In order to predict the stability and conformational flexibility of the protein–ligand (P–L) complexes, molecular dynamics (MD) studies of best-scored compounds were done by Schrodinger-Desmond programme for 10 ns under OPLS-2005 force field.¹³ The root-mean-square deviation (rmsd) plots (Supporting Information Figure S9) shows that the protein and the P–L complexes are stable at the end of the trajectory with minimization under 4 Å. The P–L interaction histogram (Figure 1g) and P–L contacts (Supporting Information Figure S10) shows that, in 10XN–Hy-ISO-VIII complex, Ala80 and Gly83 form H-bond with –NH and –O of amide, which stands for 91 and 60% of the simulation time, respectively. The π – π stacking interaction of 1,4-dioxane with Phe81 lasts for 33% of the trajectory. The –O of chromone interacts with Tyr128 for 37% of the period, which also stabilizes the complex. In 10XN–Hy-ISO-G, terminal phenolic –OHs form strong H-bond with Gly83, Leu89, and Ala80, which stands for 62, 35, and 47% of the simulation period. The terminal phenolic ring also tied up with

Phe81 by π – π stacking interaction for about 45% of the trajectory, which also contributes to the stability of the complex. In 10XQ–Hy-ISO-VIII, the –OH and –O from the benzopyran ring interact with Lys121 by forming H-bond and exist 48 and 37% of the simulation time, respectively. The terminal phenolic –OH forms strong H-bond with Tyr128 and exists over the entire period of trajectory. There exists a π – π stacking interaction between pyrazole rings with Phe81, which lasts for 36% of the overall period. The amide –NH forms H-bond with Ala80, which also favors the binding of 4g inside the binding pocket of 10XQ. The H-bond formed between the terminal phenolic –OHs with Gly83 (77%) and Ala80 (9%), and π – π stacking interaction of the benzene moiety with Phe81 stabilizes Hy-ISO-G inside 10XQ.

In Vitro Assessment of Hy-ISO-G and Hy-ISO-VIII for Antiproliferative Potential. The two best-selected semi-synthetic analogues Hy-ISO-G and Hy-ISO-VIII were subjected to detailed cytotoxicity evaluation initially by MTT assay against both cancer and normal cells (Supporting Information Figures S11 and S12). It was observed that lung cancer cells were arrested with an IC₅₀ value of 3.6 and 0.76 μM by Hy-ISO-VIII at 24 and 48 h, respectively, whereas Hy-ISO-G produced the same at 2 and 1.2 μM. In the case of melanoma cells, Hy-ISO-G was found to be more potent with IC₅₀s of 1.2 and 0.94 μM, but Hy-ISO-VIII generated IC₅₀s of 4 and 0.95 μM with 24 and 48 h incubation. Both the selected analogues were 18–60 fold more potent than the parent Hy in both the cancer cells. Generally, the selected compounds displayed a time- and dosage-dependent increase in the cytotoxicity. As a control experiment, we noticed lower cytotoxic influence in human lung fibroblast cells (WI-38) by the administration of both compounds, even at a higher dosage and incubation time. The cytotoxic effects of the compounds

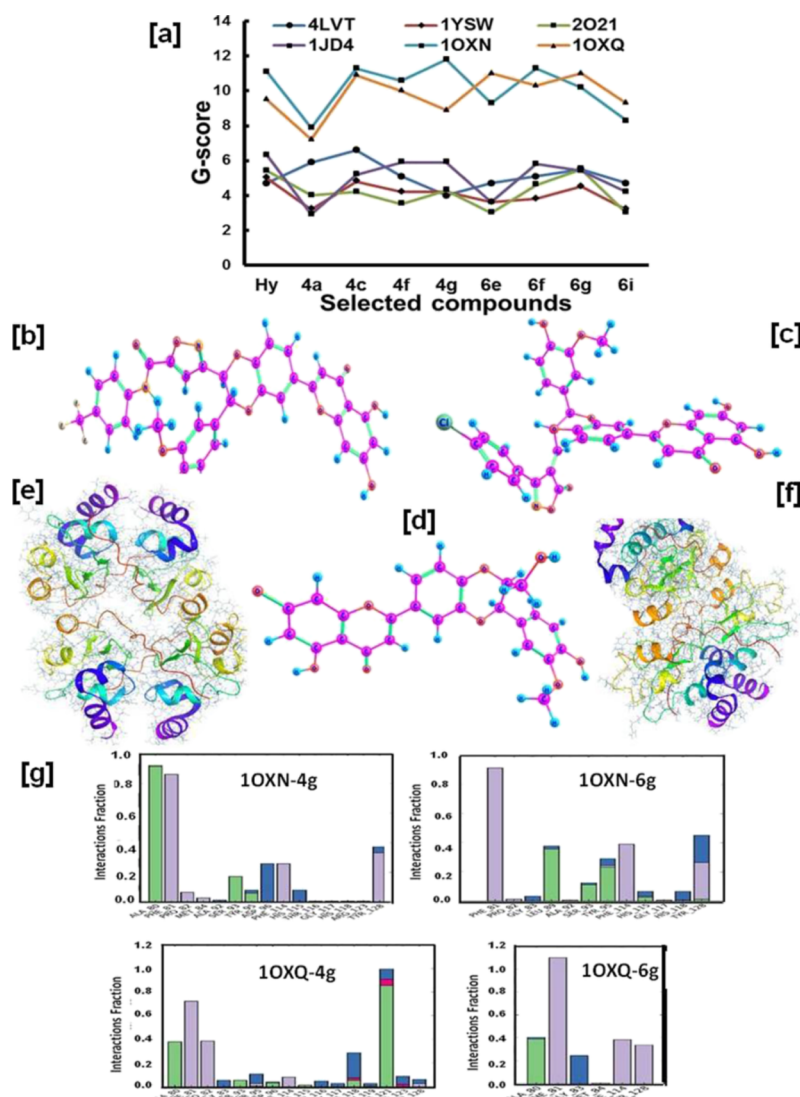


Figure 1. (a) G-score analysis of selected ligands in six different proteins-4LVT, 1YSW, 2O21, 1JD4, 1OXN, and 1OXQ; optimized structures of (b) HY-ISO-VIII (c) HY-ISO-G (d) Hy; crystal structures of proteins with PDB ID (e) 1OXN (f) 1OXQ; (g) P–L interaction histogram for 4g and 6g in 1OXN and 1OXQ.

were further confirmed by lactate dehydrogenase (LDH) assay (Supporting Information Figure S13). Plasma membrane damage due to cytotoxic agents releases LDH into the cell culture media, which could be quantified for determining the percentage of cytotoxicity caused by the agent. The cytotoxic pattern was further investigated through 5-bromo-2'-deoxyuridine (BrdU) assay (Supporting Information Figure S14) which showed a similar trend in the toxicity profile. The magnitude of absorbance for the developed color is proportional to the quantity of BrdU incorporated into cells, which is a direct indication of cell proliferation. Taken together, the detailed evaluation of the cytotoxicity confirmed that the isoxazole and isoxazolone appended NPCEs; HY-ISO-VIII and HY-ISO-G promoted significant contribution for the selective and enhanced cytotoxicity on A549 and A375 cells. The addition of 5-membered nitrogen- and oxygen-containing heterocycles on Hy effectively interacted with the proteins involved in cell proliferation by various hydrophobic interactions to limit the cancer cell proliferation. It is presumed that the metabolites formed out of the Hy core including oxidized, methylated, and sulphonated products promotes

further cell death. Enzyme-mediated breakdown of isoxazole and isoxazolone rings may occur inside the cellular micro-environment.^{12,14} Though Hy was reported as the moderate cytotoxic agent, the semi-synthetic derivatives proved to be superior cytotoxic agents with high selectivity as revealed by multiple in vitro evaluation in lung and melanoma cancer cells.

Effect on Free Radicals by Hy-ISO-G and Hy-ISO-VIII.

Earlier studies revealed the impressive radical scavenging activity of the acetone extract from which Hy was isolated.⁴ To investigate the efficacy of Hy-ISO-G and Hy-ISO-VIII toward scavenging the free radicals, DPPH radical scavenging assay, FRAP assay, and hydroxyl radical scavenging assay were performed (Supporting Information Figure S15). Unfortunately, none of the compounds including Hy showed any good antioxidant activity which rules out the chemopreventive mode of action against cancer progression. The free radical induced oxidative stress causes damage to the cells and this can be overcome by the administration of antioxidants. Natural products like polyphenols are reported to suppress the cellular antioxidant pathways that will sensitize toward chemotherapy.¹⁵ As none of the selected derivatives displayed the

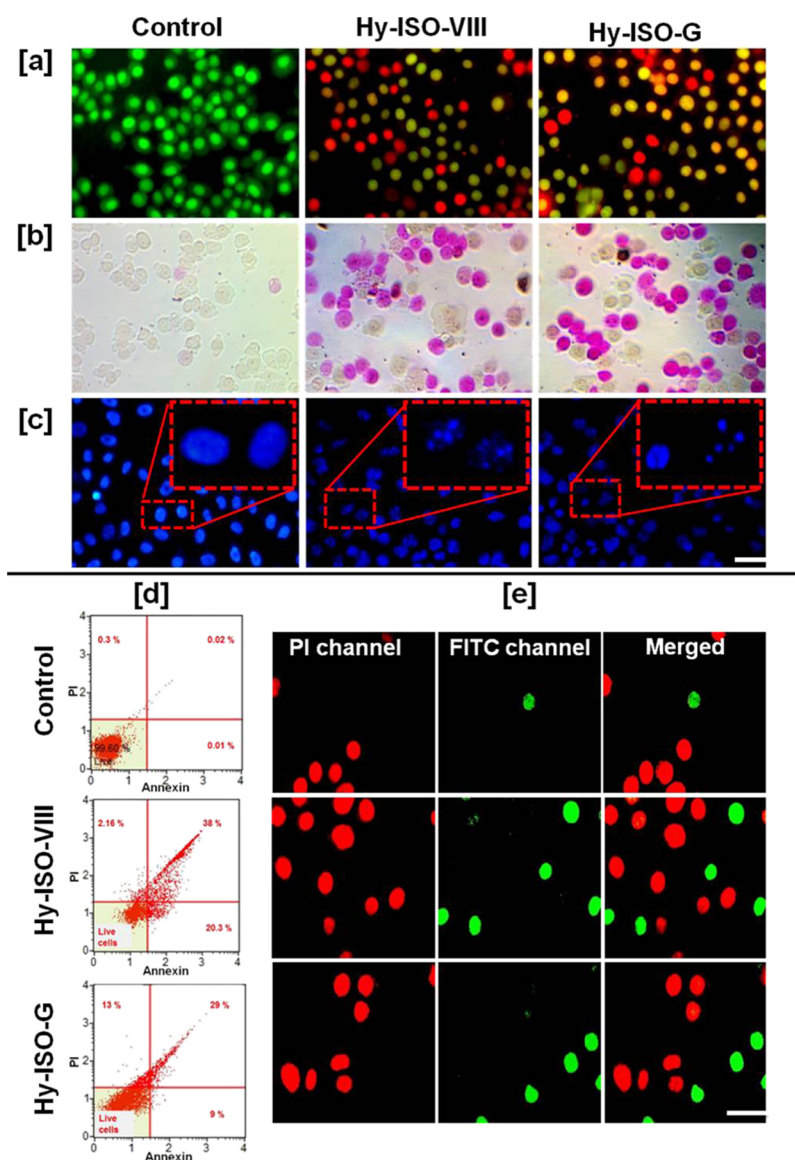


Figure 2. Induction of apoptosis by administration of HY-ISO-VIII and HY-ISO-G on A549 cells. (a) Acridine orange–ethidium bromide assay, (b) APOP assay, (c) Hoechst staining, (d) FITC-Annexin V staining, and (e) Tunnell assay. Scale bar corresponds to 50 μm .

antioxidant property, we planned to determine whether they could induce the intracellular generation of ROS. The intracellular ROS generation was analyzed in A549 cells using dichlorofluorescein diacetate (DCFDA) assay using the commonly used chemotherapeutic agent paclitaxel as a positive control. The obtained results highlighted the ROS generation capacity of both the hybrids in a dose-dependent manner, wherein Hy-ISO-G was found to be the most potent candidate (Supporting Information Figure S16). The fluorescent intensity was enhanced to 0.5–2.5 fold in case of Hy-ISO-VIII with 1 and 100 μM , respectively, whereas Hy-ISO-G enhanced the fluorescence intensity more than 3 fold even with a lower concentration (1 μM). The obtained results highlighted the mechanistic role of these novel Hy-derivatives in the generation of intracellular ROS. Isoxazole derivatives that possess anticancer properties are reported to be nitric oxide donors and the metabolites thus formed can cause cellular oxidative stress by generating ROS. In the cellular micro-environment, the reduction of N–O bond occurs and the subsequent electron transfer may result in the formation of the

radical anion and imine.^{16,17} Moreover, the oxidation of the cellular GSH will cause depletion in the reduced GSH level, which will ultimately lead to cell death. Thus, ROS generation promoted by the HY-ISO compounds retards the proliferation capability of the cancer cells. Most of the natural product-derived anticancer agents like doxorubicin (Dox), paclitaxel, and vinblastine are capable of generating intracellular ROS which further leads to DNA damage and antitumor activity.¹⁸ Similarly, our hybrid molecules that hold the advantages of biosynthesis and synthetic modification with the heterocycles might have enhanced the ROS generation capability and hence could act through the involvement of mitochondria in the cell death mechanism.

Apoptotic Evaluation of Hy-ISO-G and Hy-ISO-VIII. Morphological evaluation of A549 and A375 cells using phase-contrast microscopy after the treatment of Hy-ISO-VIII and Hy-ISO-G revealed significant reduction in the cell number with salient morphological changes associated with apoptosis. Again, we have evaluated the morphological changes through atomic force microscopy (AFM) which clearly demonstrated a

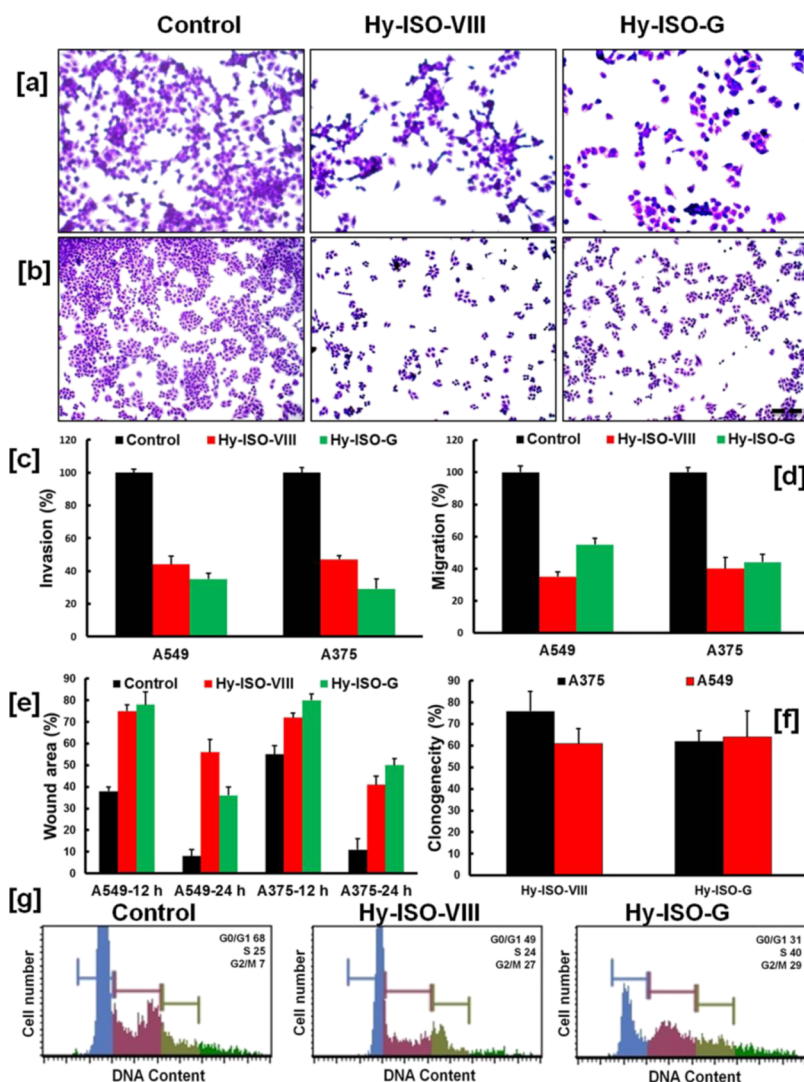


Figure 3. Antimetastatic potential of HY-ISO-VIII and HY-ISO-G (1 nM) on the invasion (a) and migration (b) of A549 cells. Scale bar corresponds to 150 μm . Quantification of (c) invasion, (d) migration, (e) wound healing, and (f) colony formation assay. Cell cycle analysis (g) with A549 cells.

change in the shape of cells from spindle to spherical with associated membrane breakage, blebbing, and leakage of intracellular components after 24 h of the treatment even with a lower concentration (1 μM) of compounds (Supporting Information Figures S17 and S18). In order to determine the mechanism of cell death induction by the compounds, various apoptotic assays were further performed. Examination of compound-treated (1 μM) cells using acridine orange–ethidium bromide staining showed a distinct color change from green to yellow/red with associated apoptotic features (Figure 2a, Supporting Information Figure S19a). Early onset of apoptosis induced by the compounds was validated in a nonfluorescent pattern using APOPercentage assay in which both the compound treated A549 and A375 cells adopted the dye intake and were stained intensely purple-red while control cells remained unstained (Figure 2b, Supporting Information Figure S19b). Later, the dye accumulation was quantified, which demonstrated a significant ($p < 0.001$) increase in the uptake efficiency upon comparison with the control cells. One of the most distinctive features of apoptosis is the DNA fragmentation and nuclear condensation, which could be clearly spotted by Hoechst 33342 nuclear staining. Both

HyISO-VIII and HY-ISO-G indicated appreciable nuclear changes with a well-defined fragmentation pattern in both A549 and A375 cells, whereas control cells remained healthy (Figure 2c, Supporting Information Figure 19c). In addition, induction of apoptotic cell death was further confirmed by annexin V staining. The annexin V positivity was significantly ($p < 0.001$) higher in the treated cells. In A549 cells, the controls were $0.2 \pm 1\%$ annexin V positives, while the compound-treated cells showed 29 ± 1.5 and $38 \pm 2.1\%$ positivity upon administration with Hy-ISO-VIII and Hy-ISO-G, respectively (Figure 2d). A similar trend was observed with A375 cells where control cells were $0.03 \pm 0.9\%$ positive, whereas the HyISO-VIII treatment caused $28 \pm 2\%$ and Hy-ISO-G generated $39 \pm 1.4\%$ positivity within 24 h (Supporting Information Figure S19d). The programmed execution of cell death was further examined with terminal deoxynucleotidyl-transferase dUTP nickend labeling (TUNEL) staining assay, where compound-treated cells were green in color, indicating TUNEL positivity, while control cells were largely TUNEL negative in nature (Figure 2e, Supporting Information Figure S20). The programmed cell death executed by the two potent semisynthetic NPCEs was indisputably established with

multiple apoptotic assays wherein the nuclear condensation and DNA fragmentation associated with programmed cell death was visualized by Hoechst staining and TUNEL assay. The distinct visualization of morphological changes with phase contrast microscopy could reveal the changes like reduction in the cell number accompanied by predominant apoptotic features. The observation of treated cells under AFM clearly revealed an additional opportunity to locate the damage of the cell membrane, whereas the untreated cell membrane remained smooth. The difference between the top and bottom of the cell morphology defined by the height difference in AFM images was well pronounced up on the treatment with our synthetic derivatives, which clearly demonstrated the early onset of programmed cell death.¹⁹ The implementation stage of apoptosis begins with the translocation of phosphatidylserine (PS) from the inner to the external surface of the plasma membrane. This translocation process accounts for the selective uptake of the APOPercentage dye by the early apoptotic cells, which lasts until the occurrence of blebbing, the classical event of apoptosis. Consequently, the PS translocation was further confirmed with annexin V staining, which could actively distinguish cells from apoptosis and necrosis. Cancer cell-selective cytotoxicity itself could be of great advantage for a lead molecule, which predominantly imparts cell death in a programmed manner. Although most of the heterocyclic anticancer agents imparts apoptotic cell death, few imparts a necrotic pathway.²⁰ Here, the heterocycle incorporated HY-ISO derivatives clearly revealed enhanced cancer cell toxicity in a programmed fashion up on comparison with the parent molecule Hy. The notion that isoxazole and isoxazolone derivatives can execute apoptosis in cancer cells could fast promote this semi-synthetic modification approach. Apoptosis is the most appreciable mode of cell death and several natural products and their derivatives have been shown to induce apoptosis in cancer cells.²¹

Effect of NPCEs on Cancer Metastasis. Because metastasis accounts for the major culprit behind cancer-associated mortalities, the antimetastatic potential of both the Hy-analogues were investigated. Hence, a promising anticancer agent should retard the metastatic potential as well. As a first step toward evaluating the antimetastatic property, we investigated the effects of both Hy-ISO-VIII and Hy-ISO-G (10 nM) on the invasion and migration ability of cancer cell lines using trans well chamber assay. While the cancer cells freely moved across the matrigel toward the lower chamber of the trans well plate, the molecules effectively prevented the invasion considerably in both the cells (Figure 3a,c, Supporting Information Figure S21). It is to be noted that both the derivatives significantly retarded the migration of cancer cells in an impressive manner (Figure 3b,d, Supporting Information Figure S21s). Later, we performed wound healing assay which demonstrated that both the molecules prevent the cancer cells from wound closure in a time-dependent manner with significant inhibition in the migration rate. The cell-free scratch zone of the treated wells are large even after 24 h, but the control wells displayed almost closure of the zone even after 12 h, which illuminates the first ray of light toward the inhibition of metastasis (Figure 3e, Supporting Information Figures S22 and S23). Finally, the ability of the Hy-ISO-VIII and Hy-ISO-G were checked for the inhibitory effect on colony formation. It was noticed that both the Hy-analogues markedly reduced the clonogenic ability of cancer cells (Figure 3f, Supporting Information Figures S24 and S25). Clonogenic

assay is still being widely used as a standard experimental procedure to understand the sensitivity of cytotoxic agents on the colony formation capability of cancer cells.²² The initial process of metastasis is the migration of cancer cells toward an approachable niche, which includes both invasion and migration. These neoplastic cells become immortal, proliferate rapidly, and become aggressive to successfully establish a favorable microenvironment through metastasis. A significant reduction in the colony formation, invasion, and migration of aggressive metastatic cancer cells by the compounds indicates their role to retard the metastatic potential. Many polyphenols, flavonoids, and most clinically used chemotherapeutic drugs inhibit tumor migration and thus prevents metastasis.^{19,23} Although the parent Hy compound previously displayed little antimetastatic property, it was indicated that the synthesized novel Hy-derivatives showed enhanced activity because of the incorporation of isoxazole and isoxazolone moieties. Polyphenols like genistein, proanthocyanidins, anthocyanins and so forth having the flavonoid core exhibit excellent anticarcinogenic property by retarding cell migration and proliferation. Compounds like oroxylin suppress the expression and activity of MMP-2/9, phosphorylation of PI3K, and thus inhibits tumor metastasis. Therefore, heterocycles associated with the drug moieties enable the inhibition of the MMP-2/9 activity and suppresses the tumor progression.¹⁹

Cell Cycle Regulation by Hy-ISO-G and Hy-ISO-VIII.

To investigate the NPCE-mediated suppression of cell proliferation, cell cycle analysis was performed with flow cytometry and colorimetric cell clock assay. Flow cytometric analyses were conducted after the DNA was stained with PI. Histograms of the flow cytometry data clearly denote the involvement of cell cycle arrest on the tested cell lines. Hy-ISO-VIII mainly follows G2/M phase cell cycle arrest in both A549 and A375 cells. In the case of Hy-ISO-G, arrest at the G2/M and S phase prevailed where a prominent S phase arrest was seen with A549 cells (Figure 3g, Supporting Information Figure S26a). Cell cycle-dependent growth regulation was further confirmed through microscopic observation with the aid of cell clock assay, which also substantiated a similar pattern of compound action (Supporting Information Figure S26b). Both the compounds showed the G2/M phase as well as S phase arrest in A549 and A375 cell. G0/G1, S, and G2/M phase cells are stained yellow, green, and dark blue, respectively. It has been well practiced that cancer cell proliferation can be blocked upon supplementing cell cycle regulators. For instance, flavonoids like apigenin²⁴ exhibited inhibitory activity by blocking cell cycle progression at the G2/M checkpoint, whereas quercetin²⁵ was known for arresting at the S phase. The S phase arrest by HY-ISO-G could be due to the interaction with DNA causing instantaneous DNA damage. Comberastatin A-4 containing isoxazole core is a promising antimetabolic agent capable of inhibiting tubulin polymerization and inducing tumor regression via antivascular activity without affecting normal cells.¹⁶ Similarly, HY-ISO derivatives might also be interacting with various cellular components, which enable them to retard proliferation potential more effectively. Therefore, the cell cycle arrest brought about by both the NPCEs proved the active involvement of multiple players of apoptosis in their antiproliferative mechanistic mode of action.

Evaluation of Mitochondrial Transmembrane Potential by the NPCEs. The elevated production of ROS exerted by the selected NPCEs indicated the involvement of

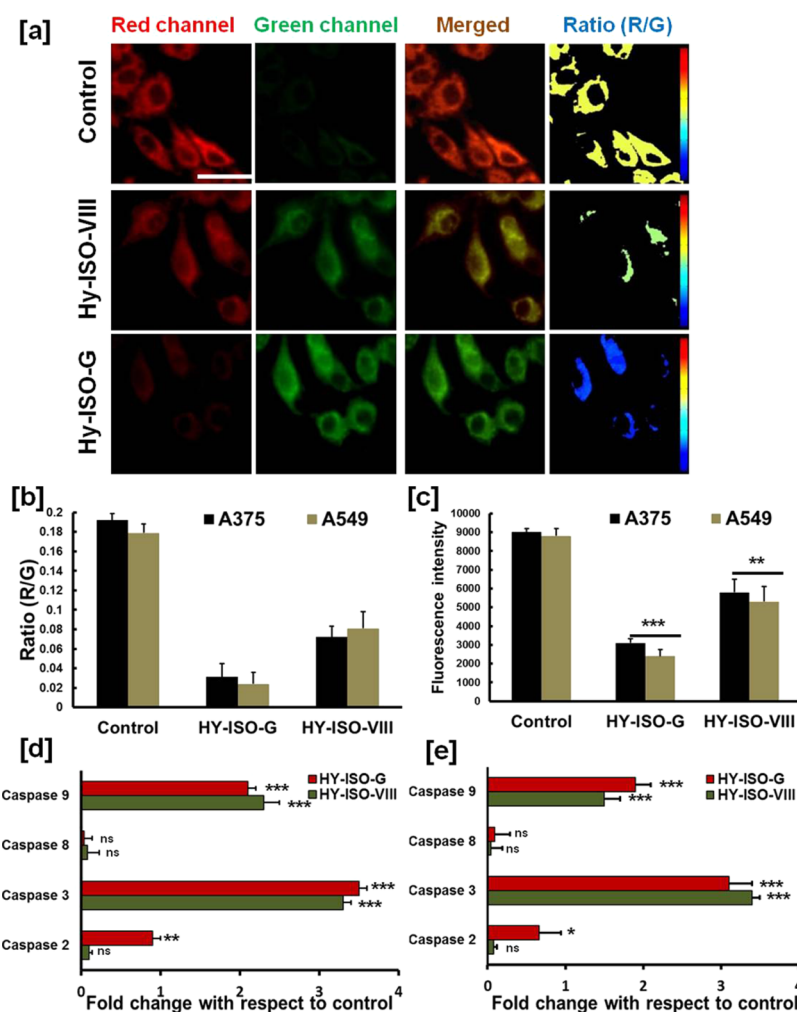


Figure 4. Changes in the mitochondrial membrane potential induced by the administration of HY-ISO-VIII and HY-ISO-G. (a) JC1 assay in A549 cells and the (b) quantification of JC1 assay in A549 and A375 cells. Scale bar corresponds to 50 μm . (c) Mitochondrial membrane potential evaluation with TMRE assay. (d) Caspase activity profiling on A549 cells (e) Caspase activity profiling on A375 cells. Results are expressed as mean \pm SD, statistically significant differences at * $p < 0.05$, ** $p < 0.01$, *** $p < 0.001$, and ns, nonsignificant, when compared with negative control.

mitochondria-mediated cell death, and hence, the mitochondrial membrane potential ($\Delta\Psi_m$) was evaluated on both A549 and A375 cells. Initially, measurement of mitochondrial depolarization was performed with the ratiometric fluorescent dye JC1 which displayed a decrease in red fluorescence and an increase in green fluorescence (Figure 4a, Supporting Information Figure S27) upon the treatment. Simultaneously, the ratio of red to green fluorescent intensity demonstrated the enhanced effect of Hy-ISO-G than Hy-ISO-VIII on both the cells (Figure 4b). Later, the $\Delta\Psi_m$ variation was further quantified with tetramethylrhodamine, ethyl ester (TMRE) mitochondrial membrane potential assay (Figure 4c). The reduction with $\Delta\Psi_m$ was highly significant with both HyISO-VIII ($p < 0.01$) and Hy-ISO-G ($p < 0.001$) in both the cell lines. TMRE is a cell permeant, positively charged dye, which readily accumulates in active mitochondria because of their relative negative charge. Depolarized or inactive mitochondria have decreased $\Delta\Psi_m$ and fail to sequester TMRE. The mitochondrial function is fundamental in controlling the life cycle of cells and plays a major role in the cancer therapeutic regimen. Manipulation of the lethal signal transduction pathways is essential to cause the permeabilization of the mitochondrial outer membrane to cause the cytosolic release

of pro-apoptotic proteins and to the impairment of the bioenergetic functions of mitochondria. Most classical anticancer agents including many derivatives with heterocyclic rings employ signaling pathways that lie upstream of mitochondria and converge on these organelles to trigger cell death.²⁶ A key step in the intrinsic apoptotic pathway is the disruption of the mitochondrial membrane.^{22,27} The indication toward the involvement of mitochondria in the cell death pathway will aid the execution of cytotoxicity in a more programmed manner. Mitochondria greatly contribute toward the most prominent source of intracellular ROS. Because the ROS generation capacity of potent Hy-analogues was already established, the additive information about the induction of mitochondrial damage could support the present observation.

Evaluation of Caspase-Mediated Apoptosis Cascade.

Cysteine-aspartic proteases or caspases are proteolytic enzymes demonstrated to execute a major role in regulating the cell cycle phases and the cell death pathways. Several synthetic and naturally occurring anticancer drugs are established to accomplish apoptosis in a caspase-dependent fashion. As a culmination of apoptosis studies, we planned to investigate the effects of both the initiator and executioner caspases in the mode of cell death induced by Hy-ISO-G and Hy-ISO-VIII.

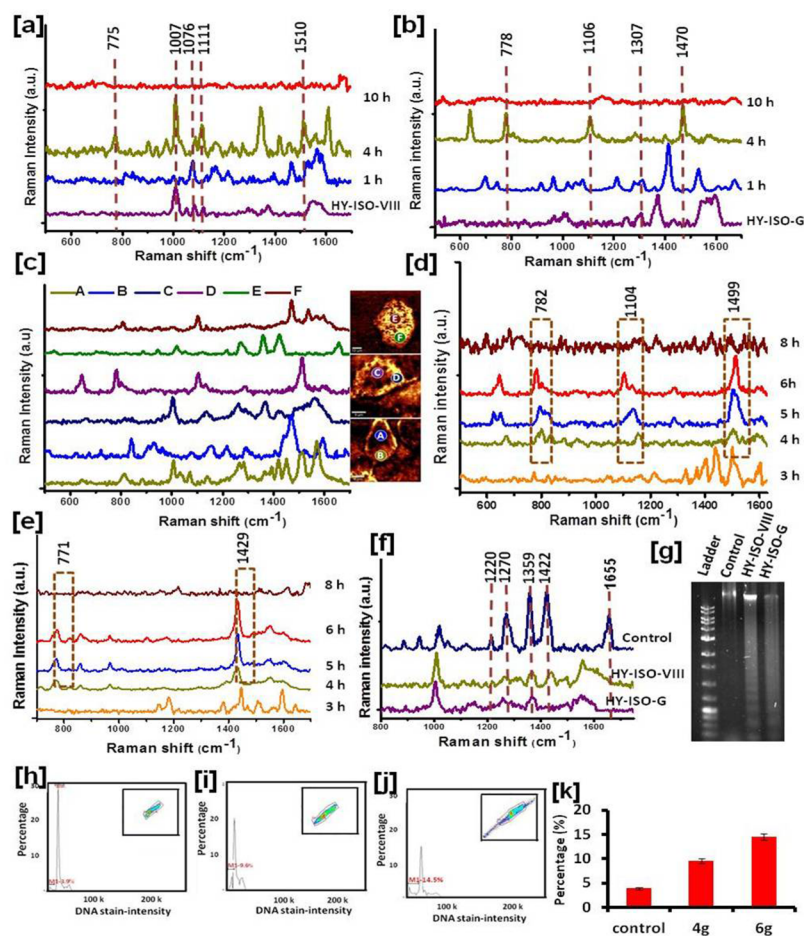


Figure 5. SERS analysis of A549 cells after administration with (a) HY-ISO-VIII and (b) HY-ISO-G. (c) SERS spectra abstracted from nuclear and cytoplasmic region of A549 cells. Time-dependent analysis of cyt *c* after administration of (d) HY-ISO-VIII and (e) HY-ISO-G on A549 cells. (f) SERS spectra and (g) gel electrophoresis analysis obtained from the isolated genomic DNA from A549 cells treated with HY-ISO-VIII and HY-ISO-G. (h) Quantification of DNA fragmentation analysis with chemometric DNA fragmentation assay in A549 cells.

Although there was a significantly ($p < 0.001$) increased activity of caspases 3 and 9 by both the compounds on A375 and A549 cells, the activity of caspase 8 was not varied (Figure 4d,e). Again, Hy-ISO-G caused increased activity on caspase 2 on A549 ($p < 0.01$) and A375 ($p < 0.05$) cells, but the mode of action with Hy-ISO-VIII was not through caspase 2. The active involvement of caspase 3 and 9 and the absence of caspase 8 confirmed the intrinsic apoptotic pathway executed by both the Hy analogues. Because the implementation of intrinsic pathway of cell death involves the engagement of mitochondria, the previous observation with the $\Delta\Psi_m$ dysfunction validates the intrinsic mode of programmed cell death.²² The loss of $\Delta\Psi_m$ releases sequestered pro-apoptotic proteins including cyt *c* into the cytoplasm which will then influence pro-caspase 9 to activate the caspase pathway for the execution of cell death. Phytochemicals have showed promising chemopreventive and therapeutic efficacy by executing apoptosis via mitochondria-mediated caspase activation. Compounds like resveratrol, berberine, apigenin, and so forth have proved to be excellent anticancer agents which perform their cytotoxic effect in the similar fashion.^{28–30} Here, the combined action of the Hy flavonoid core and the isoxazole/isoxazolone ring could effectively achieve the antiproliferative property.

Molecular-Level Investigation for Cellular Internalization and Cell Death Mechanism by SERS Spectral

and Mapping Analysis. Designed to garner the minuscule biochemical cellular changes after the treatment with the selected NPCEs, Raman spectral investigation through surface-enhanced Raman scattering was employed. Raman fingerprint analysis and mapping at a molecular level evolved as novel diagnostic strategy through SERS modality. In the SERS technique, the native Raman fingerprints of Hy-ISO-VIII that were characterized with the prominent peaks at 1009 and 1082 cm^{-1} correspond to C–C aromatic chain vibrations, and 1374 and 1547 cm^{-1} correspond to C=N (hetero ring) and CH₃ stretching of the hybrid molecule (Supporting Information Figure 28, Table S11). Similarly, the prominent Raman peaks at 1250, 1306, 1373, and 1594 cm^{-1} correspond to C–H vibration, C=O in-plane bending, CH₃ stretching, and C=N (hetero ring), respectively, in the chemical structure of Hy-ISO-G (Supporting Information Figure S29, Table S12).^{31,32} Because both the NPCEs displayed unique Raman patterns, we utilized them as the Raman signature molecule for inspecting the cellular internalization process. The unique Raman fingerprints of both the compounds were found to be merged with the molecular components of the cytoplasmic area as early as 1 h of administration. The signature peaks at 1080 and 1307 cm^{-1} identified as the marker peak of Hy-ISO-VIII (Figure 5a, Supporting Information Figure S30, Tables S13 and S15) and Hy-ISO-G (Figure 5b, Supporting Information Figure S31,

Tables S14 and S16), respectively, which confirmed the effective internalization process. During the time course study, we observed the disappearance of Raman fingerprints of Hy-analogues after 4 h in the intracellular environment. Again, the Raman spectra collected from the nuclear area after 4 h showed less-intense Raman peaks of DNA up on comparison with the negative control cells which is a definite indication to the probable DNA damage (Figure 5c). Next, the distinctive observation of characteristic Raman peaks of cyt *c* from the cytoplasm after 3–4 h inspired us to find out the pathway of the cell death process. Raman spectra abstracted from the cytoplasmic area upon the treatment of Hy-ISO-G/Hy-ISO-VIII displayed the signature peaks of cyt *c* such as 775, 1106, 1470, and 1510 cm^{-1} which indicated heme breathing, C–S stretching, C=N stretching, and the bending mode of C–N(H)–C, respectively. The two distinct marker peaks of cyt *c* at 775 and 1510 cm^{-1} were well resolved when compared to the other characteristic bands of proteins/amino acids/phospholipids in the intracellular milieu. A limiting step in the intrinsic apoptotic pathway is the damage of mitochondria and the release of cyt *c* from mitochondria into the cytosol. Next, we thought of investigating the cyt *c* kinetics in the cells administered with our semi-synthetic derivatives in a label-free manner based on marker Raman peaks which corresponds to heme molecules of cyt *c* (775 cm^{-1}). The presence of signature Raman peaks of cyt *c* was observed from 3–4 h and lasts up to 6–8 h with both the molecules in the cytoplasmic area of A549 (Figure 5d,e, Supporting Information Tables S17 and S18) and A375 cells (Supporting Information Figures S32 and S33, Tables S19 and S20). The decrease in the DNA peak intensity from the nuclear area after the treatment urged us to study the effects on the nuclear DNA. Raman spectral analysis of the isolated DNA clearly illustrated the NPCEs-induced DNA damage with typical signatures with the O–P–O backbone rupture during the DNA double-strand breakage and laddering process. The isolated DNA of the untreated cells bears all the signature peaks for a healthy DNA with high intensity while both Hy-ISO-VIII and Hy-ISO-G caused effective DNA damage on A549 (Figure 5f, Supporting Information Table S21) and A375 cells (Supporting Information Figure S34, Table S22).

We have successfully monitored the real-time cellular internalization and apoptotic events exercised by the two promising NPCEs of Hy with SERS modality using the signature Raman spectral read out. This strategy serves as a dynamic proof-of-concept for the specific and sensitive delivery of hit molecules to the target location. In most of the cases, delivery of non-fluorescent molecules was presumed by attaching an auxiliary fluorophore moiety which itself is a very tedious process. However, the present demonstration stepped-up as a newly evolved alternative pathway where rapid compound internalization was evident as early as 1 h and the persistence of the compounds up to 4 h indicated the potentiality in the subcellular environment. Under certain conditions, dihydroxylated flavonoids undergo oxidation to produce cytotoxic hydrogen peroxide. Inside the cellular matrix, P450-mediated reductive scission of isoxazole rings is reported.^{12,14} Similarly, the explored NPCEs might also have metabolised inside the cells by 4 h and the absence of any compound signatures from the nuclear area points out towards the lack of nuclear membrane penetration ability or the rapid metabolism in the cytoplasm. We have previously employed SERS for tracking the cellular internalization and metabolism

of Dox.^{33,34} Here, the cellular tracking of a nonfluorescent molecule holds special merit. Careful inspection of marked Raman spectra from the cytoplasmic area exposed the signature fingerprints of cyt *c* after 4 h compound administration. Cyt *c* acts as a trigger to the cascade activation of caspases for the orchestrated fashion of cell death. The distinctive observation with the involvement of cyt *c* in the mechanistic mode of cell death by both HY-ISO-G and HY-ISO-VIII further made an agreement with the studies with $\Delta\Psi_m$ and caspase profiling which confirmed the execution of mitochondria-mediated intrinsic pathway of apoptosis. A change in the $\Delta\Psi_m$ may be responsible for the release of the cyt *c*. The intrinsic apoptotic pathway involves the disruption of $\Delta\Psi_m$ and subsequent release of cyt *c*, which can be observed as the initiation of apoptosis before morphological changes in the apoptotic cell are visible.³⁵ SERS-based investigation was previously explored for the study of cyt *c* in living functional mitochondria³⁶ but its dynamics during apoptosis induced by any natural product or its active semi-synthetic counterpart remains elusive. Because DNA fragmentation stands alone as a gold-standard indicator of the intrinsic apoptotic pathway, we performed SERS analysis with the isolated DNA. The spectra isolated from untreated DNA showed prominent peaks at 810, 1072, 1220, 1280, and 1422 cm^{-1} , of which the first three bands are assigned to phosphodiester (Z-marker), symmetric PO_2 stretching, C–N–C stretching (nitrogen bases) and the next two are assigned to the nucleic acids and phosphates and deoxyribose, respectively.^{32,37–39} Analysis of the DNA after treatment showed a noticeable decrease in the peaks centered at 810, 1072, 1280, and 1422 cm^{-1} . The reduction in the SERS intensity of these peaks indicates the disruption of the DNA compact structure and the degradation of nitrogen bases and phosphodiester backbone (Figure 5f, Supporting Information Figure S34, Tables S21 and S22). We have previously reported the effective real-time monitoring of the DNA backbone breakage using differential SERS spectral analysis.^{33,34} Therefore, induction of apoptosis and their molecular events by SERS fingerprint analysis prevailed an unique opportunity especially in observation of dynamics of biomolecules because labeling markers may disturb the target molecules.

Analysis of NPCE-Mediated DNA Fragmentation. It was evident that apoptotic DNA fragmentation occurred during the execution of apoptosis by both NPCEs. As a proof-of-concept, DNA fragmentation was further confirmed by agarose gel electrophoresis. In DNA laddering, the longer DNA is broken down into multiple fragments which can be viewed by agarose gel electrophoresis (Figure 5g). The fragmented DNA upon the Hy-ISO-VIII and Hy-ISO-G treatment could effectively establish the nuclear damage induced by the treatment. Because the indications toward DNA laddering were observed only after 4 h of the treatment, we thought to investigate the analysis of DNA fragmentation in an early time point of 3 h according to the protocol from chemometec DNA fragmentation assay. The cells were treated with the compounds, cellular fluorescence was quantified and apoptotic cells with fragmented DNA under the M1 peak in a DNA content histogram was quantified (Figure 5h, Supporting Information Figures S35 and S36). These results show that Hy-ISO-VIII and HY-ISO-G could cause 9.6 and 14.5% DNA fragmentation as early as 3 h incubation.

Estimation of GSH in Cells Treated with NPCEs. During apoptosis under the normal physiological mechanism, cells are collapsed. Because GSH is a key modulator of cellular

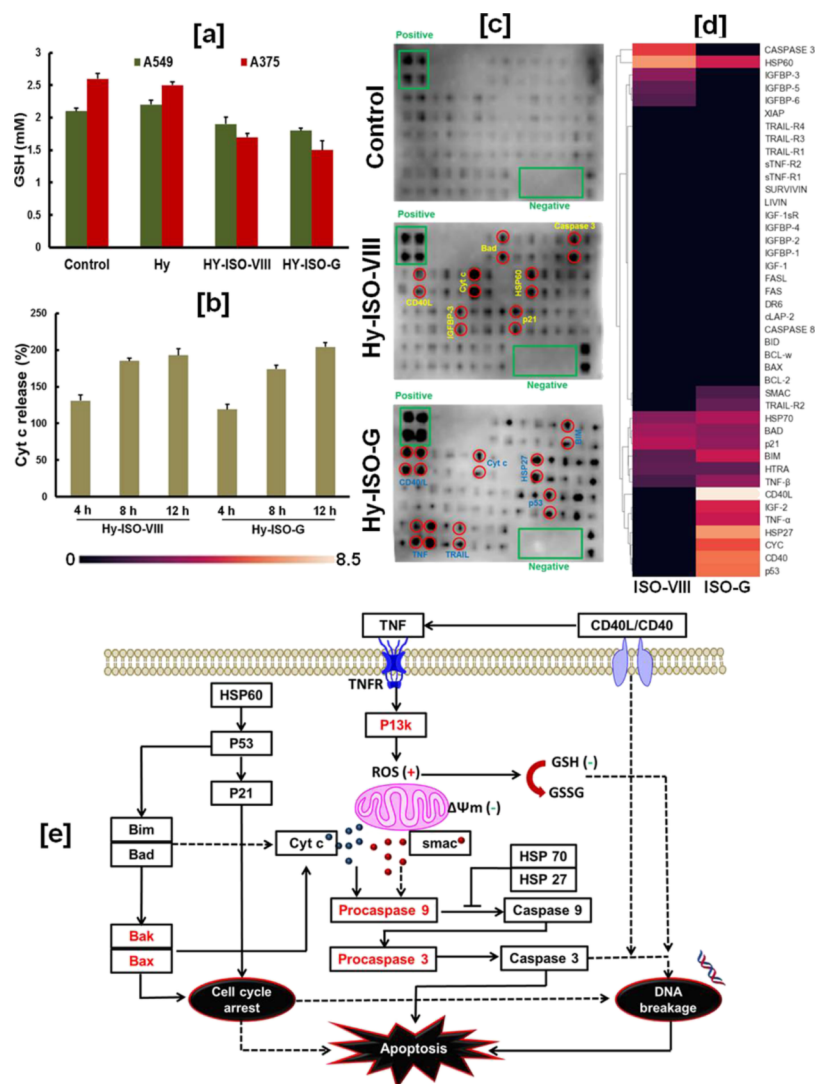


Figure 6. (a) Changes in the GSH level after the administration of HY-ISO-VIII and HY-ISO-G on A549 and A375 cells. (b) Quantification of cyt *c* in the cytoplasm in A549 cells administered with HY-ISO-VIII and HY-ISO-G. (c) Apoptotic protein chip analysis on A549 cells and (d) the corresponding dendrogram based on the hierarchical clustering. (e) Pathway deciphering the proposed mechanistic mode of action with HY-ISO-G on cancer cells. Black-colored entries are experimentally validated while the red-colored entries represent the possible players, which are not currently evaluated. Filled lines represent the direct biological effect while dotted lines denote the indirect effect.

processes, we decided to estimate the GSH level after the treatment with NPCEs. Surprisingly, significant depletion in the GSH level was observed in both A375 and A549 cells up on administration with Hy-ISO-G and Hy-ISO-VIII, whereas Hy did not account for any meaningful change (Figure 6a). The extent of ROS generation by both the selected derivatives was well proved by DCFDA analysis. Generation of ROS induces the oxidation of cytosolic GSH to GSSG that could be the underlying factor behind the depletion of the GSH level. Also some of the flavonoids are reported to form GSH adducts in the cytoplasm which drastically reduced the GSH level.¹² Depletion in the GSH level causes imbalance of intracellular redox environment which collapses the normal cellular function and leads to apoptosis. Cancer cells are ominously extra sensitive toward the changes in the levels of GSH and hence may be more vulnerable to oxidative stress and the extent of ROS exposure.⁴⁰ Our study revealed that NPCE-induced ROS generation was significantly associated with the consumption of intracellular GSH. Based on the observations with the elevation of cellular ROS and consumption of GSH,

we suggest that our NPCEs probably consume the cellular antioxidant and upsurge the ROS levels outside a certain threshold, which promote the induction of apoptosis. The flavonoid core of the molecules can form thiol conjugation with GSH and cause lowering of cellular thiol levels.¹²

Evaluation of the Involvement of Cyt *c* in the Mechanism of Action. The extent of the involvement of the intrinsic apoptotic pathway well proved by multiple assays highlights the critical role of cyt *c* in the mechanism of action related to both the semi-synthetic derivatives. Release of cyt *c* triggers the mitochondria-dependent pathways of apoptosis. Hence, we computed the binding affinity of the selected compounds Hy-ISO-VIII and Hy-ISO-G with cyt *c*. The crystallized structure of cyt *c* (PDB code: 1CGO) was obtained from RCSB PDB and it contains 127 amino acids with a resolution of 1.8 Å. The prepared receptor was used for docking against the prepared ligands. Both the compounds showed less affinity to the binding site of 1CGO with best fitting pose having *G*-score -5.5 and *D*-score -3.4 kcal/mol in the case of Hy-ISO-VIII, whereas Hy-ISO-G showed *G*-score

and *D*-score of -5.2 kcal/mol. This indicates the smooth release of *cyt c* even in the presence of both the NPCEs which points toward the possibility of *cyt c*-mediated apoptosis. However, this theoretical approximation needs to be validated experimentally in cancer cells. Hence, we have carried out the estimation of *cyt c* release to the cytoplasm during cell death induced by our NPCEs. The percentage of *cyt c* release in the untreated cells were taken as 100% and the corresponding *cyt c* level in the NPCEs treated cells at different time points were quantified (Figure 6b, Supporting Information Figure S37). There was a significant increase in the *cyt c* release from 4 to 12 h on treatment with both the compounds on A375 and A549 cells. It appears that the peak *cyt c* concentration in the cytoplasm lies within 4–8 h after the treatment in both the cell lines. The previous observation of a reduced binding affinity of both our NPCEs with *cyt c* during computational analysis is well proved with the real quantitation of cytosolic *cyt c* released from the mitochondria. Moreover, the kinetics associated with *cyt c* observed in a label-free fashion using SERS was well validated with this *cyt c* quantitation. The active involvement of *cyt c* and mechanisms to alter cellular GSH by the NPCEs points out toward its complex mechanistic mode of action in cancer cells. Induction of apoptosis by flavonoids like apigenin is reported to take place via *cyt c* release and further activation of caspases 9 and 3.¹²

Apoptosis Antibody Array. The admirable antiproliferative potentials demonstrated by the selected NPCEs made us investigate the protein-level expression variation of major players involved in the cell death pathways. This apoptotic protein chip analysis verified the unique molecular mechanism of action confined to the apoptotic pathways. Although both Hy-ISO-G and Hy-ISO-VIII shared a similar pattern of expression with majority of proteins, some key pattern expression variations also exist which highlighted the uniqueness of each derivative with respect to its structure and the mode of action (Figure 6c, Supporting Information Figure S38). In the case of cells treated with HY-ISO-G, the tumor necrosis factor (TNF) is hyper-activated by its upstream regulator CD40L/CD40 which is one among the most altered protein ligand. Activation of TNF results in the generation of ROS via the PI3k pathway which leads to the fluctuation of mitochondrial membrane potential, thereby releasing *cyt c* and smac which will not only activate all the other downstream caspases but also will lead to a greater depletion of cytosolic GSH, which will further promote apoptosis through a variety of mechanisms. A greater fold increase in the expression of other important proteins such as HSP60, p53, p21, Bim, Bad, and many others will further promote the execution of intrinsic apoptosis pathways which involves the induction of cell cycle arrest and DNA damage (Figure 6d). TNF was not activated up to a greater extent in the case of cells treated with Hy-ISO-VIII because of the lack of any variation in the protein expression with CD40L/CD40 which marks a major difference between the modes of action of both the NPCEs. Insulin-like growth factor-binding protein 3 (IGFBP3) is differently over expressed with Hy-ISO-VIII which will not only execute cell cycle arrest but also activates Bac and Bax to cause *cyt c* release. The higher fold change with the *cyt c* expression observed with Hy-ISO-VIII than HY-ISO-G could be due to the involvement of IGFBP3 in the mechanism of action of the former. A marginal increase in the expression of HTRA, which is an important player involved in the inhibition of apoptosis by Hy-ISO-VIII, was not effective enough to prevent the

activation of caspase pathway probably due to the hyper activation of all other promoters of apoptosis (Supporting Information Figure S39). The similarity in the molecular mechanism of action by both the NPCEs was clearly demonstrated with the dendrogram based on the hierarchical clustering (Figure 6e). Similarly, derivatives of oridonin and apigenin also follow an intrinsic pathway of apoptosis with the involvement of caspases, Bcl2 family proteins, *cyt c*, smac, p53, and many more which also cause cell cycle arrest. Quercetin and morin are some prominent natural products promoting apoptosis via p53-mediated activation of Bad protein.^{2,21,30,41} The mitochondria-initiated programmed cell death is the predominant apoptotic pathway operated in mammalian cells and is tightly regulated by Bcl2 family proteins. The greater involvement of these proteins by both our NPCEs observed with this array validated all the previously performed assays to substantiate the active involvement of mitochondria. Our previous attempts with computational analysis demonstrated a feeble interaction of the NPCEs with pro-apoptotic protein domains like 4LVT (Bad) and 1CGO (*cyt c*) and high docking score with an anti-apoptotic protein domain like 1OXN and 1OXQ. This observation is well substantiated with the dot blot analysis.

CONCLUSIONS

In summary, we have designed a semisynthetic approach for evaluating new NPCEs from the library of hydnocarpin-isoxazole and isoxazolone analogues. The two potent cytotoxic NPCEs; Hy-ISO-G and Hy-ISO-VIII were selected by extensive in vitro assays with complementary in silico molecular docking analysis. Subsequently, in-depth in vitro and MDs exploration were accomplished for substantiating the preferential effectiveness of antiproliferative activity toward lung adenocarcinoma and malignant melanoma cells. The selected NPCEs promote mitochondrial membrane depolarization which followed intrinsic apoptosis through the release of *cyt c*. As a new insight, the unique Raman molecular fingerprints of both the Hy-derivatives were established as a chemo-marker for the label-free analysis, especially cellular uptake and intracellular distribution and the subtle dynamics associated with the *cyt c* release kinetics. Moreover, signature Raman peaks for DNA fragmentation confirmed the molecular-level apoptotic phenomenon exerted by the selected NPCEs in SERS modality. Notwithstanding, the NPCEs effectively retard the crucial steps of metastatic cascade and colonization of neoplastic cells. Although both the NPCEs follow mitochondrial-mediated apoptosis with the generation of cellular ROS and depletion of GSH, leading to the activation of caspases, there occurs slight variation between their modes of action as well. We envisaged that MCR and [3 + 2] cycloaddition strategy to append isoxazole and isoxazolone on naturally occurring hydnocarpin become a successful blueprint to generate potential anticancer NPCEs to be followed toward drug discovery footsteps for efficacious management of metastatic cancer.

EXPERIMENTAL SECTION

Chemistry. All commercially available reagents were used without further purification. Anhydrous solvents were dried through routine protocols. All chemicals and solvents were purchased from Sigma-Aldrich, Merck, and Specrochem, used without further purification. Analytical TLC was performed on a Merck 60 F254 silica gel plate (0.25 mm thickness) and visualization was done with UV light (254

and 365 nm). Column chromatography was performed on Merck 60 silica gel (60–120 or 100–200 mesh). NMR spectra were recorded on a Bruker ADVANCE 500 NMR spectrometer, and chemical shifts are expressed in parts per million (ppm). The mass spectra were recorded on a Thermo Scientific Exactive ESI-MS spectrophotometer. The purity of all the Hy-ISO derivatives was $\geq 95\%$ as obtained from the high-performance liquid chromatography HPLC system (Shimadzu, Kyoto, Japan) with a SPD-M20A UV-vis photo diode array detector on a 250 mm \times 4.6 mm i.d., 5 μ m, YMC-Pack R&D ODS analytical column (9YMC Co., Ltd. Japan).

General Procedure for the Synthesis of Hydnocarpin Isoxazole Derivatives, General Procedure A. Synthesis of compounds 4a–j. Compound 2 was dissolved in 1:4 mixture of methanol and ethylacetate to which *N*-hydroxylamine hydrochloride (0.26 mmol) and NaOH (0.26 mmol) was added and stirred under room temperature for 10 min. To this mixture, *N*-bromosuccinimide (0.52 mmol) was added and stirred for another 10 min. Then, the 2-alkynyl derivative (0.26 mmol) was added and allowed to stir for 12 h. The reaction mixture was subjected to column chromatography and the product was isolated in good to excellent yields.

6-(5,7-Dihydroxy-4-oxo-4H-chromen-2-yl)-3-(4-hydroxy-3-methoxyphenyl)-2,3-dihydrobenzo[b][1,4]dioxine-2-carbaldehyde (2). Compound 1 (30 mg, 0.06 mmol) was dissolved in anhydrous dimethyl sulfoxide (DMSO). TFA (4.4 mg, 0.036 mmol) was added to this followed by pyridine (6.06 mg, 0.072 mmol) and allowed to stir for 5 min at room temperature. Then, *N,N'*-dicyclohexylcarbodiimide (26.7 mg, 0.13 mmol) was added to the mixture and allowed to stir at room temperature. After 24 h, 3 mL of water was added to the reaction mixture and the product was precipitated out. The precipitate was filtered and washed thoroughly with hexane and the solid obtained was dried under vacuum in order to afford compound 2 (24.6 mg, 82%) as yellow powder. ^1H NMR (500 MHz, CD_3OD): δ 12.89 (s, 1H), 9.94 (s, 1H), 7.80 (s, 1H), 7.48–7.43 (m, 2H), 7.02 (s, 1H), 6.94 (d, $J = 5$ Hz, 1H), 6.86 (d, $J = 5$ Hz, 1H), 6.77 (d, $J = 5$ Hz, 1H), 6.56 (s, 1H), 6.46 (s, 1H), 6.15 (s, 1H), 3.75 (s, 3H), 3.43 (d, $J = 5$ Hz, 1H). ^{13}C NMR (125 MHz, CD_3OD): δ 200.3, 176.06, 164.3, 163.0, 161.4, 167.3, 147.6, 146.9, 143.6, 139.9, 126.9, 123.6, 120.5, 119.9, 117.5, 115.3, 114.7, 111.7, 98.4, 94.0, 77.9, 76.33, 60.0, 55.6, 23.2. HRMS (ESI) m/z : $[\text{M} + \text{H}]^+$ calcd for $\text{C}_{25}\text{H}_{19}\text{O}_9$, 463.1029; found, 463.1027.

2-(2-(5-Benzylisoxazol-3-yl)-3-(4-hydroxy-3-methoxyphenyl)-2,3-dihydrobenzo[b][1,4]dioxin-6-yl)-5,7-dihydroxy-4H-chromen-4-one (4a). Following the general procedure A, 4a was obtained after purification by column chromatography on silica gel (EtOAc/hexanes = 70:30) as yellow solid and in 82% yield. ^1H NMR (500 MHz, acetone): δ 13.84 (s, 1H), 7.61–7.54 (m, 2H), 7.22 (dd, $J = 8.4, 1.2$ Hz, 1H), 7.10–6.91 (m, 4H), 6.88 (dd, $J = 8.1, 1.7$ Hz, 2H), 6.78 (dd, $J = 5.2, 2.6$ Hz, 3H), 5.00 (d, $J = 8.1$ Hz, 2H), 4.12 (dd, $J = 7.3, 3.2$ Hz, 3H), 3.80 (d, $J = 12.6$ Hz, 2H), 3.75 (s, 3H), 3.71–3.65 (m, 1H), 3.43 (dd, $J = 12.5, 4.1$ Hz, 2H). ^{13}C NMR (125 MHz, CD_3OD): δ 176.1, 164.3, 163.0, 161.4, 167.3, 147.6, 146.9, 143.6, 139.9, 126.9, 123.6, 120.5, 119.9, 117.5, 115.3, 114.7, 111.7, 98.4, 94.0, 77.9, 76.33, 60.0, 55.6, 23.2. HRMS (ESI) m/z : $[\text{M} + \text{H}]^+$ calcd for $\text{C}_{35}\text{H}_{28}\text{NO}_9$, 606.1764; found, 606.1752.

5,7-Dihydroxy-2-(3-(4-hydroxy-3-methoxyphenyl)-2-(4-(hydroxymethyl)-5-methylisoxazol-3-yl)-2,3-dihydrobenzo[b][1,4]dioxin-6-yl)-4H-chromen-4-one (4b). Following the general procedure A, 4b was obtained after purification by column chromatography on silica gel (EtOAc/hexanes = 70:30) as yellow solid and in 72% yield. ^1H NMR (500 MHz, acetone): δ 13.8 (s, 1H), 7.64–7.49 (m, 2H), 7.22 (dd, $J = 8.4, 1.3$ Hz, 1H), 7.81–6.89 (m, 2H), 6.78 (dd, $J = 5.2, 2.6$ Hz, 3H), 5.00 (d, $J = 8.1$ Hz, 2H), 4.12 (dd, $J = 7.3, 3.2$ Hz, 3H), 3.80 (d, $J = 12.6$ Hz, 2H), 3.75 (s, 3H), 3.71–3.65 (m, 1H), 3.43 (dd, $J = 12.5, 4.1$ Hz, 2H). ^{13}C NMR (125 MHz, CD_3OD): δ 182.1, 166.4, 163.6, 161.8, 158.9, 150.0, 147.9, 147.5, 144.6, 120.0, 119.5, 115.7, 114.3, 111.0, 104.3, 100.6, 98.6, 94.2, 56.4, 54.5, 15.7. HRMS (ESI) m/z : $[\text{M} + \text{H}]^+$ calcd for $\text{C}_{30}\text{H}_{26}\text{NO}_{10}$, 560.1557; found, 560.1548.

5,7-Dihydroxy-2-(3-(4-hydroxy-3-methoxyphenyl)-2-(5-(2-hydroxypropan-2-yl)isoxazol-3-yl)-2,3-dihydrobenzo[b][1,4]dioxin-6-yl)-4H-chromen-4-one (4c). Following the general procedure A, 4c was obtained after purification by column chromatography on silica

gel (EtOAc/hexanes = 70:30) as yellow solid and in 79% yield. ^1H NMR (500 MHz, acetone): δ 13.83 (s, 1H), 7.83 (s, 2H), 7.62–7.56 (m, 3H), 7.05–6.94 (m, 4H), 6.88 (d, $J = 8.0$ Hz, 1H), 6.76 (dd, $J = 10.2, 2.5$ Hz, 2H), 5.00 (d, $J = 8.2$ Hz, 2H), 4.45 (dd, $J = 9.2, 2.9$ Hz, 3H), 3.75 (d, $J = 9.0$ Hz, 3H), 3.46–3.40 (m, 2H), 2.65 (s, 3H), 2.41 (s, 3H). ^{13}C NMR (125 MHz, CD_3OD): δ 182.3, 166.4, 163.6, 161.8, 158.9, 158.8, 150.0, 147.7, 147.6, 147.5, 143.6, 134.2, 121.2, 120.0, 119.7, 115.8, 111.4, 109.8, 104.5, 98.3, 94.0, 92.1, 86.1, 56.1, 31.3, 23.2. HRMS (ESI) m/z : $[\text{M} + \text{H}]^+$ calcd for $\text{C}_{32}\text{H}_{30}\text{NO}_{10}$, 588.1870; found, 588.1863.

5,7-Dihydroxy-2-(3-(4-hydroxy-3-methoxyphenyl)-2-(5-(hydroxymethyl)isoxazol-3-yl)-2,3-dihydrobenzo[b][1,4]dioxin-6-yl)-4H-chromen-4-one (4d). Following the general procedure A, 4d was obtained after purification by column chromatography on silica gel (EtOAc/hexanes = 70:30) as yellow solid and in 86% yield. ^1H NMR (500 MHz, acetone): δ 13.84 (s, 2H), 7.75 (s, 2H), 7.59 (t, $J = 5.6$ Hz, 2H), 7.08–6.93 (m, 4H), 6.88 (dd, $J = 8.0, 1.5$ Hz, 1H), 6.78 (d, $J = 7.9$ Hz, 2H), 5.00 (d, $J = 8.0$ Hz, 1H), 4.15–4.07 (m, 2H), 3.76 (s, 3H), 3.50–3.37 (m, 3H). ^{13}C NMR (125 MHz, CD_3OD): δ 182.2, 166.3, 163.5, 161.6, 158.7, 158.6, 150.0, 147.7, 147.6, 147.5, 143.4, 133.8, 121.1, 120.0, 119.7, 115.7, 114.5, 111.5, 109.8, 104.4, 101.9, 98.3, 94.0, 92.5, 56.7. HRMS (ESI) m/z : $[\text{M} + \text{H}]^+$ calcd for $\text{C}_{29}\text{H}_{26}\text{NO}_{10}$, 548.1557; found, 548.1544.

5,7-Dihydroxy-2-(3-(4-hydroxy-3-methoxyphenyl)-2-(5-(*p*-tolyl)isoxazol-3-yl)-2,3-dihydrobenzo[b][1,4]dioxin-6-yl)-4H-chromen-4-one (4e). Following the general procedure A, 4e was obtained after purification by column chromatography on silica gel (EtOAc/hexanes = 70:30) as yellow solid and in 82% yield. ^1H NMR (500 MHz, DMSO) δ 13.84 (s, 1H), 9.25 (s, 1H), 7.71 (d, $J = 2.1$ Hz, 1H), 7.66 (dd, $J = 8.5, 2.1$ Hz, 1H), 7.09 (dd, $J = 14.0, 6.3$ Hz, 2H), 7.01 (t, $J = 11.8$ Hz, 1H), 6.90–6.78 (m, 2H), 5.01 (d, $J = 7.9$ Hz, 1H), 4.27 (d, $J = 3.1$ Hz, 1H), 3.77 (s, 3H), 2.50–2.49 (m, 6H). ^{13}C NMR (125 MHz, CD_3OD): δ 182.1, 169.5, 166.4, 163.3, 161.8, 158.5, 150.0, 147.7, 147.6, 147.5, 144.2, 135.0, 131.8, 129.7, 129.5, 124.9, 123.7, 120.0, 121.2, 119.7, 115.8, 114.5, 111.4, 109.7, 100.0, 98.3, 94.6, 92.4, 91.8, 56.5, 21.3. HRMS (ESI) m/z : $[\text{M} + \text{H}]^+$ calcd for $\text{C}_{35}\text{H}_{28}\text{NO}_9$, 606.1764; found 606.1759.

2-(2-(5-(Aminomethyl)isoxazol-3-yl)-3-(4-hydroxy-3-methoxyphenyl)-2,3-dihydrobenzo[b][1,4]dioxin-6-yl)-5,7-dihydroxy-4H-chromen-4-one (4f). Following the general procedure A, 4f was obtained after purification by column chromatography on silica gel (EtOAc/hexane = 70:30) as yellow solid and in 73% yield. ^1H NMR (500 MHz, acetone): δ 13.79 (s, 1H), 7.56 (d, $J = 11.5$ Hz, 4H), 7.02 (s, 2H), 6.95 (d, $J = 8.4$ Hz, 2H), 6.86 (d, $J = 8.1$ Hz, 2H), 6.79 (s, 1H), 6.76 (d, $J = 15.5$ Hz, 2H), 4.98 (d, $J = 7.6$ Hz, 3H), 4.11 (s, 2H), 3.76 (s, 3H), 3.41 (d, $J = 12.4$ Hz, 3H). ^{13}C NMR (125 MHz, CD_3OD): δ 182.2, 166.3, 163.5, 161.6, 158.7, 158.6, 150.0, 147.7, 147.6, 147.5, 143.4, 133.8, 121.1, 120.0, 119.7, 115.7, 114.5, 111.5, 109.8, 104.4, 101.9, 98.3, 94.0, 92.5, 56.7. HRMS (ESI) m/z : $[\text{M} + \text{H}]^+$ calcd for $\text{C}_{29}\text{H}_{27}\text{N}_2\text{O}_9$, 547.1717; found, 547.1716.

3-(6-(5,7-Dihydroxy-4-oxo-4H-chromen-2-yl)-3-(4-hydroxy-3-methoxyphenyl)-2,3-dihydrobenzo[b][1,4]dioxin-2-yl)-*N*-(4-(trifluoromethyl)phenyl)isoxazole-5-carboxamide (4g). Following the general procedure A, 4g was obtained after purification by column chromatography on silica gel (EtOAc/hexane = 70:30) as yellow solid and in 87% yield. ^1H NMR (500 MHz, acetone): δ 13.81 (s, 1H), 8.21 (s, 1H), 7.58 (dd, $J = 12.8, 6.3$ Hz, 2H), 6.98 (dd, $J = 24.5, 16.0$ Hz, 2H), 6.86 (d, $J = 8.0$ Hz, 1H), 6.81–6.74 (m, 2H), 4.99 (d, $J = 8.0$ Hz, 1H), 4.11 (d, $J = 4.0$ Hz, 1H), 3.75 (s, 3H), 3.42 (dd, $J = 26.1, 17.5$ Hz, 2H). ^{13}C NMR (125 MHz, CD_3OD): δ 182.2, 166.3, 165.2, 163.5, 161.6, 158.7, 158.6, 150.0, 147.7, 147.6, 147.5, 143.4, 141.2, 133.8, 132.5, 125.3, 124.6, 121.1, 120.0, 118.7, 115.7, 114.5, 110.5, 109.7, 104.4, 101.9, 98.3, 94.0, 92.5, 56.7. HRMS (ESI) m/z : $[\text{M} + \text{H}]^+$ calcd for $\text{C}_{36}\text{H}_{28}\text{F}_3\text{N}_2\text{O}_{10}$, 705.1696; found, 705.1689.

***N*-((4-Chlorophenyl)sulfonyl)-3-(6-(5,7-dihydroxy-4-oxo-4H-chromen-2-yl)-3-(4-hydroxy-3-methoxyphenyl)-2,3-dihydrobenzo[b][1,4]dioxin-2-yl)isoxazole-5-carboxamide (4h).** Following the general procedure A, 4h was obtained after purification by column chromatography on silica gel (EtOAc/hexane = 70:30) as yellow solid and in 73% yield. ^1H NMR (500 MHz, acetone): δ 13.81 (s, 1H), 8.21 (s, 2H), 7.58 (dd, $J = 8.4, 1.3$ Hz, 2H), 6.98 (dd, $J = 10.2, 2.5$ Hz,

4H), 6.86 (d, $J = 8.0$ Hz, 2H), 6.81–6.74 (m, 2H), 4.99 (d, $J = 8.0$ Hz, 2H), 4.11 (d, $J = 4.0$ Hz, 1H), 3.75 (s, 3H), 3.42 (dd, $J = 26.1$, 17.5 Hz, 2H). ^{13}C NMR (125 MHz, CD_3OD): δ 182.2, 169.5, 166.3, 165.2, 163.5, 161.6, 158.7, 158.6, 150.0, 147.7, 147.6, 147.5, 141.2, 137.5, 138.0, 134.2, 124.6, 121.1, 120.0, 118.7, 115.7, 114.5, 110.5, 109.7, 104.4, 101.9, 98.3, 94.0, 92.5, 56.7. HRMS (ESI) m/z : $[\text{M} + \text{H}]^+$ calcd for $\text{C}_{35}\text{H}_{28}\text{ClN}_2\text{O}_{12}\text{S}$, 735.1051; found, 735.1048.

N-Cyclohexyl-3-(6-(5,7-dihydroxy-4-oxo-4H-chromen-2-yl)-3-(4-hydroxy-3-methoxyphenyl)-2,3-dihydrobenzo[*b*][1,4]dioxin-2-yl)-isoxazole-5-carboxamide (4i). Following the general procedure A, 4i was obtained after purification by column chromatography on silica gel (EtOAc/hexane = 70:30) as yellow solid and in 76% yield. ^1H NMR (500 MHz, DMSO): δ 13.79 (s, 1H), 8.10 (dd, $J = 8.3$, 1.2 Hz, 2H), 7.39 (s, 2H), 7.29 (s, 4H), 7.19 (s, 2H), 7.02 (d, $J = 11.9$ Hz, 2H), 6.91–6.80 (m, 4H), 6.45 (s, 2H), 4.96 (d, $J = 7.7$ Hz, 3H), 1.47–1.40 (m, 3H), 1.25–1.17 (m, 2H); ^{13}C NMR (125 MHz, CD_3OD): δ 182.2, 166.3, 163.5, 161.6, 158.7, 158.6, 150.0, 147.7, 147.6, 147.5, 143.4, 133.8, 121.1, 120.0, 119.7, 115.7, 114.5, 111.5, 109.8, 104.4, 101.9, 98.3, 94.0, 56.7, 51.5, 34.6, 27.9, 24.4. HRMS (ESI) m/z : $[\text{M} + \text{H}]^+$ calcd for $\text{C}_{35}\text{H}_{33}\text{N}_2\text{O}_{10}$, 641.2135; found, 641.2127.

3-(6-(5,7-Dihydroxy-4-oxo-4H-chromen-2-yl)-3-(4-hydroxy-3-methoxyphenyl)-2,3-dihydrobenzo[*b*][1,4]dioxin-2-yl)-*N*-(phenylsulfonyl)isoxazole-5-carboxamide (4j). Following the general procedure A, 4j was obtained after purification by column chromatography on silica gel (EtOAc/hexane = 70:30) as yellow solid and in 80% yield. ^1H NMR (500 MHz, DMSO): δ 13.79 (s, 1H), 8.10 (dd, $J = 8.3$, 1.3 Hz, 2H), 7.39 (s, 2H), 7.29 (s, 2H), 7.19 (s, 2H), 7.02 (d, $J = 11.9$ Hz, 1H), 6.91–6.80 (m, 4H), 6.45 (s, 2H), 4.96 (d, $J = 7.7$ Hz, 2H). ^{13}C NMR (125 MHz, CD_3OD): δ 182.2, 170.2, 163.5, 161.6, 158.7, 158.6, 150.0, 147.7, 147.6, 147.5, 143.4, 133.8, 132.0, 130.8, 127.5, 121.1, 120.0, 119.7, 115.7, 114.5, 111.5, 109.8, 104.4, 101.9, 98.3, 94.0, 56.3. HRMS (ESI) m/z : $[\text{M} + \text{H}]^+$ calcd for $\text{C}_{35}\text{H}_{27}\text{N}_2\text{O}_{12}\text{S}$, 699.1285; found, 699.1281.

General Procedure for the Synthesis of Hydnocarpin-Isoxazolone Derivatives, General Procedure B. For the synthesis of compounds 6a–j, a mixture of equimolar quantities of hydroxylamine hydrochloride (0.07 g, 1 mmol) and β -ketoester (0.130 g, 1 mmol) were stirred in 1 mL of water for 5 min. Then, Hy-CHO and 10 mol % of boric acid was added and the reaction mixture was stirred at room temperature for 6 h. The solid product formed was isolated by simple filtration and washed with water.

(*E*)-3-(Chloromethyl)-4-((6-(5,7-dihydroxy-4-oxo-4H-chromen-2-yl)-3-(4-hydroxy-3-methoxyphenyl)-2,3-dihydrobenzo[*b*][1,4]dioxin-2-yl)methylene)isoxazolidin-5-one (6a). Following the general procedure B, 6a was obtained after purification by column chromatography on silica gel (EtOAc/hexane = 70:30) as yellow solid and in 73% yield. ^1H NMR (500 MHz, acetone): δ 7.51–7.44 (m, 4H), 7.03 (d, $J = 1.7$ Hz, 2H), 6.95 (d, $J = 9.1$ Hz, 2H), 6.87 (dd, $J = 8.1$, 1.8 Hz, 2H), 6.77 (d, $J = 8.1$ Hz, 2H), 6.57 (s, 2H), 6.48 (d, $J = 2.0$ Hz, 2H), 6.15 (d, $J = 1.9$ Hz, 2H), 3.75 (s, 6H), 2.71 (s, 5H). ^{13}C NMR (125 MHz, MeOD): δ 182.3, 147.9, 147.5, 144.0, 127.5, 120.6, 119.8, 117.5, 115.2, 114.9, 111.0, 103.7, 93.9, 78.6, 76.9, 60.5, 55.3. HRMS (ESI) m/z : $[\text{M} + \text{H}]^+$ calcd for $\text{C}_{29}\text{H}_{21}\text{ClNO}_{10}$, 578.0854; found, 578.0848.

(*E*)-4-((6-(5,7-Dihydroxy-4-oxo-4H-chromen-2-yl)-3-(4-hydroxy-3-methoxyphenyl)-2,3-dihydrobenzo[*b*][1,4]dioxin-2-yl)methylene)-3-methylisoxazolidin-5-one (6b). Following the general procedure B, 6b was obtained after purification by column chromatography on silica gel (EtOAc/hexane = 70:30) as yellow solid and in 81% yield. ^1H NMR (500 MHz, acetone): δ 7.51–7.44 (m, 4H), 7.03 (d, $J = 1.7$ Hz, 2H), 6.95 (d, $J = 9.1$ Hz, 2H), 6.87 (dd, $J = 8.1$, 1.8 Hz, 2H), 6.77 (d, $J = 8.1$ Hz, 2H), 6.57 (s, 2H), 6.48 (d, $J = 2.0$ Hz, 2H), 6.15 (d, $J = 1.9$ Hz, 2H), 3.75 (s, 6H), 2.71 (s, 5H). ^{13}C NMR (125 MHz, MeOD): δ 182.3, 173.8, 162.6, 159.7, 147.9, 147.6, 145.5, 144.0, 143.6, 127.5, 121.3, 120.6, 119.82, 117.5, 115.2, 114.9, 111.0, 103.7, 93.9, 87.4, 78.6, 76.9, 60.5, 55.3, 21.8. HRMS (ESI) m/z : $[\text{M} + \text{H}]^+$ calcd for $\text{C}_{29}\text{H}_{22}\text{NO}_{10}$, 544.1244; found, 544.1241.

(*E*)-4-((6-(5,7-dihydroxy-4-oxo-4H-chromen-2-yl)-3-(4-hydroxy-3-methoxyphenyl)-2,3-dihydrobenzo[*b*][1,4]dioxin-2-yl)-

methylene)-3-(trifluoromethyl)isoxazolidin-5-one (6c). Following the general procedure B, 6c was obtained after purification by column chromatography on silica gel (EtOAc/hexane = 70:30) as yellow solid and in 84% yield. ^1H NMR (500 MHz, MeOD): δ 7.51 (d, $J = 2.0$ Hz, 1H), 7.44 (dd, $J = 8.5$, 1.9 Hz, 1H), 6.97 (d, $J = 8.7$ Hz, 2H), 6.81 (dd, $J = 8.0$, 2.4 Hz, 2H), 6.57 (s, 1H), 6.38 (s, 1H), 6.13 (s, 1H), 4.92 (d, $J = 8.0$ Hz, 2H). ^{13}C NMR (125 MHz, MeOD): δ 182.3, 173.8, 164.3, 162.6, 159.7, 147.7, 147.6, 145.5, 144.1, 143.6, 127.5, 121.3, 120.6, 119.82, 117.5, 115.2, 114.9, 111.2, 103.7, 93.9, 87.4, 78.6, 76.5, 60.5, 55.3. HRMS (ESI) m/z : $[\text{M} + \text{H}]^+$ calcd for $\text{C}_{29}\text{H}_{19}\text{F}_3\text{NO}_{10}$, 598.0961; found, 598.0958.

(*E*)-4-((6-(5,7-dihydroxy-4-oxo-4H-chromen-2-yl)-3-(4-hydroxy-3-methoxyphenyl)-2,3-dihydrobenzo[*b*][1,4]dioxin-2-yl)methylene)-3-propylisoxazolidin-5-one (6d). Following the general procedure B, 6d was obtained after purification by column chromatography on silica gel (EtOAc/hexane = 70:30) as yellow solid and in 77% yield. ^1H NMR (500 MHz, MeOD): δ 7.51 (s, 1H), 7.44 (d, $J = 7.8$ Hz, 1H), 6.96 (s, 2H), 6.79 (dd, $J = 14.9$, 4.2 Hz, 2H), 6.58 (s, 1H), 6.39 (s, 1H), 6.13 (s, 1H), 3.79 (d, $J = 4.8$ Hz, 4H), 3.62 (d, $J = 12.4$ Hz, 1H), 3.40 (d, $J = 12.4$ Hz, 1H), 3.22–3.08 (m, 5H). ^{13}C NMR (125 MHz, MeOD): δ 182.3, 181.1, 164.8, 162.6, 159.7, 147.9, 147.6, 145.5, 144.0, 143.6, 127.5, 121.3, 120.6, 119.8, 117.5, 115.2, 104.1, 94.6, 87.5, 78.4, 76.7, 60.4, 56.2, 34.3, 27.5, 22.7. HRMS (ESI) m/z : $[\text{M} + \text{H}]^+$ calcd for $\text{C}_{31}\text{H}_{26}\text{NO}_{10}$, 572.1557; found, 572.1554.

(*E*)-4-((6-(5,7-dihydroxy-4-oxo-4H-chromen-2-yl)-3-(4-hydroxy-3-methoxyphenyl)-2,3-dihydrobenzo[*b*][1,4]dioxin-2-yl)methylene)-3-(4-fluorophenyl)isoxazolidin-5-one (6e). Following the general procedure B, 6e was obtained after purification by column chromatography on silica gel (EtOAc/hexane = 70:30) as yellow solid and in 82% yield. ^1H NMR (500 MHz, MeOD) δ 7.51 (s, 1H), 7.44 (d, $J = 7.8$ Hz, 1H), 6.96 (s, 2H), 6.79 (dd, $J = 14.9$, 4.5 Hz, 2H), 6.58 (s, 1H), 6.39 (s, 1H), 6.13 (s, 1H), 3.79 (d, $J = 4.8$ Hz, 4H), 3.62 (d, $J = 12.4$ Hz, 1H), 3.40 (d, $J = 12.4$ Hz, 1H), 3.22–3.08 (m, 5H). ^{13}C NMR (125 MHz, DMSO): δ 182.2, 181.1, 166.2, 164.8, 163.4, 161.7, 157.7, 148.1, 147.5, 144.0, 136.1, 127.4, 124.8, 122.7, 122.5, 121.00, 118.0, 115.8, 115.2, 104.1, 94.6, 87.4, 78.4, 76.7, 60.4, 56.2. HRMS (ESI) m/z : $[\text{M} + \text{H}]^+$ calcd for $\text{C}_{34}\text{H}_{23}\text{FNO}_{10}$, 624.1306; found, 624.1301.

(*E*)-4-((6-(5,7-Dihydroxy-4-oxo-4H-chromen-2-yl)-3-(4-hydroxy-3-methoxyphenyl)-2,3-dihydrobenzo[*b*][1,4]dioxin-2-yl)methylene)-3-(*p*-tolyl)isoxazolidin-5-one (6f). Following the general procedure B, 6f was obtained after purification by column chromatography on silica gel (EtOAc/hexane = 70:30) as yellow solid and in 85% yield. ^1H NMR (500 MHz, CDCl_3): δ 12.69 (s, 1H), 7.94 (s, 1H), 7.49 (s, 1H), 7.36 (d, $J = 8.6$ Hz, 1H), 7.28 (s, 3H), 6.99 (d, $J = 8.5$ Hz, 1H), 6.88 (s, 2H), 6.47 (s, 1H), 6.38 (s, 1H), 6.26 (s, 1H). ^{13}C NMR (125 MHz, DMSO): δ 182.3, 181.2, 162.6, 159.7, 147.9, 147.6, 145.5, 144.0, 143.6, 142.8, 131.3, 130.6, 130.4, 127.5, 121.3, 120.6, 119.8, 117.5, 115.2, 114.9, 111.0, 103.7, 93.9, 87.4, 78.6, 76.9, 60.5, 55.3, 23.8. HRMS (ESI) m/z : $[\text{M} + \text{H}]^+$ calcd for $\text{C}_{35}\text{H}_{26}\text{NO}_{10}$, 620.1557; found, 620.1552.

(*E*)-3-(4-Chlorophenyl)-4-((6-(5,7-dihydroxy-4-oxo-4H-chromen-2-yl)-3-(4-hydroxy-3-methoxyphenyl)-2,3-dihydrobenzo[*b*][1,4]dioxin-2-yl)methylene)isoxazolidin-5-one (6g). Following the general procedure B, 6g was obtained after purification by column chromatography on silica gel (EtOAc/hexane = 70:30) as yellow solid and in 87% yield. ^1H NMR (500 MHz, CDCl_3): δ 12.69 (s, 1H), 7.92–7.48 (m, 2H), 7.53–7.42 (m, 2H), 7.03 (d, $J = 1.7$ Hz, 1H), 6.82 (dd, $J = 14.8$, 4.5 Hz, 2H), 6.77 (d, $J = 8.1$ Hz, 2H), 6.57 (s, 2H), 6.48 (d, $J = 2.0$ Hz, 2H), 6.15 (d, $J = 1.9$ Hz, 2H), 5.38–5.27 (m, 2H), 3.81 (s, 3H); ^{13}C NMR (125 MHz, DMSO): δ 182.3, 181.1, 162.6, 159.7, 147.9, 147.8, 147.6, 145.5, 144.0, 143.6, 142.8, 131.3, 130.6, 130.4, 127.5, 121.3, 120.6, 119.82, 117.5, 115.2, 114.9, 111.0, 103.7, 93.9, 87.4, 78.6, 76.9, 60.5, 55.3. HRMS (ESI) m/z : $[\text{M} + \text{H}]^+$ calcd for $\text{C}_{34}\text{H}_{23}\text{ClNO}_{10}$, 640.1010; found, 640.1013.

(*E*)-4-((6-(5,7-dihydroxy-4-oxo-4H-chromen-2-yl)-3-(4-hydroxy-3-methoxyphenyl)-2,3-dihydrobenzo[*b*][1,4]dioxin-2-yl)methylene)-3-phenylisoxazolidin-5-one (6h). Following the general procedure B, 6h was obtained after purification by column chromatography on silica gel (EtOAc/hexane = 70:30) as yellow

solid and in 81% yield. ¹H NMR (500 MHz, MeOD): δ 7.53 (s, 2H), 7.18 (d, J = 8.8 Hz, 2H), 7.01–6.92 (m, 5H), 6.80 (dd, J = 14.2, 4.3 Hz, 2H), 6.61 (d, J = 8.8 Hz, 2H), 6.57 (s, 2H), 6.38 (s, 1H), 6.13 (s, 1H), 3.79 (s, 3H). ¹³C NMR (125 MHz, DMSO): δ 182.3, 181.1, 173.8, 162.5, 160.0, 147.9, 147.6, 145.3, 143.8, 143.4, 142.8, 131.3, 130.6, 130.4, 127.5, 121.3, 120.6, 119.8, 117.5, 115.2, 114.6, 111.0, 103.7, 93.9, 87.4, 78.6, 76.9, 60.5, 55.4. HRMS (ESI) *m/z*: [M + H]⁺ calcd for C₃₄H₂₄NO₁₀, 606.1400; found, 606.1407.

(*E*)-4-((6-(5,7-dihydroxy-4-oxo-4H-chromen-2-yl)-3-(4-hydroxy-3-methoxyphenyl)-2,3-dihydrobenzo[*b*][1,4]dioxin-2-yl)-methylene)-2,3-dimethylisoxazolidin-5-one (6i). Following the general procedure B, 6i was obtained after purification by column chromatography on silica gel (EtOAc/hexane = 70:30) as yellow solid and in 79% yield. ¹H NMR (500 MHz, MeOD): δ 7.50 (s, 2H), 7.43 (d, J = 8.3 Hz, 2H), 6.96 (d, J = 9.2 Hz, 2H), 6.80 (dd, 2H), 6.55 (s, 2H), 6.37 (s, 2H), 6.12 (s, 2H), 3.79 (s, 3H), 3.20 (s, 3H). ¹³C NMR (125 MHz, DMSO): δ 182.3, 181.0, 162.6, 159.7, 147.9, 147.6, 145.5, 144.0, 143.6, 127.5, 121.3, 120.6, 119.8, 117.5, 115.2, 114.9, 111.0, 103.7, 93.9, 87.4, 78.6, 76.9, 60.5, 55.3, 45.7, 21.6. HRMS (ESI) *m/z*: [M + H]⁺ calcd for C₃₀H₂₆NO₁₀, 560.1557; found, 560.1552.

(*E*)-4-((6-(5,7-dihydroxy-4-oxo-4H-chromen-2-yl)-3-(4-hydroxy-3-methoxyphenyl)-2,3-dihydrobenzo[*b*][1,4]dioxin-2-yl)-methylene)-3-methyl-2-phenylisoxazolidin-5-one (6j). Following the general procedure B, 6j was obtained after purification by column chromatography on silica gel (EtOAc/hexane = 70:30) as yellow solid and in 75% yield. ¹H NMR (500 MHz, MeOD): δ 7.86–7.72 (m, 3 H), 7.61–7.53 (m, 4H), 7.41 (d, J = 8.3 Hz, 2H), 6.96 (d, J = 9.2 Hz, 2H), 6.80 (dd, J = 14.8, 4.3 Hz, 2H), 6.53 (s, 2H), 6.22 (s, 2H), 6.12 (s, 2H), 5.39–5.27 (m, 2H), 3.79 (s, 3H). ¹³C NMR (125 MHz, DMSO): δ 182.3, 181.1, 173.8, 162.7, 160.3, 153.6, 147.9, 147.6, 145.5, 144.0, 143.6, 136.5, 134.8, 127.5, 121.3, 120.6, 119.8, 117.5, 115.2, 114.7, 111.3, 103.7, 93.9, 87.4, 78.6, 76.9, 60.5, 55.3. HRMS (ESI) *m/z*: [M + H]⁺ calcd for C₃₅H₂₈NO₁₀, 622.1713; found, 622.1715.

Cell Culture. The human lung adenocarcinoma cancer cell line A549 and human metastatic melanoma cell line A375 were obtained from American Type Culture Collection (ATCC, Manassas, VA, USA). Human lung fibroblast cell line WI-38 was kindly gifted from Indian Institute of Chemical Biology (CSIR-IICB), Kolkata, India. Cells were maintained in Dulbecco's modified Eagle medium (DMEM) with 10% fetal bovine serum and 5% CO₂ at 37 °C. Cells were cultured in glass-bottom, 96-well black plates, T25 flasks, T75 flasks, and 4-well chamber slides for various experiments 2 days prior to the conduction of experiments.

In Vitro Cytotoxicity Assays. The growth inhibition capacity of parent compounds, intermediates, and the derivatives were evaluated in cancer cell and normal cell lines initially using the MTT assay as previously reported.⁴² This assay measures cell viability by assessing the cleavage of tetrazolium salt by mitochondrial dehydrogenase. The absorbance was measured at 570 nm using a microplate spectrophotometer (BioTek Power Wave XS). Later, the cytotoxicity was confirmed with LDH assay (Pierce LDH Cytotoxicity Assay Kit-88953, USA) as per the kit protocol using respective controls. Finally, the absorbance at 490 and 680 nm is measured using a spectrophotometer to determine LDH activity. In order to confirm the cytotoxicity using another working principle, we performed BrdU assay kit (colorimetric—11647229001, Roche Diagnostics, IN), as per the instructions given in the kit and explained before,⁴³ measurements were made at 450/690 nm.

Computational Analysis. The crystallized structures of the peptide antagonists of the melanoma inhibitor of apoptosis (PDB code: 1OXN and 1OXQ), crystalline and solution structures of anti-apoptotic protein Bcl-2 (PDB code: 4LVT, 1YSW and 2O21) and the crystal structure of death-associated inhibitor of apoptosis 1, (PDB code: 1JD4) were retrieved from RCSB PDB (Protein Data Bank).⁴⁴ 1OXN and 1OXQ exist as pentamer containing 140 aminoacids, with a resolution of 2.2 and 2.3 Å, respectively. The crystal structure of Bcl-2, 4LVT contains 166 aminoacid with a resolution of 2.05 Å while the solution structures 1YSW and 2O21 contains 164 aminoacids. 1JD4 comprised 124 aminoacids with a resolution of 2.7 Å. These enzymes

were refined, optimized, and minimized by Protein Preparation Wizard of Schrodinger suite 2017-2. The grids were generated around the centroid of the workspace ligand except in 1JD4, in which the grid was generated around the centroid of the site assigned by sitemap analysis.⁴⁵ The prepared enzymes with three-dimensional grid were used for docking against the different conformers of the ligands (4a, 4c, 4f, 4g, 6e, 6f, 6g, and 6i) generated by the ligprep tool, using glide-ligand docking of Schrodinger suite.^{46,47} The docked poses were then ranked based on Dock score (*D*-score) and Glide score (*G*-score) values. The adsorption, distribution, metabolism, and excretion/toxicity were predicted based on the values for pharmacokinetic parameters available from QikProp.

A pharmacophore represent the molecular features that are necessary for molecular recognition of a ligand by the target. In order to predict the structural features/pharmacophore information of multiple ligands (1, 4a, 4c, 4f, 4g, 6c, 6f, 6g, and 6i) that are known to bind to the target, either strongly or weakly, we developed a set of hypotheses. In this approach, the pharmacophore features on each ligand are identified, and a set of common features are sought that satisfy criteria on their positions and directions, to form pharmacophore hypotheses and they can be scored on their geometric alignment. We used phase module of Schrodinger suite for pharmacophore generation.⁴⁸ Here, each ligand structure is represented by a set of points in 3D space, and the pharmacophore sites are characterized by type, location and, if applicable, directionality. We used minimum 50% match of actives and find best alignment/common features of nine ligands by six built-in features of the phase: hydrogen bond acceptor (A), hydrogen bond donor (D), hydrophobic (H), negative ionic (N), positive ionic (P), and aromatic ring (R).

In order to predict the stability and conformational flexibility of the P–L complexes, MD studies were done by Schrodinger-Desmond programme. The simulations were carried out for 10 ns under OPLS-2005 force field with 150 approximate number of frames and trajectory of 66.7 ps.¹³ All systems were solvated in orthorhombic boxes with explicit TIP4P water and the system was neutralized by adding counter ions and simulations were performed for the system under isothermal isobaric ensemble (*NPT*)⁴⁹ with the temperature of 300 K and the pressure of 1.013 bar.⁵⁰ rmsd plots for the backbone atoms for both protein and the ligand bound protein were generated to understand the relative stability of the ligand inside its binding pocket, and the ligand–receptor complexes were visualized. The P–L interaction histogram shows the interactions which favors the binding.

Antioxidant Activity. Earlier studies revealed that acetone extract of *Hydnocarpus wightiana* Blume possess anti-oxidant activity against selected free radicals. This encouraged us to examine the free radical scavenging property of the selected derivatives against multiple experimentally generated free radicals using assays such as DPPH radical scavenging assay, ferric reducing antioxidant power assay, and hydroxyl radical scavenging assay. The detailed experimental procedures adopted are described in the [Supporting Information](#) section 2.

Apoptotic Assays. Evaluation of the mode of cytotoxicity exhibited by the selected derivatives was performed on cancer cells with various apoptotic assays after administration of 20 μM of Hy-ISO-VIII and Hy-ISO-G as described previously.^{42,43,51} Morphological evaluation for apoptotic changes were performed under a phase contrast microscope (Olympus 1X51, Singapore) under suitable magnification. In order to gain a deeper understanding with the morphological changes in a more appropriate platform, AFM was employed and is described in [Supporting Information](#) section 3. Later, detailed investigation of apoptosis was performed with Hoechst, acridine orange–ethidium bromide dual staining, APOPercentage staining dye (Biocolor, Belfast, Northern Ireland), TUNEL assay (Dead End fluorometric TUNEL system G3250, Promega, USA), and finally by FITC-Annexin V staining (BD Pharmingen no. 556547, BD Biosciences, San Jose, CA) as per previously mentioned procedures and the experimental details are explained in ([Supporting Information](#) section 3).

Antimetastatic Assays. The potential of both the selected derivatives on the complex process of cancer metastasis was evaluated using multiple assays including wound healing assay, colony formation assay, invasion assay, and migration assay as described previously^{4,52} with both A549 and A375 cells. Here, a concentration below the cytotoxic potential (10 nM) was administered and the detailed experimental procedures adopted is described in [Supporting Information](#) section 4.

Cell Cycle Analysis. To study the role of NPCEs in suppression of cell proliferation and metastasis, cell cycle analysis was performed with flow cytometric analysis and also on a microscopic platform with the aid of cell clock assay with the administration of 10 nM of the compounds detailed experimental procedures adopted is described in the [Supporting Information](#) section 5.

Mitochondrial Membrane Potential Assay. Initially, JC1 assay was employed to study the depolarization of mitochondrial membrane potential using 5,5',6,6'-tetrachloro-1,1',3,3'-tetraethylbenzimidazolcarbocyanine iodide (JC-1). The cells were plated onto 12-well plates (1×10^5 cells/well) on a 5% CO₂ incubator at 37 °C. These cells were then treated with selected HY-ISO derivatives (1 μM) for 4h and were further incubated with 1 mM JC-1 in HBSS at 37 °C for 20–30 min. The cells were observed under an inverted fluorescent microscope, using a FITC filter (Olympus IX51, Singapore) after the cells had incubated at room temperature for an additional 20 min. Later, the mitochondrial membrane depolarization was further confirmed using TMRE mitochondrial membrane potential assay in which a lipophilic, cationic dye which accumulates in the negatively charged mitochondrial matrix is utilized. The cells were plated onto 12-well plates (1×10^5 cells/well) on a 5% CO₂ incubator at 37 °C. When the cells attained almost 70% confluency, they were subjected to different treatments (1 μM), cells were trypsinized, washed with ice cold phosphate buffered saline (PBS, pH 7.4) thrice, lysed, and mitochondrial membrane potential estimation was performed as per the kit protocol (TMRE-Mitochondrial Membrane Potential Assay Kit, ab113852, Abcam, Cambridge, UK). Further, measurements were made with a fluorimeter (FLx800, Bio-Tek, Winooski, VT, USA) at an excitation wavelength of 490 nm and an emission wavelength of 510 nm.

Caspase Assay. The cells were plated onto T25 flask (1×10^5 cells/well) on a 5% CO₂ incubator at 37 °C. When the cells attained almost 70% confluency, they were administered with HY-ISO-VIII and HY-ISO-G (1 μM). The effect of both initiator caspases (caspases 8, 9, and 2) and executioner caspases (caspase 3) was determined by using Apo Alert Caspase Profiling kit (Clontech, CA, USA) as per the kit protocol. Cells were treated with compounds for 12 h and finally, samples were transferred to 96-well plates for fluorimetric reading (excitation: 380 nm; emission: 460 nm), and the intensity values obtained was recorded under a spectrofluorometer (FLx800, BioTek).

Statistical Analysis. Data represent the mean ± standard deviation (SD) of three replicates, analyzed using GraphPad PRISM v5.0 (GraphPad Software Inc., San Diego, CA). Statistically significant differences were considered if $P < 0.05$, as determined using one-way analysis of variance (ANOVA). IC₅₀ values were calculated using the Easy Plot software (Spiral Software, MD). Fluorescent microscopic images were processed with Progress software, and analysis was carried out using ImageJ software (version 1.48, NIH) and MATLAB 8.3 (MATLAB R2014a, MA). WI-Tec Project plus (v 2.1) software package was used for data evaluation with the confocal Raman microscopy.

Raman Spectral Imaging. SERS experiments were performed with the aid of a confocal Raman microscope (WI-Tec, Inc., Germany) with a laser beam directed to the sample through 20× objective with a Peltier cooled CCD detector. For cellular imaging, 20 μL of gold nanoparticles was added. SERS mapping was recorded by focusing the laser beam on the cell surface selected at a position $z = 0$ μm using 0.5 as the integration time, 150 × 150 as points per line, and 50 × 50 μm mapping area along the X and Y directions. The Raman and SERS cell maps were acquired over a motorized scan stage. The chemical images were computed from the 2D collection of Raman/SERS spectra by integrating the intensity of a specific band over a

defined wave number range after baseline subtraction. A minimum of three independent measurements were made for each sample. WI-Tec Project plus (v 2.1) software package was used for data analysis. Cellular imaging and spectral analysis of genomic DNA were carried out using previously described procedure.³³

DNA Fragmentation Analysis. A549 cells were grown in 6-well plates and were subjected to the treatment with HY-ISO-VIII and HY-ISO-G. Total DNA was isolated using the DNA isolation kit from Geneaid (Cat. no. GB300, BR BIOCHEM life sciences) and the experiments were performed as per kit instructions, and later, the isolated DNA was run on agarose gels. The detailed experimental procedure is described in [Supporting Information](#) section 6.1. Further, DNA fragmentation after 3 h treatment with compounds was carried out according to the protocol from chemometec “DNA fragmentation assay” (application note no. 3003. rev. 1.4). NucleoCounter NC-3000 (chemometec) was used for quantification and interpretation. The experimental details are given in [Supporting Information](#) section 6.2.

GSH Estimation. Estimation of the cellular GSH was determined from the cell lysates of A375 and A549 cells. Briefly, cells were plated onto 12-well plates (1×10^5 cells/well) on a 5% CO₂ incubator at 37 °C. When the cells attained almost 70% confluency, they were subjected to different treatments; cells were trypsinized, washed with ice cold PBS, (pH 7.4) thrice, lysed, and GSH estimation was performed as per kit protocol (K251-100, BioVision, USA). Further, measurements were made with a fluorimeter (FLx800, Bio-Tek, Winooski, VT, USA) at an excitation wavelength of 360 nm and an emission wavelength of 460 nm.

Cyt c Quantitation. Cancer cells were maintained in 10% DMEM and were treated with Hy-ISO-VIII and Hy-ISO-G (20 μM) for 4 to 12 h. The cytosolic level of cyt c was estimated using an ELISA kit (KH01051, Invitrogen, Camarillo, CA) as per instructions given. The protein content was normalized using BCA assay (Thermo Fisher Scientific, IL, USA). Finally, the absorbance at 450 nm was measured using a microplate spectrophotometer (BioTek Power Wave XS). Concentration of the controls and test samples were obtained from the standard curve of cyt c and the data were expressed after the respective controls were normalized to be 100%.

Apoptosis Antibody Array. Semi-quantitative analysis of 43 human apoptosis markers were performed using the human apoptosis antibody array membrane (ab134001, Abcam, Cambridge, MA) according to the manufacturer's instructions. Cancer cells were treated with Hy-ISO-VIII and Hy-ISO-G (20 μM) for 12 h while maintaining control cells without the treatment, and the experiments were performed as per kit instructions. Signals were quantified by a chemiluminescence system (Bio-Rad, CA, USA) immediately after the addition of detection buffers with an exposure time limited within 30 seconds. Densitometry data of the membrane were analyzed using ImageJ software (version 1.48, NIH, USA). For each array membrane, the density of each spot was normalized with respect to its own positive controls and later each treatment was compared with respect to the vehicle control membrane. The fold change was calculated using the intensity value. Proteins that are 2-fold and above, which are differentially expressed with a p value of <0.05 (using Student's t -test), were subjected to unsupervised hierarchical clustering using the cluster map function available in the seaborn library of an object-oriented programming language, python.

■ ASSOCIATED CONTENT

📄 Supporting Information

The Supporting Information is available free of charge on the ACS Publications website at DOI: [10.1021/acs.jmedchem.9b01098](https://doi.org/10.1021/acs.jmedchem.9b01098).

All procedures, supporting figures, and tables ([PDF](#))

■ AUTHOR INFORMATION

Corresponding Authors

*E-mail: manumjoseph2000@gmail.com (M.M.J.).

*E-mail: manojkumart@gmail.com (T.K.M.).

*E-mail: kkmaiti@niist.res.in (K.K.M.).

ORCID 

Kaustabh K. Maiti: 0000-0003-3368-6929

Notes

The authors declare no competing financial interest.

ACKNOWLEDGMENTS

K.K.M. thanks the Department of Science and Technology (DST) Nano Mission, Government of India (SR/NM/NS-1152/2016), CSIR Mission mode project, Nano biosensor and microfluidics for healthcare (HCP-0012). Dr. K. G. Raghu, Principal Scientist, APTD, CSIR-NIIST for providing the plant material. Dr. K. V. Radhakrishnan, Sr. Principal Scientist, CSTD, CSIR-NIIST for valuable suggestions. AcSIR PhD student J.S.A. thanks the Department of Science and Technology (DST)-INSPIRE for research fellowship. M.M.J. thanks the Science and Engineering Research Board (SERB), DST, Government of India for the National Post-Doctoral Research Fellowship (PDF/2016/001391).

ABBREVIATIONS

AFM, atomic force microscopy; BrdU, 5-bromo-2'-deoxyuridine; cyt c, cytochrome c; DCFDA, dichlorofluorescein diacetate; GSH, glutathione; JC1, 5,5,6,6-tetrachloro-1,10,3,3'-tetraethylbenzimidazolcarbocyanine; LDH, lactate dehydrogenase; MCR, multi-component reaction; MTT, 3-(4,5-dimethylthiazol-2-yl)-2,5-diphenyltetrazolium bromide; P-L, protein-ligand; PS, phosphatidylserine; SASA, solvent-accessible surface area; SERS, surface-enhanced Raman spectroscopy; TMRE, tetramethylrhodamine, ethyl ester

REFERENCES

- (1) Decorte, B. L. Underexplored Opportunities for Natural Products in Drug Discovery. *J. Med. Chem.* **2016**, *59*, 9295–9304.
- (2) Cragg, G. M.; Newman, D. J.; Snader, K. M. Natural Products in Drug Discovery and Development. *J. Nat. Prod.* **1997**, *60*, 52–60.
- (3) Sahoo, M. R.; Dhanabal, S. P.; Jadhav, A. N.; Reddy, V.; Muguli, G.; Babu, U. V.; Rangesh, P. *Hydnocarpus*: An Ethnopharmacological, Phytochemical and Pharmacological Review. *J. Ethnopharmacol.* **2014**, *154*, 17–25.
- (4) Mathai, B. M.; Joseph, M. M.; Maniganda, S.; Nair, J. B.; Arya, J. S.; Karunakaran, V.; Radhakrishnan, K. V.; Maiti, K. K. Guanidinium Rich Dendron-Appended *Hydnocarpin* Exhibits Superior Anti-Neoplastic Effects through Caspase Mediated Apoptosis. *RSC Adv.* **2016**, *6*, 52772–52780.
- (5) Martins, P.; Jesus, J.; Santos, S.; Raposo, L.; Roma-Rodrigues, C.; Baptista, P.; Fernandes, A. Heterocyclic Anticancer Compounds: Recent Advances and the Paradigm Shift towards the Use of Nanomedicine's Tool Box. *Molecules* **2015**, *20*, 16852–16891.
- (6) Joseph, M. M.; Narayanan, N.; Nair, J. B.; Karunakaran, V.; Ramya, A. N.; Sujai, P. T.; Saranya, G.; Arya, J. S.; Vijayan, V. M.; Maiti, K. K. Exploring the Margins of SERS in Practical Domain: An Emerging Diagnostic Modality for Modern Biomedical Applications. *Biomaterials* **2018**, *181*, 140–181.
- (7) Kang, B.; Austin, L. A.; El-Sayed, M. A. Observing Real-Time Molecular Event Dynamics of Apoptosis in Living Cancer Cells Using Nuclear-Targeted Plasmonically Enhanced Raman Nanoprobes. *ACS Nano* **2014**, *8*, 4883–4892.
- (8) Sun, L.; Yu, C.; Irudayaraj, J. Surface-Enhanced Raman Scattering Based Nonfluorescent Probe for Multiplex DNA Detection. *Anal. Chem.* **2007**, *79*, 3981–3988.
- (9) Kozikowski, A. P.; Tapadar, S.; Luchini, D. N.; Kim, K. H.; Billadeau, D. D. Use of the Nitrile Oxide Cycloaddition (NOC) Reaction for Molecular Probe Generation: A New Class of Enzyme

Selective Histone Deacetylase Inhibitors (HDACIs) Showing Picomolar Activity at HDAC6. *J. Med. Chem.* **2008**, *51*, 4370–4373.

(10) Neelapapu, R.; Holzle, D. L.; Velaparthy, S.; Bai, H.; Brunsteiner, M.; Blond, S. Y.; Petukhov, P. A. Design, Synthesis, Docking, and Biological Evaluation of Novel Diazide-Containing Isoxazole- and Pyrazole-Based Histone Deacetylase Probes. *J. Med. Chem.* **2011**, *54*, 4350–4364.

(11) Simoni, D.; Roberti, M.; Invidiata, F. P.; Rondanin, R.; Baruchello, R.; Malagutti, C.; Mazzali, A.; Rossi, M.; Grimaudo, S.; Capone, F.; Dusonchet, L.; Meli, M.; Raimondi, M. V.; Landino, M.; D'Alessandro, N.; Tolomeo, M.; Arindam, D.; Lu, S.; Benbrook, D. M. Heterocycle-Containing Retinoids. Discovery of a Novel Isoxazole Arotinoid Possessing Potent Apoptotic Activity in Multidrug and Drug-Induced Apoptosis-Resistant Cells. *J. Med. Chem.* **2001**, *44*, 2308–2318.

(12) Spencer, J. P. E.; Abd El Mohsen, M. M.; Rice-Evans, C.; Rice-Evans, C. Cellular Uptake and Metabolism of Flavonoids and Their Metabolites: Implications for Their Bioactivity. *Arch. Biochem. Biophys.* **2004**, *423*, 148–161.

(13) Guo, Z.; Mohanty, U.; Noehre, J.; Sawyer, T. K.; Sherman, W.; Krilov, G. Probing the α -Helical Structural Stability of Stapled p53 Peptides: Molecular Dynamics Simulations and Analysis. *Chem. Biol. Drug Des.* **2010**, *75*, 348–359.

(14) Murray, J. C. In vitro metabolism studies on the isoxazole ring scission in the anti-inflammatory agent leflunomide to its active alpha-cyanoenol metabolite A771726: mechanistic similarities with the cytochrome P450-catalyzed dehydration of aldoximes. *Drug Metab. Dispos.* **2003**, *31*, 1240–1250.

(15) Sznarkowska, A.; Kostecka, A.; Meller, K.; Piotr, K. Inhibition of Cancer Antioxidant Defense by Natural Compounds. *Oncotarget* **2017**, *8*, 15996–16016.

(16) Sysak, A.; Obmińska-Mrukowicz, B. Isoxazole Ring as a Useful Scaffold in a Search for New Therapeutic Agents. *Eur. J. Med. Chem.* **2017**, *137*, 292–309.

(17) Zhang, D.; Raghavan, N.; Chen, S.-Y.; Zhang, H.; Quan, M.; Lecureux, L.; Patrone, L. M.; Lam, P. Y. S.; Bonacorsi, S. J.; Knabb, R. M.; Skiles, G. L.; He, K. Reductive Isoxazole Ring Opening of the Anticoagulant Razaxaban Is the Major Metabolic Clearance Pathway in Rats and Dogs. *Drug Metab. Dispos.* **2008**, *36*, 303–315.

(18) Yokoyama, C.; Sueyoshi, Y.; Ema, M.; Mori, Y.; Takaishi, K.; Hisatomi, H. Induction of oxidative stress by anticancer drugs in the presence and absence of cells. *Oncol. Lett.* **2017**, *14*, 6066–6070.

(19) Alqathama, A.; Prieto, J. M. Natural Products with Therapeutic Potential in Melanoma Metastasis. *Nat. Prod. Rep.* **2015**, *32*, 1170–1182.

(20) Kitchin, K. T.; Brown, J. L.; Lijinsky, W. Biochemical studies of six nitrogen-containing heterocycles in rat tissues. *Biochem. Pharmacol.* **1989**, *38*, 2733–2738.

(21) Priyadarisini, R. V.; Murugan, R. S.; Maitreyi, S.; Ramalingam, K.; Karunakaran, D.; Nagini, S. The Flavonoid Quercetin Induces Cell Cycle Arrest and Mitochondria-Mediated Apoptosis in Human Cervical Cancer (HeLa) Cells through P53 Induction and NF- κ B Inhibition. *Eur. J. Pharmacol.* **2010**, *649*, 84–91.

(22) Xu, S.; Yao, H.; Luo, S.; Zhang, Y.-K.; Yang, D.-H.; Li, D.; Wang, G.; Hu, M.; Qiu, Y.; Wu, X.; Yao, H.; Xie, W.; Chen, Z.-S.; Xu, J. A Novel Potent Anticancer Compound Optimized from a Natural Oridonin Scaffold Induces Apoptosis and Cell Cycle Arrest through the Mitochondrial Pathway. *J. Med. Chem.* **2017**, *60*, 1449–1468.

(23) Jiang, Y.-L.; Liu, Z.-P. Natural Products as Anti-Invasive and Anti-Metastatic Agents. *Curr. Med. Chem.* **2011**, *18*, 808–829.

(24) Wang, W.; Heideman, L.; Chung, C. S.; Pelling, J. C.; Koehler, K. J.; Birt, D. F. Cell-Cycle Arrest at G2/M and Growth Inhibition by Apigenin in Human Colon Carcinoma Cell Lines. *Mol. Carcinog.* **2000**, *28*, 102–110.

(25) Srivastava, S.; Somasagara, R. R.; Hegde, M. Quercetin, a Natural Flavonoid Interacts with DNA, Arrests Cell Cycle and Causes Tumor Regression by Activating Mitochondrial Pathway of Apoptosis. *Sci. Rep.* **2016**, *6*, 24049.

- (26) Desai, A.; Qazi, G.; Ganju, R.; El-Tamer, M.; Singh, J.; Saxena, A.; Bedi, Y.; Taneja, S.; Bhat, H. Medicinal Plants and Cancer Chemoprevention. *Curr. Drug Metab.* **2008**, *9*, 581–591.
- (27) Li, Z.; Gao, Q. Induction of Apoptosis in HT-29 Cells by Quercetin through Mitochondria-Mediated Apoptotic Pathway. *Anim. Cells Syst.* **2013**, *17*, 147–153.
- (28) Gerauer, H.; Wachter, Y.; Zunino, S. J. Resveratrol Induces Extensive Apoptosis by Depolarizing Mitochondrial Membranes and Activating Caspase-9 in Acute Lymphoblastic Leukemia Cells. *Cancer Res.* **2001**, *16*, 4731–4739.
- (29) Mantena, S. K.; Sharma, S. D.; Katiyar, S. K. Berberine, a natural product, induces G1-phase cell cycle arrest and caspase-3-dependent apoptosis in human prostate carcinoma cells. *J. Med. Chem.* **2006**, *5*, 296–308.
- (30) Wang, I.-K.; Lin-Shiau, S.-Y.; Lin, J.-K. Induction of Apoptosis by Apigenin and Related Flavonoids Through Cytochrome c Release and Activation of Caspase-9 and Caspase-3 in Leukaemia HL-60 Cells. *Eur. J. Cancer* **1999**, *35*, 1517–1525.
- (31) Keresztury, G.; Holly, S.; Besenyi, G.; Varga, J. Vibrational Spectra of Monothiocarbamates-II* IR and Raman Spectra, Vibrational Assignment, Conformational Analysis and ab initio Calculations of S-methyl-N, N-Dimethylthiocarbamate. *Spectrochim. Acta, Part A* **2007**, *49*, 2007–2026.
- (32) Movasaghi, Z.; Rehman, S.; Rehman, I. U. Raman Spectroscopy of Biological Tissues. *Appl. Spectrosc. Rev.* **2015**, *42*, 493–541.
- (33) Narayanan, N.; Nair, L. V.; Karunakaran, V.; Joseph, M. M.; Nair, J. B.; Ramya, A. N.; Jayasree, R. S.; Maiti, K. K. Investigation of Apoptotic Events at Molecular Level Induced by SERS Guided Targeted Theranostic Nanoprobe. *Nanoscale* **2016**, *8*, 11392–11397.
- (34) Ramya, A. N.; Joseph, M. M.; Maniganda, S.; Karunakaran, V.; Sreelekha, T. T.; Maiti, K. K. Emergence of Gold-Mesoporous Silica Hybrid Nanotheranostics: Dox-Encoded, Folate Targeted Chemotherapy with Modulation of SERS Fingerprinting for Apoptosis Toward Tumor Eradication. *Small* **2017**, *13*, 1700819.
- (35) Gottlieb, E.; Armour, S. M.; Harris, M. H.; Thompson, C. B. Mitochondrial Membrane Potential Regulates Matrix Configuration and Cytochrome c Release during Apoptosis. *Cell Death Differ.* **2003**, *10*, 709–717.
- (36) Brazhe, N. A.; Evlyukhin, A. B.; Goodilin, E. A.; Semenova, A. A.; Novikov, S. M.; Bozhevolnyi, S. I.; Chichkov, B. N.; Sarycheva, A. S.; Baizhumanov, A. A.; Nikelshparg, E. I.; Deev, L. I.; Maksimov, E. G.; Maksimov, G. V.; Sosnovtseva, O. Probing Cytochrome c in Living Mitochondria with Surface-Enhanced Raman Spectroscopy. *Sci. Rep.* **2015**, *5*, 13793.
- (37) Sitter, D. Vibrational Spectroscopy of Chemisorbed Fatty Acids with Inelastic Electron Tunneling. *Science* **2000**, *192*, 1128–1130.
- (38) Wei, L.; Yu, Y.; Shen, Y.; Wang, M. C.; Min, W. Vibrational Imaging of Newly Synthesized Proteins in Live Cells by Stimulated Raman Scattering Microscopy. *Proc. Natl. Acad. Sci. U.S.A.* **2013**, *110*, 11226–11231.
- (39) Lyng, F. M.; Faoláin, E. Ó.; Conroy, J.; Meade, A. D.; Knief, P.; Duffy, B.; Hunter, M. B.; Byrne, J. M.; Kelehan, P.; Byrne, H. J. Vibrational spectroscopy for cervical cancer pathology, from biochemical analysis to diagnostic tool. *Exp. Mol. Pathol.* **2007**, *82*, 121–129.
- (40) Circu, M. L.; Aw, T. Y. Glutathione and Apoptosis. *Free Radical Res.* **2008**, *64*, 689–706.
- (41) Park, C.; Lee, W.; Go, S.-I.; Nagappan, A.; Han, M. Morin, a Flavonoid from Moraceae, Induces Apoptosis by Induction of BAD Protein in Human Leukemic Cells. *Int. J. Mol. Sci.* **2015**, *16*, 645–659.
- (42) Joseph, M. M.; Aravind, S. R.; Varghese, S.; Mini, S.; Sreelekha, T. T. PST-Gold Nanoparticle as an Effective Anticancer Agent with Immunomodulatory Properties. *Colloids Surf., B* **2013**, *104*, 32–39.
- (43) Joseph, M. M.; Nair, J. B.; Maiti, K. K.; Therakathinal, T. S. Plasmonically Enhanced Galactoxyloglucan Endowed Gold Nanoparticles Exposed Tumor Targeting Biodistribution Envisaged in a Surface-Enhanced Raman Scattering Platform. *Biomacromolecules* **2017**, *18*, 4041–4053.
- (44) Franklin, M. C.; Kadkhodayan, S.; Ackerly, H.; Alexandru, D.; Distefano, M. D.; Elliott, L. O.; Flygare, J. A.; Mautisa, G.; Okawa, D. C.; Ong, D.; Vucic, D.; Deshayes, K.; Fairbrother, W. J. Structure and Function Analysis of Peptide Antagonists of Melanoma Inhibitor of Apoptosis (ML-IAP). *Biochemistry* **2003**, *42*, 8223–8231.
- (45) Halgren, T. New Method for Fast and Accurate Binding-Site Identification and Analysis. *Chem. Biol. Drug Des.* **2007**, *69*, 146–148.
- (46) Friesner, R. A.; Banks, J. L.; Murphy, R. B.; Halgren, T. A.; Klicic, J. J.; Mainz, D. T.; Repasky, M. P.; Knoll, E. H.; Shelley, M.; Perry, J. K.; Shaw, D. E.; Francis, P.; Shenkin, P. S. Glide: A New Approach for Rapid, Accurate Docking and Scoring. 1. Method and Assessment of Docking Accuracy. *J. Med. Chem.* **2004**, *47*, 1739–1749.
- (47) Steinbrecher, T. B.; Dahlgren, M.; Cappel, D.; Lin, T.; Wang, L.; Krilov, G.; Abel, R.; Friesner, R.; Sherman, W. Accurate Binding Free Energy Predictions in Fragment Optimization. *J. Chem. Inf. Model.* **2015**, *55*, 2411–2420.
- (48) Dixon, S. L.; Knoll, E. H.; Rao, S. N.; Shaw, D. E.; Friesner, R. A. PHASE: A New Engine for Pharmacophore Perception, 3D QSAR Model Development, and 3D Database Screening: 1. Methodology and Preliminary Results. *J. Comput.-Aided Mol. Des.* **2006**, *20*, 647–671.
- (49) Azam, M. A.; Jupudi, S. Extra Precision Docking, Free Energy Calculation and Molecular Dynamics Studies on Glutamic Acid Derivatives as MurD Inhibitors. *Comput. Biol. Chem.* **2017**, *69*, 55–63.
- (50) Singh, S. P.; Gupta, D. Discovery of Potential Inhibitor against Human Acetylcholinesterase: A Molecular Docking and Molecular Dynamics Investigation. *Comput. Biol. Chem.* **2017**, *68*, 224–230.
- (51) Kamath, P. R.; Sunil, D.; Joseph, M. M.; Abdul Salam, A. A.; Sreelekha, T. T. Indole-Coumarin-Thiadiazole Hybrids: An Appraisal of Their MCF-7 Cell Growth Inhibition, Apoptotic, Antimetastatic and Computational Bcl-2 Binding Potential. *Eur. J. Med. Chem.* **2017**, *136*, 442–451.
- (52) Cao, Y.; Zhao, M.; Zhu, Y.; Zhu, Z.-H.; Oberer, L.; Duan, J.-A. Diselaginellin B, an Unusual Dimeric Molecule from *Selaginella pulvinata*, Inhibited Metastasis and Induced Apoptosis of SMMC-7721 Human Hepatocellular Carcinoma Cells. *J. Nat. Prod.* **2017**, *80*, 3151–3158.